Jimmy B. Lomax 732

Final Report:

FEASIBILITY STUDY OF SCANNING CELESTIAL ATTITUDE DETERMINATION SYSTEM (SCADS) FOR SMALL SCIENTIFIC SPACECRAFT (S^3)

Contract No. NAS5-10367

Control Data Project No. 9574

RD 2004

September 1, 1967

Prepared for:

National Aeronautics and Space Administration
Goddard Space Flight Center
Greenbelt, Maryland

Aerospace Research Department
CONTROL DATA CORPORATION
8100 34th Avenue South
Minneapolis, Minnesota 55440

Final Report:

FEASIBILITY STUDY OF SCANNING CELESTIAL ATTITUDE DETERMINATION SYSTEM (SCADS) FOR SMALL SCIENTIFIC SPACECRAFT (S^3)

Contract No. NAS5-10367

Control Data Project No. 9574

RD 2004

September 1, 1967

Prepared for:

National Aeronautics and Space Administration
Goddard Space Flight Center
Greenbelt, Maryland

Aerospace Research Department
CONTROL DATA CORPORATION
8100 34th Avenue South
Minneapolis, Minnesota 55440

ABSTRACT

This report describes the feasibility of using an electro-optical celestial scanning sensor on board the Small Scientific Spacecraft (S^3) for determination of the spacecraft attitude by utilizing star measurements. The sensor basically consists of a wide-angle lens with a transparent slit positioned on the focal surface, a photomultiplier detector positioned behind the slit aperture and star signal processing electronics. For a spin stabilized S^3 vehicle, the sensor rotates with the vehicle. For non-spinning vehicles, the slit is rotated by a synchronous motor. After automatic identification of the stars detected, the vehicle attitude is determined by computer solution of the system constraint equations.

The study effort was largely devoted to the areas of optical design, electrical design, signal detection analysis, evaluation of system operational constraints, and system error analysis. Standardized sensor designs were recommended for application to all S^3 orbital configurations.

FOREWORD

This report was prepared by Control Data Corporation, Research Division, under National Aeronautics and Space Administration, Goddard Space Flight Center, Contract No. NAS5-10367. Since the requirements for this study were similar to requirements for other SCADS applications, some of the material presented in this report is similar to previously documented literature relating to SCADS sensors.

The Control Data Project Engineer and principal investigator was Donald F. Nickel. Other areas of technical responsibility were assigned as follows: C. B. Grosch, mathematical analysis, error analysis, detailed star availability, and bright body interference; R. W. Peterson, sun shield design and particle radiation study; J. S. Newcomb, optical design; H. R. Paetznick, computer programming. The above named personnel were also contributing authors of this report. R. L. Lillestrand assisted as technical consultant and as liaison with NASA.

Control Data Corporation would particularly like to acknowledge the technical guidance of the National Aeronautics and Space Administration Technical Project Officer, Irving B. Lowen, and the NASA S^3 Associate Project Scientist, Dr. Robert A. Hoffman.

TABLE OF CONTENTS

Title Page		i
Abstract		iii
Foreword		v
Table of Contents		vii
List of Figures		x
List of Tables		xv
Glossary		xvi
I.	INTRODUCTION	1
	A. Statement of Problem	1
	B. Orbital Configurations for S^3	2
	C. Basic Description of Sensor	4
	D. Overall Summary of Study	6
II.	DETERMINATION OF ATTITUDE FROM STAR TRANSITS	9
III.	DESCRIPTION OF SENSOR DESIGN PARAMETERS	13
IV.	DESIGN ANALYSIS AND PROCEDURE	17
	A. Determination of Cant Angle	17
	B. Determination of Field of View	20
	C. Selection of Photomultiplier	27
	D. Sensitivity of Photomultiplier to Star Radiation	29
	E. Electronic Filter Analysis	38
	F. Determination of Optical Aperture	58
	G. Sun Shield Analysis	65
	H. Lens System f/number	73
	I. Blur Spot Size	74
	J. Slit Reticle Dimensions	75
V.	REQUIRED DESIGN PARAMETERS FOR SPIN STABILIZED VEHICLE	79
	A. Elliptical Equatorial Orbit	84
	1. Cant Angle	84
	2. Field of View	87
	3. Optical Aperture	88
	4. Blur Spot Size	88
	5. Filter Cut-off Frequency	89
	B. Near-circular, Near-polar Orbit	90
	1. Cant Angle	90
	2. Field of View	92
	3. Optical Aperture	93
	4. Blur Spot Size	93
	5. Filter Cut-off Frequency	93

TABLE OF CONTENTS (continued)

	C. Longitude-Synchronous	95
	1. Cant Angle	95
	D. Near-circular, Near-equatorial	96
	1. Cant Angle	96
VI.	STANDARDIZED SENSOR DESIGN PARAMETERS	97
VII.	OPTICAL DESIGN	103
VIII.	DETAILED STAR AVAILABILITY	111
	A. Elliptical Equatorial Orbit	111
	B. Near-circular, Near-polar, Spin Stabilized Satellite	111
	C. Near-circular, Near-polar, Magnetically Stabilized Satellite	115
	D. Near-circular, Low Altitude Orbit	115
	E. Longitude-Synchronous, Gravity Gradient	115
IX.	ERROR ANALYSIS	121
	A. Transit Time Errors Due to Shot Noise	121
	B. Attitude Error Analysis	133
X.	EVALUATION OF OPERATIONAL CONSTRAINTS	141
	A. Sun and Earth Interference	142
	1. Elliptical Equatorial Orbit	142
	2. Near-polar, Near-circular, Spin Stabilized Orbit	144
	3. Magnetically Stabilized Satellite	156
	4. Near-circular, Low Altitude Orbit	156
	5. Longitude-Synchronous Orbit	163
	B. Particle Radiation Restrictions	173
	1. Bremsstrahlung	173
	2. X-Ray Prediction by Bremsstrahlung in Aluminum	173
	3. Cerenkov Radiation	182
	4. Shielding the Photocathode	190
	5. Allowable Noise	193
	6. Luminescence	196
	7. Electron Microscope Data	197
	8. Strontium 90 Irradiation	198
	9. Shielding Requirement of S^3	203
XI.	ELECTRONIC DESIGN	205
	A. Electronics for Spin Stabilized Vehicle	205
	1. Photomultiplier Overload Protection	212
	2. Design of High Voltage Power Supply	213
	B. Field Stabilized Vehicle	221
	C. Clock Resolution and Stability Required for SCADS-S^3	225

TABLE OF CONTENTS (concluded)

XII.	ESTIMATED SENSOR VOLUME, WEIGHT, AND POWER	229
	A. Volume	229
	B. Weight	232
	C. Power	234
XIII.	TEST PROCEDURES	237
	A. Component Tests	238
	1. Optical System	238
	2. Photomultiplier and Power Supply	239
	3. Sun Shutter	239
	4. Motor Drive	239
	B. Laboratory Bench Test	240
	C. Field Test with Real Stars	243
	D. Prototype Environmental Tests	245
	E. Flight Model Environmental Tests	246
REFERENCES		247
APPENDIX A	Orientation of a Rigid Torque-Free Body By Use of Star Transits	251
APPENDIX B	Attitude Determination for the Gravity-Gradient and Magnetically Stabilized Modes	257
APPENDIX C	Data Sheets for EMR-541N Photomultiplier	267

LIST OF FIGURES

Figure	Title	Page
1	Basic Sensor Configuration for Spin Stabilized S^3 Vehicle	5
2	Relation Between $\hat{n}$ and $\hat{s}$ at the Instant of Transit	10
3	SCADS Design Parameters	14
4	Light Scattering When Incident Rays are Less Than 90^o to Optical Axis	19
5	Field of View Required to Include Three Stars Brighter Than Magnitude M_V	24
6	Elemental Scanned Area on Celestial Sphere	25
7	Cathode Radiant Sensitivity and Spectral Energy Distribution of Vega	30
8	Effective Spectral Energy Distribution for Vega and EMR-541N Cathode	32
9	Comparison of Photomultiplier Spectral Response and Spectral Energy Distribution of "Red" Stars	33
10	Effective Spectral Energy Distribution for "Red" Stars	35
11	Filtering of Star Pulse	39
12	Percent of Star Radiation Passing Scanning Slit	43
13	Normalized Ratio of Peak Signal-to-RMS Noise for Two Pole Filter	52
14	Star Pulse Input Signal to Filter, f(t); Filter Impulse Response, h(t); and Output Signal, y(t)	55
15	Practical Circuit Configuration Having Quadratic Transfer Function for Low Pass Active Filter	57
16	Connected Cones for Radiation Shielding	66
17	Radiation Shield	67
18	Specular Reflecting Radiation Shield	69
19	Minimum Cone Size as a Function of Sun Angle Off Optical Axis (Field of View, 20 Degrees)	71
20	Geometry for Determination of Slit Dimensions	76
21	Schematic of Typical Vehicle Assembly and Optical Axis Location (approximate)	80
22	The Elliptical Equatorial Orbit	85

LIST OF FIGURES (continued)

23	Angular Subtent of Earth Versus Satellite Position	86
24	Geometry of Field of View for Near-circular, Near-polar, Spin Stabilized Orbits	91
25	Collapsible Sun Shield	101
26	.4" Clear Aperture Optical System Scan Period, 15 Seconds min.	107
27	.8" Clear Aperture System, Scan Period 4 to 15 Seconds	108
28	2.0" Clear Aperture Optical System, Scan Period ½ Second to 4.5 Seconds	109
29	Number of Stars in Field of View as a Function of Sun's Right Ascension and Various Photographic Magnitude Limits--Elliptical Equatorial Orbit	112
30	Assumed Effective Field of View for Near-circular, Near-polar, Spin Stabilized Orbit	113
31	Number of Stars in Field of View as a Function of Orbital Normal's Right Ascension--Near-circular, Near-polar, Spin Stabilized Orbit	114
32A	Probability of Finding Various Numbers of Stars in Field of View of $M_p \leq 4$. Magnetically Stabilized Satellite	116
32B	Probability of Finding Various Numbers of Stars in Field of View of $M_p \leq 3$. Magnetically Stabilized Satellite	117
32C	Probability of Finding Various Numbers of Stars in Field of View of $M_p \leq 2$. Magnetically Stabilized Satellite	118
33	Number of Stars in Field of View as a Function of Direction of Spin Axis for Near-circular, Low Altitude Orbit ($i = 33^o$)	119
34	Number of Stars in Field of View as a Function of True Anomaly for Gravity Gradient Stabilized Satellite	120
35	Threshold Crossing of Noise-free Star Pulse	122
36	Leading Edge Threshold Crossing	125
37	Total Attitude Error, Σ, for the Elliptic Equatorial Orbit	135

LIST OF FIGURES (continued)

38	Probability of Total Attitude Error Being $\leq$ a Given Value for Elliptic Equatorial Orbit	136
39	Attitude Error for the Near-circular, Polar, Spin Stabilized Satellite	137
40	Attitude Error for the Magnetically Stabilized Satellite	138
41	Attitude Error for the Near-equatorial, Low Altitude Orbit	139
42	Attitude Error for the Gravity Gradient Stabilized Satellite	140
43	Best Case Viewability	143
44	Worst Case Viewability	145
45	The Sun's Position with Respect to Orbital Plane	147
46	The Vectors $\hat{P}_1$ and $\hat{P}_2$	149
47	Viewability for Circular, Near-polar, Spin Stabilized Orbit, $\beta_E = \beta_S = 70^o$, $\epsilon = 90^o$	152
48	Viewability for Circular, Near-polar, Spin Stabilized Orbit, $\beta_E = 50^o$, $\beta_S = 70^o$, $\epsilon = 90^o$	153
49	Viewability for Circular, Near-polar, Spin Stabilized Orbit, $\beta_E = \beta_S = 70^o$, $\epsilon = 56^o$	154
50	Viewability for Circular, Near-polar, Spin Stabilized Orbit, $\beta_E = 50^o$, $\beta_S = 70^o$, $\epsilon = 56^o$	155
51	Orientation of S^3 with Respect to Magnetic Field	157
52	Viewability for Magnetically Stabilized Satellite, $\beta_S = \beta_E = 70^o$, $\epsilon = 90^o$	158
53	Viewability for Magnetically Stabilized Satellite, $\beta_S = 70^o$, $\beta_E = 50^o$, $\epsilon = 90^o$	159
54	Viewability for Magnetically Stabilized Orbit, $\beta_E = \beta_S = 70^o$, $\epsilon = 56^o$	160
55	Viewability for Magnetically Stabilized Satellite, $\beta_S = 70^o$, $\beta_E = 50^o$, $\epsilon = 90^o$	161
56	Geometry of Near-circular, Low Altitude Orbit	162
57	Viewability for Low Inclination, Low Altitude Orbit, $\beta_E = \beta_S = 70^o$, $\alpha = 0^o$	164
58	Viewability for Low Inclination, Low Altitude Orbit, $\beta_E = 50^o$, $\beta_S = 70^o$, $\alpha = 0^o$	165

LIST OF FIGURES (continued)

59	Viewability for Low Inclination, Low Altitude Orbit, $\beta_E = \beta_S = 70^o$, $\alpha = 90^o$	166
60	Viewability for Low Inclination, Low Altitude Orbit, $\beta_E = 50^o$, $\beta_S = 70^o$, $\alpha = 90^o$	167
61	Limiting Detectable Star Magnitude Versus Normal Stellar Background Level x 2^n. Optical Aperture = .8 inch	168
62	Limiting Detectable Star Magnitude Versus Normal Stellar Background Level x 2^n. Optical Aperture = 2 inches	169
63	Reticle Shutter	171
64	No. of Photons and Energy Radiated Bremsstrahlung	177
65	$X_1 = .25$ gms/cm^2	178
66	$X_1 = 2.5$ gms/cm^2	179
67	Average Photon Energy Brem strahlung	180
68	Number of Bremsstrahlung Protons as a Function of Shield Thickness of Aluminum, Incident Electron Energy as a Parameter	181
69	Cerenkov Factor	184
70	Electron Map AE2 Omnidirectional Flux at the Geomagnetic Equator (Electron/cm^2 sec)	188
71	Range of Electrons and Protons in Aluminum	189
72	Quantum Efficiency 541E-05M Typical	191
73	Star Signal Flow Diagram	206
74	S^3 Electronics Block Diagram	206
75	Waveforms Illustrating Background Filtering	208
76	Block Diagram for High Voltage Power Supply	214
77	Voltage Doubler Circuit	216
78	Voltage Tripler Circuit	216
79	Interlaced Dual Even-Odd Multiplier	218
80	Cockroft-Walton Multiplier for EMR 14 Stage Photomultiplier Tube	219
81	Charging Time of a 14 Stage Cockroft-Walton Multiplier	220

LIST OF FIGURES (concluded)

82	SASI Motor Block Diagram	223
83	Laboratory Test Fixture for SCADS	241

APPENDIX B

B-1	The Coordinate System S_2	261
B-2	The Slit Plane with Respect to S	264

LIST OF TABLES

Table	Title	Page
I	Classes of Orbits	3
II	Total Number of Stars in Celestial Sphere Brighter than Visual Magnitude M_V	21
III	Maximum Allowable Cant Angle as Function of Boom Length	22
IV	Limiting Star Magnitude Versus Field of View	87
V	Required Optical Aperture to Detect Star Magnitude M_V	88
VI	Required Optical Aperture Versus Scan Period	94
VII	Optimum Filter Frequencies at Specific Scan Periods	94
VIII	Scan Period Required for Motor Driven Reticle	99
IX	Sun Shield Dimensions for 70° Sun Angle	100
X	Sun Shield Dimensions for 50° Sun Angle	100
XI	Design Parameter Summary	102
XII	Off-the-Shelf Lenses Available for Testing	105
XIII	Slit Width Interpolation Factor Versus Signal-to-Noise Ratio	130
XIV	Interpolation Factor Versus Threshold Level	131
XV	Interpolation Factor for Large Signal-to-Noise Ratios	131
XVI	Ranges of True Anomaly and Time for Which There Is No Usable Field, Some Usable Field, and Total Usable Field	146
XVII	S^3 Clock Resolution	227
XVIII	Recommended Number of Stages for SCADS-S^3 Clock	228
XIX	Estimated Volume of SCADS-S^3 Sensor	230
XX	Sun Shield Volume	231
XXI	Estimated Weight of SCADS-S^3 Sensor	232
XXII	Estimated Power Required for SCADS-S^3 Sensor	234

GLOSSARY

a (Section V)	=	distance from center of vehicle baseplate to center of lens
α	=	the right ascension of the optical axis
α (Section IV-G)	=	angle of the sun shield's outer cone with respect to the optical axis
α (Section V)	=	azimuth angle subtended at the base plate center by the boom and the projection of the line from the base plate center to the lens. The projection being on the base plate.
α_i	=	right ascension of the i^{th} star
β	=	angle between the sun and the optical axis
β (Section X-A)	=	angle between (center of earth) - sun vector and (center of earth) - satellite vector
β_E	=	the angle between the optical axis and the vector from the spacecraft to any point on the viewable sunlit earth
β_s	=	the angle between the spacecraft-sun vector and the optical axis
b (Section V)	=	length of boom measured from center of base plate
$\widehat{BC}$	=	the blur spot size defined as the angle subtended by the star image (in the focal plane) as measured from the plane containing the biconvex equivalent of the optical system
C_s	=	stray capacity at photodetector output
C_2 and C_1	=	capacitors in an active filter
d	=	the field image size defined as the maximum diameter of the full field image in the lens focal plane
D	=	optical system clear aperture
δ	=	declination of the optical axis
δ_i	=	declination of the i^{th} star
ϵ_o	=	the optical efficiency defined as the ratio of the incident star energy incident on the focal plane to the radiant star energy incident on the lens clear optical aperture

F	=	equivalent focal length of a complex lens which is defined as the distance from the central plane of a thin biconvex lens, whose magnification is the same as the complex lens, to the image plane when the lens is focused on an object at infinity
$f_b = \Delta f$	=	noise equivalent bandwidth of the electronic filter
f_c	=	electronic filter frequency parameter
$f(\lambda)$	=	monochromatic intensity of star radiant energy at wavelength λ
f/no.	=	the ratio of the lens focal length, F, to the optical aperture, D
FOV	=	optical system field of view which is defined as the full field angle subtended by a simple convex lens equivalent of the optical system
f(t)	=	noise-free output signal from the photodetector which is the input signal to the detection electronics
γ	=	angle subtended from the vehicle spin axis to a star as observed from the axis of the equivalent biconvex lens
Γ	=	cant angle at which the optical axis is inclined with respect to the vehicle spin axis (principal body axis)
G(t)	=	time profile of the radiant star energy passing through a slit scanning a star image at a uniform time rate
H(s)	=	transfer function of electronic filter
h(t)	=	impulse response of the electronic filter
I	=	angle between the optical axis vector and the vector normal to the (earth-center)-spacecraft vector when the two vectors lie in the same plane
I_B	=	average current produced by stellar background radiation striking the photodetector
I_{BD}	=	average value of noise current due to the stellar background plus dark current
I_D	=	average dark current of the photodetector

$I_{KS} = I_S$	=	average current produced by star radiation striking the photodetector
I_{RMS}	=	root-mean-square (RMS) value of noise current
I_T	=	threshold value of current
L	=	dimension of the specular reflecting sunshield which is minimized
λ	=	wavelength of light
λ_s	=	average number of photons received from the star per unit time
M_c	=	magnitude correction factor for a given class star spectrum which must be added to the visual magnitude to obtain the actual instrument magnitude
M_I	=	instrument magnitude determined by the star spectral energy distribution and the instrument spectral response
M_p	=	photographic star magnitude
M_v	=	visual star magnitude
$\hat{n}$	=	unit vector normal to the plane determined by the slit's projection on the celestial sphere (Figure 2)
N_B	=	the stellar background radiation which characterizes the integrated intensity of the weak star radiation contributed per unit area on the celestial sphere
n_{BD}	=	the average effective number of equally weighted photocathode emissions due to background plus dark current which occur during time interval T_s
N_f	=	the false detection rate which characterizes the expected number of false star detections per scan period caused by random noise
N_R	=	RMS noise level per unit bandwidth at the electronic filter output
N_S	=	number of radial slits
n_s	=	the average effective number of equally weighted photocathode emissions due to star signal current I_S occurring during a transit interval T_s
n_T	=	the average number of electron emissions from the cathode during time interval T_s which occur at the threshold level
ω_c	=	$2\pi f_c$

GLOSSARY (continued)

P_d	=	the detection probability which determines the chances of detecting the star signal given the condition that a star brighter than the limiting magnitude has transited the slit
$\hat{P}_1$	=	unit vector from earth's center in the direction of the point on the earth's horizon nearest to the spacecraft spin axis
$\hat{P}_2$	=	unit vector from the earth's center in the direction of a point lying on the boundary between the sunlit and dark region of the earth
ϕ (Section V-A)	=	half angle subtended by the earth as seen from the spacecraft
ϕ (Section X-A)	=	angle from orbital normal and vector from spacecraft to earth's horizon
r	=	sun shield cone dimension which is minimized
$\hat{r}$	=	unit vector from earth's center in the direction of the satellite
R (Section IV-J)	=	radial distance from the intersection of the optical axis and the focal plane to the star image centered in the slit
R (Section X-A)	=	earth radius
$R = \overline{fb}$ (Section IV-G)	=	knife edge sun shield cone dimension which is minimized
R_i	=	random variable having a uniform distribution between 0 and 1.
R_L	=	load resistor at photodetector output
R_2 and R_1	=	resistors in an active filter
ρ (Section X-A)	=	angle between the spacecraft-sun vector and the vector from the spacecraft to on the sunlit earth nearest the spacecraft spin axis
ρ_{ij}	=	correlation coefficient between the random noise current I_i at time t_i and current I_j at time t_j
$\hat{s}$	=	unit vector to the star
S_A	=	total slit area as projected onto the celestial sphere

GLOSSARY (continued)

S_K	=	sensitivity of the photomultiplier cathode to stellar radiation
$\frac{S}{N}$	=	ratio of peak signal to RMS noise at the filter output
$\widehat{SW}$	=	rotational slit width
σ	=	dispersion of the star image diffraction pattern on the focal plane
$\frac{\sigma_I}{I}$	=	ratio of the RMS variation in the signal peak to the average value of the signal peak
$\sigma(\theta)$	=	RMS value of the rotational angle error for a star transit
$\sigma(t_s)$	=	RMS value of the star pulse transit times
T	=	scan period
t_a	=	threshold crossing time of the star pulse leading edge
t_b	=	threshold crossing time of the star pulse trailing edge
t_s	=	transit time of a star pulse
T_s	=	time required for the center point of the star image to cross the slit
θ	=	the uncanted field of view centered on the spin axis
θ (Section V)	=	the angle subtended at the lens center by the optical axis and a line connecting the boom end to the lens center
ν	=	true anomaly (angle between earth center-spacecraft vector and the earth center-orbital perigee vector)
W_s	=	linear dimension of the slit width in the focal plane at radial distance R from the optical axis
x	=	outside diameter of the knife edge sun shield
y	=	height of the knife edge sun shield
y_{peak}	=	peak value of the electronic filter output signal

$y(t)$	=	output signal from the electronic filter
z_i	=	angle between the optical axis and the i^{th} star

Section X-B

c	=	light velocity
E	=	energy of mono-energetic, normally incident electrons
E_c	=	Cerenkov radiation energy per electron
ϵ_o	=	optical efficiency
ϵ_q	=	quantum efficiency
F	=	ratio of peak signal to RMS noise
k	=	number of photoevents produced by each fast incident electron having energy greater than 1 Mev
ℓ	=	photocathode window thickness
L	=	earth radii
m	=	electron mass
N	=	average number of photons produced at angular frequency ω
N_β	=	faint star background in tenth magnitude stars per square degree
N_B	=	average cathode photoelectron rate due to faint star background
N_C	=	average cathode photoelectron rate due to Cerenkov radiation
N_p	=	average cathode photoelectron rate due to photoevents produced by particle radiation
n_o	=	photon density per second incident on the earth's atmosphere from Vega
n_{pe}	=	expected number of cathode photoelectrons per second due to electrons having energy above 1 Mev
ω	=	radiation angular frequency
p	=	electron momentum
ϕ	=	electron flux density
R_c	=	photocathode radius
S	=	average cathode photoelectron rate due to star radiation
τ	=	range of photons in aluminum

GLOSSARY (continued)

Section X-B

ν	=	occurrence rate of photoevents
v	=	electron velocity
X_o	=	range of electrons with energy E_o in aluminum

SCANNING CELESTIAL ATTITUDE DETERMINATION SYSTEM (SCADS) FOR SMALL SCIENTIFIC SPACECRAFT (S^3)

I. INTRODUCTION

The purpose of this feasibility study is to describe the attitude determination problem for the Small Scientific Spacecraft (S^3), the method of solution using a Scanning Celestial Attitude Determination System (SCADS), and the instrumentation required to acquire data for the solution.

A. Statement of Problem

The basic motivation for this study is that of determining the three axis attitude (pitch, roll, and yaw) of a S^3 space vehicle using an electro-optical celestial scanning sensor. By scanning the celestial sphere, the sensor must provide measurements of star positions so the spacecraft attitude can be determined to an accuracy of 0.1 degree by a computer at a ground station. The basic problem considered in this study is to determine the required design parameters for a SCADS sensor, with emphasis directed toward minimizing size, weight, and power. Additional emphasis is directed toward design of a standardized sensor which can be employed in a wide variety of orbital configurations and associated environments. The spacecraft may be either spin stabilized or local vertical stabilized and it is required to operate in several classes of orbital configurations. It is also required for spin stabilized vehicles that the spin axis nutation and the spin period be determined, with the required spin period accuracy being given as .03%. Nutation is defined in References [1] (p. 165) and [2].

B. Orbital Configurations for S^3

Four general classes of orbits are to be considered. These classes are summarized in Table I.

For the spin stabilized satellite, the spin axis will nearly coincide with the longitudinal axis of the satellite. For the elliptical equatorial orbit, the satellite will be intermittently torqued so that the angle between the sun and the spin axis will lie between 20° and 70°.

The magnetically stabilized satellite will be passively stabilized so that the longitudinal axis will nearly coincide with the local direction of the magnitude field, but the satellite may very slowly roll about this direction.

In later sections, we will treat each of these orbits in more detail.

TABLE I

CLASSES OF ORBITS

Orbit	Apogee Ht.	Perigee Ht.	Inclination	Stabilization	Direction of Longitudinal Axis
Elliptical Equatorial	25,600 km	250 km	0^{o}	Spin- 15 sec period	Equatorial Plane
Near-circular Near-polar	500 km	300 km	$90^{o} \pm 10^{o}$	a) Spin- 30 sec period	Normal to orbital plane
				b) Magnetic	Along field
				c) Spin- 0.5 sec period	Normal to orbital plane
Longitude-Synchronous	35,000 km	35,000 km	33^{o}	Gravity Gradient	Toward Earth's Center
Near-circular Low Altitude	300 km	350 km	33^{o}	Spin- 120 sec	Ecliptic Plane

C. Basic Description of Sensor

The study first describes the mathematical model and the constraint equations from which the spacecraft attitude may be determined from star transit data. Next the major sensor design parameters are defined followed by the formulation of a design procedure. The ideal design parameters are then determined for each orbital configuration from which a set of standardized sensor parameters are selected. Sensor operational constraints are evaluated. Finally sensor size, weight, and power are estimated.

The sensor must operate in two vehicle stabilization modes, spin stabilized and field (magnetic or gravity) stabilized. Figure 1 shows the basic sensor configuration for the spin stabilized vehicle. The basic sensor components are a wide-angle lens with a slit positioned on the focal surface, a photomultiplier detector positioned behind the slit aperture, and star signal processing electronics. A sun shield is required to shield against scattered radiation from the sun or sun-illuminated earth and moon. The sensor for the spin stabilized mode consists of no moving parts, rotates with the spin stabilized vehicle which causes star images to transit the slit. Radiant star energy passing through the slit is converted into electrical pulses which are then processed by the system electronics. The basic electronic function is to digitally encode the time that each star brighter than a fixed threshold transits the slit.

The sensor for the field stabilized vehicle is similar to the spin stabilized version except that a synchronous motor must be added to rotate the slit reticle at a constant angular rate to provide the scanning motion.

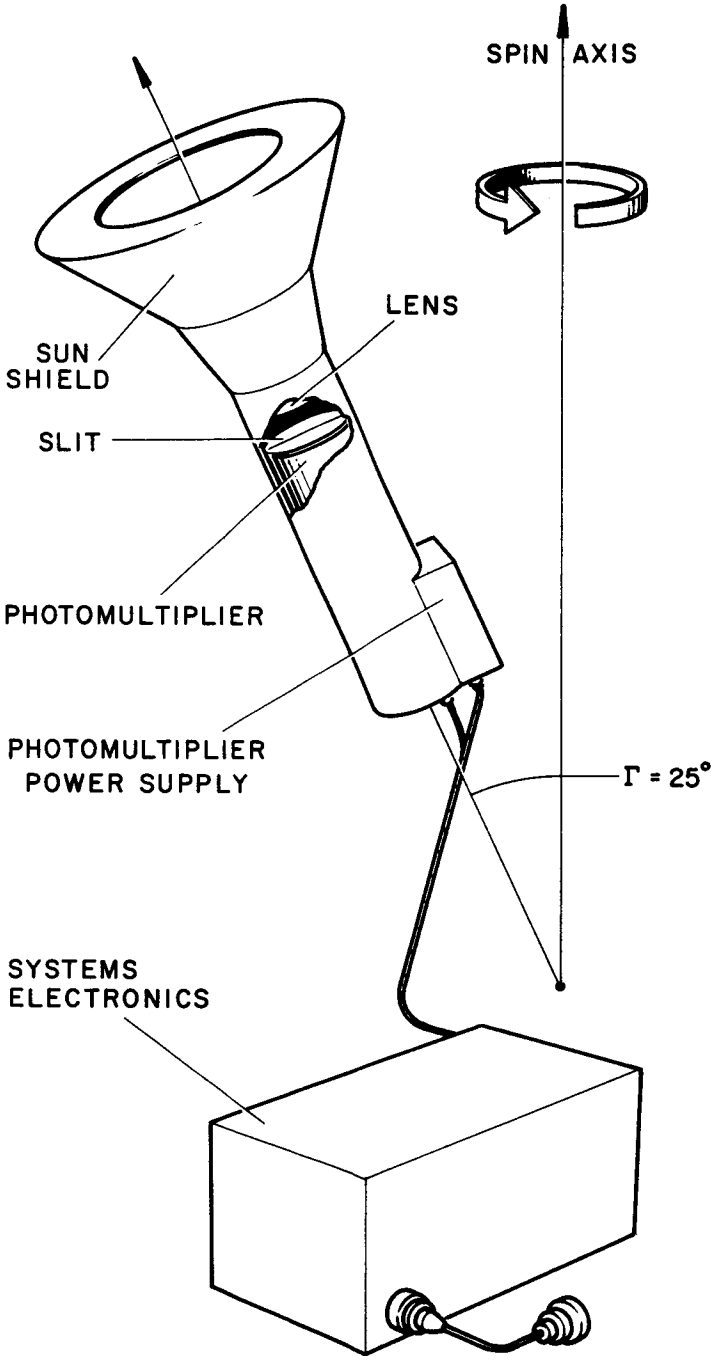

FIGURE 1: Basic Sensor Configuration for Spin Stabilized S^3 Vehicle

D. Overall Summary of Study

As a result of this feasibility study, it can be generally concluded that a small, standardized SCADS sensor could be successfully employed to determine the S^3 spacecraft attitude accurate to 0.1 degree RMS per axis for a wide variety of orbital configurations.

Some of the gross characteristics of the SCADS-S^3 sensor are summarized below:

Cant Angle (spin stabilized vehicle) = 40^o
Field of View = 40^o
Optical Aperture:
.8 inch for scan periods $\geq$ 4 seconds
2.0 inch for scan periods $\geq$ ½ second
Number of slits - One (radial to spin axis)
Rotational Slit Width - 18 arc-minutes
Photomultiplier - EMR 541N
Required Star Magnitude Threshold - $+2^m.5$
Detection Probability - .95
Average False Detection Rate - One per five scan periods
Estimated Sensor Size (excluding Sun Shield)
(a) Spin Stabilized Vehicle
1. For D = .8 inch, volume = 19.7 in^3
2. For D = 2.0 inches, volume = 27.4 in^3
(b) Field Stabilized Vehicle - 23.7 in^3
Estimated Sensor Weight
(a) Spin Stabilized Vehicle
1. For D = .8 inch, weight = 2.2 pounds
2. For D = 2.0 inches, weight = 3.4 pounds
(b) Field Stabilized Vehicle - 2.7 pounds
Estimated Sensor Power
(a) Spin Stabilized Vehicle - 1.0 watt

(b) Field Stabilized Vehicle - 2.2 watts

It may be emphasized here that the sensor design can be further standardized if the size and weight of the two inch optical aperture could be tolerated for all missions.

II. DETERMINATION OF ATTITUDE FROM STAR TRANSITS

The general method of attitude determination by use of transit times of known stars across a slit will now be discussed. At this point, we assume transit data has been received from the vehicle and has previously been tagged, i.e., known stars have been associated with each transit time.

A slit is scribed on the focal plane of an optical system. Such a slit describes a curve when projected on the celestial sphere. If the slit is a straight line and the optical system is distortion free, then the curve is a great circle. Such will be considered the case here.

The instrumentation is such that the slit is either fixed with respect to the satellite (spin stabilized satellites) or rotates with respect to the satellite in some precisely known manner (non-spin stabilized satellites). In either case, the great circle projection of the slit can be described by an equation which contains only known parameters if such an equation is written utilizing a coordinate system fixed in the satellite.

At the instant a star transits the slit, we know the star lies on the slit's projection. Hence, at this instant we may write,

$$\hat{n} \cdot \hat{s} = 0 \tag{1}$$

where

$\hat{n}$ = unit vector normal to the plane determined by the slit's projection on the celestial sphere;

$\hat{s}$ = unit vector to the star (Figure 2).

Since the slit is in a known position with respect to the satellite, $\hat{n}$ is easily written in a coordinate system fixed in the satellite. On the other hand $\hat{s}$ is most easily written in a celestial coordinate system (a system in

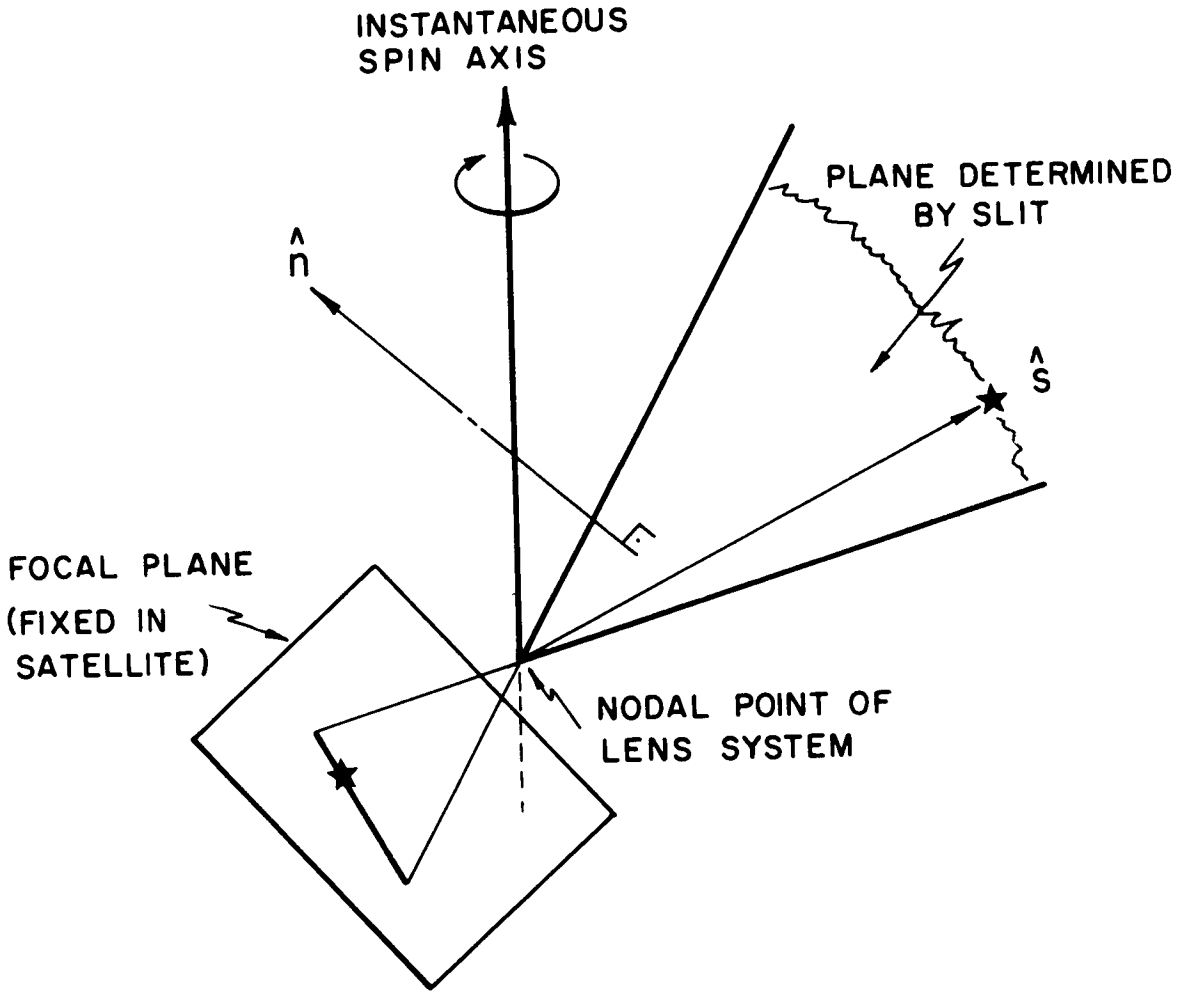

FIGURE 2: Relation Between $\hat{n}$ and $\hat{s}$ at the Instant of Transit

which the star directions are catalogued). In order to write these vectors in the same coordinate system, parameters which specify the orientation of the coordinate system fixed in the body with respect to the celestial system must be introduced. However, these are the very parameters we are interested in determining.

In order to introduce parameters which allow $\hat{n}$ and $\hat{s}$ to be written in the same coordinate system, the physics which govern the attitude motion of the satellite must be considered. As of this writing three basic models have been considered. These models assume the following types of constraints on the satellite dynamics:

(1) spinning rigid, nearly symmetric, torque free body;

(2) spinning rigid, nearly symmetric, nearly torque free body;

(3) attitude controlled such that roll, pitch, and yaw are slowly varying functions of time (slow with respect to the scan period of the slit which is rotated with respect to the satellite).

Of these models, (1) has been analyzed, programmed, and applied. A discussion may be found in References [1] and [2]. For convenience, Reference [2] has been included in this report as Appendix A. Models (2) and (3) have been analyzed, but not programmed. The total problem as it evolves about model (3) is given in Appendix B.

The models (1) and (3) imply total problems which are much easier than that presented by model (2). For model (2), a system of differential equations is forced upon us which does not appear to have a convenient analytical solution. Fortunately, it does not appear we need such a model for the S^3 missions.

In general then, model (1) can be applied to the spin stabilized missions of the S^3 series, and model (3) can be applied to the non-spin stabilized missions. However, it was pointed out by NASA-GSFC that the assumption of a

rigid body is not adequate in a time interval near a period in which the satellite passes from light to dark side of the earth or vice versa. During these time intervals the satellite's booms significantly expand or contract. This deficiency of the model may be overcome by allowing the two nearly equal moments of inertia to be functions of time or (as suggested by NASA-GSFC) by allowing the spin and precession rates to be linear functions of time. Of these methods, the first is more correct but implies more analysis. A start on such an analysis is given in Reference [3]. The second method can be easily incorporated into the present program.

III. DESCRIPTION OF SENSOR DESIGN PARAMETERS

This section will define the most significant design parameters for the SCADS sensor. After these parameters have been defined, a logical design procedure will be developed in the next section for determining the required parameters.

The SCADS sensor basically consists of three subsystems, namely, the optical system, the photomultiplier, and the electronics. In defining the SCADS parameters, it will be assumed that the S^3 vehicle is spin stabilized with the SCADS sensor axis fixed in the vehicle and that the sensor rotates as the vehicle rotates about its angular momentum vector. The design parameters are similarly defined for a SCADS sensor aboard a non-spinning, field stabilized vehicle. The parameters of the optical system will be defined first.

Figure 3 illustrates the parameters associated with the optical system for a SCADS sensor aboard a spin stabilized vehicle. In Figure 3 the instantaneous position of the field of view and slit are shown projected on a sphere where the slit rotation about the vehicle spin axis is fixed at an azimuth angle, Ω, with respect to the plane of the figure. The star image shown within the slit is displaced at a zenith angle, γ, from the vehicle spin axis. From Figure 3, the parameters associated with the optical system may be adequately characterized as follows:

(a) the cant angle, Γ, is defined as the angle at which the optical axis is inclined with respect to the vehicle spin axis (body principal axis);

(b) the equivalent focal length, F, of a complex lens is the distance from the central plane of a thin biconvex lens, whose magnification is the same as the complex lens, to the image plane when the lens is focused on an object at infinity;

(c) the field of view, FOV, is the full field angle subtended by a simple biconvex lens equivalent of the optical system;

(d) the optical aperture, D, is defined as the diameter of the clear aperture of the optical system;

(e) the lens f number, f/no., is defined as the ratio of the focal length, F, to the optical aperture, D;

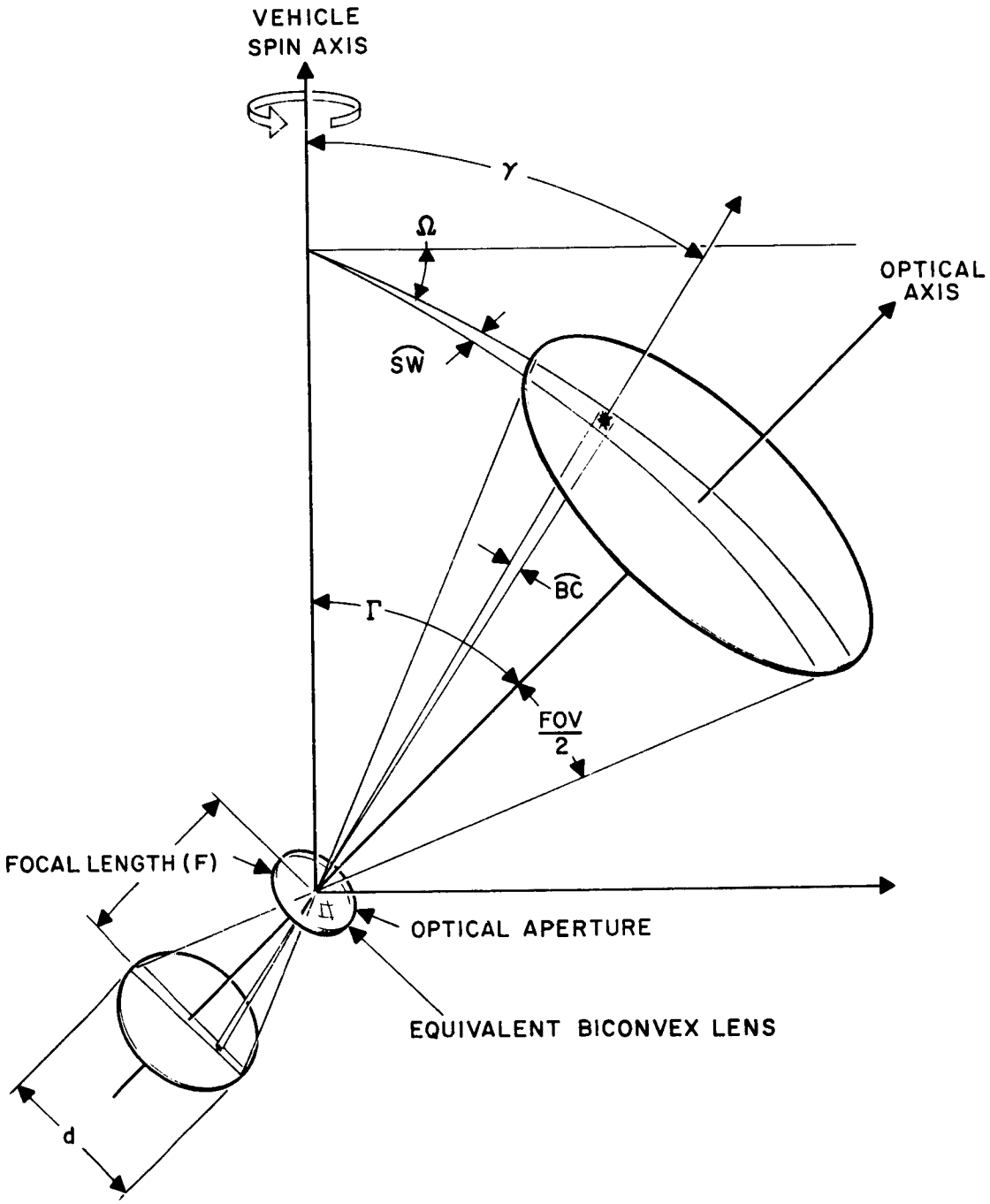

FIGURE 3: SCADS Design Parameters

(f) the blur spot size, $\widehat{BC}$, is defined as the angle subtended by the star image (in the focal plane) as measured from the intersecting point of the optical axis and the plane containing the biconvex equivalent of the optical system;

(g) the field image size, d, is defined as the maximum diameter of the full field image in the lens focal plane;

(h) the optical efficiency, ϵ_o, is defined as the ratio of the radiant star energy incident on the focal plane to the radiant star energy incident on the lens clear optical aperture.

Closely related to the parameters of the optical system are the slit parameters in the lens focal plane. In order to obtain uniform transit times of the stars across a slit, the slit configuration is taken as a portion of a pie-shaped section as shown in Figure 3. The slit is symmetrical about a line (great circle as projected on the celestial sphere) radial to the spin axis. The width of the slit is characterized by a rotational angle, $\widehat{SW}$.

Several major parameters satisfactorily characterize the SCADS photomultiplier. Of particular importance are the photomultiplier sensitivity to stellar radiation, S_K, the cathode dark current, I_D, and the physical dimensions.

The threshold detection of star signals in the presence of shot noise at the photomultiplier output requires electronic analog signal filtering (smoothing). The electronic filter is adequately characterized by its transfer function, H(s), and the cut-off frequency, f_c, which most nearly matches the filter impulse response and the star signal.

The most important parameters characterizing the sun shield are its height above the optics and its outside diameter. These dimensions are dependent upon the optical field of view, the optical aperture, and the angle, β, between the sun and the optical axis.

Other important parameters must be defined in order to adequately describe the above sensor characteristics. These parameters include:

(a) the limiting magnitude star, M, which must be detected in order to insure that three stars brighter than this magnitude are within the field of view for a given probability;

(b) the stellar background radiation, N_B, which characterizes the integrated intensity of the weak star radiation contributed per unit area on the celestial sphere;

(c) the false detection rate, N_f, characterizes the expected number of false star indications per scan period caused by random background noise;

(d) the detection probability, P_d, determines the chances of detecting the star signal given the condition that a star brighter than the limiting magnitude has transited the slit.

IV. DESIGN ANALYSIS AND PROCEDURE

After the SCADS design parameters have been properly defined, it is necessary to formulate a logical design procedure which will lead to an orderly determination of each parameter. An optimum design procedure should rely upon a minimum number of arbitrary assumptions and should ideally consist of an ordered sequence of computations which systematically determines each parameter characterizing the sensor. Because the major parameters characterizing the SCADS sensor are strongly interrelated, it is not possible to independently calculate most of these parameters. Consequently, because of the parameter dependence, there can be absolutely no unique solution which is independent of any initial assumptions but rather a subset of solutions each of which will be strongly influenced by the initial assumed conditions. By making several initial, rational assumptions, it is possible to devise a reasonable and logical design procedure which yields a satisfactory solution. In most cases, these initial, rational assumptions must be based somewhat on physical (size, weight, power, standardization, etc.) and geometrical (sun interference, etc.) restrictions imposed by the nature of the specific problem.

The design procedure for a SCADS system aboard a spin stabilized vehicle differs only slightly from a design procedure for a SCADS sensor aboard a field stabilized vehicle. The design procedure for a spin stabilized sensor will be discussed first.

A. Determination of Cant Angle

The first logical step in the design procedure for a SCADS sensor aboard a spin stabilized vehicle is to determine the cant angle of the optical axis with respect to the vehicle spin axis. The cant angle should be chosen so as to minimize the interference caused by the reflection of sun radiation from the earth, moon, sun shield, and/or spacecraft. The interference results when reflected solar radiation contributes to an increased background noise level which causes a decrease in sensor sensitivity and accuracy in star detection.

In a space environment, direct or reflected (from earth, moon, and/or spacecraft) radiation causes no interference when the angle of the incident light rays are greater than or equal to 90^{o} to the optical axis. This situation is illustrated in Figure 4 where incident rays at an angle $\beta < 90^{o}$ to the optical axis can cause scattered light to enter the sensor optical aperture and hence increase the noise background; however, for $\beta \geq 90^{o}$ complete shielding is accomplished. It should be emphasized that with a properly designed shield, SCADS sensor operation is achievable if the sun radiation incidence angle is less than 90^{o}; however, interference caused by direct or reflected solar radiation is clearly minimized when its incidence angle is 90^{o} or greater to the optical axis. Hence, the best cant angle should be chosen which maximizes the time that the angle of incident solar radiation (direct or reflected) is greater than or equal to 90^{o} to the optical axis.

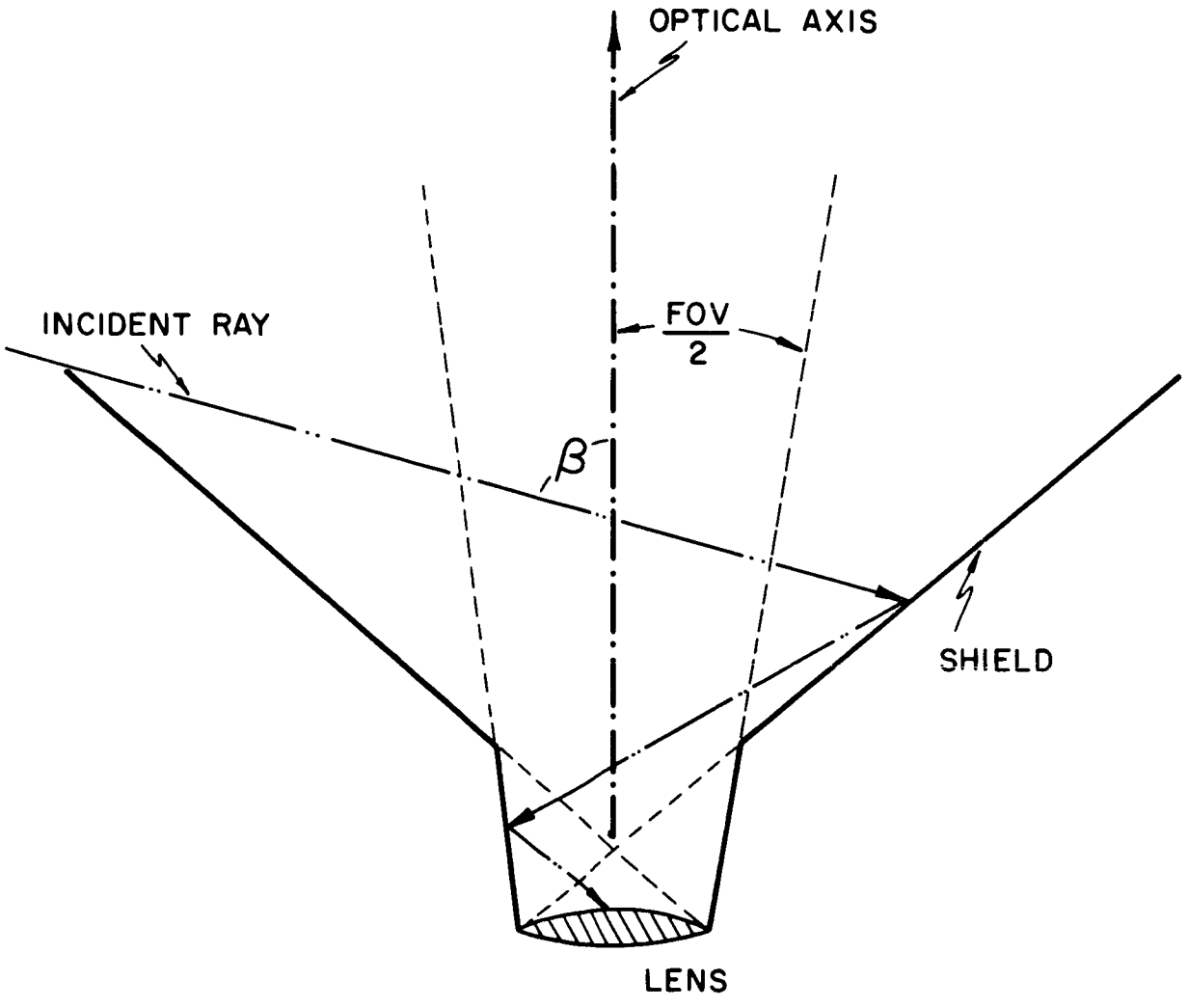

FIGURE 4: Light Scattering When Incident Rays Are Less Than 90° to Optical Axis

B. Determination of Field of View

After the cant angle has been determined, the next logical step in the design procedure is to determine the optical field of view, FOV. The required field of view is dependent upon how many star transits must be detected per scan period in order to obtain a solution to the attitude determination problem. The number of star transits required for a solution depends upon the number of slits in the focal plane reticle. For SCADS-S^3 the on-board data processing and data transmission must both be minimized, so a single slit is required. For a single slit reticle, a minimum of three detected star transits per scan period is required in order to perform the star identification step in the attitude determination procedure. Hence the field of view must be sufficiently large so that the area scanned per scan period on the celestial sphere contains with a high probability at least three stars brighter than the detection threshold.

Clearly, the detection threshold (limiting required detectable magnitude) must be given before the field of view can be determined. Here is where a reasonable initial assumption must be made since there is no unique solution for the detection threshold. For instance, a small field of view requires detection of dim stars, whereas a large field of view requires detecting only brighter stars. However, for a given scan period, detection of dim stars will require a large optical aperture whereas detection of bright stars will require a small optical aperture. It is desirable to have both the field of view and the optical aperture small, but this is not possible. Generally for a SCADS type sensor a field of view larger than 40° is not practical because very wide field of view lens designs are difficult and do not yield sufficient image quality. Also, for SCADS-S^3 the optical aperture must not be larger than two inches. Consequently, the detection threshold must be chosen so all these restrictions are met.

Another rather broad restriction can be derived from the size of the star catalog required for the star identification procedure. It is desirable

that the number of stars in the star catalog should be as small as possible in order to simplify the star identification. Table II lists the total number of stars in the celestial sphere brighter than visual magnitude M_V.

TABLE II

TOTAL NUMBER OF STARS IN CELESTIAL SPHERE BRIGHTER THAN VISUAL MAGNITUDE M_V

Total Number of Stars	Visual Magnitude M_V
1	-1.0
2	- .5
2	0
9	.5
12	1.0
20	1.5
41	2.0
79	2.5
149	3.0
247	3.5
437	4.0
789	4.5

If all orbital configurations and stabilization modes for the SCADS-S[3] sensor are considered, almost any point on the celestial sphere is a potential pointing direction for the spin axis with the exclusion of the region about the North and South Poles. For the spin stabilized modes, the vehicle spin axis lies approximately in the equatorial plane. Since the optical axis will be canted by an angle Γ with respect to the spin axis, the instantaneous optical axis will be pointed somewhere in a rather broad band about the celestial equator. Since the galactic equator is inclined by approximately 62 degrees with respect to the celestial equator, the optical axis will be pointed

in regions of both high and low star densities. Consequently, for purposes of determining the field of view required to enclose with a high probability three stars brighter than magnitude M_V, it is permissible to consider the optical axis to be randomly pointed on the celestial sphere. A computer program has been written to determine the required area enclosed on the celestial sphere in order to include three stars brighter than visual magnitude M_V with a given probability.

The computer program positioned the optical axis at 2580 uniformly spaced points on the celestial sphere. This was achieved by incrementing the declination of the zenith in steps of 4° from -88° to $+88^\circ$ declination. The number of right ascensions was determined by

$$N = [90 \cos \delta], \text{ for } -88^\circ \leq \delta \leq 88^\circ$$

where $[x]$ = greatest integer $\leq x$.

As special cases, the optical axis was centered at $\delta = +90^\circ$ and $\delta = -90^\circ$.

The program was initialized with the reading in of the star data (right ascension, declination, and magnitude) cards, which were sorted from brightest to dimmest. The star data was obtained from the 789 stars brighter than +4.5 magnitude listed in Atlas Coeli. Then, a declination was fixed, and the right ascension values were computed and fixed.

The zenith angles of all 789 stars were then computed using the relationship,

$$\cos z_i = \sin \delta \sin \delta_i + \cos \delta \cos \delta_i \cos (\alpha - \alpha_i)$$

where

z_i = zenith angle of the i^{th} star = angle between optical axis and i^{th} star

α_i = right ascension of the i^{th} star

δ_i = declination of the i^{th} star

δ = declination of the optical axis

α = the right ascension of the optical axis.

Next, a magnitude limit was set. For a fixed position of the optical axis, zenith angles of all stars brighter than this limit were ordered from smallest to largest. The first, second, third, and fourth smallest angles then corresponded to one-half the required field of view to see one, two, three, or four stars in the field of view, respectively. The magnitude limit was then lowered in steps of +.5 and the sort repeated. This was done for nine magnitude limits from 0 to +4.0 in steps of .5. Then the right ascension of the optical axis was stepped and the above procedure repeated.

After all computations were completed and tabulated, the results were plotted as shown in Figure 5. As an example, Figure 5 shows that three or more stars of magnitude +3.5 or brighter were always within a $60^{\circ} = \theta$ field of view for each of the 2580 pointing directions. Here the field of view was taken to be the entire field with no central dead zone, and the optical axis was coincident with the spin axis. Hence, the area scanned on the celestial sphere by a field of view of θ is given by (See Figure 6)

$$S_A = \int_{\theta_1 = 0}^{\theta_2 = \frac{\theta}{2}} \int_{\phi = 0}^{\phi = 2\pi} \sin\theta \, d\phi d\theta = 2\pi \left(1 - \cos\frac{\theta}{2}\right) \text{ steradians}$$

where θ = the uncanted field of view centered on the spin axis.

In order to insure that three or more stars brighter than magnitude M are scanned by a field of view whose optical axis is canted at an angle Γ with respect to the spin axis, the area scanned by the canted field of view must be equivalent to S_A. Therefore, the required canted field of view is given by

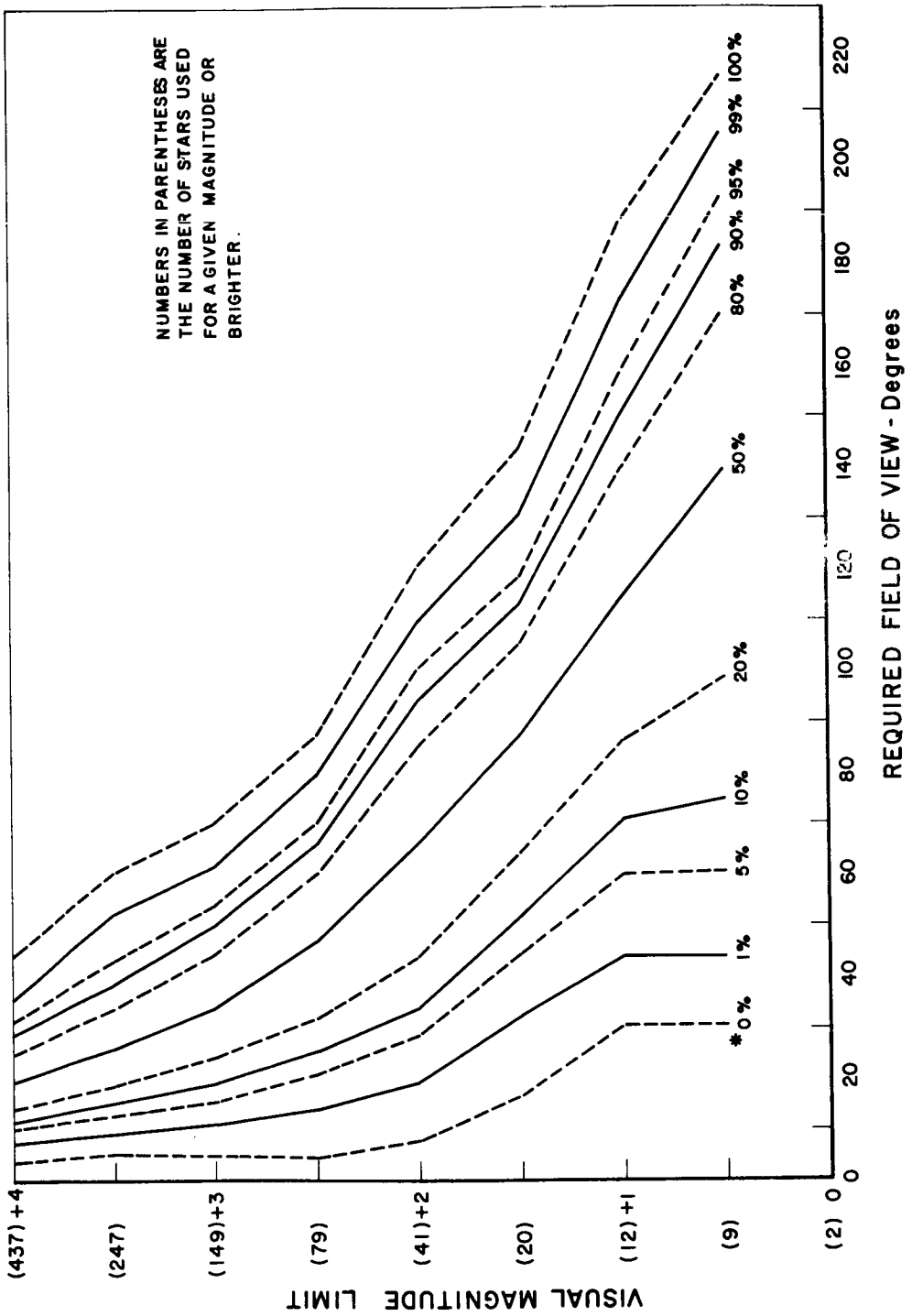

FIGURE 5: Field of View Required to Include Three Stars Brighter Than Magnitude M_V

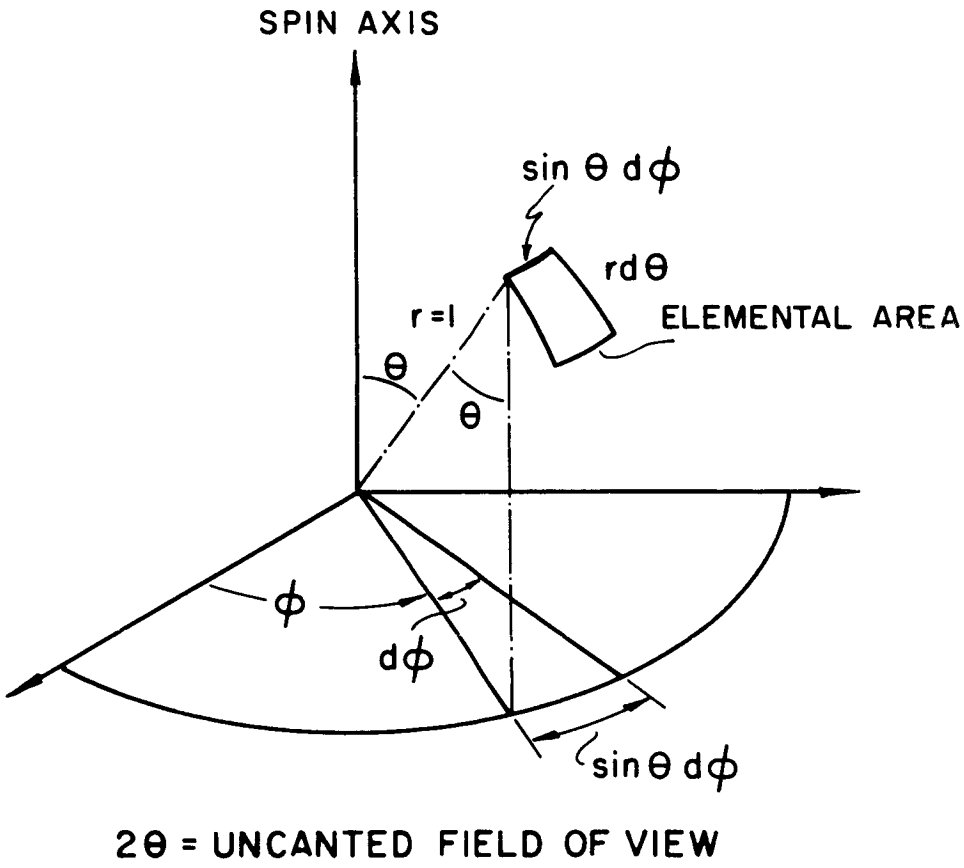

FIGURE 6: Elemental Scanned Area on Celestial Sphere

$$2\pi[\cos(\Gamma - FOV/2) - \cos(\Gamma + FOV/2)] = 2\pi(1 - \cos\theta/2)$$

which may be rewritten as

$$\sin\frac{FOV}{2} = \frac{(1 - \cos\frac{\theta}{2})}{2\sin\Gamma}$$

It is clear that if we select the limiting detectable star magnitude, then the required field of view is determined for a single slit system for a given cant angle and a randomly pointed sensor.

Because of convenience due to existing data, the field of view is initially determined above from data obtained by using visual star magnitudes, although as will be seen later in this section, the photomultiplier response is more closely matched to the photographic star magnitudes. Consequently, a detailed star availability search will be described in Section VIII using photographic star magnitudes. The results of that section confirm that the initial estimate of the field of view using visual magnitudes is sufficiently accurate. Evidently the statistical distribution of stars for this application is such that the required field of view is not strongly dependent on star color classification.

C. Selection of Photomultiplier

In order to achieve adequate signal-to-noise ratios with a minimum aperture optical system for the detection of star signals with the S^3 sensor, it is required that the photodetector for S^3 be a photomultiplier. Previous investigations have shown that current solid state detectors are inadequate or at best marginal for a SCADS-type sensor rotating at relatively short scan periods. One of the principal reasons for the superiority of photomultipliers is the relatively noise-free gain achieved by the electron multiplication provided by the secondary emissions of the photomultiplier dynode chain [4]. The dynode chain provides adequate gain to raise the signal levels well above the level of the thermal Johnson noise of the photodetector load resistor.

Extensive investigation has been performed in the applicability of photomultiplier tubes for SCADS systems. The results of these investigations have shown that venetian blind tubes are optimum for several reasons; in particular, the rugged tube structure, the large photocathode area, and the high multiplier gain are some of its outstanding characteristics. Venetian blind photomultipliers have been utilized in two previous SCADS-type experimental systems. For a Breadboard Design of a SCADS System (NAS5-9661), a venetian blind tube designated as the EMR-543A (manufactured by Electro-Mechanical Research, Inc.) was employed. For the ATS Self-Contained Navigation System Experiment, the venetian blind photomultiplier employed was an EMR-541E. Both tubes were ruggedized and capable of withstanding the environment of space vehicle launching. Since both tube types supplied by EMR performed satisfactorily, this feasibility study will primarily consider EMR photomultipliers.

The cathode type employed by the photomultiplier is particularly important in SCADS sensor applications. It is desirable that the cathode exhibit high quantum efficiency and a low dark emission rate. EMR has given letter designations to indicate different cathode types. For example, the EMR-543A has a cathode designated as an "A" cathode, and its response conforms closely

to an S-4 response with a typical peak quantum efficiency of 14 percent and a cathode dark current of .274 x 10^{-15} ampere per square centimeter of cathode area at +20°C. Similarly, the EMR-541E has an "E" cathode which conforms closely to a S-20 response with a typical peak quantum efficiency of 25 percent and a cathode dark current of .407 x 10^{-16} ampere per square centimeter at +20°C. The "E" cathode has a broad range of spectral response plus its peak sensitivity corresponds closely with the spectral energy distribution of blue stars. More recently EMR has announced the "N" type cathode which has a higher quantum efficiency than the "A" type but somewhat less efficient than the "E" type. The "N" cathode response conforms closely to the S-11 response. Typical peak quantum efficiency of the "N" cathode is 21.5 percent, however its dark current is .51 x 10^{-17} ampere per square centimeter at +20°C. Hence, its dark current characteristic is much superior to either the "A" or "E" cathodes. In addition, the "N" cathode can withstand a much higher temperature (+150°C) than either the "A" (+75°C) or "E" (+85°C) cathodes. The high temperature characteristic is particularly attractive since some cathode heating is likely to occur whenever the sensor sees either direct sun radiation or earth-reflected sun radiation.

Because of its desirable characteristics of relatively high quantum efficiency, low dark current,and tolerance to high temperatures, the EMR type "N" cathode is recommended for the SCADS-S^3 sensor. The type "N" cathode is currently available in two ruggedized EMR photomultipliers, the EMR-541N and the EMR-543N. The active cathode diameter of the EMR-541N is 25 millimeters and the active cathode diameter of the EMR-543N is 43 millimeters. Because of its smaller size, the EMR-541N has been selected for application in the SCADS-S^3 sensor.

Data sheets for the EMR-541N photomultiplier are shown in Appendix C.

D. Sensitivity of Photomultiplier to Star Radiation

For a given photomultiplier it is possible to determine the response of the tube to star radiation. To calculate signal currents at the photomultiplier output, it is necessary to know the absolute spectral energy distribution (ASED) for the star spectral class which contains the greatest percentage of stars. It has been shown that star spectral class A contains the greatest percentage of the 100 brightest stars [5]. Code (1960)[6] has published data from which the ASED of Vega (spectral class A0) can be calculated.

Code gives the monochromatic magnitudes of Vega as a function of wave number (inverse of wavelength). These magnitudes can be converted to monochromatic magnitudes as a function of wavelength by using the transformation[7]

$$M(\lambda) = m(1/\lambda) + 5 \log_{10} \left[\frac{\lambda}{\lambda_o}\right].$$

In this case λ_o = .556 micron. The monochromatic intensity of Vega at wavelength λ relative to the intensity at λ_o can be obtained from the expression

$$\frac{f(\lambda)}{f(\lambda_o)} = 10^{-.4[M(\lambda) - M(\lambda_o)]}$$

where $M(\lambda_o) = 0.0$ at λ_o = .556 micron. The relative spectral energy distribution (RSED) for Vega can be obtained by plotting $f(\lambda)/f(\lambda_o)$ versus λ. By determining f(.556), the absolute spectral energy distribution of Vega can be obtained. Based on measurements, Code has adopted a monochromatic flux value of 3.8×10^{-12} watt per square centimeter micron at .556 micron from a star of visual magnitude $M_v = 0.0$. Figure 7 shows a plot of the absolute spectral energy distribution for Vega.

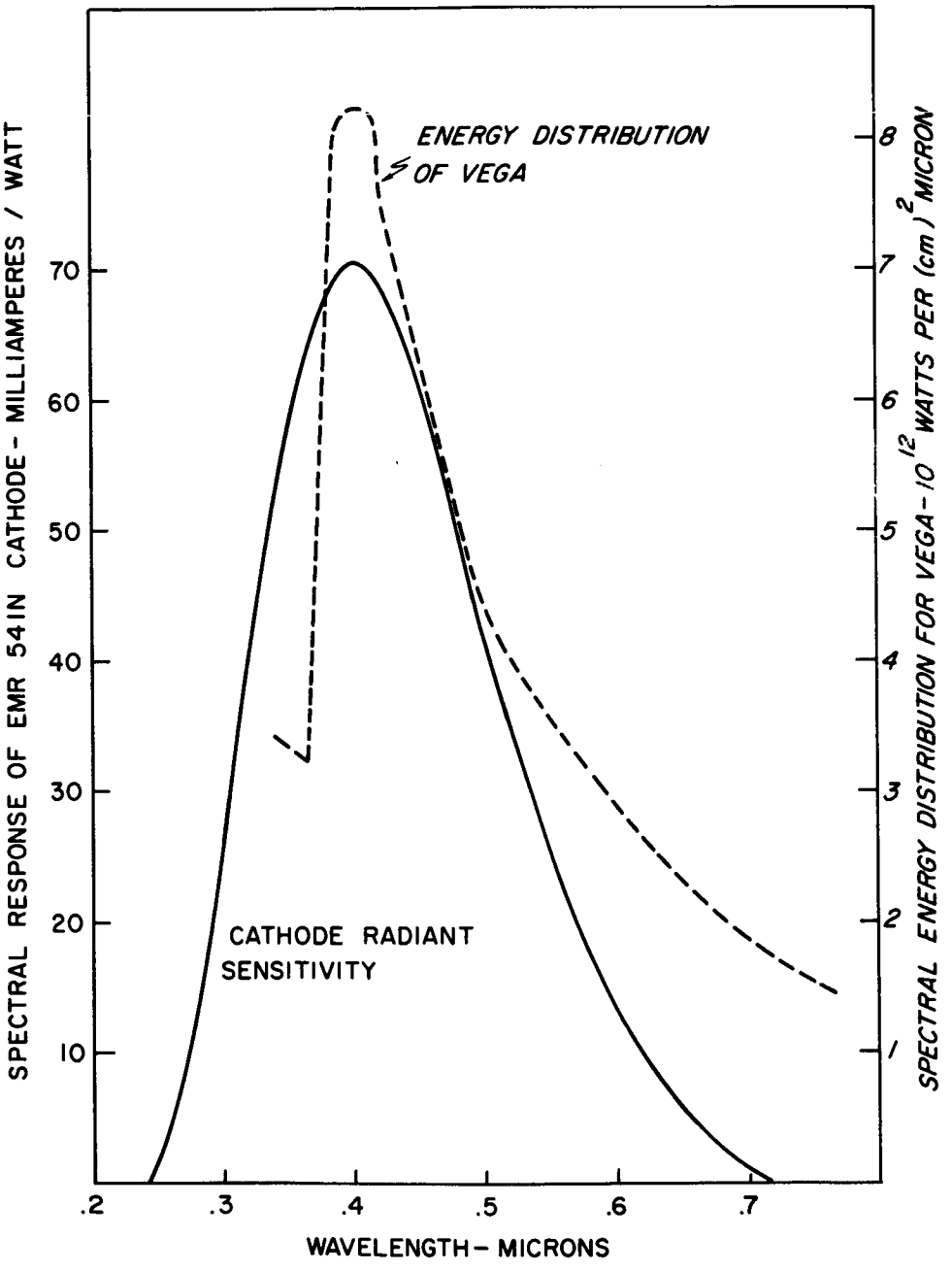

FIGURE 7: Cathode Radiant Sensitivity and Spectral Energy Distribution of Vega

The absolute spectral energy distribution for Vega is modified by the spectral response of the photomultiplier cathode, resulting in an effective spectral energy distribution for Vega as shown in Figure 8. The spectral response of the EMR-541N cathode is shown in Figure 7. Numerical integration of the effective spectral energy distribution in Figure 8 yields a cathode current of 7.92×10^{-14} ampere per square centimeter of optical aperture. The visual magnitude of Vega is +0.04. The cathode current for a Vega type star of visual magnitude M_v can be obtained by scaling the cathode current by the factor $10^{-.4(M_v-.04)} = 1.04 \times 10^{-.4M_v}$. So a class AO star of visual magnitude M_v causes a cathode current of $S_K = 8.25 \times 10^{-14} \times 10^{-.4M_v}$ ampere per square centimeter for 100 percent optical efficiency.

Similar calculations have been made for the "E" and "A" cathodes. The results of these calculations are stated as follows for a $0^m.0$ visual magnitude class AO star and 100 percent optical efficiency:

"E" cathode sensitivity - 10.3×10^{-14} ampere per square centimeter
"A" cathode sensitivity - 5.49×10^{-14} ampere per square centimeter.

It is of interest to determine the type N cathode response to stars of different spectral classification, particularly for those stars whose energy distributions peak at a longer wavelength than do the class A stars. Figure 9 shows the spectral energy distribution for a $0^m.0$ visual magnitude class M2Ia star (Betelgeuse class). The resulting effective spectral energy distribution is shown in Figure 10. Numerical integration of the effective spectral energy distribution of Figure 10 results in a cathode current of

$$S_K = 2.14 \times 10^{-14} \times 10^{-.4M_v} \quad \frac{\text{amp}}{(\text{cm})^2}$$

for 100% optical efficiency. Similarly, Figure 9 shows the spectral energy distribution for a $0^m.0$ visual magnitude class K5III star (Aldebaran class).

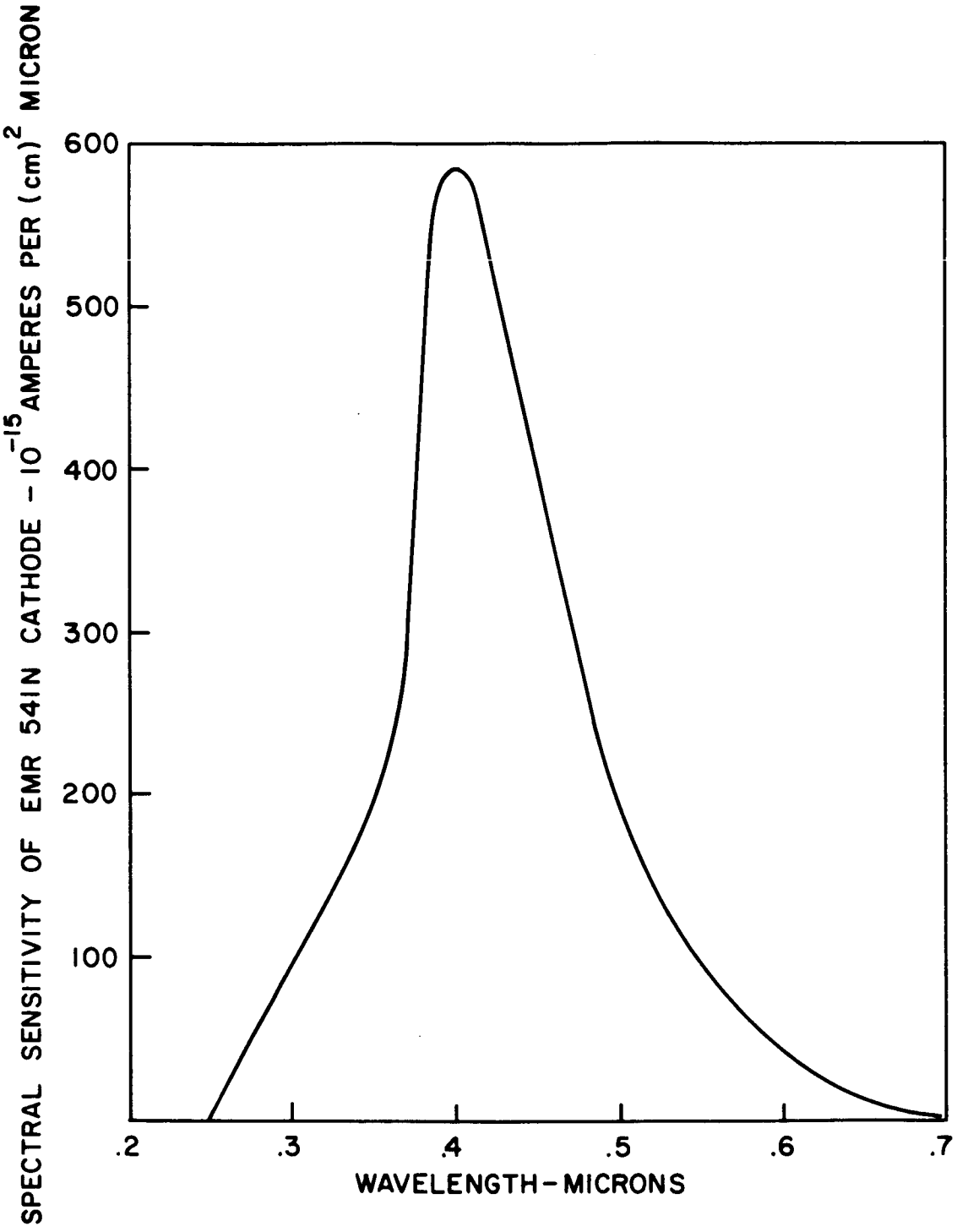

FIGURE 8: Effective Spectral Energy Distribution for Vega and EMR-541N Cathode

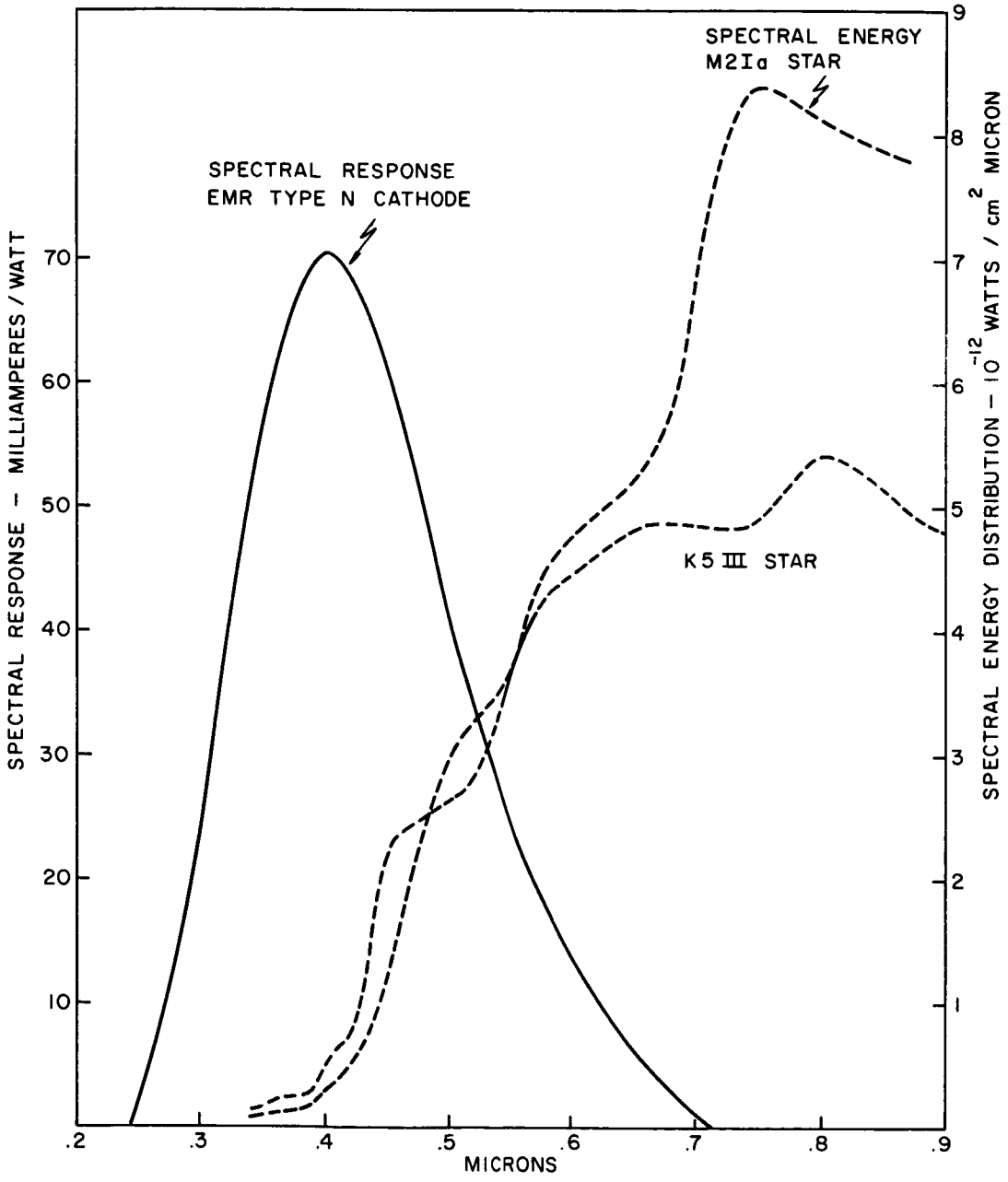

FIGURE 9: Comparison of Photomultiplier Spectral Response and Spectral Energy Distribution of "Red" Stars

Numerical integration of the effective spectral energy distribution of Figure 10 results in a cathode current of

$$S_K = 2.33 \times 10^{-14} \times 10^{-.4M_v} \frac{amp}{(cm)^2}$$

for 100% optical efficiency.

The reason that different values of cathode current result from stars of the same visual magnitude but different spectral class can be explained by the fact that the combined spectral response of the visual photometric system (V filter and 1P21 photomultiplier) does not match the spectral response of the EMR541N photomultiplier. The discrepancy is not particularly troublesome to a SCADS sensor since star intensity data is not essential in solving the attitude determination problem. Even if star intensity were of importance, it would be possible to determine an instrument magnitude for each star class by assigning a correction factor to the visual magnitude. For instance, for a class M2 star the magnitude correction factor can be determined by $\frac{8.25}{2.14} = 10^{+.4M_c}$. Hence, the instrument magnitude for a class M2 star would be

$$M_I = M_v + M_c$$

In order to more accurately determine the magnitude correction factor, the spectral response of the lens system should be included in the star effective spectral energy distribution.

The actual instrument response as a function of color class and star magnitude is not particularly important except in performing the detailed star availability search. For this task, it is necessary to give some consideration to the instrument response to red stars in order to insure that three or more stars in the field of view, regardless of color class, exceed the threshold limit. Adequate consideration to this problem is given by working

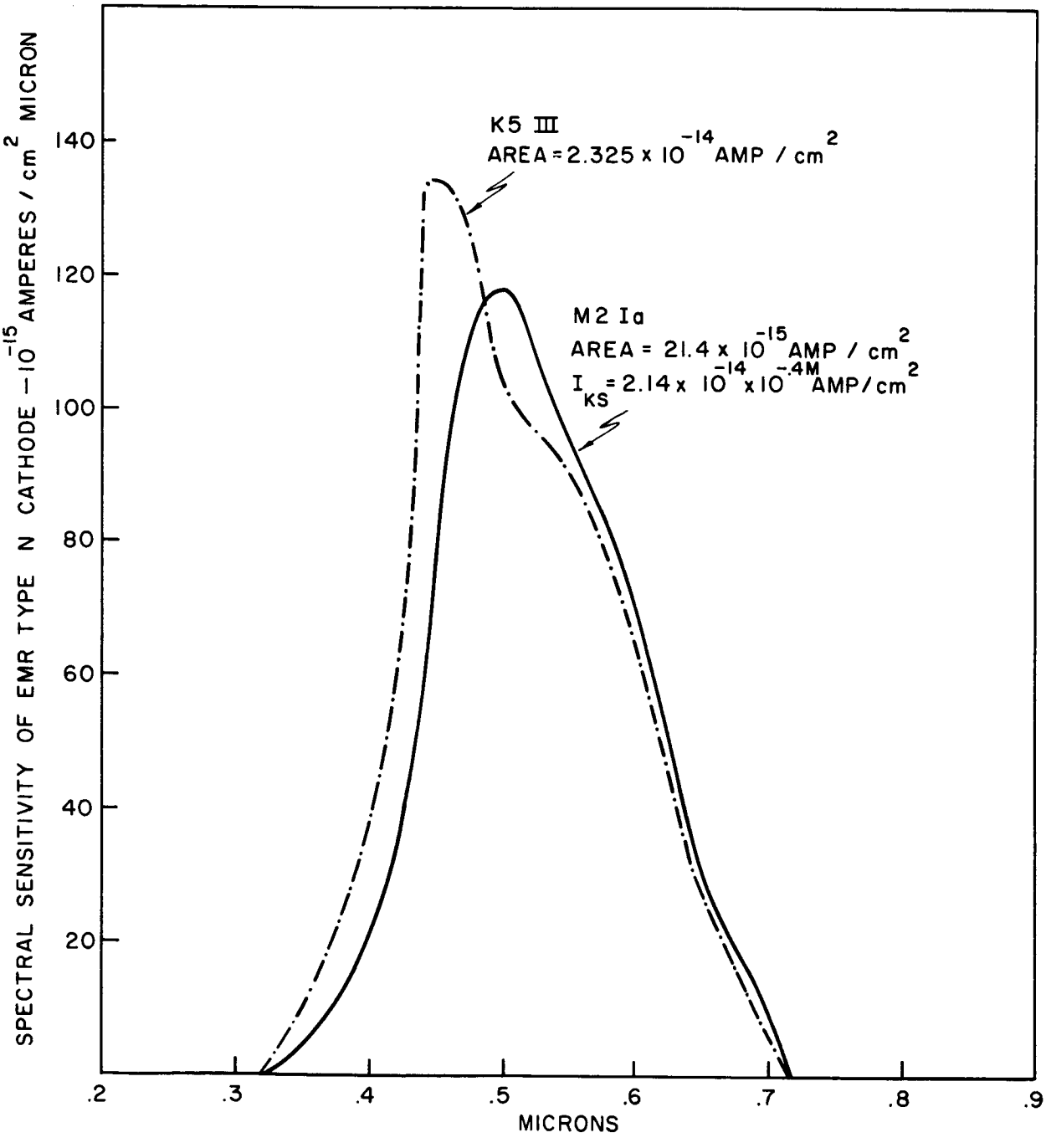

FIGURE 10: Effective Spectral Energy Distribution for "Red" Stars

with star magnitudes which more closely match the actual instrument response. As has been shown, visual magnitudes are not suitable since the instrument response from a class M star is down by 1.47 magnitude from the instrument response from a class A star having the same visual magnitude. However, it can be shown that photographic magnitudes are suitable for performing the star availability search.

Although the instrument is calibrated on the absolute spectral energy distribution of the blue star Vega using its visual magnitude, the relative and absolute instrument responses for photographic magnitudes can be readily determined. The photographic star magnitudes can be obtained from the transformation[8]

$$M_p = (M_B - M_v) - .11 + M_v$$

where M_B = the blue magnitude of the star,
and $M_B - M_v$ = star color index.

Two specific stars will now be considered, one blue and the other red. For the blue star Vega (class A0, $M_v = +.04$), its color index $M_B - M_v = 0.0$, so $M_p = -0.7$. For the red star Betelgeuse (class M2, $M_v = 0.7$), its color index is $M_B - M_v = 1.86$, so $M_p = 2.44$. So for photographic magnitudes, red stars appear much dimmer than blue stars which have visual magnitudes comparable to the red stars. This more nearly agrees with the relationship for the instrument responses derived respectively for blue and red stars.

The instrument response to a class A0 star of magnitude M_v has been determined as

$$S_K = 8.25 \times 10^{-14} \times 10^{-.4M_v}$$

In terms of photographic magnitudes, the instrument response is given by

$$S_K = 8.25 \times 10^{-14} \times 10^{+.4(M_B - M_V)}\ 10^{-.4(M_p + .11)}$$

Now for stars which are more red than the spectral class AO stars, the color index $M_B - M_V \geq 0$[8], so for a given photographic magnitude the instrument response to red stars is always greater than is the instrument response to class AO stars. Hence by calibrating the instrument on a class AO star (color index $M_B - M_V = 0.0$) and employing photographic magnitudes, it is certain that for the limiting photographic magnitude, adequately detectable signals will be received for almost all star classes since most stars are more red than spectral class AO[5]. Photographic magnitudes will be used for the detailed star availability search described in Section VIII.

E. Electronic Filter Analysis

The next step in the design procedure requires determination of the optical aperture. This requires analysis of the star signal detection problem which must be preceded by an analysis of the signal filtering problem.

Figure 11 shows the photomultiplier output as a series of impulses where each impulse corresponds to a single randomly emitted electron from the photocathode. For very weak light intensities, the average photocathode emission rate is relatively low so that star detection by electronic counting of the individual emissions during a sliding time interval T_s is practical. However, for a SCADS sensor, the stellar background plus bright star intensities make star detection by counting individual photocathode emissions impractical. Instead, time averaging of the photomultiplier output signal and subsequent threshold level detection is more practical. Time averaging of the star signal is performed with an electronic low pass filter. Because of the random emissions of the photoelectrons from the cathode while the star is in the slit, the time averaged star signal contains a random amplitude noise component superimposed on its true average value. The random noise amplitude component is commonly referred to as shot noise.

The ability to detect star pulses from a photodetector in the presence of shot noise caused by background and star radiation is greatly influenced by the design parameters of the low pass electronic filter shown in Figure 11. Analysis of the filtering problem is complicated by the fact that the RMS noise is dependent on the amplitude of the signal as described by the shot noise equation,

$$I_{RMS} = \left[2e\ (I_S + I_B + I_D)\Delta f\right]^{\frac{1}{2}} \qquad (1)$$

where

I_S = average current produced by star radiation striking the photodetector

I_B = average current produced by stellar background radiation striking the photodetector

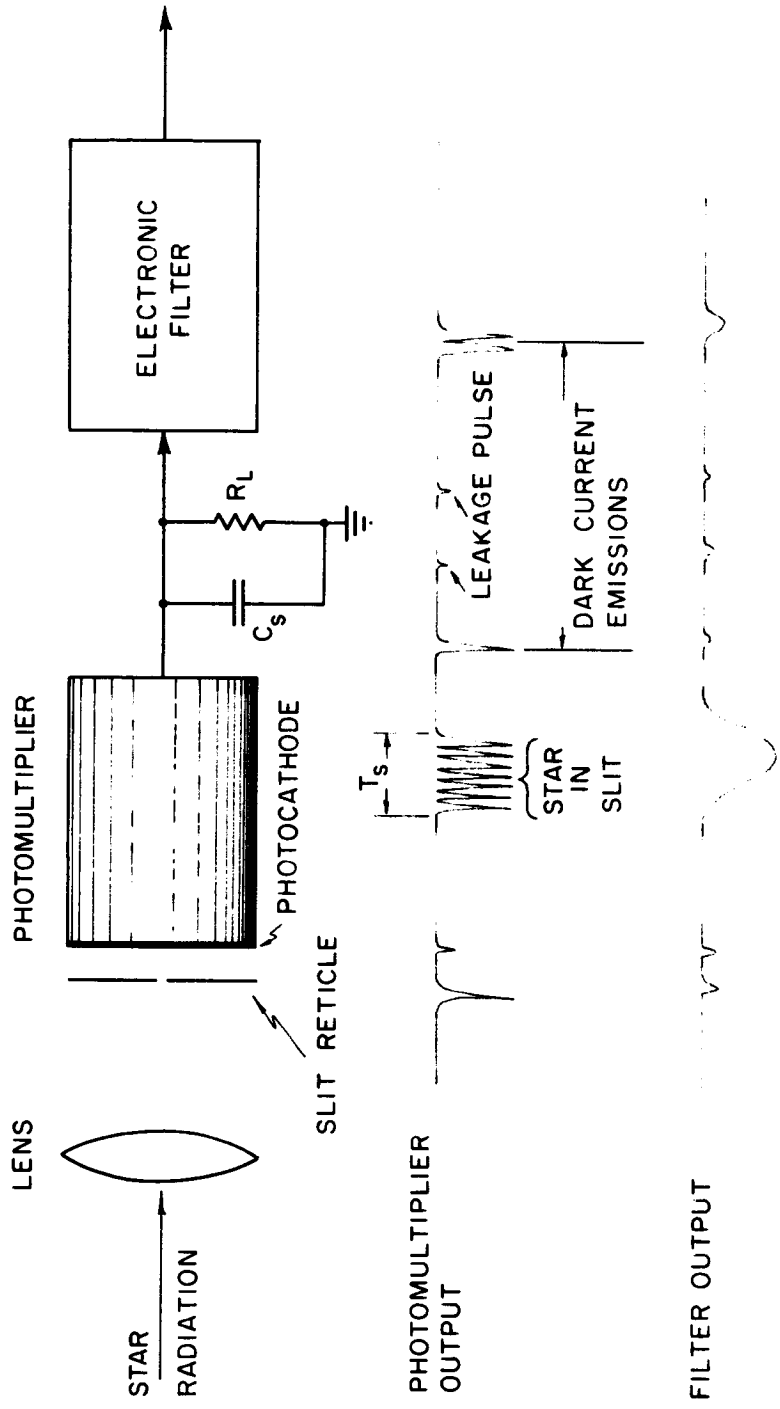

FIGURE 11: Filtering of Star Pulse

I_D = average dark current of the photodetector
Δf = noise equivalent bandwidth of the electronic filter.

Because the noise is dependent upon the signal, the noise is non-stationary. Consequently, to achieve optimum filtering it is apparent that the parameters of a linear filter must change with the amplitude of the signal, i.e., the filter parameters must be time variant and be capable of adapting with the magnitude of the pulse being filtered. It is impractical to implement a time variant linear filter, so to simplify matters, it will be assumed that the RMS noise is not dependent upon the signal level, in which case, the noise is considered stationary. Therefore, only linear time invariant filters will be considered.

The objective in filtering star pulses in the presence of shot noise is to minimize the attenuation of the signal while maximizing the attenuation to the RMS noise. This is equivalent to maximizing the ratio of peak signal to RMS noise. If the bandwidth of the filter passband is wide compared with that occupied by the signal energy, extraneous noise is introduced by the excess bandwidth and lowers the output signal-to-noise ratio. On the other hand, if the filter bandwidth is narrower than the bandwidth occupied by the signal, the noise energy is reduced along with a considerable part of the signal energy. The net result is again a lower signal-to-noise ratio. Thus for a given filter transfer function with a given input signal, there is an optimum bandwidth at which the signal-to-noise ratio is a maximum. For a given input signal, different filter transfer functions will yield differing maximum signal-to-noise ratios at the respective optimum bandwidths. The filter transfer function which yields the highest possible output signal-to-noise ratio is called a matched filter. It can be shown that the impulse response of the matched filter is the reverse image of the input signal; that is, it is the same as the input signal run backward in time[9]. Therefore, if the input signal is symmetrical in time, the impulse response of the matched filter must also be symmetrical. The output signal from any filter can be described by the convolution integral of the filter impulse response

and the input signal.

$$y(t) = \int f(\tau) \cdot h(t - \tau)\, d\tau \tag{2}$$

where

$f(t)$ = the input signal

$h(t)$ = the filter impulse response.

So if the input signal is symmetrical, then the output signal from a matched filter is also symmetrical.

A matched filter may not be physically realizable depending upon the form of the input signal it is required to match. If a matched filter is not physically realizable, then the desired filter is a physically realizable filter which has the highest output signal-to-noise ratio for the given input signal. If one filter transfer function has a higher maximum signal-to-noise ratio than another transfer function for a given input signal, then the filter with the higher signal-to-noise ratio is closest to matching the signal. So by calculating and comparing the maximum signal-to-noise ratios for two or more filter transfer functions and a given input signal, the filter most closely matching the input signal may be determined.

The form of the star pulse from the photodetector of a scanning optical system depends upon the energy density profile of the star image blur circle and the relative size of the rotating slit with respect to the blur circle. If the optical system produces a diffraction pattern that is two dimensional Gaussian, the energy density in the focal plane is given by[10]

$$I(x, y) = \frac{\epsilon_o \lambda_s}{2\pi\sigma^2} \exp\left[- \frac{1}{2\sigma^2} (x^2 + y^2) \right] \tag{3}$$

where

ϵ_o denotes the optical efficiency,

λ_s = average number of photons received from the star per unit time,

σ = dispersion of the diffraction pattern on the focal plane,

and the slit width is chosen such that 80 percent of the star radiation passes the slit when the blur circle is centered in the slit. If T_s equals the time it takes the center of the star image to cross the slit, then the average photon arrival rate at the photomultiplier is described by[10]

$$f_s(t) = \epsilon_o \lambda_s G(t) \tag{4}$$

where

$$G(t) = \Phi\left(\frac{t}{\sigma} + \frac{T_s}{2\sigma}\right) - \Phi\left(\frac{t}{\sigma} - \frac{T_s}{2\sigma}\right)$$

and

$$\Phi(t) = \frac{1}{\sqrt{2\pi}} \int_{-\infty}^{t} e^{-\frac{1}{2}x^2}\, dx.$$

Note that 80 percent of the star radiation passes through the slit when[10]

$$\frac{T_s}{2} = 1.28\ \sigma.$$

The function G(t) is graphed in Figure 12.

The average value of the photodetector output signal will be described by

$$f(t) = K\ G(t) \tag{5}$$

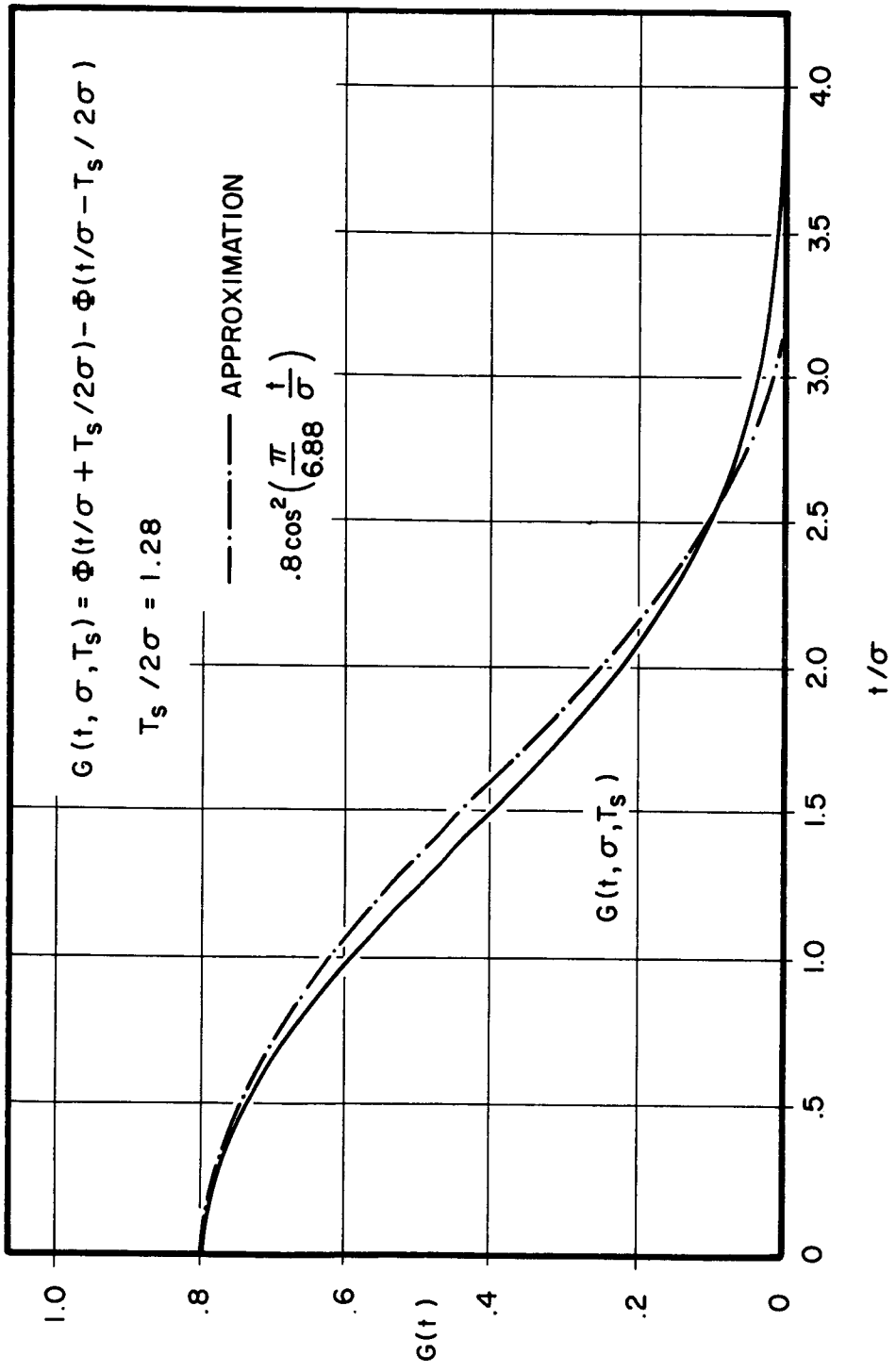

FIGURE 12: Percent of Star Radiation Passing Scanning Slit

The impulse response in Equation (2) can be obtained analytically by finding the inverse Laplace transform of the filter transfer function, H(s). In general, H(s) will contain terms of the form

$$\frac{2[a(\frac{s}{\omega} + \alpha) + b\beta]}{(\frac{s}{\omega} + \alpha)^2 + \beta^2} \tag{6}$$

whose inverse transform is of the form

$$h_i(t) = 2a\ \omega\ e^{-\alpha\omega t} \cos\ (\beta\omega t) + 2b\ \omega\ e^{-\alpha\omega t} \sin\ (\beta\omega t) \tag{7}$$

Equation (2) cannot be integrated in closed form after substitution of Equations (5) and (7). However, G(t) can be approximated by

$$\begin{aligned} f(t) &= (.8) \cos^2\left(\frac{\pi}{2k}\frac{t}{\sigma}\right) \quad \text{for } -k\sigma \leq t \leq +k\sigma \\ &= 0 \qquad\qquad\qquad\qquad\ \ \text{elsewhere;} \end{aligned} \tag{8}$$

where k is selected to "minimize" the discrepancy between G(t) and f(t). It can be shown that[10]

$$\int_{-\infty}^{+\infty} G(t)\ dt = T_s \tag{9}$$

Also

$$\int_{-\infty}^{+\infty} f(t)\ dt = .8\ k\sigma \tag{10}$$

Now if $G(t)/T_s$ and $f(t)/.8\ k\sigma$ are considered as probability density functions, their second moments can be equated to determine k. It has been shown that the second moment[10]

$$\int_{-\infty}^{+\infty} t^2 \frac{G(t)}{T_s} dt = \sigma^2 \left[1 + \frac{1}{3}\left(\frac{T_s}{2\sigma}\right)^2\right] \tag{11}$$

The second moment for $f(t)/(.8\ k\sigma)$ has been evaluated as

$$(.8) \int_{t=-k\sigma}^{t=+k\sigma} t^2 \frac{\cos^2 \frac{\pi}{2k}\frac{t}{\sigma}}{(.8\ k\sigma)} = (k\sigma)^2 \frac{2}{\pi^2}\left[\frac{\pi^2}{6} - 1\right] = (k\sigma)^2\ (.130688)$$

For $T_s/2\sigma = 1.28$, $k = 3.44$. Hence,

$$\begin{aligned} f(t) &= (.8) \cos^2 At \qquad \text{for } -\frac{\pi}{2A} \le t \le \frac{\pi}{2A} \\ &= 0 \qquad\qquad\qquad\ \text{elsewhere;} \end{aligned} \tag{12}$$

where

$$A = \frac{\pi}{6.88\sigma}$$

The function $f(t) = (.8) \cos^2 At$ is shown graphed in Figure 12. By shifting the time axis of Figure 12, G(t) can be approximated by

$$\begin{aligned} f(t) &= (.8) \sin^2 At = (.8)/2\ (1 - \cos^2 At) \text{ for } 0 \le t \le \pi/A \\ f(t) &= 0 \qquad\qquad\qquad\qquad\qquad\qquad \text{elsewhere.} \end{aligned} \tag{13}$$

Now Equation (2) can be integrated analytically after substitution of Equations (7) and (13).

The optimum value for ω_c is that value which maximizes the ratio

$$\frac{S}{N} = \frac{y_{peak}(t, \omega_c)}{I_{RMS}} \tag{14}$$

where

$$I_{RMS}^2 = N_R^2 \int_0^{\infty} |H(f)|^2 \, df = N_R^2 \frac{\omega_c}{2\pi} \frac{1}{2} \int_{-\infty}^{+\infty} |H(jx)|^2 dx \qquad (15)$$

= mean noise output power from the filter with white noise input[11].

$$j(x) = j \frac{\omega}{\omega_c} = \frac{s}{\omega_c}$$

N_R = input RMS noise per unit bandwidth

$$= [2e(I_S + I_B + I_D)]^{\frac{1}{2}}$$

Comparing Equations (1) and (15) shows that the noise equivalent bandwidth is given by

$$\Delta f = \frac{\omega_c}{4\pi} \int_{-\infty}^{+\infty} |H(jx)|^2 \, dx \qquad (16)$$

Since the integral in Equation (15) evaluates to a constant, the value of ω_c which maximizes Equation (14) may be simply determined from the ratio

$$\frac{y_{peak}(t, \omega_c)}{\sqrt{\omega_c}} \qquad (17)$$

If two or more filter transfer functions are to be compared, Equation (15) must be evaluated and used to determine Equation (14) for each case. The transfer function which has the largest maximum value for Equation (14) has the impulse response which most closely matches the given input signal.

By comparing the maximum value of Equation (14) for a two pole transfer function with the maximum value of Equation (14) for the six pole case, it is

possible to compare the effectiveness of each filter.

The two pole transfer function of a linear phase shift versus frequency filter is given by[12]

$$H(s) = \frac{1}{4\left(\frac{s}{\omega_c}\right)^2 + 3\left(\frac{s}{\omega_c}\right) + 1} = \frac{1}{4}\left\{\frac{2\,b\beta}{\left(\frac{s}{\omega_c} + \alpha\right)^2 + \beta^2}\right\} \tag{18}$$

where

$b = 1.51186$

$\alpha = .375$

$\beta = .331$

The numerator of Equation (14) will be evaluated by writing the analytic expression for y(t) and then numerically determining $y_{peak}(t, \omega_c)$ with a programmed digital computer. In order to determine y(t), the filter impulse response must be known. The filter impulse response is

$$\begin{aligned} h(t) &= \frac{2}{4}\, b\, \omega\, e^{-\alpha\omega t} \sin(\beta\omega t) \quad \text{for } t \geq 0 \\ h(t) &= 0 \qquad\qquad\qquad\qquad\quad \text{for } t < 0. \end{aligned} \tag{19}$$

The expression for y(t) is given as follows by the convolution integral:

$$y(t) = \int f(\tau) \cdot h(t - \tau)\, d\tau \tag{20}$$

where

$$\begin{aligned} f(\tau) &= \sin^2 A\tau = \frac{1}{2} - \frac{\cos 2A\tau}{2} \quad \text{for } 0 \leq \tau \leq \frac{\pi}{A} \\ f(\tau) &= 0 \qquad\qquad\qquad\qquad\quad \text{elsewhere.} \end{aligned} \tag{21}$$

and in general

$$\frac{h(t-\tau)}{k} = \sum_i \left[2\, a_i\, \omega\, e^{-\alpha_i \omega (t-\tau)} \cos\left\{\beta_i \omega (t-\tau)\right\} + 2 b_i \omega\, e^{-\alpha_i \omega (t-\tau)} \sin\left\{\beta_i \omega (t-\tau)\right\} \right]$$

Since the terms of y(t) are similar for a given value of subscript i, the derivation will proceed for all terms having the same subscript. The terms of y(t) for the remaining subscripts are then summed to give the final result. For the remainder of the derivation let

$$a = a_i \omega \qquad b = b_i \omega$$
$$\alpha = \alpha_i \omega \qquad \beta = \beta_i \omega$$

$$\begin{aligned}
\frac{y_i(t)}{k} &= (2a \cos \beta t + 2b \sin \beta t)\, \frac{e^{-\alpha t}}{2} \int e^{\alpha \tau} \cos \beta \tau \, d\tau \\
&\quad + (2a \sin \beta t - 2b \cos \beta t)\, \frac{e^{-\alpha \tau}}{2} \int e^{\alpha \tau} \sin \beta \tau \, d\tau \\
&\quad - (2a \cos \beta t + 2b \sin \beta t)\, \frac{e^{-\alpha t}}{2} \left\{ \int \frac{e^{\alpha \tau}}{2} \cos[(2A + \beta)\, \tau] \, d\tau \right. \\
&\qquad \left. + \int \frac{e^{\alpha \tau}}{2} \cos[(2A - \beta)\, \tau] \, d\tau \right\} \\
&\quad + (-2a \sin \beta t + 2b \cos \beta t)\, \frac{e^{-\alpha t}}{2} \int e^{\alpha \tau} \cos 2A\tau \sin \beta \tau \, d\tau
\end{aligned} \tag{22}$$

For $0 \le t \le \frac{\pi}{A}$,

$$\frac{y_i(t)}{k} = -\frac{1}{2}(a \cos \beta t + b \sin \beta t) \left\{ \frac{\alpha \cos[(2A+\beta)t] + (2A+\beta) \sin[(2A+\beta)\, t]}{\alpha^2 + (2A + \beta)^2} \right. + \left. \frac{\alpha \cos[(2A-\beta)t] + (2A-\beta) \sin[(2A-\beta)\, t]}{\alpha^2 + (2A - \beta)^2} \right\}$$

$$+\frac{1}{2}(a\cos\beta t + b\sin\beta t)e^{-\alpha t}\left\{\frac{\alpha}{\alpha^2+(2A+\beta)^2}+\frac{\alpha}{\alpha^2+(2A-\beta)^2}\right\}$$

$$+\frac{1}{2}(-a\sin\beta t + b\cos\beta t)\left\{\begin{array}{l}\dfrac{\alpha\sin[(\beta+2A)t]-(\beta+2A)\cos[(\beta+2A)t]}{\alpha^2+(\beta+2A)^2}\\[2ex] +\dfrac{\alpha\sin[\beta-2A)t]-(\beta-2A)\cos[(\beta-2A)t]}{\alpha^2+(\beta-2A)^2}\end{array}\right\}$$

$$+\frac{1}{2}(-a\sin\beta t + b\cos\beta t)e^{-\alpha t}\left\{\frac{(\beta+2A)}{\alpha^2+(\beta+2A)^2}+\frac{(\beta-2A)}{\alpha^2+(\beta-2A)^2}\right\}$$

$$+\frac{a\alpha+b\beta}{\alpha^2+\beta^2}-\left[\frac{a\alpha+b\beta}{\alpha^2+\beta^2}\right]e^{-\alpha t}\cos\beta t$$

$$+\left[\frac{a\beta-b\alpha}{\alpha^2+\beta^2}\right]e^{-\alpha t}\sin\beta t \qquad (23)$$

For $t > \frac{\pi}{A} = 6.5 = R$

$$\frac{y_i(t)}{k} = (a\cos\beta t + b\sin\beta t)e^{-\alpha t}\left\{\frac{e^{\alpha R}(\alpha\cos\beta R+\beta\sin\beta R)-\alpha}{\alpha^2+\beta^2}\right\}$$

$$+(a\sin\beta t - b\cos\beta t)e^{-\alpha t}\left\{\frac{e^{\alpha R}(\alpha\sin\beta R-\beta\cos\beta R)+\beta}{\alpha^2+\beta^2}\right\}$$

$$- \frac{1}{2}(a \cos \beta t + b \sin \beta t)e^{-\alpha t} \left\{ \frac{e^{\alpha R}[\alpha \cos[(2A + \beta)R] + (2A + \beta) \sin[(2A+\beta)R]]}{\alpha^2 + (2A + \beta)^2} \right.$$

$$+ \frac{e^{\alpha R}[\alpha \cos[(2A - \beta)R] + (2A - \beta) \sin[(2A-\beta)R]]}{\alpha^2 + (2A - \beta)^2}$$

$$\left. + \frac{\alpha}{\alpha^2 + (2A + \beta)^2} + \frac{-\alpha}{\alpha^2 + (2A - \beta)^2} \right\}$$

$$+ \frac{1}{2}(- a \sin \rho t + b \cos \beta t)e^{-\alpha t}e^{\alpha R} \left\{ \frac{\alpha \sin[(\beta+2A)R] - (\beta+2A) \cos[(\beta+2A)R]}{\alpha^2 + (\beta + 2A)^2} \right.$$

$$\left. + \frac{\alpha \sin[(\beta-2A)R] - (\beta-2A) \cos[(\beta-2A)R]}{\alpha^2 + (\beta - 2A)^2} \right\}$$

$$+ \frac{1}{2}(- a \sin \beta t + b \cos \beta t)e^{-\alpha t} \left\{ \frac{(\beta + 2A)}{\alpha^2 + (\beta + 2A)^2} + \frac{(\beta - 2A)}{\alpha^2 + (\beta - 2A)^2} \right\}$$

$$\text{Finally, } y(t) = \sum_i y_i(t) \tag{24}$$

The denominator of Equation (14) may be evaluated by finding the partial fraction expansion of the integrand of Equation (15) and then applying the residue theorem for integrating about a closed contour [13]. The terms of the partial fraction expansion whose poles are in the upper half of the complex plane have been determined to be

$$\frac{(1.51186 - j\ 1.3333)}{(x + .3307 - j\ .375)}\ ,\ \frac{(-1.51186 - j\ 1.3333)}{(x - .3307 - j\ .375)}$$

The complex number in each numerator is the residue of the integrand at the pole in the denominator. Now, by applying the residue theorem to evaluate

the contour integral along a contour enclosing the upper half of the complex plane

$$\int_{-\infty}^{+\infty} |H(jx)|^2 \, dx = (.25)^2 \, 2\pi \, j \, [-2j(1.3333)] \tag{25}$$

So the noise equivalent bandwidth is

$$\Delta f = .5236 \, f_c$$

and

$$N^2 = N_R{}^2 \, \omega_c (.288675)^2$$

Equation (14) has been numerically determined versus ω_c for an arbitrarily chosen value of σ = .945 second in Equation (12). The results are graphed in Figure 13.

The results show that for σ = .945 second, the maximum output signal-to-noise ratio occurs for ω_c = 1.425. Hence, the product of $\sigma \, \omega_c$ at the highest signal-to-noise ratio is

$$\sigma \, \omega_c = (.945)(1.425) = 1.3466. \tag{26}$$

This represents the condition for which the filter impulse response is most closely matched to the input signal.

$$f(t) = \sin^2 \left(\frac{\pi}{6.88} \, \frac{t}{\sigma} \right), \text{ for } 0 \leq t \leq 6.88 \, \sigma$$
$$= 0 \qquad \text{elsewhere.}$$

For the two pole transfer function, the maximum output signal-to-RMS noise ratio occurring for ω_c = 1.425 is 2.1659. Evaluation of Equation (14) for a

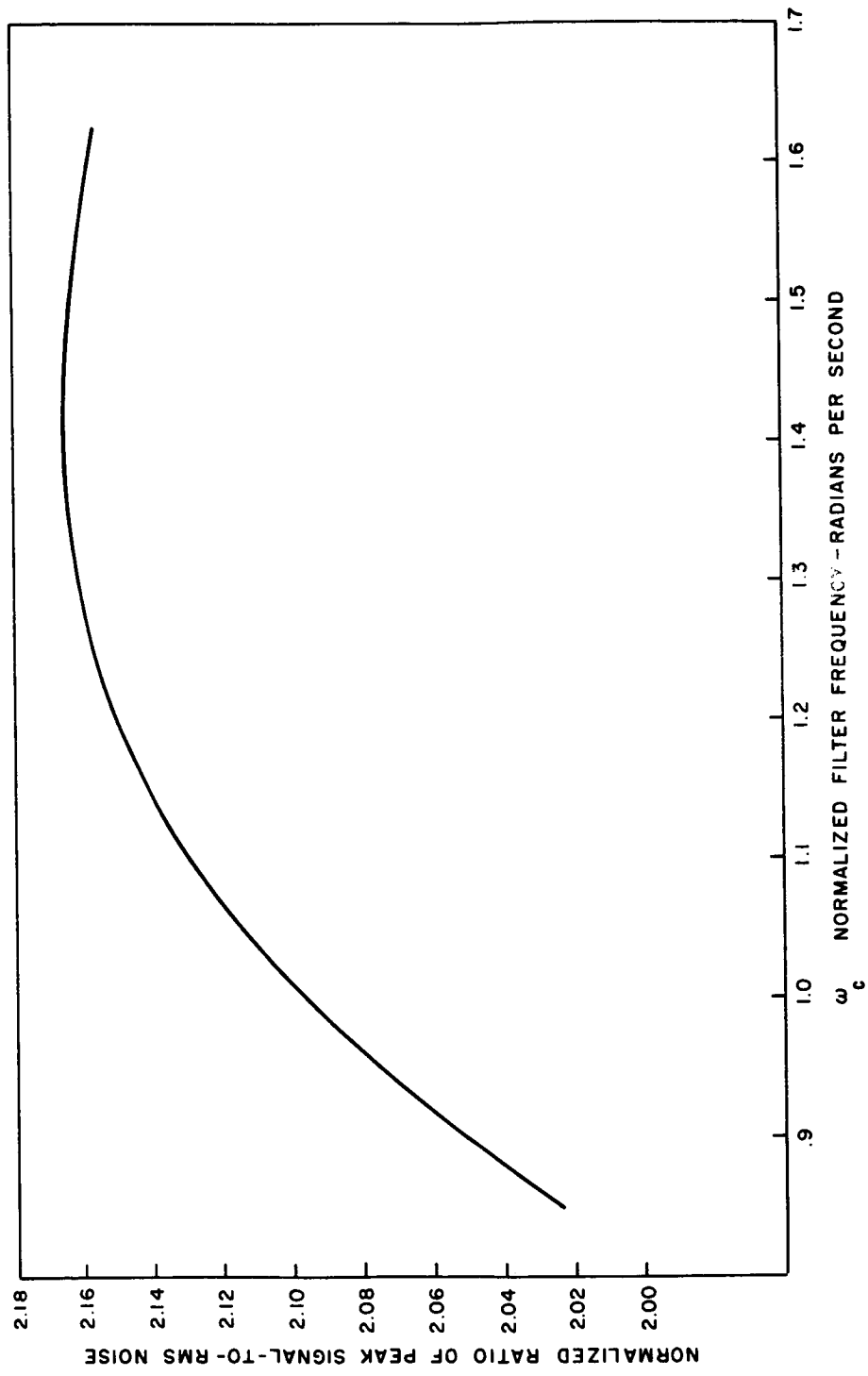

FIGURE 13: Normalized Ratio of Peak Signal-to-RMS Noise for Two Pole Filter

six pole linear phase versus frequency filter shows that there is only a loss of 1.8 percent in the ratio of peak signal-to-RMS noise for a two pole filter when compared to its six pole counterpart. This result tends to indicate that a two pole linear phase filter is adequate to smooth star pulses for applications where exceptional system accuracies are not required.

Further analysis shows that Equation (26) may be rewritten in terms of the slit transit time, T_s. Since $T_s = 2.56\sigma$

$$\omega_c = \frac{3.4473}{T_s} \text{ radians per second.} \tag{27}$$

But for a slit radial to the spin axis, T_s is related to the scan period, T, and slit width, $\widehat{SW}$, by

$$T_s = \frac{\widehat{SW} \cdot T}{21,600} \text{ seconds}$$

where

$\widehat{SW}$ = slit width in arc minutes projected onto the celestial sphere, and
T = scan period in seconds, so

$$\omega_c = \frac{74,461.68}{\widehat{SW} \cdot T} \text{ radians per second.} \tag{28}$$

Equation (28) gives the value of ω_c which matches the two pole filter impulse response to the signal for a given scan period. A question of particular interest concerns the change in the filter response if the scan period varies while the filter parameter, ω_c, remains fixed. This question may be reasonably answered by observing Figure 13. For this figure, the signal was fixed and ω_c was varied by almost a factor of two causing an approximate change in peak signal-to-noise ratio of only 6.5%. Therefore, it can be

reasonably concluded that the scan period can change over a relatively broad range without causing intolerable or catastrophic degradation in the performance of a fixed frequency filter.

Figure 14 shows a plot of the noise-free input signal, f(t), and the noise-free output signal, y(t), for $\omega = 1.425$ and $\sigma = .945$. As shown in Figure 16 for $\omega = 1.425$, the noise-free input peak of unity is reduced by the filter to an output peak equal to .7464. The peak of the noise-free input signal corresponds to 80 percent of the star radiation striking the photocathode. Since I_S = the average current produced by 100 percent of the star radiation striking the photodetector, then the input signal peak corresponds to .8 I_S. Hence, the output signal peak corresponds to $(.7464)(.8)I_S = .597\ I_S$. Consequently, the peak output signal-to-RMS noise ratio is expressed by

$$\frac{S}{N} = \frac{(.597)\ I_S}{(1.26)[2e(.8\ I_S + I_B + I_D)\ \Delta f]^{\frac{1}{2}}} \tag{29}$$

where

$$\Delta f = \frac{(.524)(11851)}{\widehat{SW} \cdot T} = \frac{6210}{\widehat{SW} \cdot T}$$

and the denominator factor of 1.26 accounts for noise introduced by the photomultiplier dynode chain[4]. Figure 14 also shows the filter impulse response, h(t), plotted for $\omega = 1.425$.

If measurements of the star signal peaks were made at the filter output for a given star, it would be expected that the RMS variation in these measurements would be $N \cdot G_t$ where G_t is the photomultiplier tube gain. If the variation of the intensity measurement, $\frac{\sigma_I}{I}$, is defined as the ratio of the RMS variation in the signal peak to the average value of the signal peak, then this ratio must be equivalent to the reciprocal of the peak signal-to-

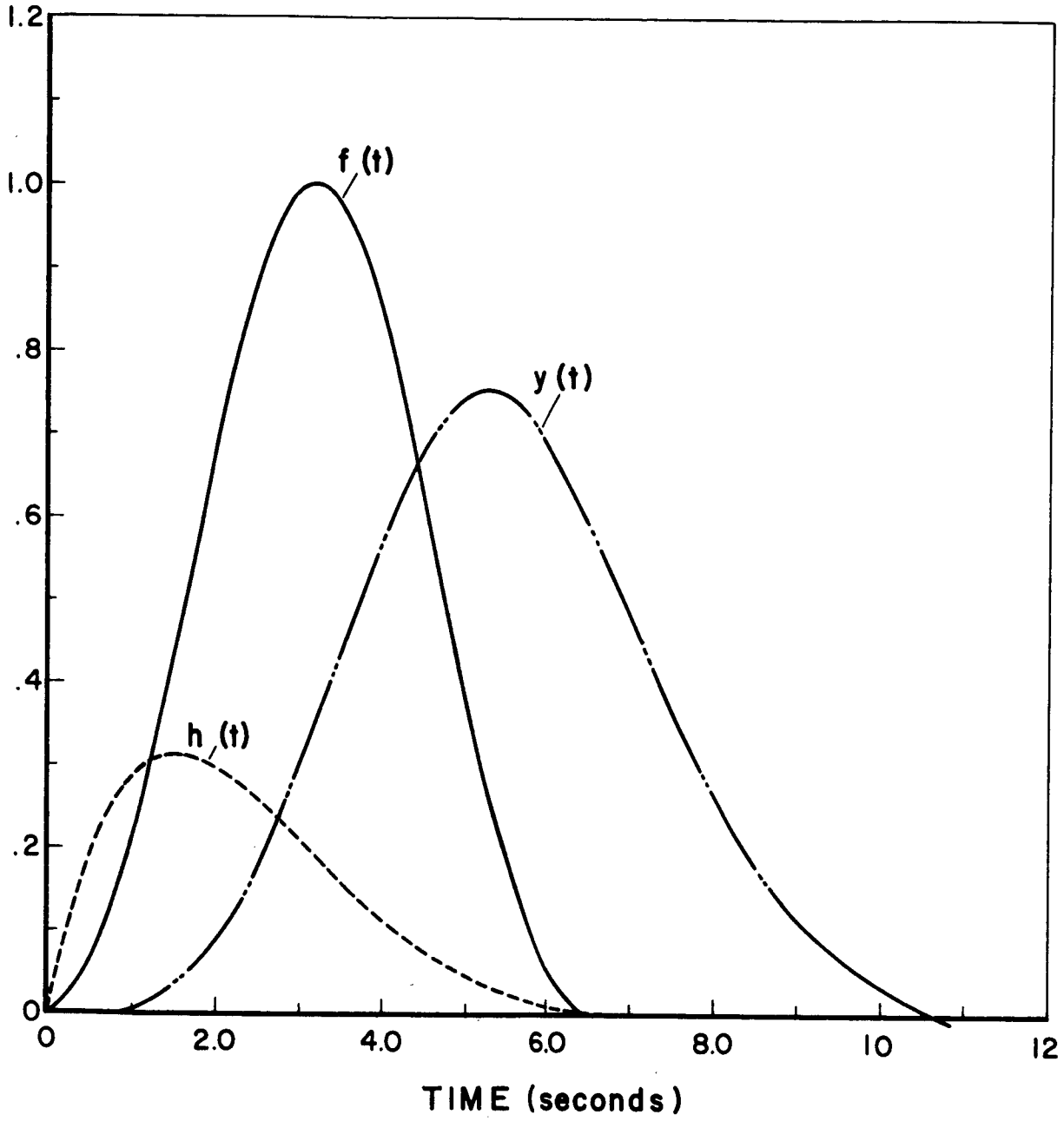

FIGURE 14: Star Pulse Input Signal to Filter, f(t); Filter Impulse Response, h(t); and Output Signal, y(t)

RMS noise ratio. Hence:

$$\frac{\sigma_I}{I} = \frac{N}{S} .$$

The second order transfer function of Equation (18) may be implemented by the circuit shown in Figure 15. The design procedure for obtaining the values of R and C involves matching the poles of the desired filter transfer function with the poles of the circuit transfer function. If K = 1 in Figure 15, then

$$C_1 C_2 R_1 R_2 = \frac{4}{\omega_c^2} \tag{30}$$

and

$$C_2(R_2 + R_1) = \frac{3}{\omega_c}$$

Now let $R_2 = R_1 = R$, so that

$$C_2 = \frac{3}{2R\omega_c} \quad \text{and} \quad C_1 = \frac{8}{3\omega_c R} \tag{31}$$

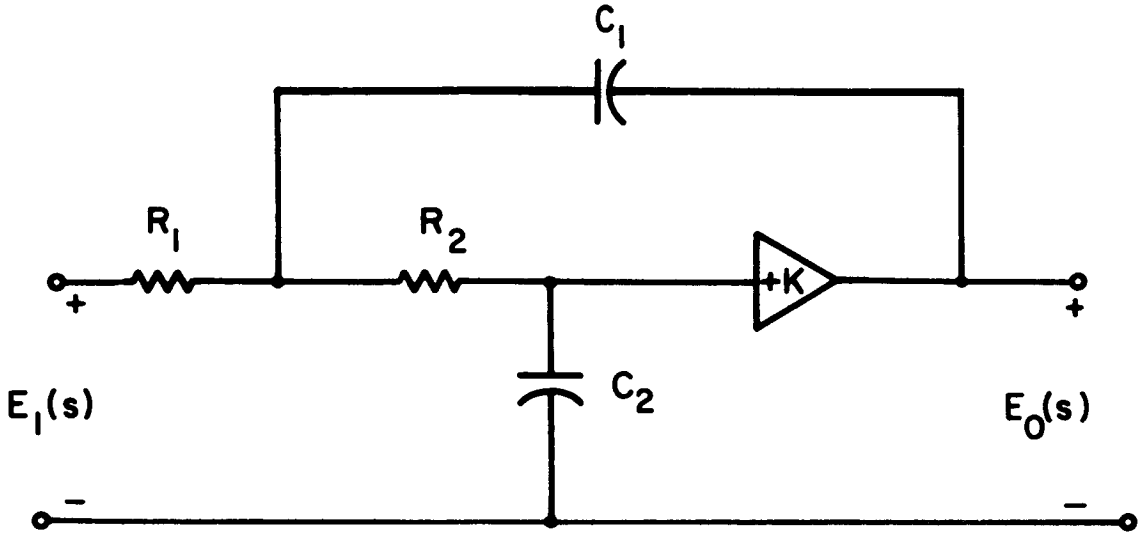

$$\frac{E_o(s)}{E_1(s)} = \frac{K}{\left[s^2 C_1 C_2 R_1 R_2 + s\left\{C_2 R_2 + C_2 R_1 + (1 - K) C_1 R_1\right\} + 1\right]}$$

FIGURE 15: Practical Circuit Configuration Having Quadratic Transfer Function for Low Pass Active Filter

F. Determination of Optical Aperture

In order to determine the required optical aperture, it is first necessary to analyze the problem of star signal detection. For the SCADS-S[3] sensor, star signal detection will be achieved by threshold detection of the filtered analog signal. In this section, determination of the threshold level for a permissible false detection rate will be based on results derived by S. O. Rice[14]. The required optical aperture diameter will then be determined to detect a given magnitude star with a fixed detection probability.

Rice has shown that a noise signal at the output of a low pass filter having an amplitude probability density function which is normal will pass through the threshold value I_T with a positive slope an average number of times per second equal to

$$(1.155)\ \exp-\frac{1}{2}\left(\frac{I_T - I_{BD}}{I_{RMS}}\right)^2 \quad f_b \tag{32}$$

where

I_T = threshold value of current
I_{BD} = average value of noise current
I_{RMS} = RMS value of noise current
f_b = noise equivalent bandwidth of low pass filter in cycles per second.

It has been shown in Section IV-E that the noise equivalent bandwidth for a two pole linear phase shift versus frequency filter has been determined to be

$$f_b = \frac{6205.15}{\widehat{SW} \cdot T} \text{ cycles per second} \tag{33}$$

where

$\widehat{SW}$ = slit width in arc minutes projected onto the celestial sphere,

T = scan period in seconds.

Hence, the average number of threshold crossings per scan period, N_f, equals

$$N_f = \frac{7166.95}{\widehat{SW}} \; e^{-\frac{1}{2}\left(\frac{I_T - I_{BD}}{I_{RMS}}\right)^2} \tag{34}$$

So

$$\frac{I_T - I_{BD}}{I_{RMS}} = \left[2 \ln \frac{7166.95}{N_f \cdot \widehat{SW}}\right]^{\frac{1}{2}} \tag{35}$$

The values of I_T, I_{BD} and I_{RMS} are taken as current values at the output of the photocathode. The value of I_{RMS} is obtained from the shot noise equation with an additional factor included to account for photomultiplier noise. The current levels at the photomultiplier output can be obtained by multiplying all three values by a noise-free constant equal to the gain of the dynode chain. So at the cathode, the RMS noise equals

$$I_{RMS} = 1.3\left[2e \; I_{BD} \; \Delta f\right]^{\frac{1}{2}}, \quad (e = \text{charge on an electron}) \tag{36}$$

where the factor of 1.3 is included to account for noise introduced by the photomultiplier dynode chain[4]. In Section IV-E it has been shown that the noise equivalent bandwidth for the two pole filter may be expressed as

$$\Delta f = f_b = \frac{.2873}{T_s} \text{ cycles per second} \tag{37}$$

where T_s = time required for the center of the star image blur circle to cross the slit.

Next, the following quantities may be introduced,

$$n_T = \frac{I_T\, T_s}{e} \tag{38}$$

$$n_{BD} = \frac{I_{BD}\, T_s}{e}$$

where n denotes the average effective number of equally weighted photocathode emissions occurring during a transit interval, T_s. After substitution of Equations (36), (37), and (38), Equation (35) may be rewritten as

$$n_T = (1.3936)\left[n_{BD} \ell n \frac{7166.95}{N_f \cdot \overline{SW}}\right]^{\frac{1}{2}} + n_{BD} \tag{39}$$

The limiting detectable star magnitude can be determined by considering the value of I required in order to exceed the detection threshold I_T a specified fraction of the time referred to as the detection probability. Consequently, the detection level must be

$$I_T \leq I_{BD} + I - k\, I_{RMS}$$

where

I = the peak value of the star signal at the filter output,

I_{RMS} = the RMS output noise generated by the average peak signal level at the input to the low pass filter, and

k = constant determined by the required detection probability, P_d.

The constant k is determined from $P_d = \frac{1}{\sqrt{2\pi}\, I_{RMS}} \int_{-\infty}^{k\, I_{RMS}} \exp\left[-\frac{1}{2}\left(\frac{I}{I_{RMS}}\right)^2\right] dI.$

In Section IV-E it has been shown that the peak value of the star signal at the output of a two pole linear phase filter is

$$I = .597\, I_s \tag{41}$$

where I_s = the average photocathode current produced by 100 percent of the star radiation striking the photocathode. Equation (41) assumes that 80 percent of the star radiation passes the slit when the blur circle is centered in the slit. The RMS noise current in Equation (40) is given by

$$I_{RMS} = 1.3 \left[2e(.8\ I_s + I_{BD})\ f_b\right]^{\frac{1}{2}} \tag{42}$$

Substitution of Equations (37), (38), and (39) into Equation (40) yields

$$(n_T - n_{BD} - .597\ n_s)^2 = \left\{-k(1.3)\left[(.5746)(.8\ n_s + n_{BD})\right]^{\frac{1}{2}}\right\}^2 \tag{43}$$

Equation (43) can be written as a quadratic in n_s

$$(.597\ n_s)^2 - n_s\left[1.194(n_T - n_{BD}) + (1.3\ k)^2\ (.5746)(.8)\right]$$

$$+ (n_T - n_{BD})^2 - (1.3\ k)^2\ (.5746)\ n_{BD} = 0 \tag{44}$$

From a table of the error function, k = 1.66 for a detection probability of 0.95. So Equation (44) becomes

$$(.3564)n_s^2 - n_s\left[1.194(n_T - n_{BD}) + 2.141\right] + (n_T - n_{BD})^2 - 2.676\ n_{BD} = 0 \tag{45}$$

The limiting detectable star magnitude, M, can now be obtained by equating

$$I_s = \frac{n_s e}{T_s} = \epsilon_o\ S_K\ 10^{-.4M}\ \frac{\pi}{4}\ D^2 \tag{46}$$

where

ϵ_o = efficiency of the optical system,

S_K = sensitivity of the cathode to a zero magnitude star per unit area of optical aperture,

D = diameter of the optical aperture.

So

$$M = 2.5 \log_{10}\left[\frac{\pi}{4} D^2 \left(\frac{T_s}{n_s \cdot e}\right) \epsilon_o S_K\right] \text{ or} \tag{47}$$

$$D = \left[\frac{4\ 10^{.4M}}{\pi\ \epsilon_o\ S_K} \left(\frac{n_s \cdot e}{T_s}\right)\right]^{\frac{1}{2}} \tag{48}$$

The optical aperture, D, can be determined if the following quantities are known or assumed:

(a) S_K = photocathode sensitivity,
(b) θ_2 = angle between the field of view outer edge and the spin axis,
(c) θ_1 = angle between the field of view inner edge and the spin axis,
(d) $\widehat{SW}$ = rotational slit width
(e) N_S = number of radial slits
(f) N_B = equivalent stellar background,
(g) ϵ_o = efficiency of optical system,
(h) I_D = dark current of the photocathode,
(i) M = limiting detectable magnitude,
(j) N_f = an average number of false star detections per scan period,
(k) T = scan period.

Items (a) through (h) are required to determine

$$I_{BD} = I_B + I_D$$

where I_B = cathode current generated by stellar background radiation striking the photocathode. The stellar background radiation, N_B, is commonly expressed in terms of tenth magnitude stars per square degree of slit area projected

onto the celestial sphere. The total slit area projected onto the celestial sphere is

$$S_A = N_S \frac{\widehat{SW}}{60} (\cos \theta_1 - \cos \theta_2) \frac{180}{\pi} (\text{degree})^2$$

where $\widehat{SW}$ is expressed in arc minutes.

With S_K expressed in terms of amperes per square centimeter and D in centimeters, I_B, can be determined for a given D by

$$I_B = \epsilon_o \cdot N_B \cdot S_A \cdot S_K \times 10^{-4} \frac{\pi}{4} D^2 \tag{49}$$

The solution for D must be obtained by an iterative numerical method since D cannot be expressed explicitly from Equations (39), (45), (48) and (49). It is also necessary to assume specific values for ϵ_o, N_B, N_f, and $\widehat{SW}$. These parameters cannot be solved for explicitly; however, realistic values can be assigned for each based on either experience or a worst case condition.

For instance, the true efficiency, ϵ_o, of an optical system is a complex function of multiple variables describing a lens system. Since part of the design problem is to determine a SCADS lens system, it is required that a realistic overall optical efficiency be assumed. Such a realistic value is $\epsilon_o = .5 = 50\%$. In general, this is somewhat below the efficiency of the actual lens; however, it represents a suitable assumption.

For the case of the stellar background, N_B, a worst case value will be assumed based on total integrated starlight for stars of sixth magnitude and weaker[8]. Over the celestial sphere, the background level varies from 15 to 323 tenth magnitude (photographic) stars per square degree. Hence, the stellar background is taken as N_B = 325 tenth magnitude stars per square degree.

In the case of the false detection rate, N_f, the choice is somewhat arbitrary. False detections are undesirable since they lengthen the computer running time of the star identification procedure and contribute no information in terms of attitude determination. In addition, the useful capacity of data storage and telemetry transmission is reduced. For the SCADS-S[3] design procedure, the average false detection rate is taken as N_f = one per five scan periods.

The choice of slit width, $\widehat{SW}$, is probably the toughest to make since it involves the accuracy of the overall system. It is desirable to make the slit as wide as possible since for a given scan period this causes a star to be in the slit longer and therefore allows a longer integration (time averaging) of the star pulse. It can be shown that for a given false detection rate and detection probability, a wider slit allows a smaller optical aperture. However, widening the slit reduces the accuracy with which the star can be located. So the slit should be selected to be as wide as possible and still meet the system accuracy requirement. Experience in performing error analysis has shown that with input azimuth errors to the constraint equations of three arc-minutes, the three axis attitude errors are six arc-minutes or less for approximately 80 percent of the time. Experience in performing error analysis has also shown that the azimuth position of a star can be located with an accuracy better than one-sixth of the slit width. So for a three arc-minute or less RMS azimuth error, the maximum allowable slit width, $\widehat{SW}$, is 18 arc-minutes for SCADS-S[3]. A detailed error analysis confirming the above assumptions will be presented in Section VIII.

G. Sun Shield Analysis

The primary purpose of the shield for the SCADS-S^3 sensor is to prevent direct sunlight from falling on the lens surface. Several theoretical shield designs are discussed in this section which can accomplish this mission.

The designs presented here are generally of two connected cones, of which the one next to the optics is primarily delineated by the field of view. This inner cone is slightly larger than the field of view. The other larger cone serves to shield the inner one from all direct sunlight. Since direct sunlight does generally fall on the outer cone its angle is taken large enough so that it cannot be "seen" by any part of the optics.

This is shown schematically in Figure 16 where θ is the field of view and cone angle of the inner cone, α is the angle of the outer cone with respect to the optical axis, β is the minimum allowable angle made by the sun's rays with the optical axis, and D is the diameter of the optics.

In general, the smallest possible cone is desired, which will occur when the distance $\overline{ab} = r$ is a minimum. It can be shown that this occurs for an angle α satisfying

$$\tan \alpha + \cot (\alpha - \theta/2) = \cot (\beta - \alpha) \qquad (50)$$

Generally for angles of β such that the sun is close to the edge of the field of view, this type of baffle becomes very large in size, and it is desirable to look for ways to make it smaller.

One method is to truncate the top cone and replace the missing portion by a baffle with a knife edge stop around the field of view as shown in Figure 17, thus also providing some flexibility. With this design there is still no sun illuminated surface exposed directly to the lens.

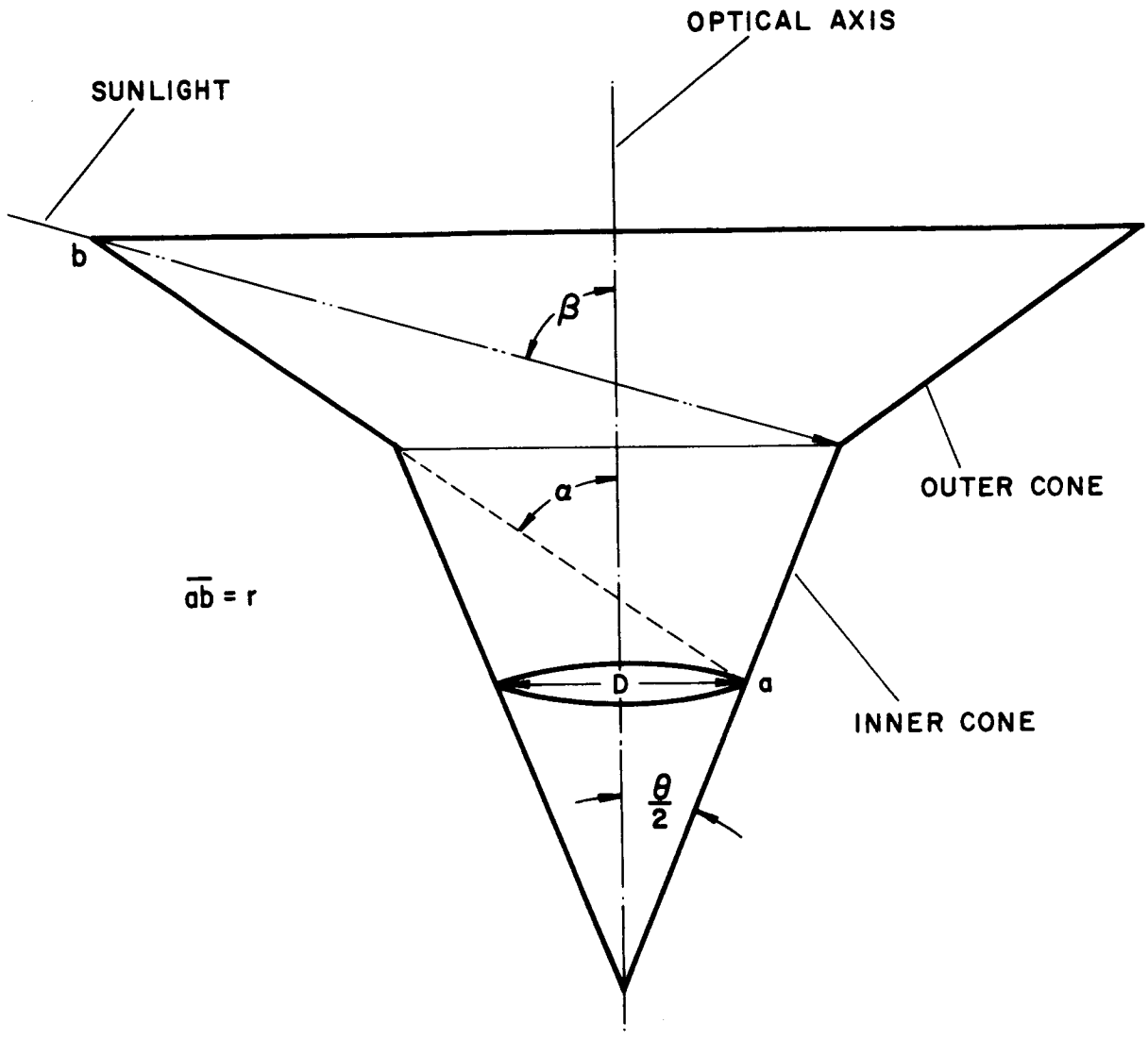

FIGURE 16: Connected Cones for Radiation Shielding

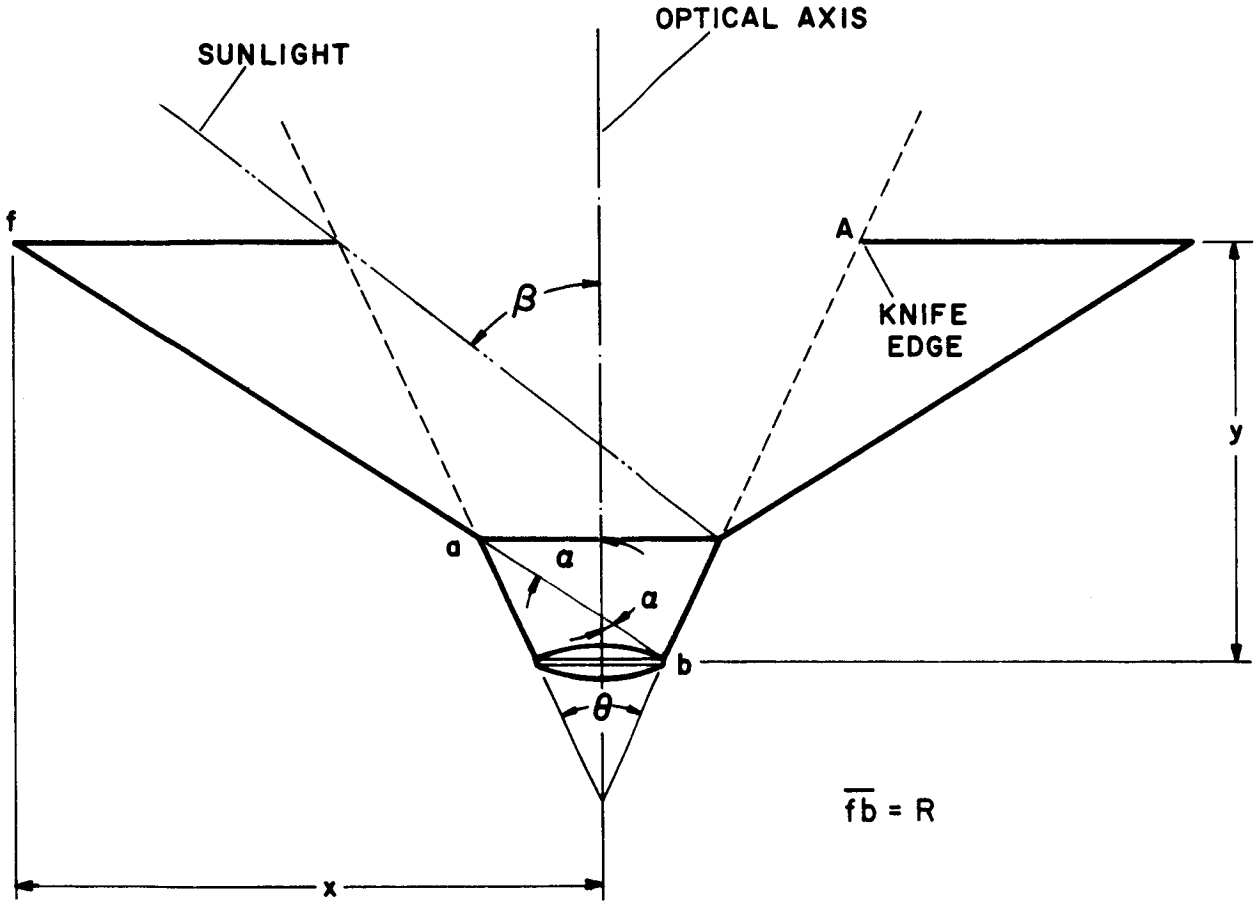

FIGURE 17: Radiation Shield

The disadvantage of this design is that now the lens is exposed to light which has been scattered twice off the inner surfaces of the outer cone and baffle. The lens is also exposed to light diffracted and reflected off the knife edge of the baffle at A. Diffraction off the knife edge may be reduced by approximately a factor of ten by serrating the knife edge, producing a sawtooth edge in the manner of Purcell and Koomen[15]. The serrations, however, must be accurately made with sharp, smooth edges and are obviously harder to make than a nonserrated knife edge. It is necessary to mention also that the knife edge (or sawtooth) must be very sharp to minimize the specular reflection from it directly into the optics.

For this design the distance $\overline{bf}$ is minimized with respect to α and the minimum occurs when

$$\cot(\alpha + \beta) + \tan \alpha = \cot (\alpha - \theta/2). \tag{51}$$

Up to this point the cone interior has been regarded as a diffuse reflector. If we could obtain purely specular reflecting surfaces, the cone of Figure 18 is possible. It may be shown that in this case the cone ideally need be only

$$L = D/2 \csc \theta/2 \, (\csc(\beta - \theta/2) - 1) \tag{52}$$

in length.

Since scattering will occur to some extent from any specular reflector this design is really feasible only insofar as this scattering is kept within bounds. Lengthening the cone and/or increasing the cone angle may also be used to reduce light into the lens. Moreover, if the lens is antireflection coated for normal rays, rays at 60 degrees are totally reflected. This characteristic may be used to reduce scattered light into the photomultiplier. (It should be noted that the cone designs of Figures 16 and 17 may also advantageously make use of specular reflectors of low optical efficiency.)

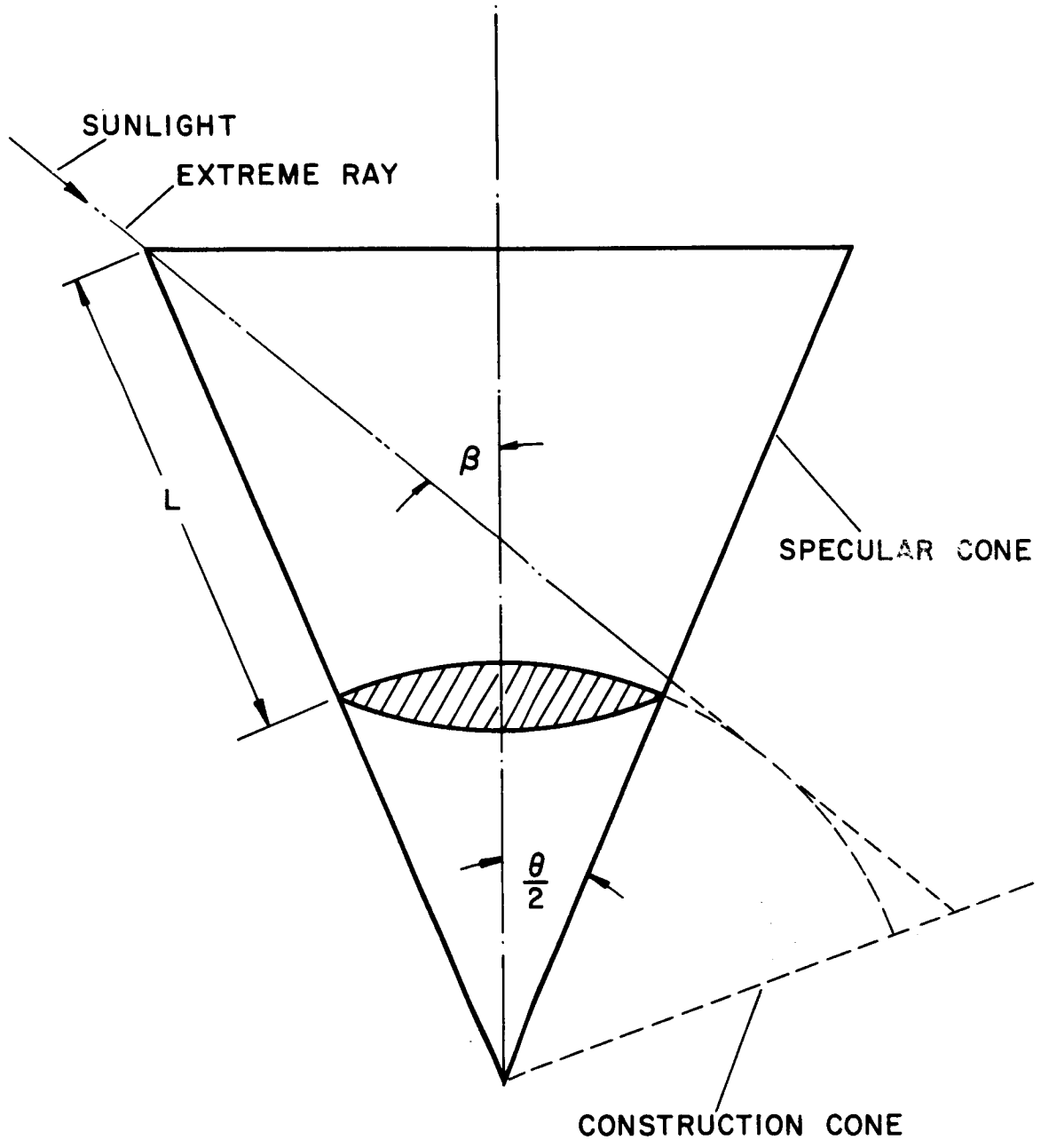

FIGURE 18: Specular Reflecting Radiation Shield

An antireflecting black paint with absorption of 99.9 percent ("Parson's Black") is available. Generally two reflections will occur before stray light in the designs of Figures 16 and 17 reaches the lens. This implies that in order to compete with these designs, diffuse reflection off the surface of the specular cone of Figure 18 must be held below one part in a million. This requirement means a high optical finish on a metallic surface and renders this solution somewhat speculative.

The edges of the lens elements will have to be coated with a light absorbing coating, or antihalation coating, to cut down scattering within the lens system. Scratches and dust on the lens elements, seeds, bubbles, and other inhomogeneities in the glass will also add to the scattering effects. Indeed, the problems regarding unwanted light resemble those encountered in solar coronographs.

For the "ideal" baffle (double cone without the knife edge) the length of a cone diagonal is given by

$$r = D \frac{\cos \alpha \sin(\beta + \theta/2)}{\sin(\alpha - \theta/2) \sin(\beta - \alpha)} \tag{53}$$

That same quantity for the cone with a knife edge baffle is given by

$$R = D \frac{\cos^2 \theta/2 \sin(\alpha + \beta)}{\cos(\beta - \theta/2) \cos \alpha \sin(\alpha - \theta/2)} \tag{54}$$

For a given field of view, θ, and sun angle off the optical axis, β, the outer cone angle α which minimizes r and R are given in Equations (50) and (51), respectively. Using these α, θ = 20 degrees, and various sun angles β the minimum cone sizes have been calculated and are given in Figure 19. It is interesting to note that, although at "small" sun angles (20 degrees to 30 degrees) a substantial size reduction results from the use of a knife edge baffle, the knife edge baffle rapidly loses its size advantage as the sun

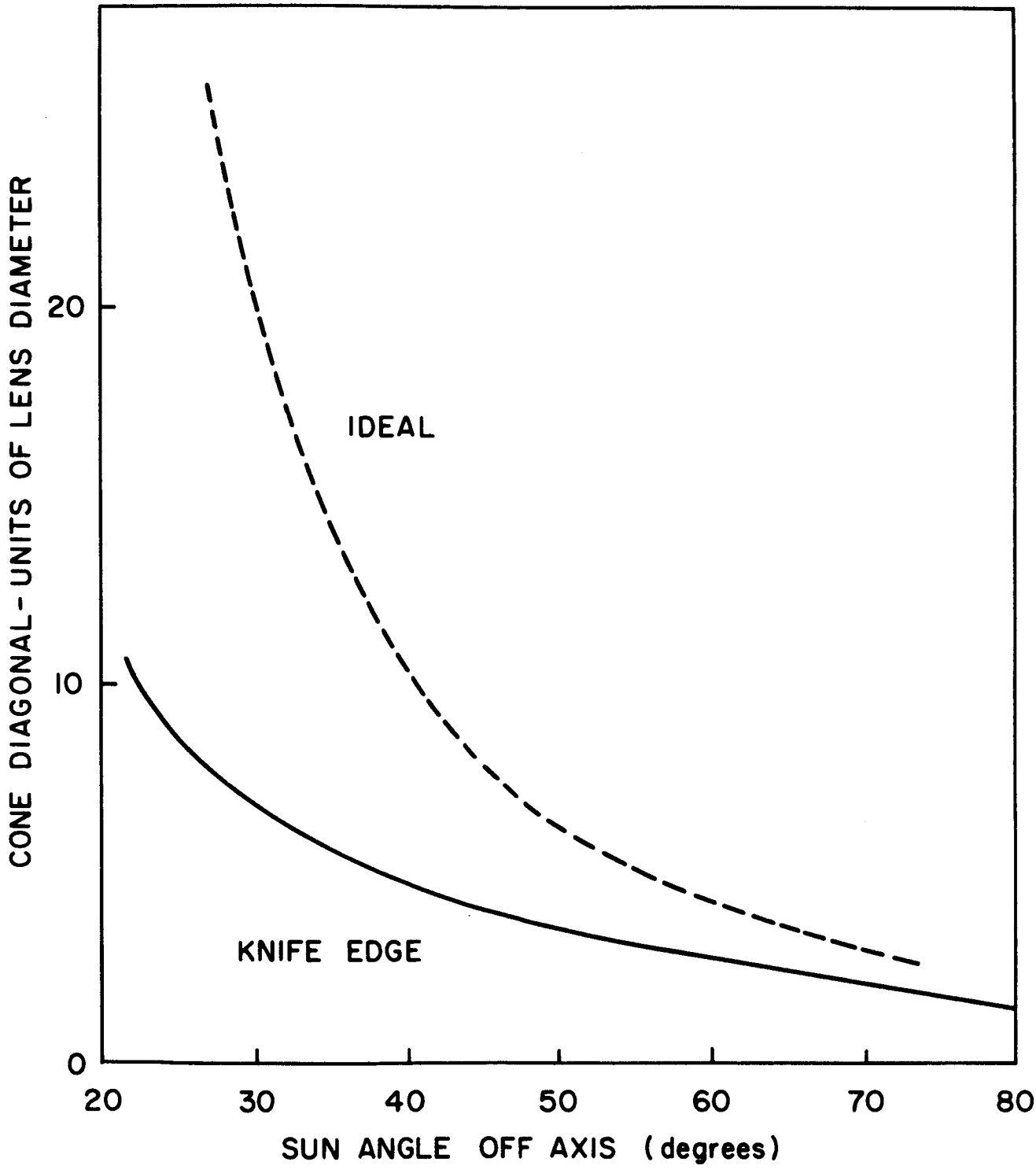

FIGURE 19: Minimum Cone Size as a Function of Sun Angle Off Optical Axis (Field of View, 20 Degrees)

angle increases.

The required shield dimensions can be determined for the knife edge shield of Figure 17. The maximum radius and height of the shield are respectively given as

$$x = D\left\{\frac{\cos \theta/2}{\sin(\alpha - \theta/2)}\left[1 + \frac{\cos \beta \sin(\alpha + \theta/2)}{\cos \alpha \sin(\beta - \theta/2)}\right] \sin \alpha - \frac{1}{2}\right\}$$

and

$$y = D \frac{\cos \theta/2}{\sin(\alpha - \theta/2)}\left[1 + \frac{\cos \beta \sin(\alpha + \theta/2)}{\cos \alpha \sin(\beta - \theta/2)}\right] \cos \alpha$$

H. Lens System f/number

In order to detect stars across the full field of view without employing a field condensing lens or fiber optics, the full field image diameter, d, of the optical system must be less than or equal to the active cathode diameter of the photomultiplier. Consequently, the optical system focal length, F, must be restricted since from Figure 3 it can be seen that

$$F = \frac{d}{2 \tan \frac{FOV}{2}}$$

Therefore, the f/number

$$f/n \leq \frac{d}{2D \tan \frac{FOV}{2}}$$

I. Blur Spot Size

The blur spot image of a star in the lens focal plane must be contained within the slit width if the signal is to be maximized as the star transits the slit. From Figure 3 and the law of cosines with the adjacent sides equal to γ, the blur circle, $\widehat{BC}$, can be related to the rotational slit width, $\widehat{SW}$. Since

$$\cos \widehat{BC} = \cos \gamma \cos \gamma + \cos \widehat{SW} \sin \gamma \sin \gamma$$

$$= \cos^2 \gamma + \sin^2 \gamma \cos \widehat{SW}$$

then

$$\frac{1 - \cos \widehat{BC}}{2} = \sin^2 \gamma \frac{(1 - \cos \widehat{SW})}{2}$$

and

$$\sin^2 \frac{\widehat{BC}}{2} = \sin^2 \gamma \sin^2 \frac{\widehat{SW}}{2}$$

Hence, for small angles

$$\widehat{BC} = \widehat{SW} \sin \gamma$$

Clearly, $\widehat{BC}$ must be smallest when $\gamma = \Gamma - \frac{FOV}{2}$, so

$$\widehat{BC} \leq \widehat{SW} \sin (\Gamma - \frac{FOV}{2})$$

J. Slit Reticle Dimensions

Figure 3 illustrates the slit in the focal plane of the optical system and its projection on the celestial sphere. As a part of the sensor design, it is required to determine the dimensions of the slit reticle. Figure 20 shows the geometry relating the rotational slit width, $\widehat{SW}$; the focal length, F; the cant angle, Γ; and the slit dimensions.

Let R = the radial distance from the intersection of the optical axis and the focal plane to the star image in the slit. Then the width of the slit, W_s, at radius R is given by

$$W_s = \widehat{BC} \cdot h$$

where $\widehat{BC}$ = the angle subtended from the lens nodal point by the slit width at radius R from the focal plane center;

h = distance from the center of the simple biconvex lens (optical system equivalent) to a point at radial distance R from the focal plane center.

The angle $\widehat{BC}$ is given by

$$\widehat{BC} = \widehat{SW} \sin (\Gamma - \delta)$$

where $\widehat{BC}$ and $\widehat{SW}$ are in radians

$$h = \frac{R}{\sin \delta}$$

$$\delta = \tan^{-1} \left(\frac{R}{F}\right) ,$$

$$\text{so } W_s = \frac{R\ \widehat{SW}}{\sin \delta} \sin (\Gamma - \delta)$$

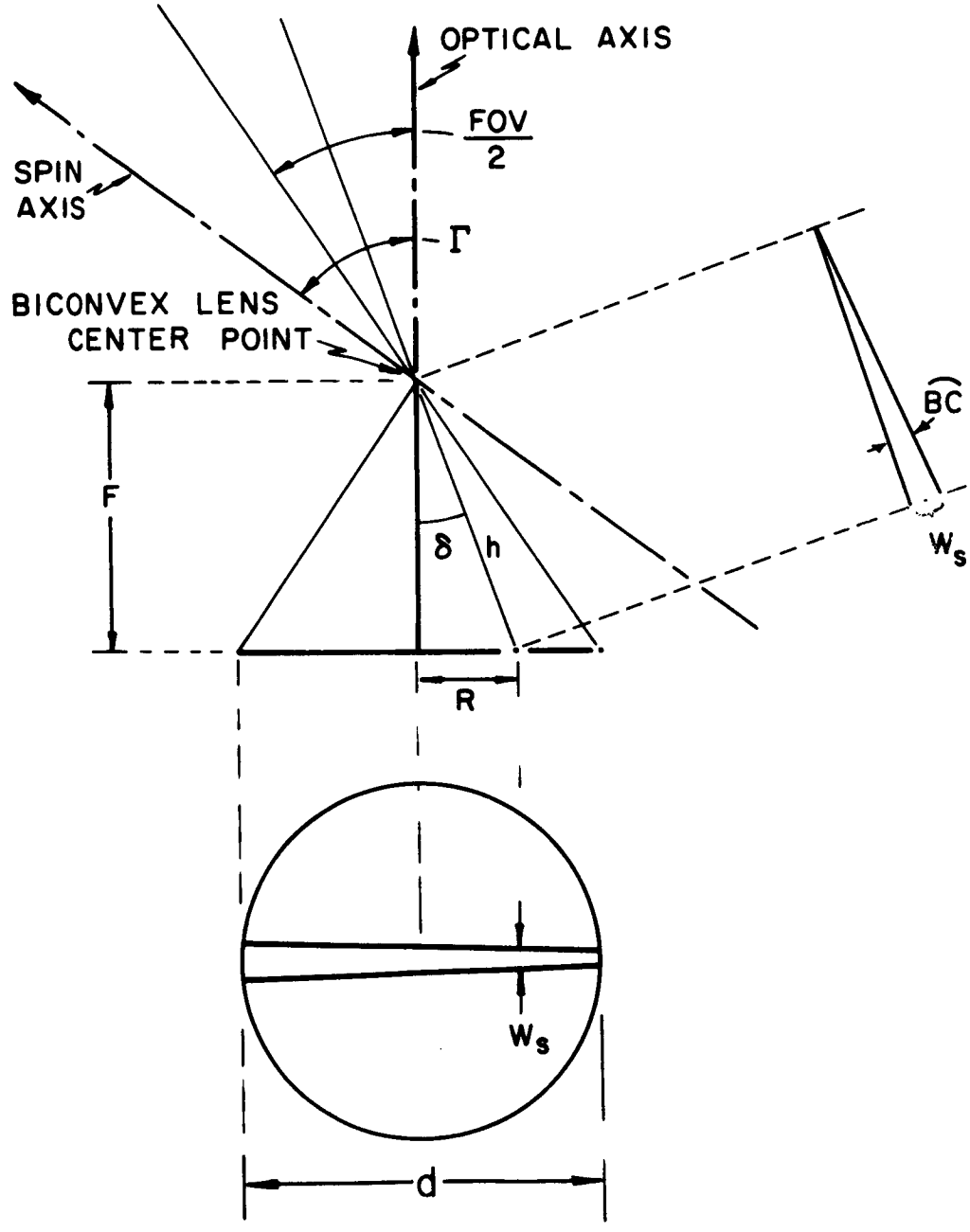

FIGURE 20: Geometry for Determination of Slit Dimensions

$$W_s = \widehat{SW} \, [F \sin \Gamma - R \cos \Gamma],$$

where W_s is expressed in the same units as both F and R. Consequently, the slit width in the focal plane varies as a linear function of R, as expected.

V. REQUIRED DESIGN PARAMETERS FOR SPIN STABILIZED VEHICLE

In the previous section, some essential analysis was presented and a design procedure was developed. In this section the design procedure will be employed to obtain the design parameters required for each spin stabilized configuration. Then from the results of this section, the final sensor design parameters will be chosen so the standard modular design requirement will be satisfied. The sensor components for the non-spin stabilized sensor configurations will then be selected from the spin stabilized parameters with some added modifications, such as a motor driven reticle. The non-spin stabilized vehicle configurations include the magnetically oriented vehicle for the circular polar orbit and the synchronous gravity gradient configuration.

The first step in the design procedure for each spin stabilized orbital configuration is to determine the cant angle of the optical system with respect to the vehicle spin axis. In addition to the restrictions placed upon the cant angle by the proximity of the sun, earth, or moon, further restrictions are imposed by the booms and antennas extending from the spacecraft, all of which can cause reflections into the SCADS sensor. The restrictions imposed by the booms and antennas prevail for all orbital configurations, so therefore the discussion which follows applies to all spin stabilized configurations.

The S^3 satellites may have four booms which are from four to five feet in length. These booms cause restrictions on the field of view, for sunlight may be reflected off the booms into a poorly positioned field of view.

In Figure 21, we picture a typical assembly of a S^3 satellite as presented in Reference [16]. Our optical axis is pictured as piercing the satellite in the middle of a panel. The angle between the line joining this piercing point and the end of the nearest boom and the optical axis is θ. Now we are forced to direct the optical axis so that θ does not become too small.

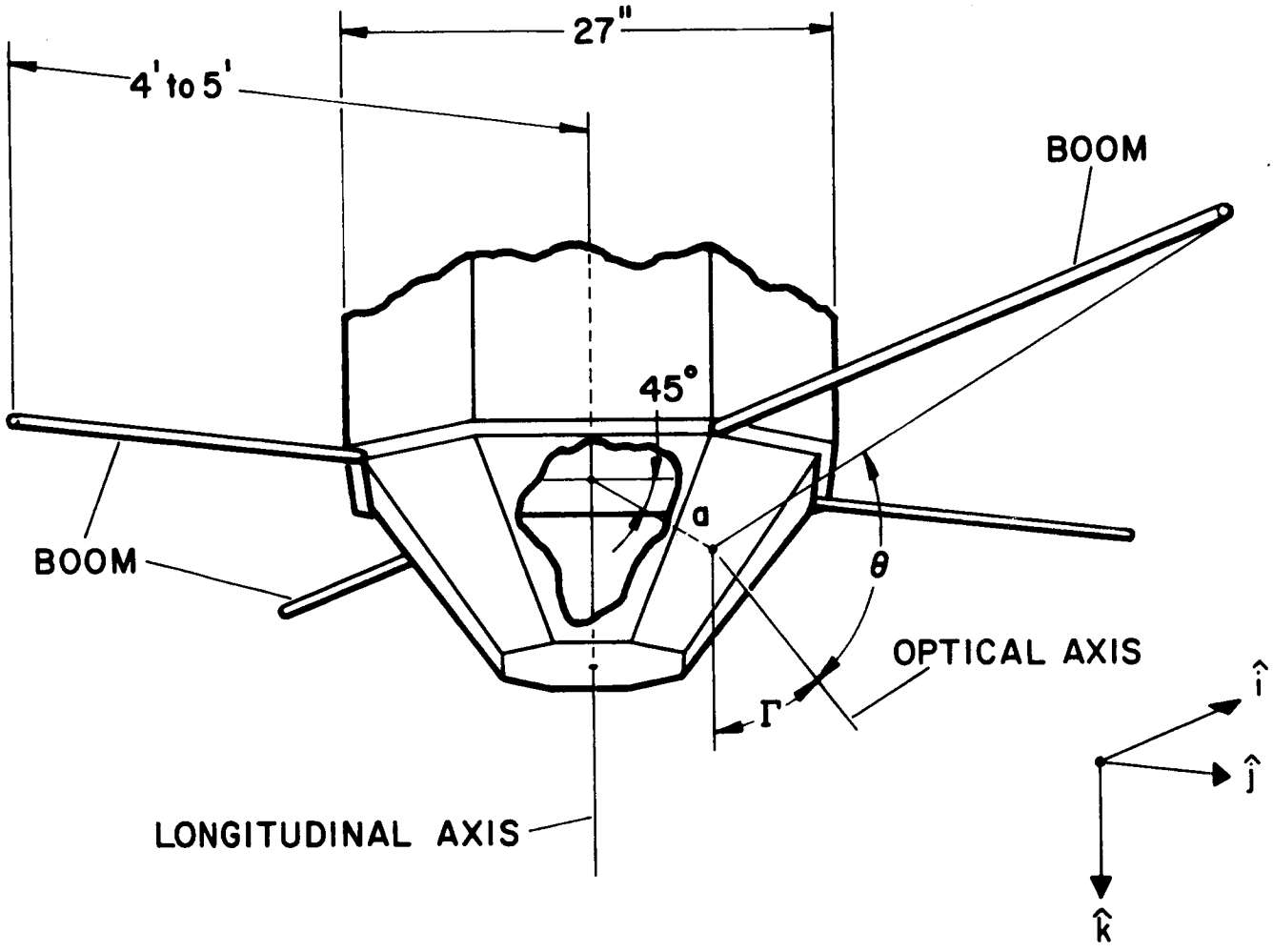

FIGURE 21: Schematic of Typical Vehicle Assembly and Optical Axis Location (approximate)

The minimum value of θ is somewhat argumentative. If the end of the boom were a light source as bright as the sun itself, then θ (min) = 70° for a knife edge cone designed to shield for a 70° sun angle. However, a more realistic assumption (but less conservative) is that reflected light from the boom's end cannot directly strike the lens. For a knife edge cone designed to shield for a 70° sun angle, this latter assumption implies θ (min) = 50°.

It can be shown that the maximum allowable cant angle, Γ, (Figure 3) is given by

$$\tan \Gamma = \frac{-B\,x + A\sqrt{A^2 + B^2 - x^2}}{-A\,x - B\sqrt{A^2 + B^2 - x^2}} \qquad (55)$$

where $A = a \sin 45^{\circ}$

$B = a \sin 45^{\circ} - b \cos \alpha$

$x^2 = \cos^2\theta\,(a^2 + b^2 - 2ab \sin 45^{\circ} \cos \alpha)$

here a = distance of center of base plate to center of lens (Figure 21)

b = length of boom measured from center of base plate (4' to 5')

45° = elevation of center lens with respect to base plate

α = azimuth of center of lens, i.e. the angle from the boom to the projection of the line from the base plate's center to the lens; the projection being on the base plate

0° = azimuth of boom

0° = elevation of boom.

Equation (55) may be derived as follows: Erect a triad of unit vectors such that $\hat{k}$ is parallel to the longitude axis of the satellite and $\hat{i}$ and $\hat{j}$ are parallel to the booms (Figure 21). Then, a vector from the center of the base plate to the end of a boom is $b\hat{i}$. A vector from the center of the base plate to the point at which the optical axis pierces the panel is $a \cos 45^{\circ}$ $(\cos \alpha\, \hat{i} + \sin \alpha \hat{j} + \hat{k})$. Also, a unit vector parallel to the optical axis is $\sin \Gamma \cos \alpha \hat{i} + \sin \Gamma \sin \alpha \hat{j} + \cos \Gamma\, \hat{k}$. (56)

Assume the optical axis is positioned at the maximum allowable cant angle. Then,

$$\begin{aligned} &\left|(b - a\cos 45^{\circ}\cos\alpha)\,\hat{i} - a\cos 45^{\circ}(\sin\alpha\,\hat{j} + \hat{k})\right|\cos\theta \\ &= \left[(b - a\cos 45^{\circ}\cos\alpha)\,\hat{i} - a\cos 45^{\circ}(\sin\alpha\,\hat{j} + \hat{k})\right] \\ &\cdot (\sin\Gamma\cos\alpha\,\hat{i} + \sin\Gamma\sin\alpha\,\hat{j} + \cos\Gamma\,\hat{k})\,. \end{aligned} \tag{57}$$

Hence,

$$x\cos\theta = -a\sin 45^{\circ}\cos\Gamma + (b\cos\alpha - a\sin 45^{\circ})\sin\Gamma. \tag{58}$$

If the above equation is solved for $\tan\Gamma$, two solutions are obtained, one of which is redundant, the other is given by (55).

We may assume a = 14 inches; then the following table is constructed.

TABLE III

MAXIMUM ALLOWABLE CANT ANGLE AS FUNCTION OF BOOM LENGTH, LENS POSITION, AND MINIMUM ALLOWABLE SHIELD ANGLE

b (ft)	α	θ	Γ
4	45°	51°	97.9°
5	45°	51°	100.5°
4	45°	70°	51.5°
5	45°	70°	50.1°
4	22.5°	51°	61.0°
5	22.5°	51°	56.8°
4	22.5°	70°	38.6°
5	22.5°	70°	34.7°

From this table, we see that the choice of four or five feet makes little difference in the maximum allowable cant angle. Mounting considerations favor an azimuth of $\alpha = 22.5^{\circ}$ rather than 45°. We may conservatively conclude that the cant angle Γ of 40° or less will not cause difficulties with light reflected from the booms into the optics. Moreover, no special mounting constraints of stray light shield designs are imposed by the booms for cant angles of 40° or less.

A. Elliptical Equatorial Orbit

1. Cant Angle

The first class of orbits we will consider is the elliptic equatorial orbit as pictured in Figure 22.

The satellite is to be spin stabilized with the spin axis in the equatorial plane. The spin period is about 15 seconds. Torques will be intermittently applied to the satellite so that the angle between the spin axis and the sun will be confined in an interval from 25° to 70°.

In order to avoid the sun, we thus may locate the optical axis of the SCADS-S^3 sensor near the negative spin axis. If the optical axis were to be along the negative spin axis, then the smallest angle between the sun and optical axis would be 110°. However, if the optical axis is along the negative spin axis, then the earth would periodically enter the field of view.

The earth subtends a relatively large angle, so its size cannot be ignored. Figure 23 is a plot of the half angle, ϕ, subtended by the earth as a function of the true anomaly ν (Figure 22). Note that this angle varies from 73° at perigee to 10° at apogee. So in order to avoid the earth entering the field of view, the optical axis would have to be at least 73° from the negative spin axis. With this "cant angle" sunlight reflections inside the sun shield may cause some difficulties. Moreover, the satellite's booms may reflect light into the optics.

As previously discussed, a conservative estimate of the maximum cant angle such that boom reflections cause no problems is 40°. With this cant angle, the sun will always be 70° or more from the optical axis. The stray light shield must then be designed to effectively shield for such angles. Hence the choice of a cant angle of 40° is optimum, and the stray light problem is that presented by the sunlit position of the earth. This

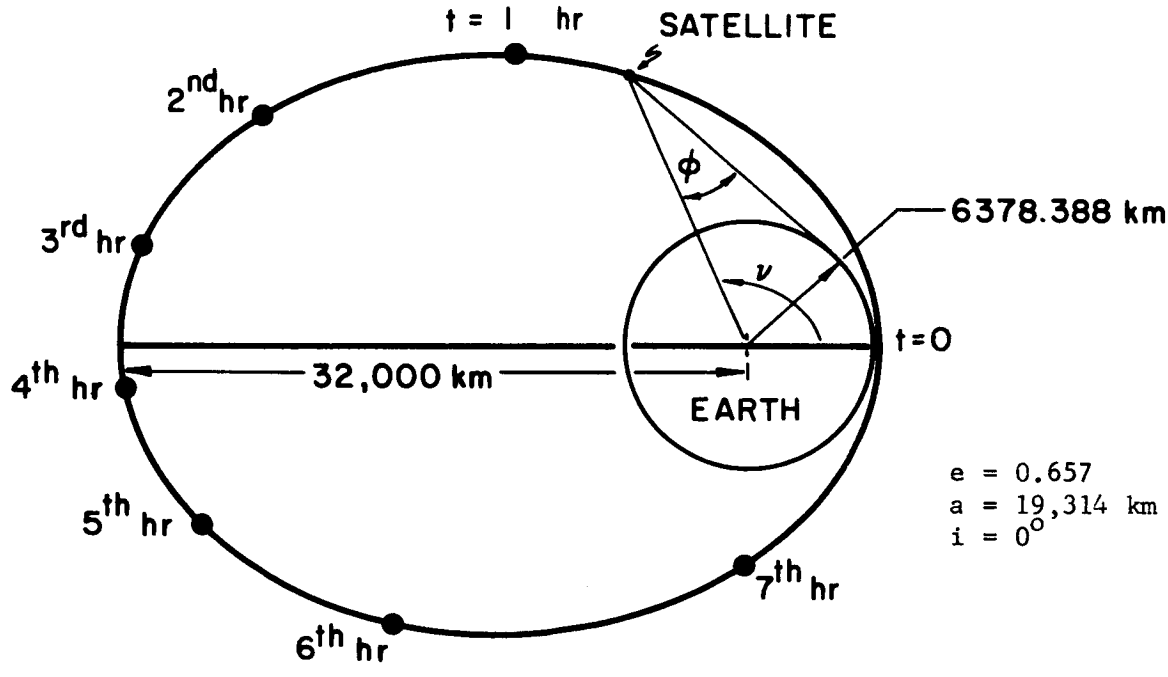

FIGURE 22: The Elliptical Equatorial Orbit

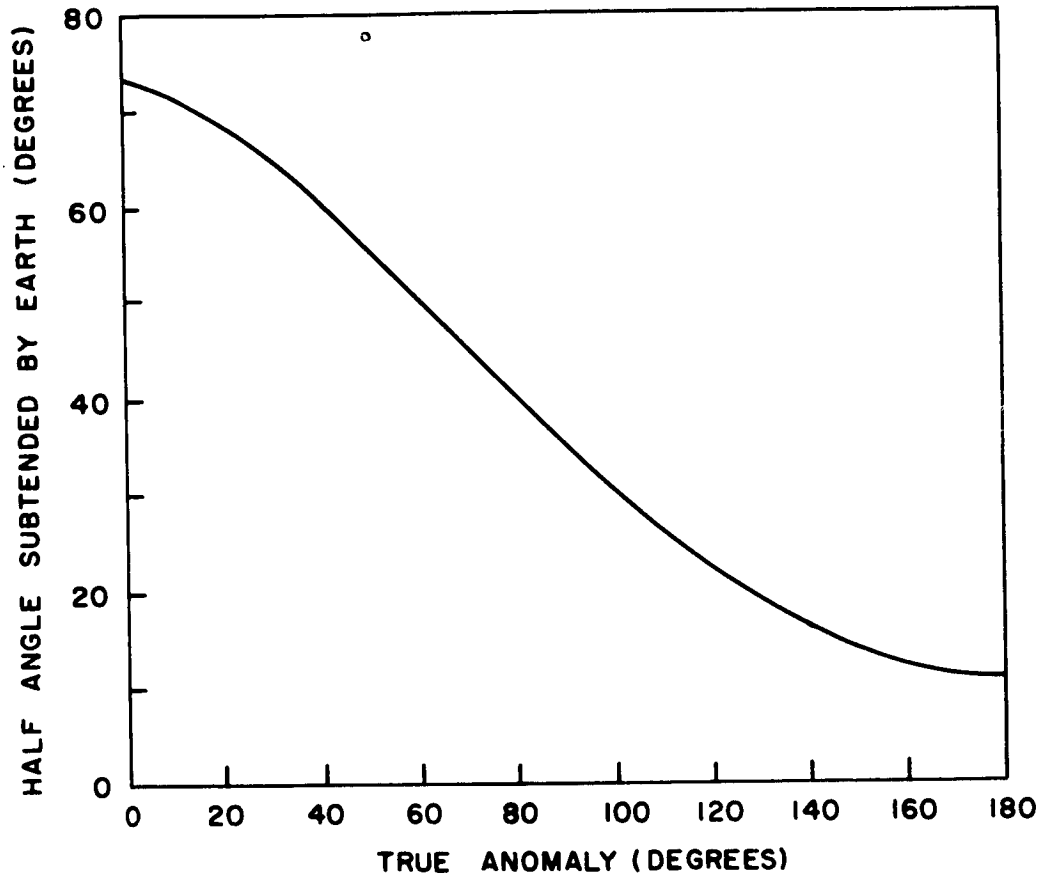

FIGURE 23: Angular Subtent of Earth Versus Satellite Position

operational constraint is discussed in Section X.

2. Field of View

In Section IV-A, it was shown that the optical field of view is given by

$$\sin FOV/2 = \frac{(1 - \cos \theta/2)}{2 \sin \Gamma}$$

where θ is obtained from Figure 5 in order to have three stars brighter than magnitude M_v in the field of view with probability .99. Tabulated below are the corresponding values of M_v, θ, and FOV for $\Gamma = 40^o$.

TABLE IV

LIMITING STAR MAGNITUDE VERSUS FIELD OF VIEW

M_v	θ	FOV
3.5	60^o	12^o
3.0	70^o	16.2^o
2.5	88^o	25.2^o
2.1	112^o	40^o
2.0	122^o	47.2^o

It should be noted that as the field of view increases, the magnitude detection limit, M_v, decreases so that only the brighter stars need be detected. The brighter the star required for detection, the smaller may be the optical aperture. However, as the field of view becomes large the physical limitations of optical design in achieving satisfactory image quality become a dominant factor. For this reason, the field of view for the elliptical equatorial orbit is determined to be 40^o.

A detailed star availability search using a 40° field of view for the elliptical equatorial orbit is described in Section VIII.

3. Optical Aperture

The optical aperture will now be determined based on the discussion in Section IV-F. For the elliptical equatorial orbit, the scan period has been specified as T = 15 seconds. With this scan period value, the optical aperture has been determined to be D = .26 inch for Γ = FOV = 40°.

It is interesting to compare the above value for D with the values of D required for other sets of θ and M_v. Values of D are tabulated below:

TABLE V

REQUIRED OPTICAL APERTURE TO DETECT STAR MAGNITUDE M_v

M_v	θ (degrees)	FOV (degrees)	D (inches)
3.5	60°	12°	.52
3.0	70°	16.2°	.39
2.5	88°	25.2°	.30
2.1	112°	40°	.26

4. Blur Spot Size

For Γ = FOV = 40° and $\widehat{SW}$ = 18 arc-minutes, the blur spot must subtend an angle $\widehat{BC}$ given by

$$\widehat{BC} \leq 18 \sin 20^{\circ} = 6.2 \text{ arc minutes.}$$

5. Filter Cut-Off Frequency

From Equation (28) with T = 15 seconds and $\widehat{SW}$ = 18 arc-minutes, the filter cut-off frequency is determined to be f_c = 43.8 cps.

B. Near-Circular, Near-Polar Orbit

1. Cant Angle

The near-circular, near-polar class of orbits is to have inclinations of $90^{\circ} \pm 10^{\circ}$ and vary in height from 300 km to 500 km. These heights imply an orbital period of about 101 minutes. The sun's position with respect to the orbital plane is not specified.

Within this class of orbits, the stabilization modes are to be as follows:

(1) Spin stabilized with a spin period at some value within the range 30 seconds to 0.5 second, the spin axis being along the orbital normal;

(2) Magnetically stabilized with the longitudinal axis of the satellite being parallel to the local direction of the earth's magnetic field.

The instrumentation and cant angle will be different for the two modes. Let us first consider the spin stabilized mode.

The comparatively low altitude orbit causes us considerable difficulty in avoiding radiation from earth reflected sunlight. At an altitude of 300 km the half-angle subtended by the earth is 73°, while this angle is reduced to 68° at 500 km.

In Figure 24, we picture the geometry of the field of view as projected on the celestial sphere. This figure would be an accurate representation of the effective field of view if the sun did not exist. Later, in Section X-A, we will show the degradation of the effective field of view due to the sun and the sunlit earth. In the figure, we have chosen a projection so that the orbital path is a circle on the projection. The orbital normal, which is also the satellite spin axis, lies on the center of this circle (Figure 26).

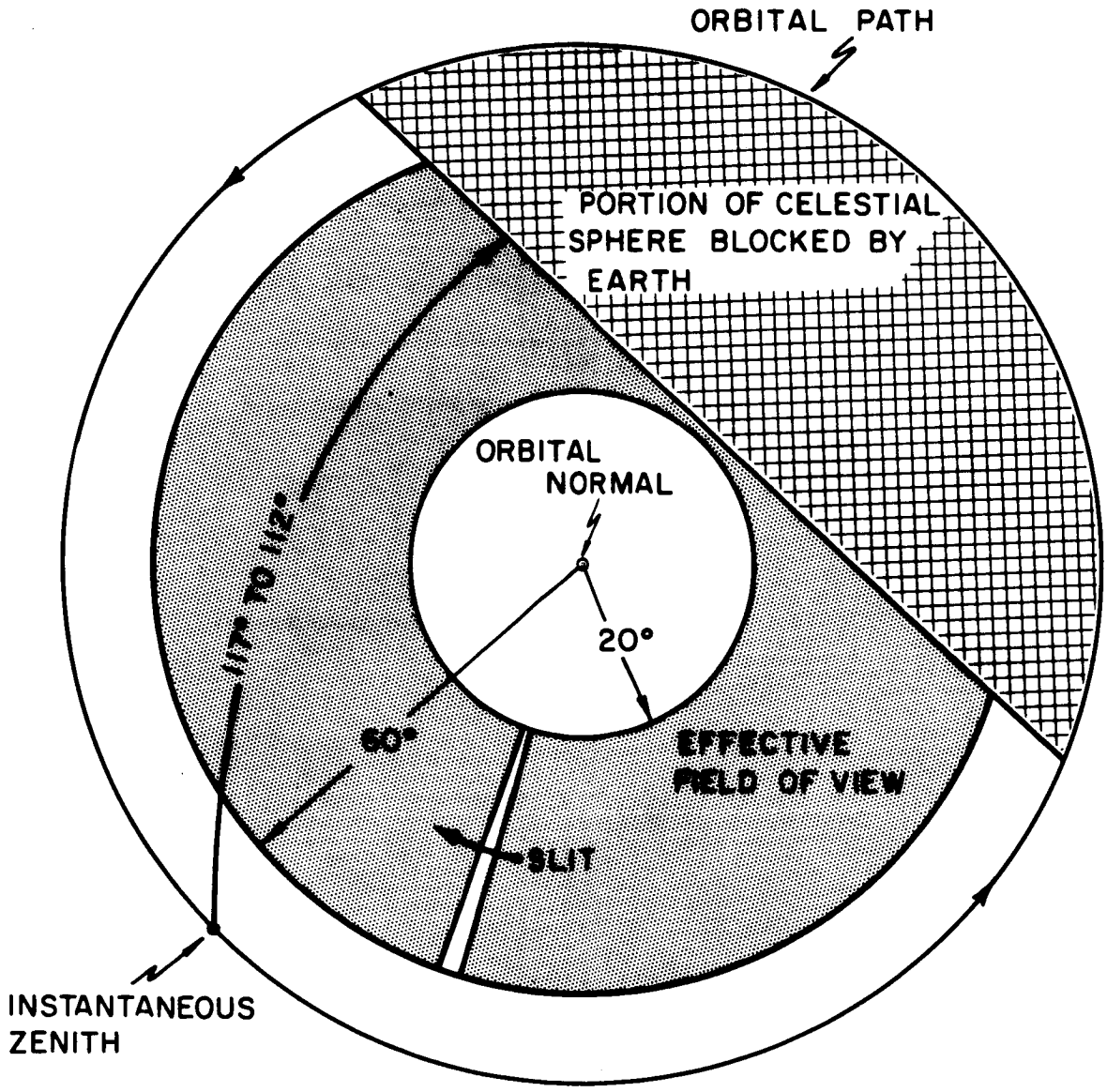

FIGURE 24: Geometry of Field of View for Near-circular, Near-polar, Spin Stabilized Orbits

A portion of the stellar field will be obscured because of the opaque earth. This obscured region will lie from 112^{o} to 117^{o} from the satellite instantaneous zenith. Again, we choose to cant the instrument 40^{o} from the orbital normal (spin axis). A large cant angle is desirable, for then a large portion of the effective field of view will be displaced from the earth. However, because of the boom restrictions, 40^{o} is the maximum cant angle. The effective field of view is that portion of the celestial sphere which is not obscured by the earth and bounded between two circles with common center at the orbital normal and radii of 60^{o} and 20^{o}, respectively (Figure 24). Hence, a 360^{o} azimuthal direction is not available except near the inner edge of the effective field of view. On the average, 98^{o} of the azimuth direction are obscured. Note, however, that the obscured region is not fixed, but moves as the satellite moves.

Our discussion thus far has assumed that the sun does not exist. In Section X we will evaluate the additional loss of field of view because of intense radiation from the sun and the sunlit earth. Because of the sun radiation and earth reflected radiation approximately 150^{o} of the azimuth direction will be obscured on the average.

The magnetically stabilized satellite may possess a small but undetermined roll about the satellite's longitudinal axis. Hence, if the optical axis were canted from the longitudinal axis, its position about this axis would be simply a matter of chance. Moreover, no increase in the effective field of view is obtained by choosing a non-zero cant angle (which is not the case for the spin stabilized satellites). Thus, we recommend a zero cant angle for this mode. With this cant angle, we will be able to detect stars only when the satellite is in the northern hemisphere (or southern hemisphere, dependent on the location of the instrument).

2. Field of View

For the near-circular, near-polar spin stabilized mode, the average loss

of the field of view is approximately 150° of each scan rotation. Consequently, only 210° of each scan rotation can be utilized to view stars. This being the case, then with $\Gamma = 40^{\circ}$, the required field of view would have to be greater than 40° in order to instantaneously have three stars brighter than +2.1 magnitude in the field of view with probability .99. But in order to permit a reasonable optical design, the field of view will be restricted to 40° which now requires detecting dimmer stars. So if θ is determined, then M_v can be determined. From Section III-B, it follows that

$$\left(\frac{210}{360}\right) 2 \sin \Gamma \sin \frac{FOV}{2} = 1 - \cos \theta$$

So from Figure 5, M_v must equal +2.5 in order to instantaneously have three stars brighter than magnitude M_v with probability better than .99.

3. Optical Aperture

For the circular polar orbit, the scan period can range from ½ second to 30 seconds. With Γ = FOV = 40° and M_v = +2.5, the required optical aperture has been determined as a function of scan period. The required value of D for specific values of T are tabulated in Table VI on the following page.

4. Blur Spot Size

Since Γ = FOV = 40° and $\overset{\frown}{SW}$ = 18 arc-minutes, the blur spot must subtend an angle $\overset{\frown}{BC} \leq 6.2$ arc-minutes.

5. Filter Cut-Off Frequency

The filter cut-off frequencies may be determined for $\overset{\frown}{SW}$ = 18 arc-minutes and specific values of T within the range $.5 \leq T \leq 30$ seconds. Several values of f_c are tabulated in Table VII on the following page for specific values of T.

TABLE VI

REQUIRED OPTICAL APERTURE VERSUS SCAN PERIOD

T (seconds)	D (inches)
0.5	2.04
1	1.44
2	1.02
5	.64
7	.54
8	.51
9	.48
12	.42
15	.37
20	.32
25	.29
30	.26

TABLE VII

OPTIMUM FILTER FREQUENCIES AT SPECIFIC SCAN PERIODS

T (seconds)	f_c (cycles per second)
0.5	1312
1.0	656
2	328
5	131
7	94
8	82
9	73
12	54.7
15	43.8
20	32.8
25	26.3
30	21.9

C. Longitude-Synchronous

1. Cant Angle

At synchronous heights the half-angle subtended by the earth is only 8^{o}. Moreover, the satellite is gravity gradient stabilized so that the longitudinal axis has a direction which is approximately away from the earth's center.

Since the satellite is not, or is only weakly, yaw stabilized, there is no advantage to canting the optical system from the longitudinal axis. We will thus choose the optical axis along the longitudinal axis in a direction opposite to that of the earth's center. With this choice, earth reflected radiation will cause no difficulties, but the sun will cause interferences which will render the SCADS instrument inoperable about 39% of each orbital period (24 hours).

Since the satellite for this orbital configuration is field stabilized, the remaining sensor design parameters are covered in the next section where the standardized sensor design parameters are determined.

D. Near-Circular, Near-Equatorial

1. Cant Angle

The last orbital class (Table I, page 3) is also spin stabilized. As is common to all the spin stabilized modes, we choose a 40° cant angle for this mode. As previously, the field of view is also 40°.

Since the scan period for this orbital configuration is much greater than for the spin stabilized, circular-polar, orbital configurations, the remaining design parameters will be covered when standardized sensor design parameters are determined in Section VI.

VI. STANDARDIZED SENSOR DESIGN PARAMETERS

In the previous section, the ideal sensor design parameters were derived for each spin stabilized vehicle configuration. In this section, a set of standardized sensor design parameters for the spin stabilized configurations will be selected from the set of ideal parameters. The set of selected standardized sensor design parameters are then no longer optimum for each scan period; however, they will be adequate to operate over a limited range of scan periods.

From the selected set of spin stabilized design parameters, a set of design parameters will be selected for a non-spin stabilized sensor. These parameters are then coupled with a motor drive reticle to comprise the SCADS sensor for the non-spin stabilized vehicle.

For all spin stabilized configurations, the cant angle of the optical axis with respect to the vehicle spin axis has been determined as 40° based largely on the light scattering restrictions imposed by the experimental booms extending from the S^3 vehicle. The optical field of view has also been determined as 40° for all spin stabilized configurations. Although a larger field of view would have permitted smaller optical apertures, the optical design would become increasingly more difficult for a larger field of view, especially for the image quality needed to realize the required system accuracy. It is, therefore, fortunate that the best cant angle and field of view are standard for all spin stabilized configurations; however, such a fortunate situation does not exist for the optical aperture.

As can be seen from Table VI of Section V, the ideal optical aperture is strongly dependent upon the scan period. However, by appropriate selection of D, the optical aperture is adequate to permit SCADS operation over a broad range of scan periods. Examining the ideal optical aperture required for various scan periods for the circular polar orbit, we observe that a 0.4 inch optical aperture will suffice for any scan period greater than or

equal to 15 seconds. This aperture is sufficiently large to realize SCADS operation for both the elliptical equatorial orbit configuration (T = 15 seconds) and the circular equatorial configuration (T = 120 seconds), both of which are spin stabilized. Then by doubling this aperture, it is possible to operate for all scan periods greater than or equal to four seconds. Finally with a two inch optical aperture, SCADS can operate for all scan periods greater than ½ second.

It should be noted that the two inch optical aperture can be employed for all S^3 spin stabilized configurations; however, the size and weight of the large aperture lens is undesirable for the longer scan periods where the large aperture is not required. It is desirable, however, to have a single lens design to cover all cases in order to standardize the optical system. The requirements are clearly conflicting and the alternatives pending are difficult to evaluate, since two optical apertures (D = 2.0 and D = .8) are also adequate to cover all spin stabilized configurations. However, it is reasonable that three optical apertures give greater flexibility in approximating the ideal condition at the expense of sacrificing a more standardized design.

In keeping with the attempt to standardize the SCADS lens requirements, one of the three optical apertures already selected for the spin stabilized sensor should be used in the non-spin stabilized SCADS sensor. When the S^3 vehicle is not spin stabilized, the scanning must be performed by a motor driven reticle and the optical axis coincides with the reticle spin axis, i.e., the cant angle is zero. Now each of the three lens systems discussed for the spin stabilized sensor has a 40^o field of view. From Figure 5 we can see that for $\theta = 40^o$, three stars brighter than $M_v = +4.0$ are in the field of view with probability .99. Now with $M_v = +4$ and the slit width = 18 arc-minutes, we can determine the scan period necessary to detect stars of fourth magnitude for a given optical aperture. By performing the computations we can tabulate the required scan periods as follows.

TABLE VIII

SCAN PERIOD REQUIRED FOR MOTOR DRIVEN RETICLE

D(inches)	T (seconds)
.4	29
.8	7.25
2.0	1.25

By examining the results, it is seen that the 0.4 inch aperture requires a relatively long scan period. However, the 0.8 inch aperture requires a reasonable scan period, so this aperture is chosen for the non-spinning vehicle sensor. It may be mentioned that the two inch aperture is undesirable because of its size and weight, but again the two inch aperture could be used as a single standard lens if its size and weight were tolerable.

The image quality required for each spin stabilized sensor is 6.2 arc-minutes for all three apertures; however, the image quality for the 0.8 inch aperture must be somewhat better since the cant angle is zero for the non-spin stabilized sensor. For the 0.8 inch aperture, the blur spot size must be for an 18 arc-minute slit;

$\widehat{BC} \leq 18 \sin 5^{\circ} = 1.5$ arc-minutes @ 5° off-axis
$\widehat{BC} \leq 18 \sin 20^{\circ} = 6.0$ arc-minutes @ 20° off-axis.

The slit for the non-spin stabilized sensor should have a 5° dead zone (no slit) radius at the center in order to avoid an infinitely small slit width dimension and excessively long star transits from stars close to the optical axis.

The dimensions have been determined for a knife edge bright source shield for each of the three lens apertures. For a 40° field of view and light rays

incident at an angle of $\beta = 70^{\circ}$ to the optical axis, the angle α has been determined as 63.44° and the shield dimensions have been tabulated as follows.

TABLE IX

SUN SHIELD DIMENSIONS FOR 70° SUN ANGLE

Lens Aperture D (inches)	Maximum Shield Diameter (inches)	Maximum Shield Height (inches)	Volume (in^3)
.4	1.15	.49	.5
.8	2.3	.97	4.0
2.0	5.8	2.4	64.4

Similarly, for a 40° field of view but for light rays incident at an angle of $\beta = 50^{\circ}$ to the optical axis, the angle α has been determined as 58° and the shield dimensions have been tabulated as follows.

TABLE X

SUN SHIELD DIMENSIONS FOR 50° SUN ANGLE

Lens Aperture D (inches)	Maximum Shield Diameter (inches)	Maximum Shield Height (inches)	Volume (in^3)
.4	2.7	1.1	6.3
.8	5.4	2.2	50
2.0	13.5	5.5	780

Although the shield size for $\beta = 50^{\circ}$ is much bigger than for $\beta = 70^{\circ}$, the larger shield will allow SCADS operation closer to the sun or sunlit earth. For the larger cone sizes, however, it would be advantageous to design a mechanically collapsible shield that would be latched into a collapsed state before and during vehicle launch and then electro-mechanically extended upon command after launch. A sketch for such a shield is shown in Figure 25.

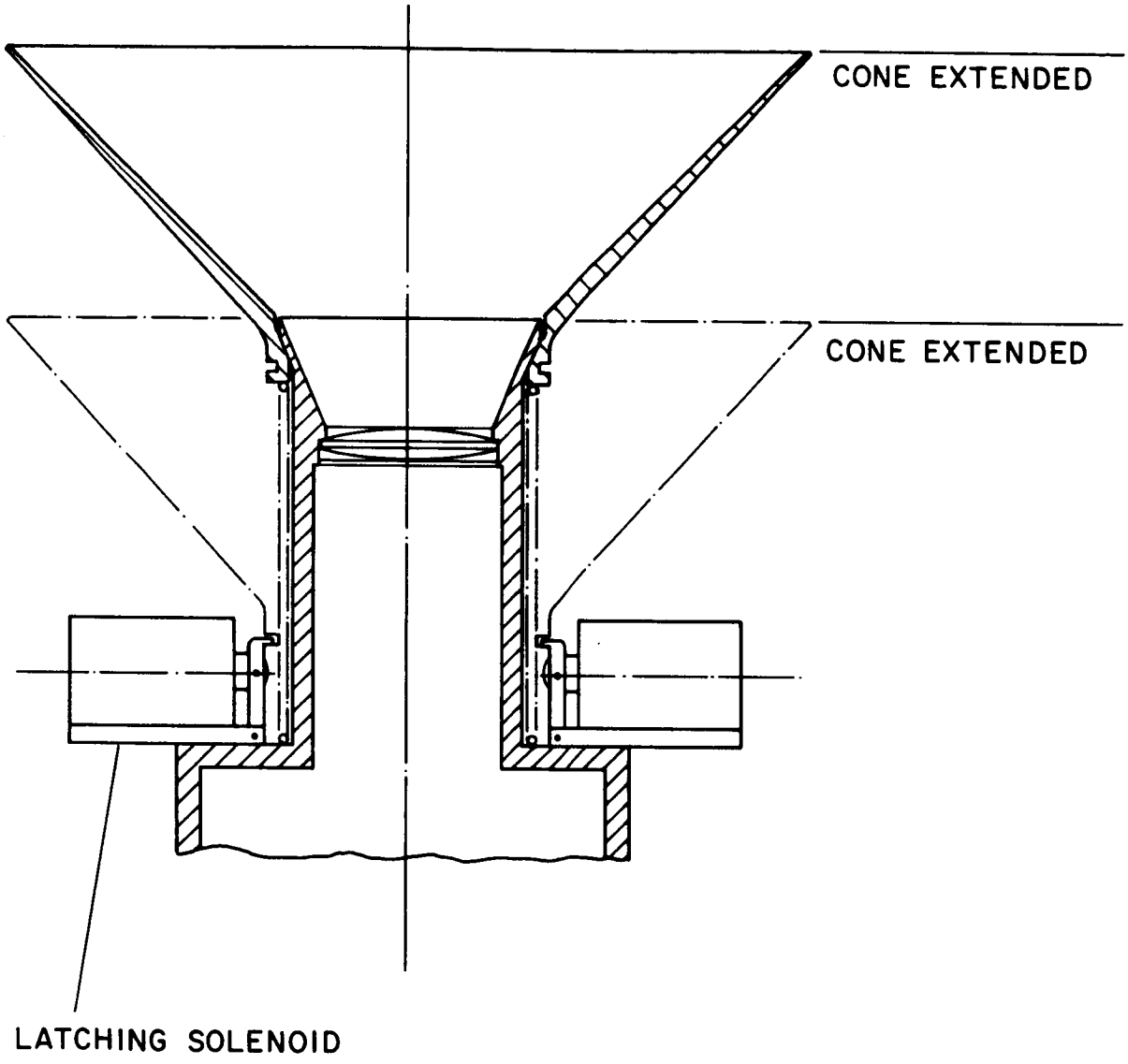

CONE RELEASE MECHANISM

FIGURE 25: Collapsible Sun Shield

TABLE XI

DESIGN PARAMETER SUMMARY

Photomultiplier: EMR 541N

Field of View: 40^{o}

Orbit Configuration	Lens Required: Cant Angle (Degrees)	Lens Required: Optical Aperture (Inches)	Lens Required: f/number	Lens Required: Spot Size Arc-minutes
Elliptical Equatorial (T = 15 seconds) Near-Circular, Near Polar (T $\geq$ 15 seconds) Near-Circular, Near-Equatorial (T = 120 seconds)	40^{o} 40^{o} 40^{o}	.4	$\leq$ 3.38	$\leq$ 6.2
Near-Circular, Near Polar (T $\geq$ 4 seconds) Synchronous Gravity Gradient (non-spin stabilized) Near-Circular, Near-Polar (magnetically aligned non-spin stabilized)	40^{o} 0^{o} 0^{o}	.8	$\leq$ 1.69	$\leq$ 1.5 @ 5^{o} off-axis (a) $\leq$ 6.2 @ 20^{o} off-axis
Near-Circular, Near-Polar (T $\geq$ ½ second)	40^{o}	2.0	$\leq$ 2.0 (b)	$\leq$ 6.2

Note: (a) This requirement could be relaxed at the expense of system accuracy for stars near the optical axis in the non-spin stabilized mode.

(b) Condensing lens required.

VII. OPTICAL DESIGN

The design of the sensor optics is very closely connected to the scan period of the satellite on which the scanning system is placed. For short scan periods, large clear aperture lenses, resulting in a large sensor in both weight and volume, are required. For a long scan period, smaller clear aperture lenses are needed, resulting in a sensor of reduced weight and volume. In order to provide minimum size sensors over the given range of 120 seconds to ½ second scan period, the sensor design requirements were divided into three groups according to the scan period covered. The classification is shown below.

Sensor Classifications

Scan Period	Clear Aperture Diameter	Maximum Rel. Aperture f/number	Blur Circle Diameter
15 seconds minimum	.4 inch	3.38	6.2 arc-min. max.
4 seconds minimum	.8 inch	1.69	1.5 arc-min.@ 5° off-axis 6.0 arc-min. @ 20° off-axis
½ second minimum 4 seconds maximum	2.0 inches	2.0	6.2 arc-min. max.

All lenses have a 40° field of view.

Lenses satisfying these requirements can be obtained in two ways:

(1) designing a lens especially for the requirements, with consideration of factors such as qualifications for space flight, minimum size, weight, and cost; and

(2) testing off-the-shelf lenses for suitability.

Method (1) offers the possibility of a minimum size lens configuration with functional operation assured. The design and fabrication costs will be

substantial; the per lens costs will not go down unless the numbers required are large. Method (2), should suitable lenses be found, is less expensive than Method (1); furthermore, should the lenses passing the tests be standard production lenses, the availability of lenses for future sensors at reasonable prices is assured.

An investigation of available lenses for testing was carried out. Table XII lists lenses suitable by aperture, focal length, and field of view for S^3 sensor service. Each of these lenses must be checked for image quality. All of the lenses listed below are for photographic purposes, and information, if any, about the image quality of the lens, is not applicable to celestial scanner type service. Should the lens prescription be available for a given lens, computer ray tracing should be performed, which would yield exact and detailed information about its performance, including blur spot diagrams, modulation transfer functions, image spread functions, and Conrady Sums.

The collection of light passing through the slit in the image plane is accomplished by an end window photomultiplier placed under the slit. If the photocathode is placed essentially in contact with the slit, the minimum overall length of the sensor is obtained, but the following difficulties arise:

(1) the image plane can never be larger than the diameter of the sensitive area of the photocathode, thereby restricting the field of view of the lens clear aperture;

(2) the response of the photomultiplier is sensitive to local variations of sensitivity in the photocathode surface; and

(3) when the image plane is exposed to bright objects, the concentration of illumination on the photocathode could cause local degradation of the light sensitive surface.

Item (1) is not a problem for the .4 or .8 optical apertures ;however, it is a problem for the two inch aperture. Item (2) is not a serious problem for the S^3 sensor since intensity measurements are not required. For Item (3), a

TABLE XII

OFF-THE-SHELF LENSES AVAILABLE FOR TESTING

Sensor Period	Focal Length	Relative Aperture(f/)	Commercial Name	Price	Maximum FOV
15 sec min	35 mm	f/2.5	Telsar	$44.50	66.4°
		f/2.8	Westron	49.50	
		f/2.8	Schneider Xenagon	119.50	
		f/2.8	Carl Zeiss Biometer	199.50	
		f/2.8	Romura	129.50	
		f/2.8	Tamar	139.50	
		f/2.8	Biogon	149.50	
		f/1.8	Carl Meyer Special	169.50	
		f/2.8	Rodenstock Heligon	89.50	
4-15 sec.	40 mm	f/2.0	Taylor-Cooke Speed	179.50	46°
		f/1.9	Carl Meyer	149.50	
		f/1.8	Astro Tachar	199.50	
		f/2.0	Kinoptik Apochromat		
		f/2.0	Zeiss Biotar		
		f/1.8	Kowa Cine Prominar		
		f/1.9	Rodenstock Heligon	94.50	
		f/2.0	Rodenstock Kilar	89.50	
		f/1.9	Schneider Xenon	99.50	
½-4 sec.	76 mm	f/1.5	Carl Zeiss Biotar	299.00	40°
		f/1.5	Carl Meyer Speed Lens	299.00	
	100 mm	f/2.0	Erneman Ernostar	219.50	39.2°

small reticle shutter can be employed if the sensor is aboard a spin stabilized vehicle. Hence, if the vehicle is spin stabilized and requires an optical aperture less than .8 inch, a condensing lens is not required if a reticle shutter is employed. However, for a two inch optical aperture, a condensing lens is required in order to condense all the energy passing the slit onto the active photocathode. Also, for a sensor aboard a non-spinning vehicle, a condensing lens is recommended because of the difficulty of fabricating a large aperture, fast acting shutter.

The optical schematics for the .4 inch and .8 inch optical apertures without condensing lenses are shown respectively in Figures 26 and 27.

The light condensing system recommended is a pair of plano-convex lenses with their convex surfaces in contact. The focal length of the combination of the two lenses is chosen so that when the plane surface of one of the lenses is as close as possible to the slit, the exit pupil of the sensor lens is imaged on the photomultiplier cathode. The optical schematic for the two inch optical aperture and associated condensing lens system is shown in Figure 28. The lens exit pupil in Figure 28 was larger than the photocathode, so the collection lenses reduced the exit pupil image to fill the photomultiplier. The light collector lenses are made of flint glass with refraction index of 1.600 for yellow light; glass of lower index, while having slightly better transmission properties, would result in a physically larger pair of lenses; glass of higher index of refraction would result in smaller lenses but poorer transmission in the short wavelength region.

As the physical separation between the image plane and the photomultiplier cathode becomes larger, the possibility of using glass fiber optics to transmit light from the slit to the photocathode becomes more attractive; when the image plane-photocathode distance is too short, the practical bending radius of the fibers in bringing light from the edges of the slit into the center limits the closeness of approach. The light collection system for the ½ to four second sensor would represent a marginal case for fiber optics versus condensing lenses.

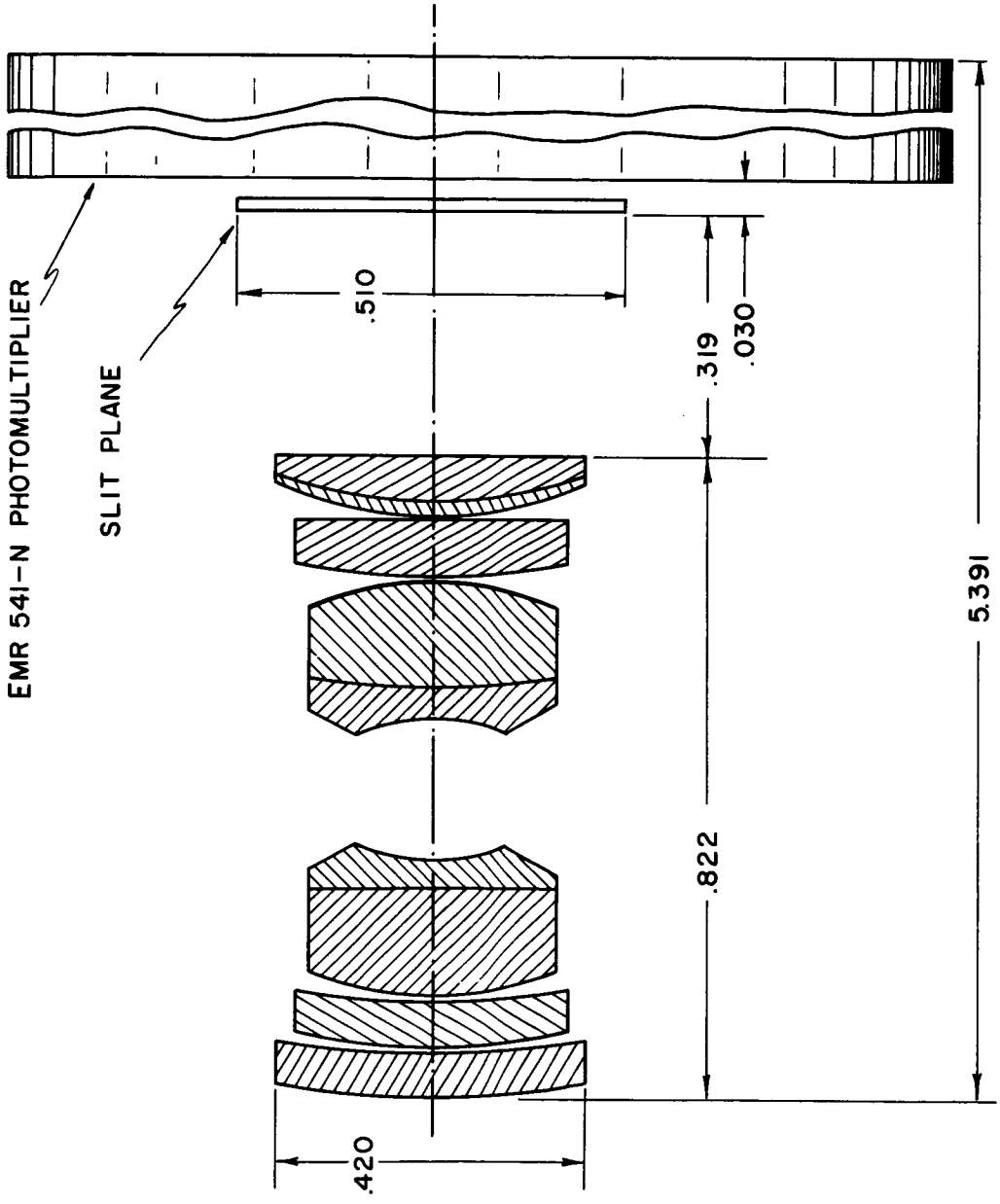

FIGURE 26: .4" Clear Aperture Optical System Scan Period, 15 seconds min.

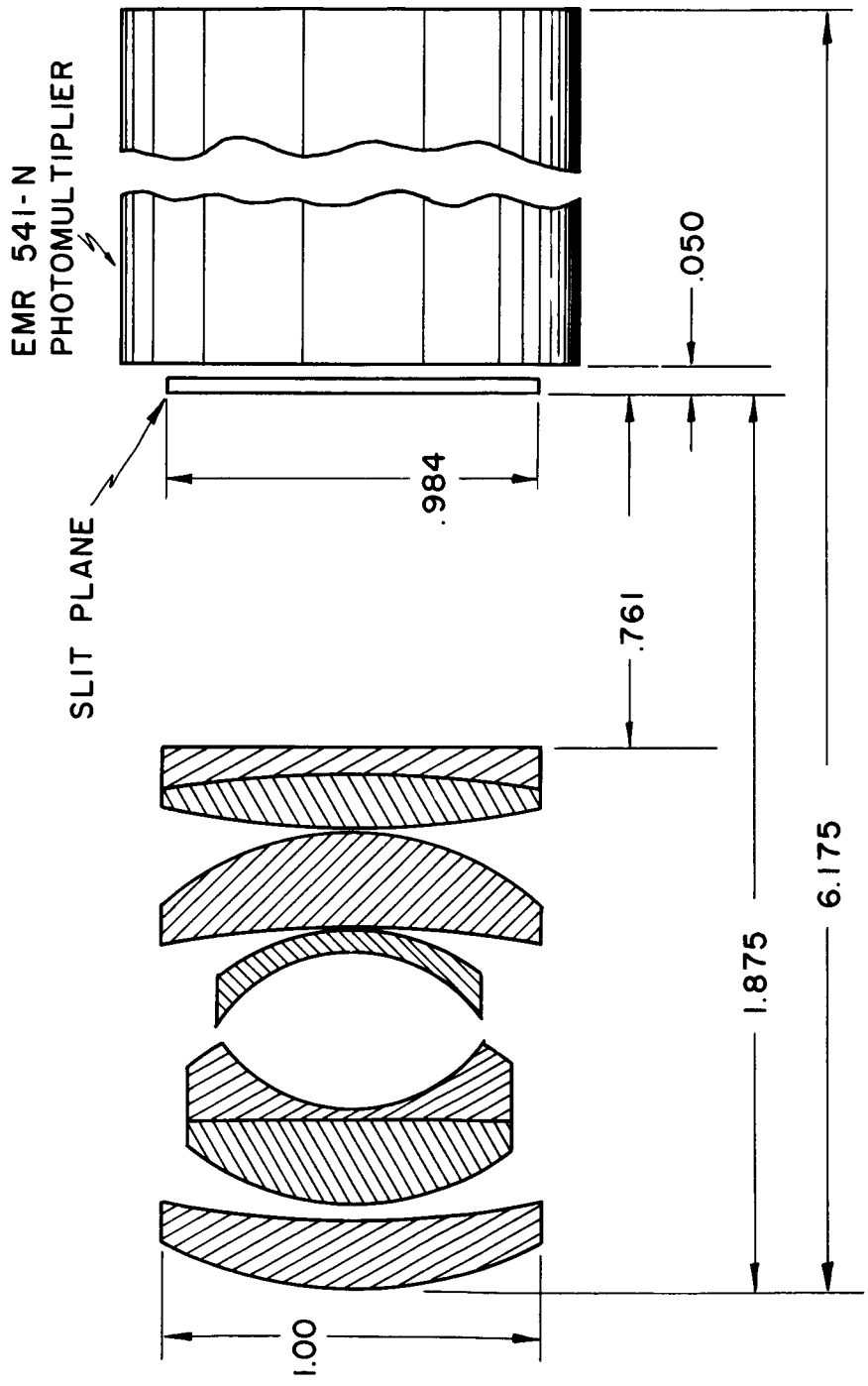

FIGURE 27: .8" Clear Aperture System, Scan Period 4 to 15 Seconds

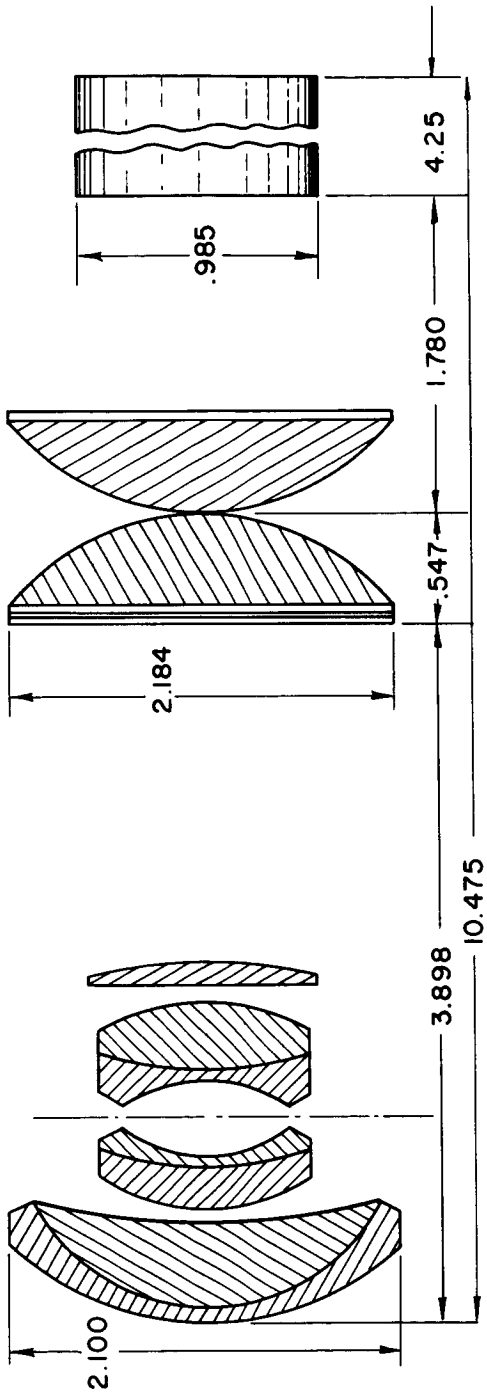

FIGURE 28: 2.0" Clear Aperture Optical System, Scan Period ½ Second to 4.5 Seconds

VIII. DETAILED STAR AVAILABILITY

In previous sections, we have given the parameters for all five modes of the S^3 mission. We will now investigate the star availability.

A. Elliptical Equatorial Orbit

Figure 29 gives the number of stars in the effective field of view as a function of the right ascension of the sun for three limits of the detectable photographic magnitude. The satellite will be torqued so that the angle between the spin axis and the sun will lie between 25° and 70°. However, the spin axis is in the equatorial plane. In deriving this graph, we assume the spin axis makes an angle of 47.5° with the sun and has a right ascension less than that of the sun. Note that a limit of 2.1 photographic magnitude is sufficient to yield three or more stars for all right ascensions.

B. Near-Circular, Near-Polar, Spin Stabilized Satellite

For the spin stabilized mode of the near-circular, near-polar orbits, a full 360° of unblocked azimuth is never available except near the inner edge of the field (see Figure 24). In order to determine the star availability we now arbitrarily assume that 150° of the azimuthal directions are obscured as pictured in Figure 30. Recall that the true obscured region will not be fixed as pictured in Figure 30, but will move as the satellite's position changes.

Figure 31, then, yields the number of stars in the assumed field of view as a function of the right ascension of the orbital normal (a polar orbit was assumed) for various limiting photographic magnitudes.

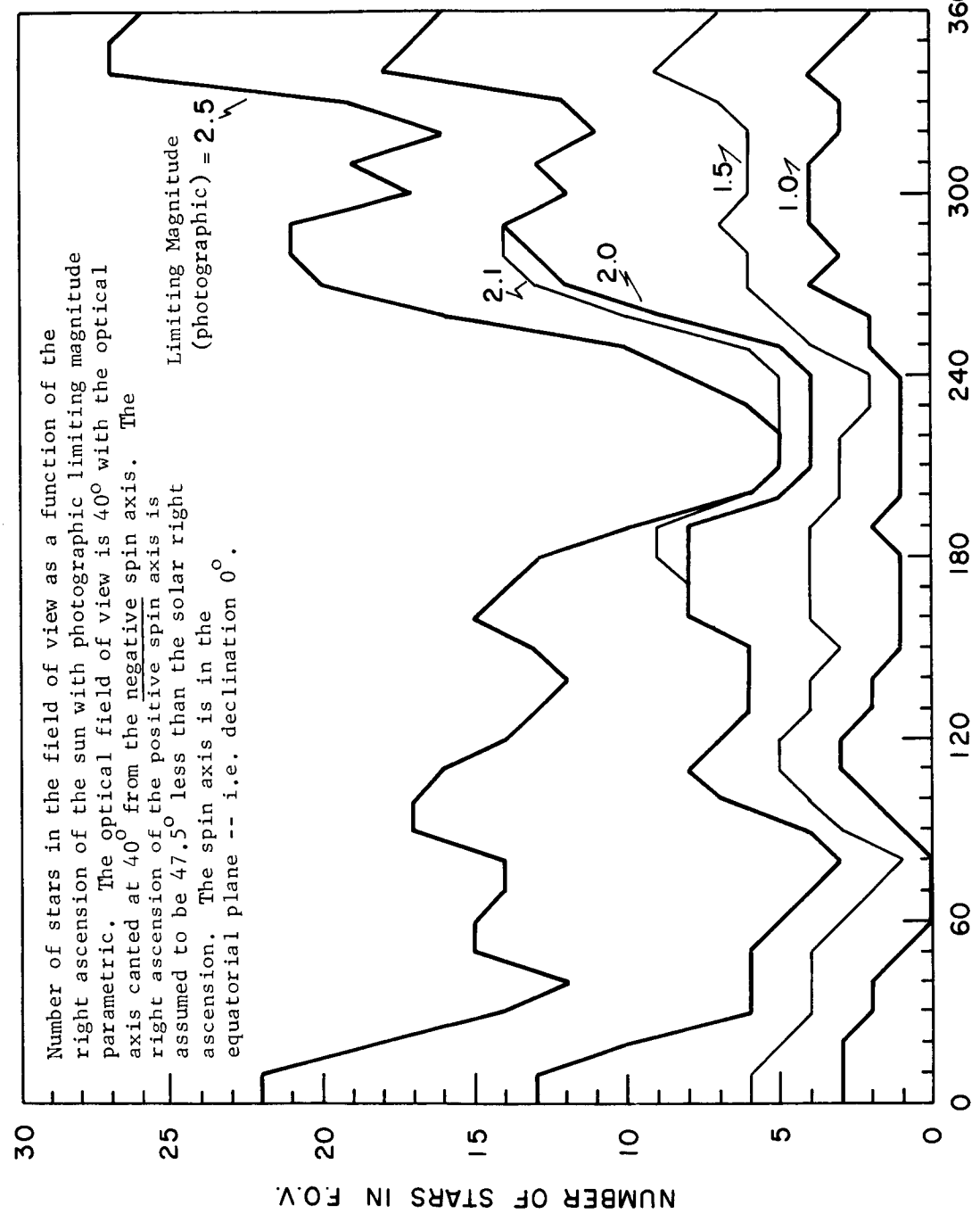

FIGURE 29: Number of Stars in Field of View as a Function of Sun's Right Ascension and Various Photographic Magnitude Limits - Elliptical Equatorial Orbit

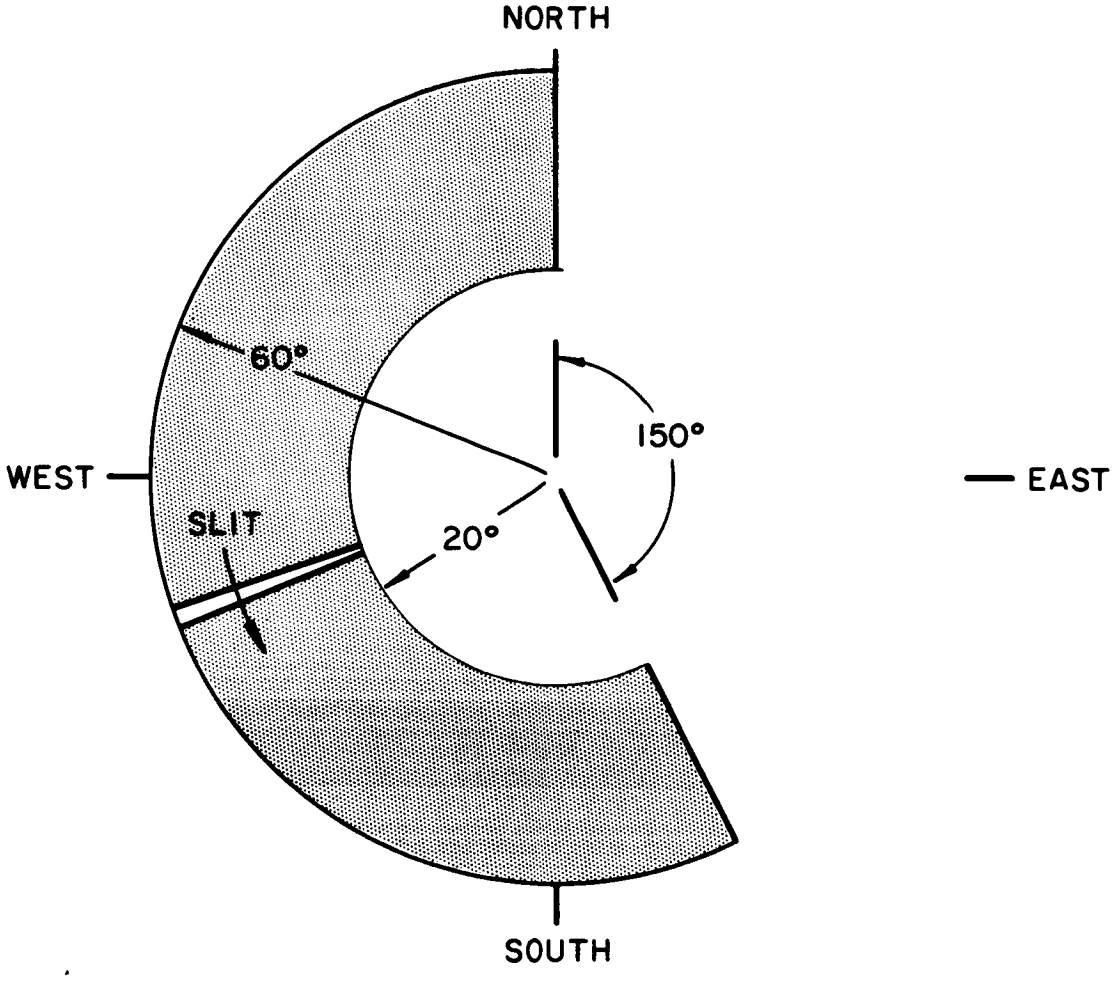

FIGURE 30: Assumed Effective Field of View for Near-Circular, Near-Polar, Spin Stabilized Orbit

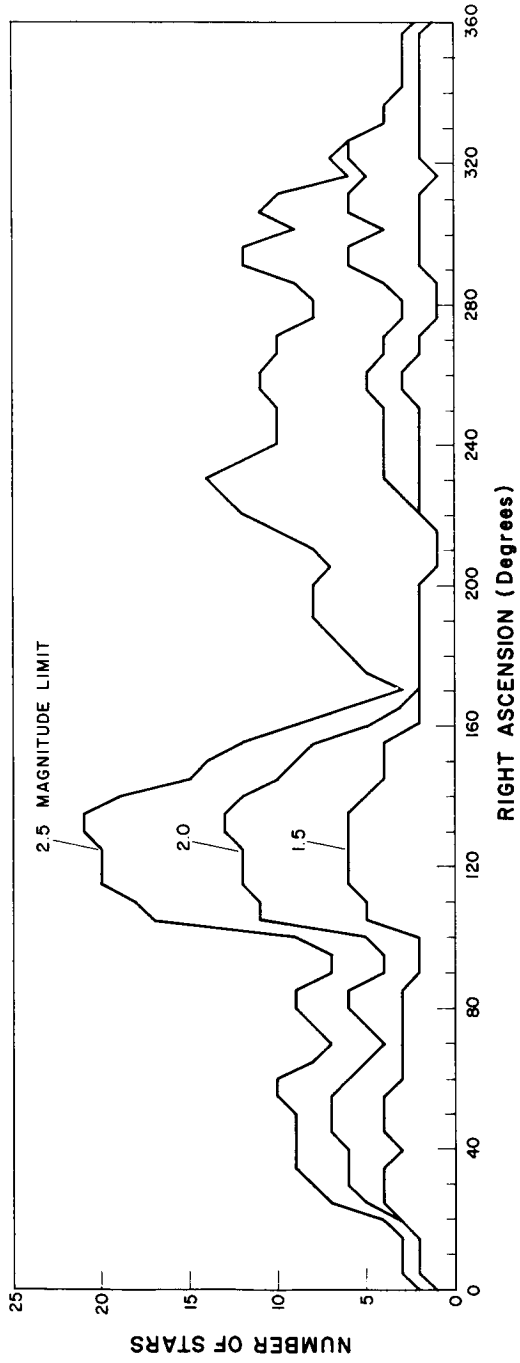

FIGURE 31: Number of Stars in Field of View as a Function of Orbital Normal's Right Ascension - Near-Circular, Near-Polar, Spin Stabilized Orbit

C. Near-Circular, Near-Polar, Magnetically Stabilized Satellite

Recall that for this mode, a single sensor was adequate only in the northern hemisphere. Figure 32, a, b, and c, gives the probability of finding n stars in the field of view brighter than photographic magnitude 4.0, 3.0, and 2.0 respectively as a function of n. Only the northern hemisphere was investigated. It can be expected that if the optical axis were directly opposite to that assumed, then the results for the southern hemisphere would be quite similar to those shown.

D. Near-Circular, Low Altitude Orbit ($i = 33^{o}$)

For this orbit, we graph the number of stars in the field of view as a function of the position of the spin axis along the ecliptic. Results are shown in Figure 33.

E. Longitude Synchronous - Gravity Gradient

Finally, we graph the number of stars in the field of view as a function of the true anomaly for the gravity gradient stabilized mode (Figure 34).

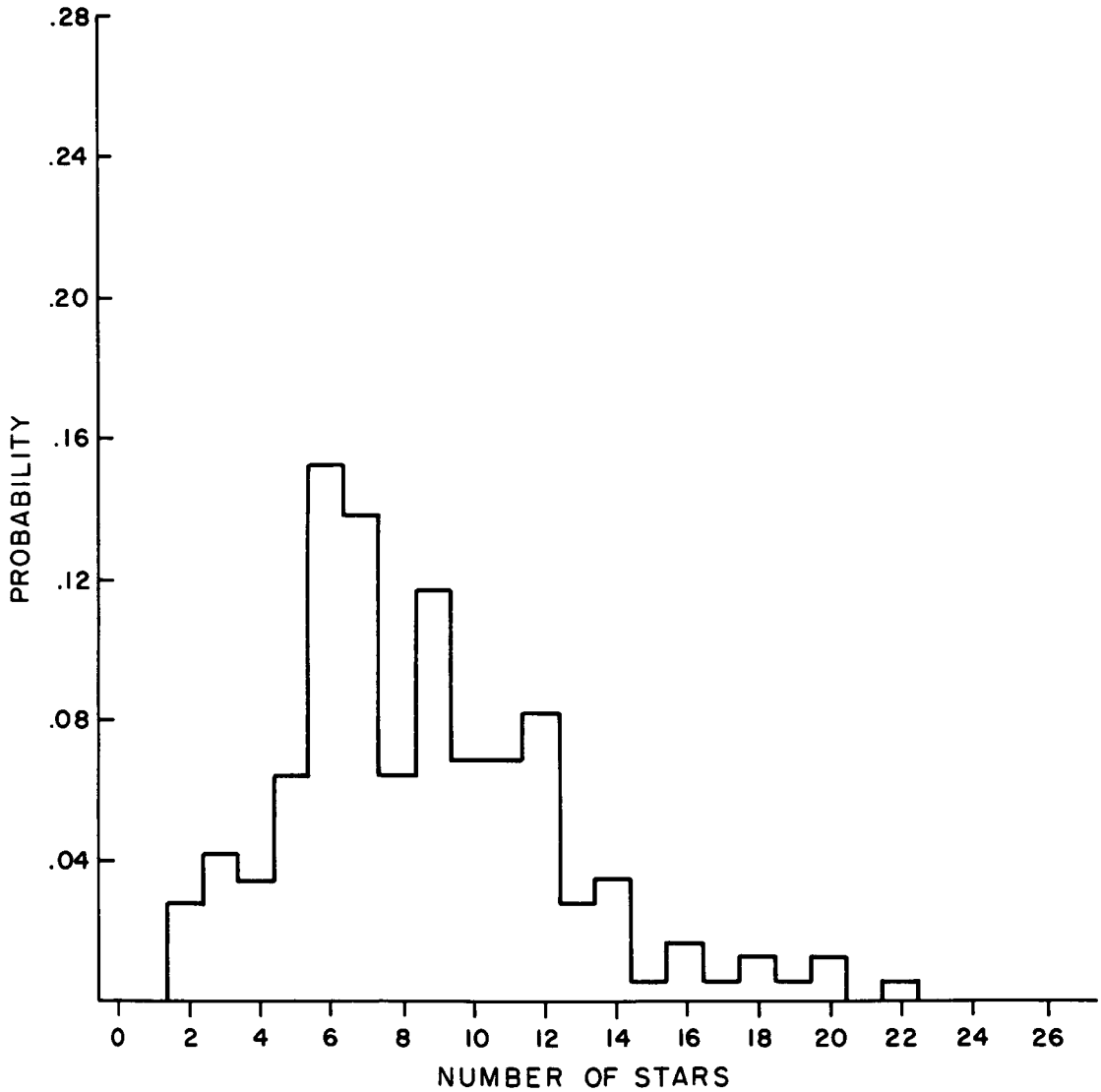

FIGURE 32A: Probability of Finding Various Numbers of Stars in Field of View of $M_p \leq 4$. Magnetically Stabilized Satellite

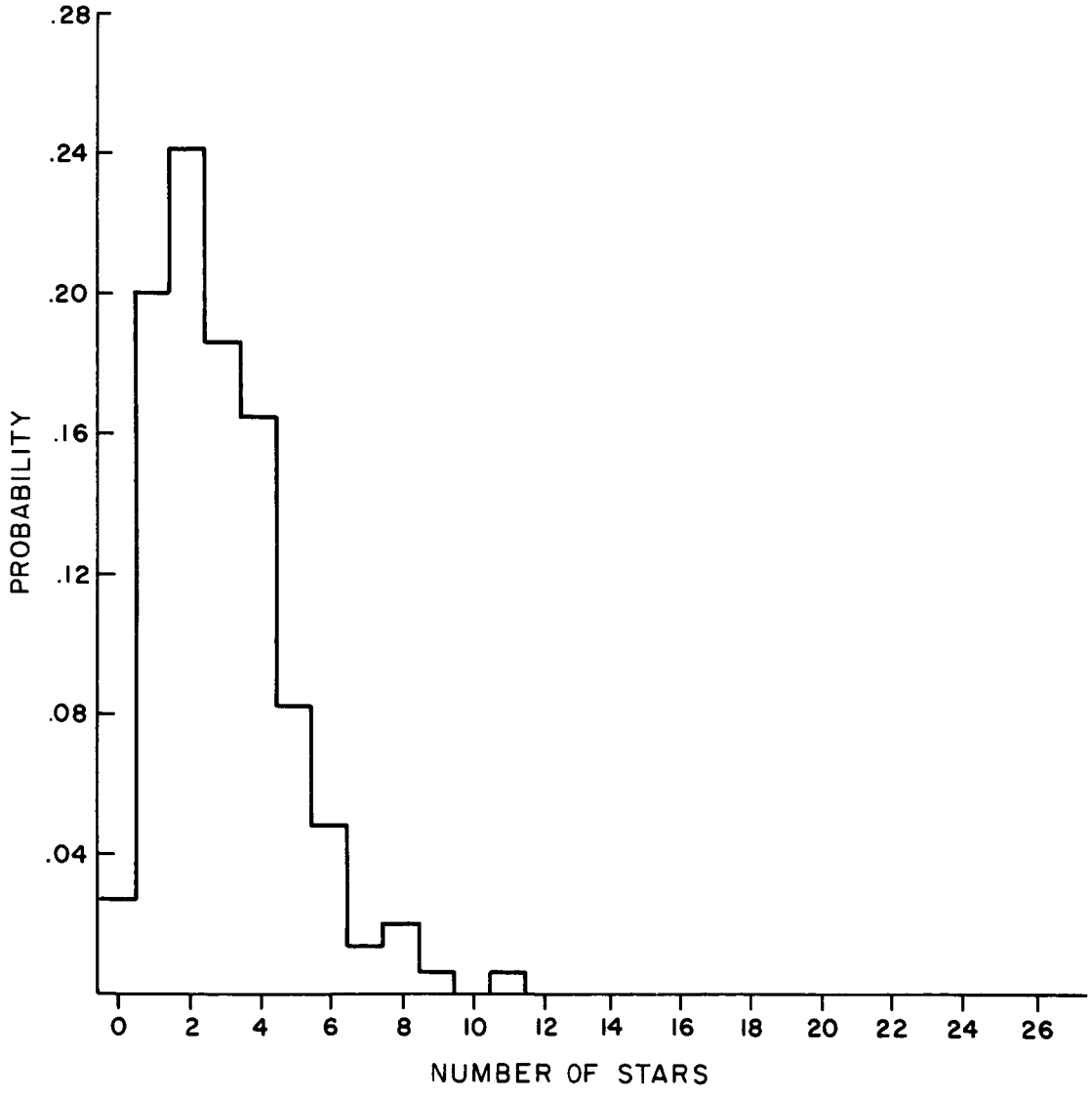

FIGURE 32B: Probability of Finding Various Numbers of Stars in Field of View of $M_p \leq 3$. Magnetically Stabilized Satellite

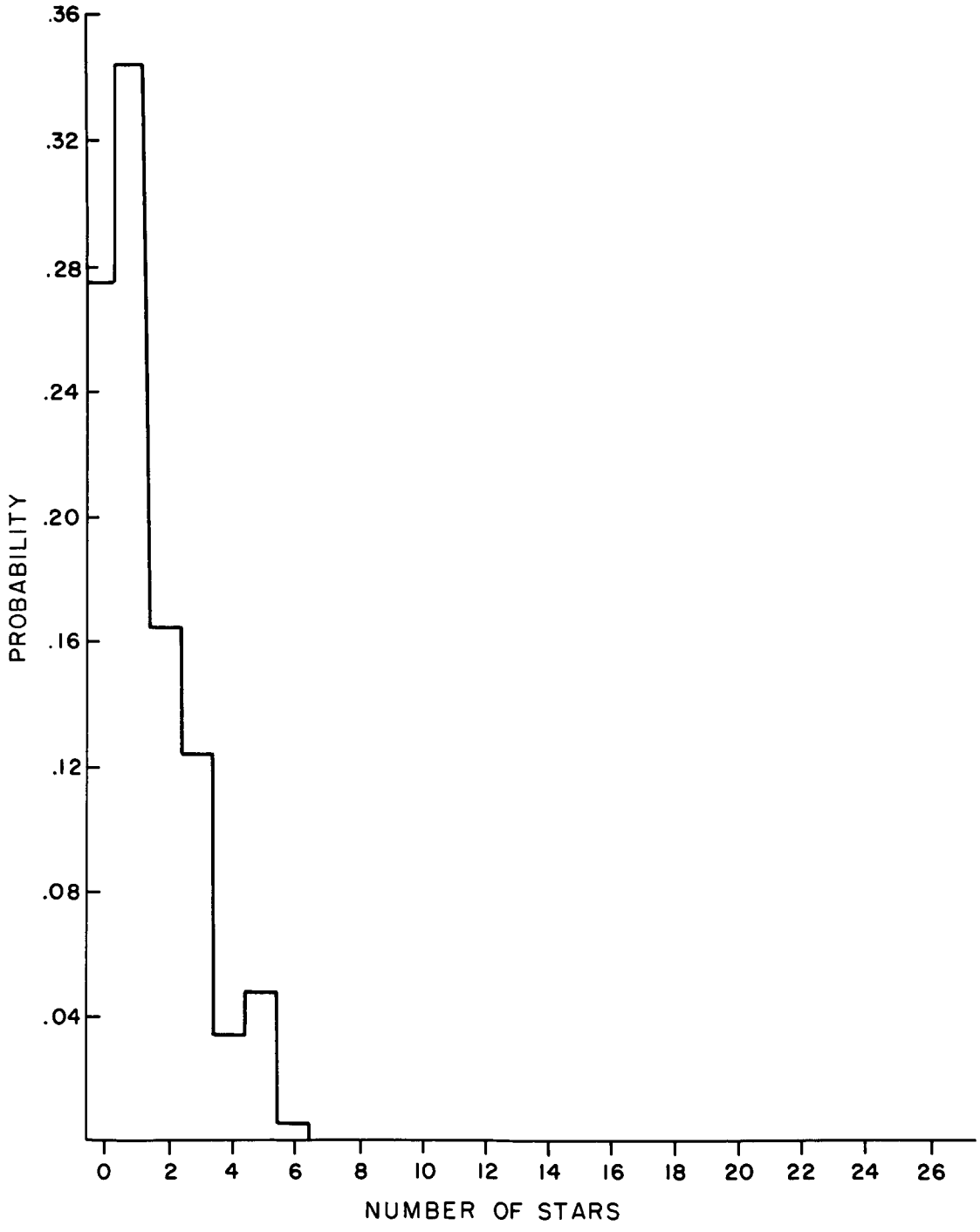

FIGURE 32C: Probability of Finding Various Numbers of Stars in Field of View of $M_p \leq 2$. Magnetically Stabilized Satellite

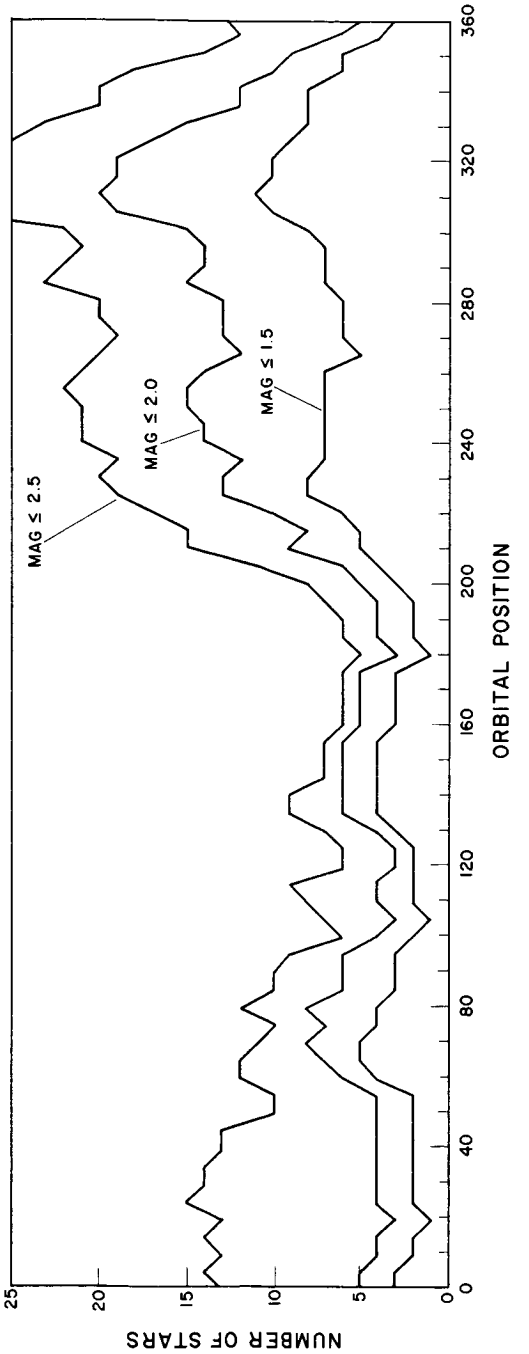

FIGURE 33: Number of Stars in Field of View as a Function of Direction of Spin Axis for Near-Circular, Low Altitude Orbit ($i = 33^{o}$)

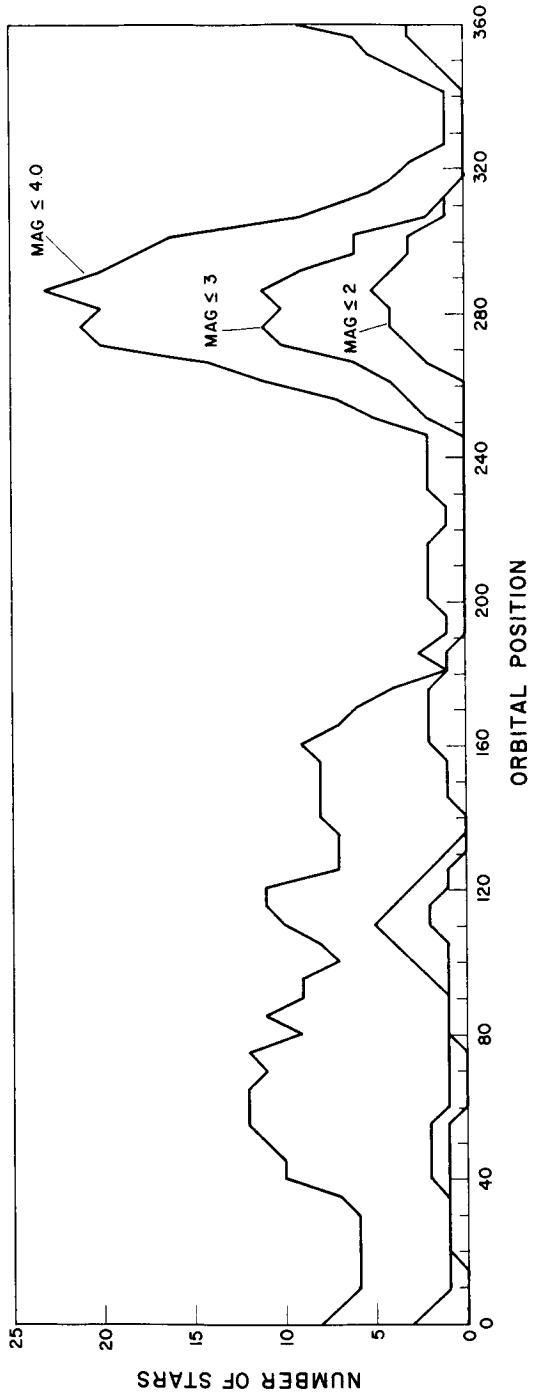

FIGURE 34: Number of Stars in Field of View as a Function of True Anomaly for Gravity Gradient Stabilized Satellite

IX. ERROR ANALYSIS

A. Transit Time Errors Due to Shot Noise

The random arrivals of radiant energy photons from the star and the random emission of electrons in the photomultiplier give rise to random amplitude fluctuations of the filtered star pulse. These random fluctuations cause variations in the leading edge and trailing edge threshold crossings of the star pulse which causes an uncertainty in the transit time obtained from averaging these threshold crossings. This section will describe a method for estimating the transit time uncertainty. The method basically consists of a computer simulation for which a model for threshold crossings of a noisy star pulse is established. The random noise is generated from computer generated random numbers for a large number of star pulses. The average of the threshold crossings is determined for each pulse and then the variance in this average is determined for all pulses.

Consider a noise free star pulse, $y(t)$, shown in Figure 35. Assume that the pulse came from a star of limiting detectable magnitude and that a threshold level, I_T, has been established as described in Section IV-F. The noise characteristics will be assumed stationary, although actually, the RMS noise increases as the average signal level increases. However, the actual RMS value of the noise at the threshold cannot be larger than the RMS value for an average noise level equal to I_T. Consequently, it is reasonable to expect that the resulting transit time variance will be slightly pessimistic.

The expression for the filter noise free output $y(t,\sigma)$ has been analytically determined in Section IV-E. Also, the peak value of $y(t)$ corresponds to $.597\ I_S$, and $\sigma = \frac{T_s}{2.56}$, so the nominal leading edge threshold crossing, t_a, and the nominal trailing edge threshold crossing, t_b, can also be analytically determined. In sufficiently small time intervals about both t_a and t_b, the slope of $y(t)$ may be assumed constant. It may be further assumed that the star signal slope having superimposed noise must also be constant in small

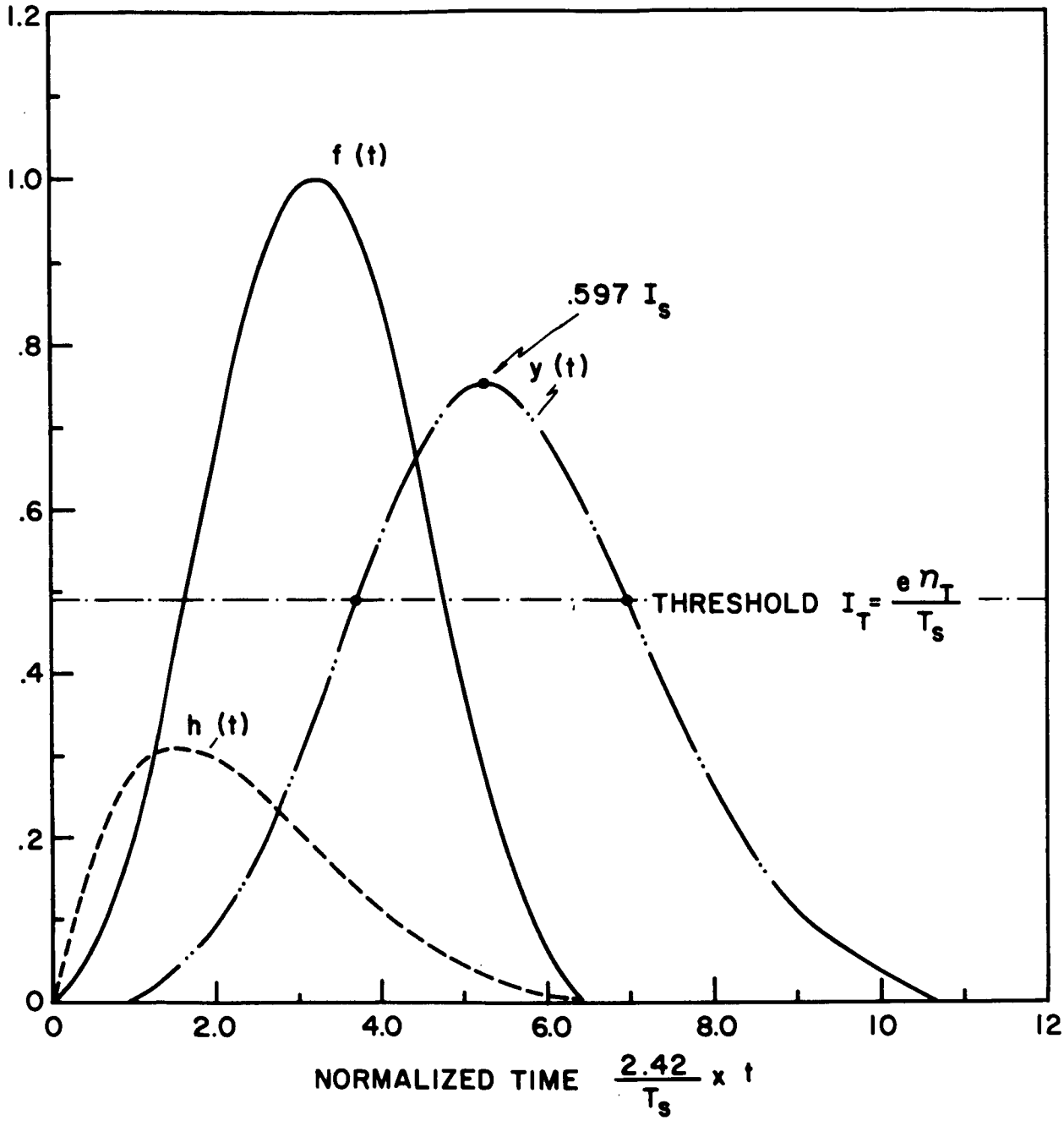

FIGURE 35: Threshold Crossing of Noise-Free Star Pulse

intervals about t_a and t_b, since the filter holding time will not permit rapidly changing output excursions. However, because of the effect of the filter holding time, the noise amplitudes at time $t_2 = t_a + \Delta t$ must be correlated to the noise amplitudes at time $t_1 = t_a - \Delta t$. Similarly, the noise amplitudes at times $t_3 = t_b - \Delta t$ and $t_4 = t_b + \Delta t$ are correlated to the amplitudes at t_1.

It has been shown that high density shot noise has a normal probability density function[14]. So at time t_1, the amplitude density function of the noise is given by

$$p(I_1) = \frac{1}{\sqrt{2\pi}\,\sigma_1} \exp\left[-\frac{1}{2}\left(\frac{I_1}{\sigma_1}\right)^2\right] \tag{59}$$

where σ_1 = RMS value of I_1.

At time t_2, the amplitude density function is given by[17]

$$p(I_2|I_1) = \frac{1}{\left[2\pi\,\sigma_1^2\,(1-\rho_{12}^2)\right]^{\frac{1}{2}}} \exp\left[-\frac{(I_2 - \rho_{12}I_1)^2}{2\,\sigma_1^2\,(1-\rho_{12}^2)}\right] \tag{60}$$

where ρ_{12} is the correlation coefficient between the random variable I_2 at t_2 and I_1 at t_1.

Similarly, at time t_3 the amplitude density function is

$$p(I_3|I_1) = \frac{1}{\left[2\pi\,\sigma_1^2\,(1-\rho_{13}^2)\right]^{\frac{1}{2}}} \exp\left[-\frac{(I_3 - \rho_{13}\,I_1)^2}{2\,\sigma_1^2\,(1-\rho_{13}^2)}\right] \tag{61}$$

and at time t_4 the density function is

$$p(I_4|I_3) = \frac{1}{\left[2\pi\ \sigma_1^2(1 - \rho_{34}^2)\right]^{\frac{1}{2}}} \exp\left[-\frac{(I_4 - \rho_{34}I_3)^2}{2\ \sigma_1^2\ (1 - \rho_{34}^2)}\right] \tag{62}$$

Figure 36 shows the time interval close to the leading edge threshold crossing with the noise amplitudes I_1 and I_2 superimposed on y(t) at times t_1 and t_2, respectively. With the noise superimposed, the threshold crossing is shifted from the noise free crossing time, t_a to time t_{a1}. Since the slope of the noisy signal is assumed constant between t_2 and t_1, the shifted threshold crossing may be easily determined analytically for specific values of I_1 and I_2.

Specific values of I_1 and I_2 are determined from uniformly distributed random numbers generated by the computer random number generator. The random numbers, R_i, can take on any values between 0 and 1.0. Then the cumulative normal function is evaluated so that

$$.5 + \frac{1}{\sqrt{2\pi}} \int_0^{x_1} e^{-y^2/2} dy = R_1 \tag{63}$$

from which $I_1 = x_1\sigma_1$. Similarly, I_2 is obtained by evaluating

$$.5 + \frac{1}{\sqrt{2\pi}} \int_0^{x_2} e^{-y^2/2}\ dy = R_2 \tag{64}$$

$$\text{from which } I_2 = x_2\sigma_1(1 - \rho_{12}^2)^{\frac{1}{2}} + \rho_{12}\ I_1 \tag{65}$$

The shifted trailing edge threshold crossing may be similarly determined. Random numbers R_3 and R_4 are generated and the cumulative normal functions

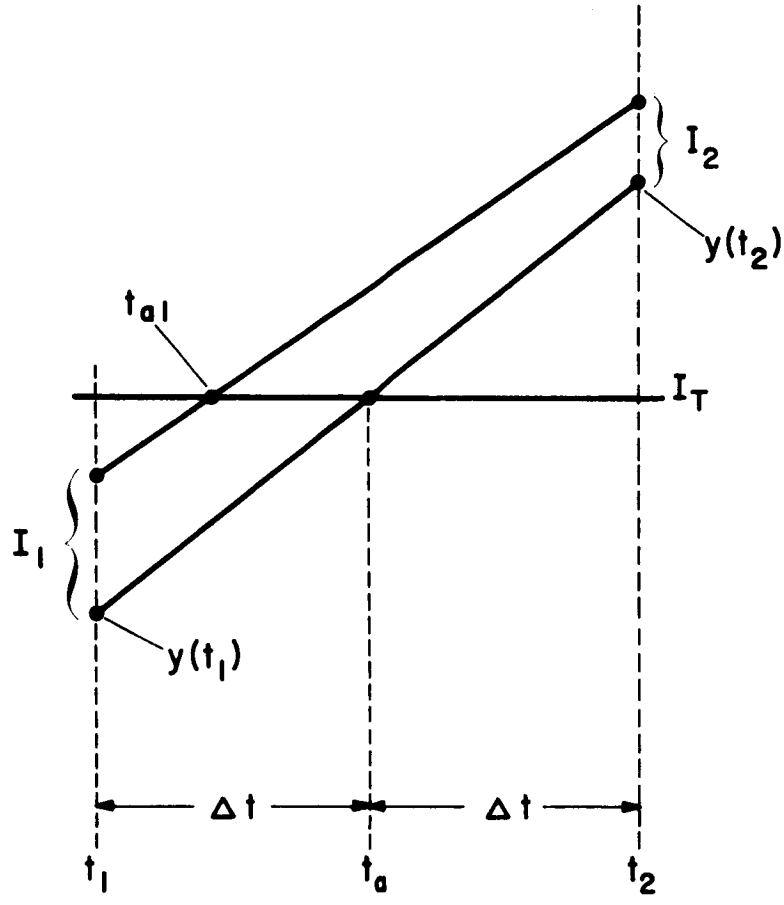

FIGURE 36: Leading Edge Threshold Crossing

$$.5 + \frac{1}{\sqrt{2\pi}} \int_0^{x_3} e^{-y^2/2}\, dy = R_3 \tag{66}$$

$$.5 + \frac{1}{\sqrt{2\pi}} \int_0^{x_4} e^{-y^2/2}\, dy = R_4 \tag{67}$$

are evaluated. The noise amplitudes are determined from

$$I_3 = x_3\, \sigma_1 (1 - \rho_{13}^2)^{\frac{1}{2}} + \rho_{13} I_1 \tag{68}$$

$$I_4 = x_4\, \sigma_1 (1 - \rho_{34}^2)^{\frac{1}{2}} + \rho_{34} I_3 \tag{69}$$

After superimposing the noise amplitudes upon the noise-free signal, y(t), at times t_3 and t_4, respectively, the shifted trailing edge threshold crossing, t_{b1}, can easily be determined analytically.

The transit time for the noisy star pulse is computed as

$$t_{s1} = \frac{(t_{a1} + t_{b1})}{2} \quad . \tag{70}$$

After this a new set of random numbers, R_1 through R_4, and their corresponding noise amplitudes is determined from which t_{s2} is determined. After repeating this procedure a large number of times to obtain t_{s3}, t_{s4}, etc., the variance of the transit times, $\sigma(t_s)$, is computed.

In order to compute the random noise amplitudes, I_j, it is necessary to determine the correlation coefficients ρ_{1j} for j = 2, 3. The correlation coefficient, ρ_{12}, is defined as[18]

$$\rho_{12} = \frac{E[I(t_1),\ I(t_2)]}{(\mathrm{Var}[I(t)])} \tag{71}$$

where

$I(t_1)$ = the value of the shot noise current at time t_1
$I(t_2)$ = the value of the shot noise current at time t_2
σ_1^2 = Var[I(t)] = amplitude variance of the noise current.

It has been shown that[18]

$$E[I(t_1),\ I(t_2)] = \frac{I_T}{e} \int_0^{t=\infty} h(t) \cdot h(t+\tau)\, dt \tag{72}$$

where h(t) = impulse response of the filter transfer function

$$\tau = t_2 - t_1$$

Also,[18]

$$\mathrm{Var}[I(t)] = E[I^2(t)] = \frac{I_T}{e} \int_0^{\infty} h^2(t)\, dt \tag{73}$$

The impulse response for a two pole filter is given by

$$h(t) = K\, e^{-at} \sin bt \tag{74}$$

So

$$E[I(t_1),\ I(t_2)] = K^2\, e^{-a\tau} \cos b\tau \int_0^{\infty} e^{-2at} \sin^2 bt\, dt \tag{75}$$

$$+ \frac{K^2}{2}\, e^{-a\tau} \sin b\tau \int_0^{\infty} e^{-2at} \sin 2bt\, dt$$

$$= K^2 e^{-a\tau} \left\{ \frac{\cos b\tau}{a\left[\left(\frac{2a}{b}\right)^2 + 4\right]} + \frac{\sin b\tau}{4b\left[\left(\frac{a}{b}\right)^2 + 1\right]} \right\}$$

Also,

$$\sigma_1^2 = \mathrm{Var}[I(t)] = K^2 \int_0^\infty e^{-2at} \sin^2 bt \, dt \tag{76}$$

$$= \frac{K^2}{\left[\left(\frac{2a}{b}\right)^2 + 4\right]}$$

So

$$\rho_{1j} = e^{-a\tau} \left\{ \cos b\tau + \left(\frac{a}{b}\right) \sin b\tau \right\} \tag{77}$$

From Section IV-E, the two pole linear phase versus frequency filter has

$$a = .375\ \omega_c$$
$$b = .3307\ \omega_c$$

For

$$\rho_{12},\ \tau = t_2 - t_1 = 2\ \Delta t$$
$$\rho_{13},\ \tau = t_b - t_a$$
$$\rho_{34},\ \tau = 2\ \Delta t$$

Consequently, $\rho_{34} = \rho_{12}$.

Note that for $\tau = 0$, $\rho = 1$ as expected.

A computer simulation was performed for the optimum parameters determined for the elliptical equatorial orbit. It should be recalled that the optimum parameters were determined as

$FOV = 40^{o}$ = field of view

$M_p = 2.1$ = limiting detectable photographic star magnitude

$D = .26$ inch = optical aperture.

Corresponding to these parameters, it has been determined that

$n_s = 163$

$n_T = 342$

$n_{BD} = 278$

$T_s = 1.25 \times 10^{-2}$ seconds

where n_s = the average effective number of equally weighted photocathode emissions due to star signal current I_s occurring during a transit interval T_s;

n_T = the average number of electron emissions from the cathode during time interval T_s which occur at the threshold current level;

n_{BD} = the average effective number of equally weighted photocathode emissions due to background plus dark current which occur during time interval T_s;

T_s = time required for the center point of the star image to cross the slit.

The results of the computer simulation are summarized below, in Table XIII, for three star magnitudes. For each case the background level was fixed at $n_{BD} = 278$, the threshold level was fixed at $n_T = 342$, and $\Delta t = \frac{T_s}{20}$. The ratio of peak signal to RMS noise was obtained from Equation (29)

$$\frac{S_{peak}}{N_{RMS}} = \frac{.606\, n_s}{(.8n_s + n_{BD})^{\frac{1}{2}}} \quad . \tag{78}$$

TABLE XIII

SLIT WIDTH INTERPOLATION FACTOR VERSUS SIGNAL-TO-NOISE RATIO

n_s	M_p	$\frac{T_s}{\sigma(t_s)}$	$\frac{S_{peak}}{N_{RMS}}$
163	2.1	6.7	4.9
410	1.1	10.7	10.1
1025	.1	16.7	18.8

The ratio $\frac{T_s}{\sigma(t_s)}$ compares the time required for a point source to cross the slit to the uncertainty in the transit time. This ratio may be further interpreted as a comparison between the rotational slit width and the azimuth angular uncertainty in locating the star transit. This is equivalent to saying the star transit time uncertainty depends on how well the detection electronics can interpolate the rotational slit width. Consequently, the ratio $\frac{T_s}{\sigma(t_s)}$ is referred to as the slit width interpolation factor.

Note that for a fixed threshold, the interpolation factor increased as the ratio $\frac{S_{peak}}{N_{RMS}}$ increased.

If n_s is fixed at 1025, corresponding to a star photographic magnitude of .1, and the detection threshold is raised above $n_T = 342$, it is interesting to note the change in the interpolation factor as the threshold is increased. Here again Δt was set at $\frac{T_s}{20}$ and $n_{BD} = 278$. The results of increasing the threshold are tabulated below.

By expressing the threshold level as a percentage of the peak, it can be noticed that the interpolation factor is largest when the threshold is set at approximately 50% of the star pulse peak.

TABLE XIV

INTERPOLATION FACTOR VERSUS THRESHOLD LEVEL

$n_T - n_{BD}$	$\frac{n_T}{.597\ n_s}$	$\frac{T_s}{\sigma(t_s)}$
100	16.3%	20.8
333	54.5%	29.8
566	92.5%	25.4

If the standardized optical aperture chosen for the elliptical equatorial orbit is .8 inch and the detection threshold is set to detect stars brighter than 2.1 magnitude, then the interpolation factor should be greater than for the .26 inch optical aperture. The interpolation factor is tabulated below for the .8 inch optical aperture and star magnitudes of 2.1, 1.1, and 0.1.

TABLE XV

INTERPOLATION FACTOR FOR LARGE SIGNAL-TO-NOISE RATIOS

n_s	M_p	$\frac{S_{peak}}{N_{RMS}}$	$\frac{T_s}{\sigma\ (t_s)}$
1512	2.1	14.9	19.6
3800	1.1	30.7	39.1
9520	.1	57.2	59.5

It can be seen that standardizing the optical aperture tends to increase the slit width interpolation factor for those scan periods where the standardized aperture is significantly larger than the optimum required aperture. For a fixed optical aperture, a decreased scan period will cause a decrease in the interpolation factor since the peak signal-to-RMS noise

ratio is decreased. Consequently, for these scan periods where the standardized optical aperture exceeds the required optical aperture, the system accuracy should be better than for the scan period where the standardized optical aperture equals the optimum aperture.

It is reasonable to expect the interpolation factors for the other orbital configurations to behave in a similar manner as for the elliptical equatorial orbit, hence, the interpolation factors for the other orbital configurations are not presented.

B. Attitude Error Analysis

To gain some insight as to the error magnitudes which might be expected, a somewhat simplified error analysis was performed. For this error analysis, we assumed the slit is spinning uniformly about a fixed axis. We then investigated the errors in right ascension and declination of the spin axis, and the error in the azimuth of the zero reference for each of the five orbital classes.

The input error was the error in measurement of the transit time for the spin stabilized satellites, and a rotation error for the field stabilized satellites. An error in transit time can be easily converted to an error in measurement of the angle from the zero reference to the slit at the instant of a star transit. Thus,

$$\sigma(\theta) = \frac{\sigma(t_s)}{T}$$

where

$\sigma(\theta)$ = standard deviation of rotation error,
$\sigma(t_s)$ = standard deviation of transit time error,
T = scan period.

If we assume the interpolation factor is greater or equal to six, then for $\widehat{SW}$ = 18 arc-minutes, we may assume $\sigma(\theta) \leqq 3$ minutes of arc. $\sigma(\theta) = 3$ arc-minutes was then used as the basic input error. The output error was then computed for various pointing directions for each of the five modes. A description of the geometry for each mode was given in Section V.

The output errors were then computed as a function of parameters which define the direction of the satellite's longitudinal axis. Results are shown in Figures 37 to 42. We assume no loss of field of view except for the near-circular, near-polar, spin stabilized orbital class, in which case we assume 150° of azimuthal directions are lost due to scanning through the earth. Also,

only star transit data for a single scan is used to determine the attitude error. In these figures the total attitude error is defined as

$$\sum = \sqrt{\sigma^2(\alpha) + \sigma^2(\delta) + \sigma^2(\beta)}$$

where

$\sigma(\alpha)$ = standard deviation of error in the right ascension of the spin axis,

$\sigma(\delta)$ = standard deviation of the error in the declination of the spin axis,

$\sigma(\beta)$ = standard deviation of the azimuth error of the reference direction.

In comparing these figures, we note that the least favorable case is that of the near-circular, near-polar, spin stabilized orbit. This fact occurs because for this case, 150° of the azimuthal directions are lost from the effective field of view as shown in Figure 30.

Figure 37 yields the total error as a function of the sun's right ascension for the elliptical equatorial orbit. In deriving this curve, we assume the angle between the sun and the spin axis is 45° (its average value) and has a right ascension which lags the sun. In Figure 38 we plot the probability that the total error is less than or equal to a given value for the elliptical equatorial orbit.

For the other orbital classes we do not graph the total error as a function of position, but plot only the probability data since the latter is of more interest.

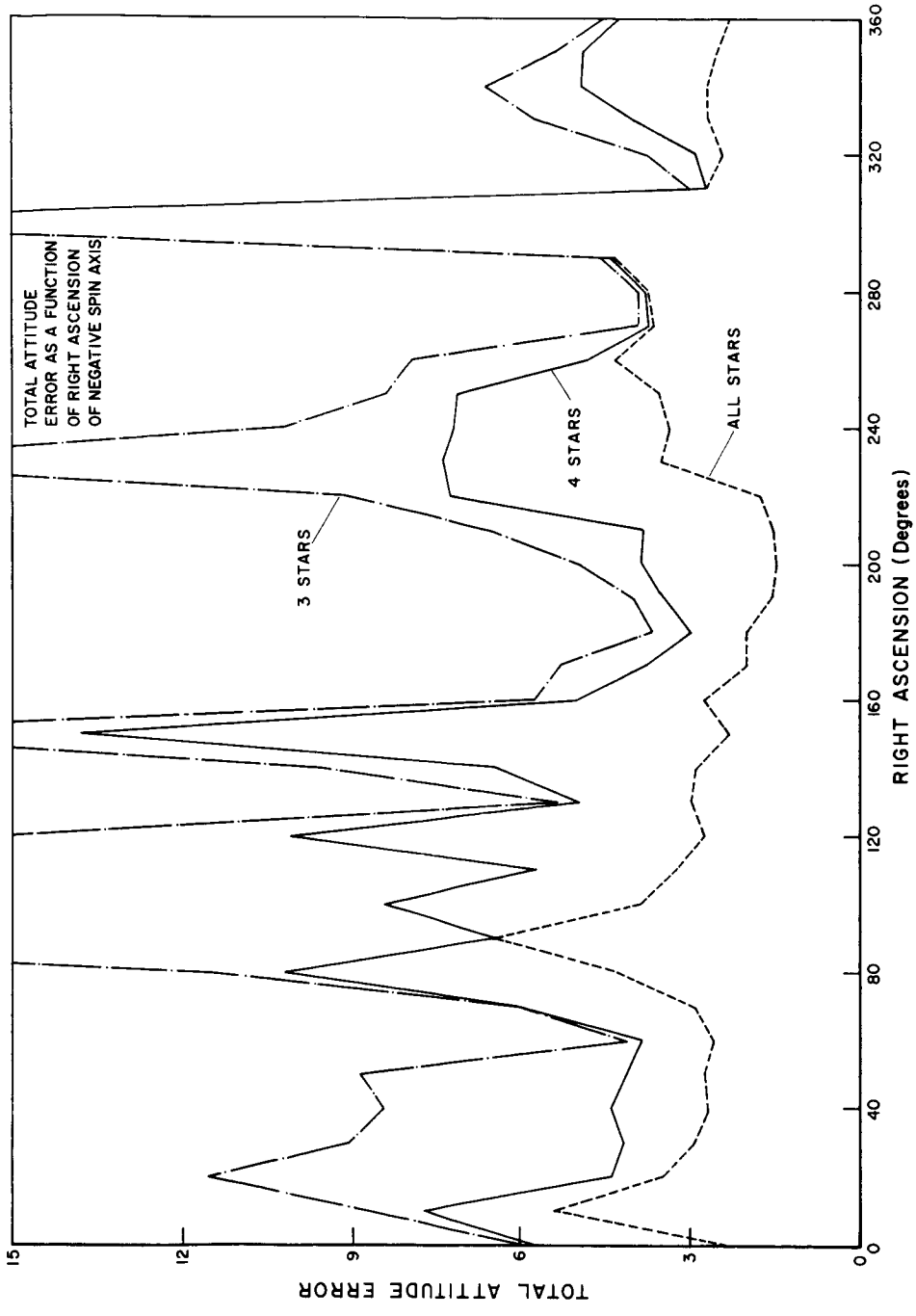

FIGURE 37: Total Attitude Error, $\sum\angle$, for the Elliptic Equatorial Orbit

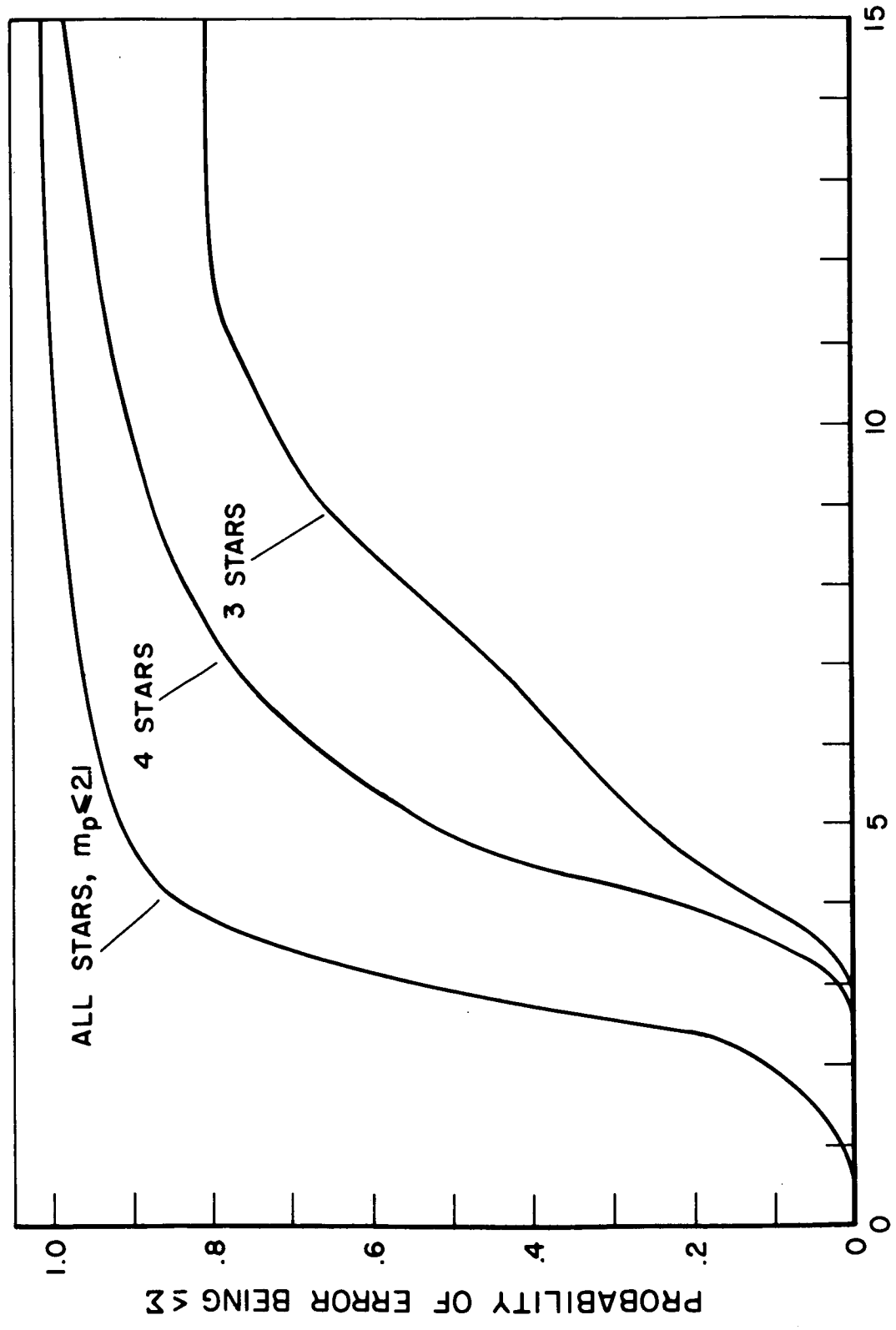

FIGURE 38: Probability of Total Attitude Error Being ≤ a Given Value for Elliptic Equatorial Orbit

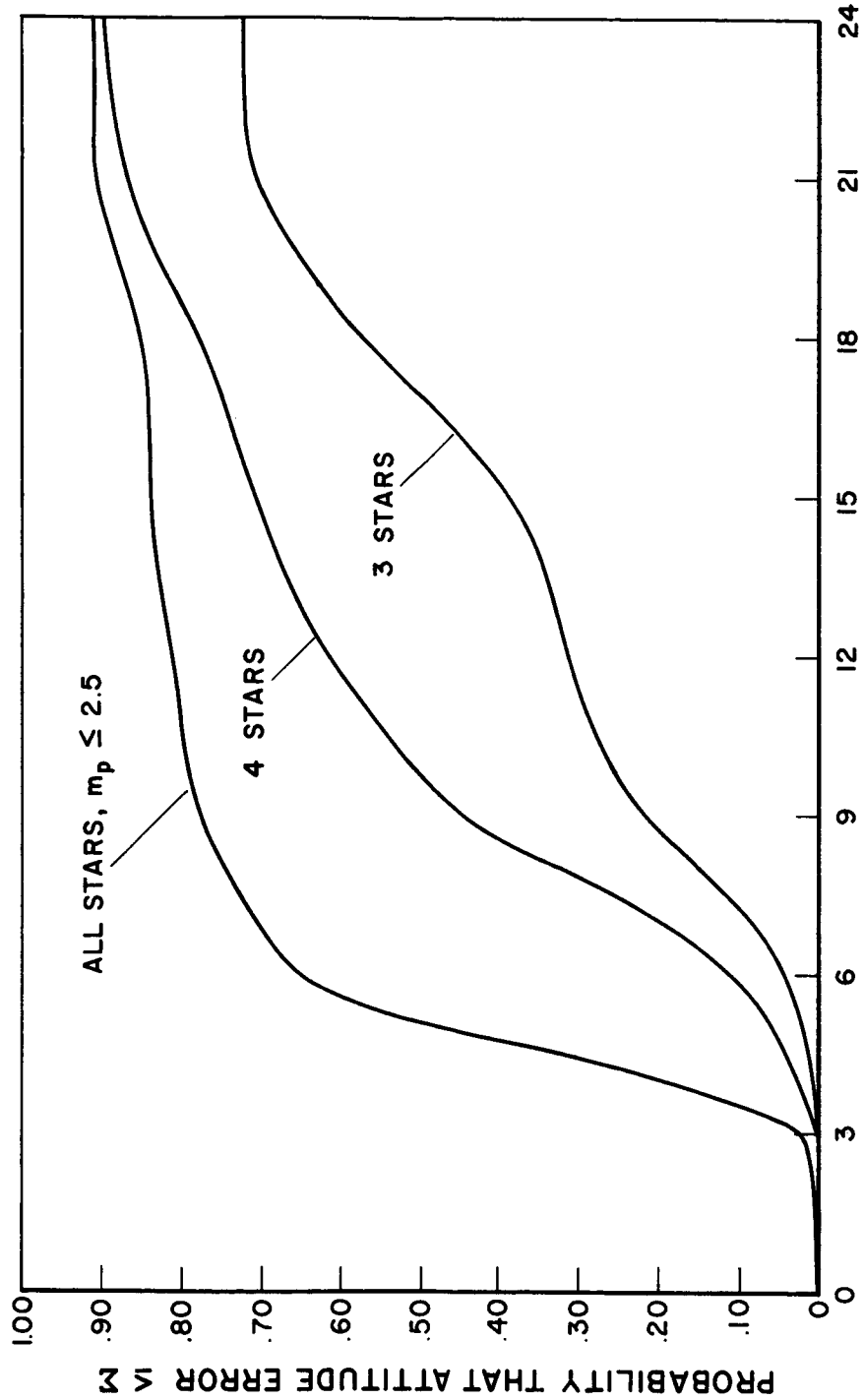

FIGURE 39: Attitude Error for the Near-Circular, Polar, Spin Stabilized Satellite

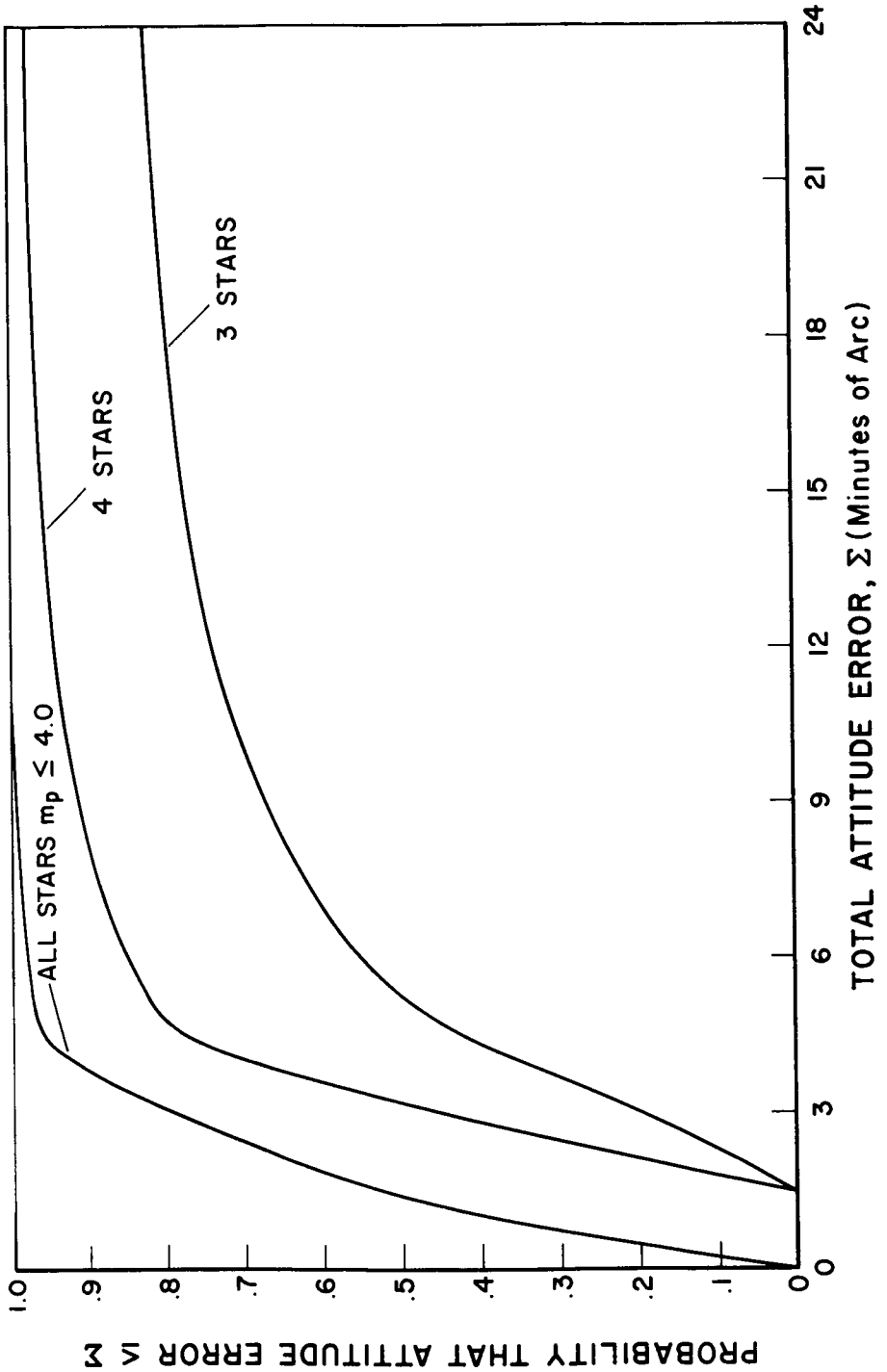

FIGURE 40: Attitude Error for the Magnetically Stabilized Satellite

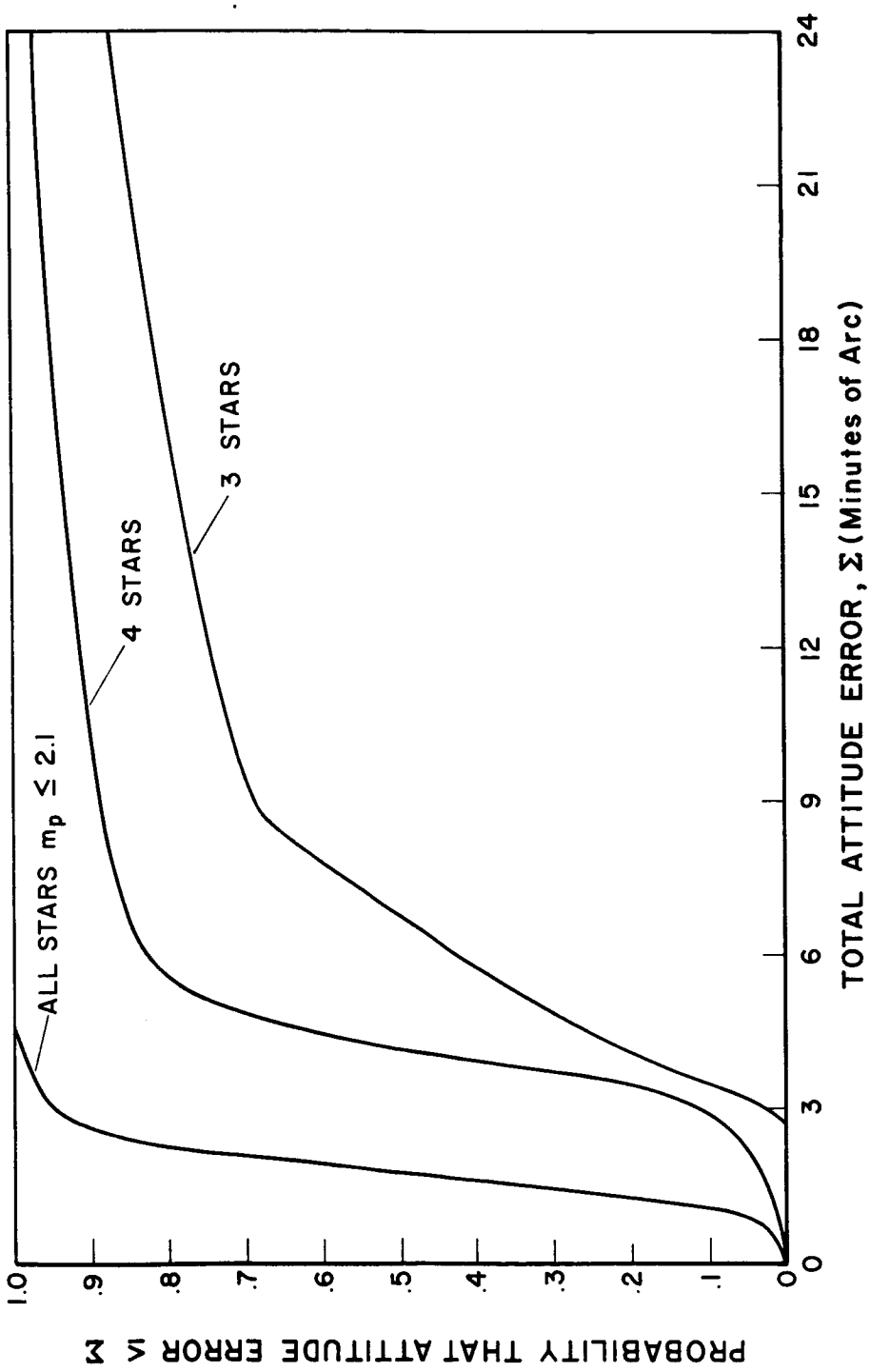

FIGURE 41: Attitude Error for the Near-Equatorial, Low Altitude Orbit

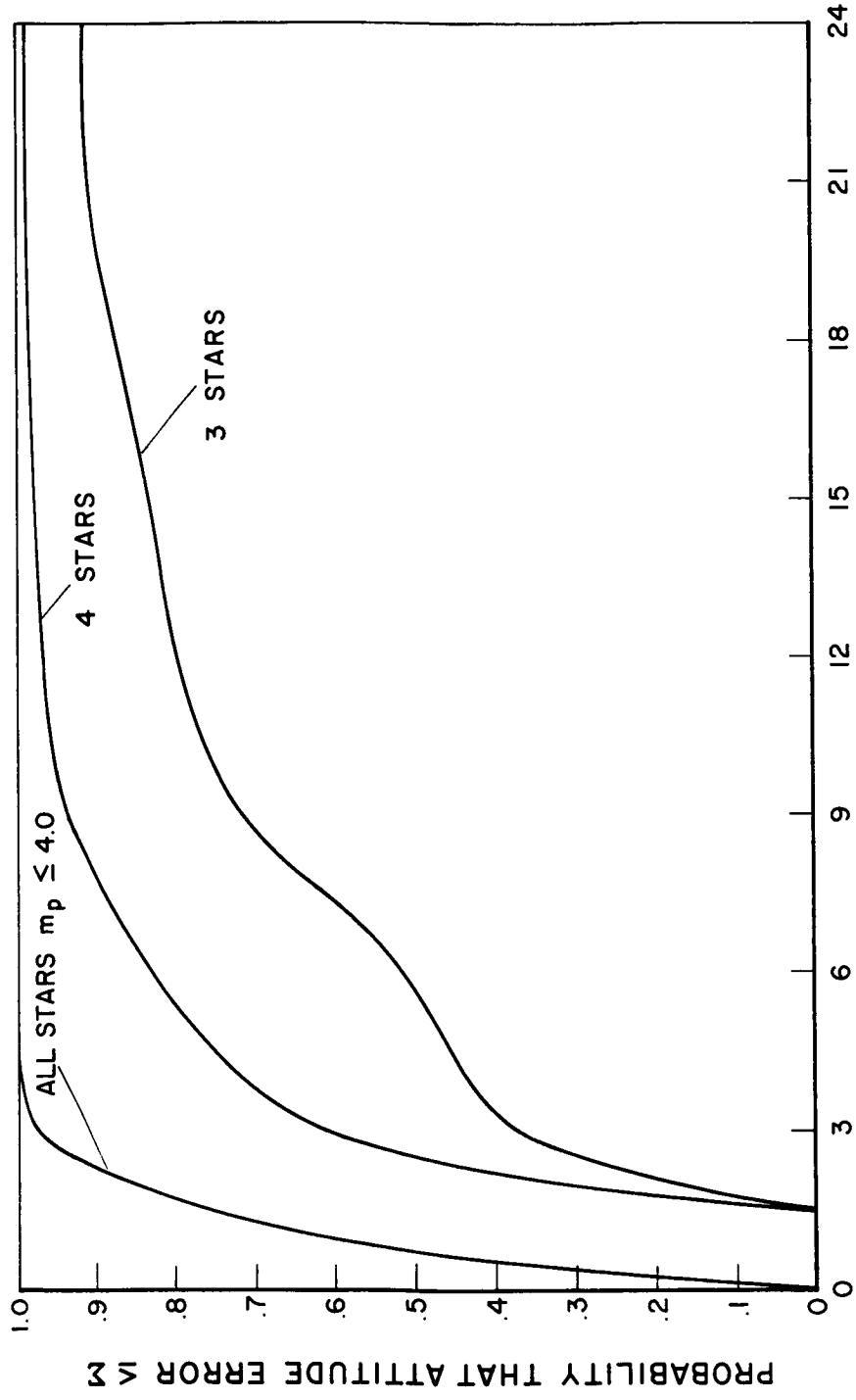

FIGURE 42: Attitude Error for the Gravity Gradient Stabilized Satellite

X. EVALUATION OF OPERATIONAL CONSTRAINTS

In this section, we first evaluate the loss of field of view and operation time because of interference caused by sun radiation or earth reflected sun radiation. We need not concern ourselves to a great extent over interference caused by moon or planet reflected sun radiation. Indeed, the planets may be utilized by the instrument just as the stars are utilized. The full or partial moon is too bright a target to be utilized. Instead, we will reject the moon by use of an overload protection circuit as explained in Section XI. Such a rejection will cause a loss in the scanned region, but the loss will be less than a few degrees since the full moon subtends an angle no larger than $\frac{1}{2}$ degree.

The second part of this section will be concerned with the problems caused by high energy particles.

A. Sun and Earth Interference

Since the sun is a target roughly 10^{12} times brighter than the stars we are attempting to detect and the sunlit earth is an extended target 10^{11} times brighter, considerable difficulties are presented by these light sources. In this section we will assume that the system operation becomes marginal if

(1) the angle between the sun and optical axis is less than β_S or the angle between any point on the viewable sunlit earth and the optical axis is less than β_E;

(2) the earth itself (sunlit or dark) obscures the effective field of view.

We will assume $\beta_S = 70^\circ$, and $\beta_E = 70^\circ$ or 50°. Results for both values of β_E will be generally presented. These values of β_S and β_E are felt to be realistic and yield a small shield as shown in Section IV-G. Dimensions of the required shields are given in Section VI.

Let us now evaluate the implications of our assumptions for the various classes of orbits.

1. Elliptical Equatorial Orbit

The geometry of the elliptical equatorial orbit has been discussed in Section V and is pictured in Figure 22. Recall that the angle between the sun and the spin axis is confined in an interval from 25° to 70°. A cant angle of 40° from the negative spin axis was chosen. Hence, with $\beta_S = 70^\circ$ direct sun radiation causes no restrictions.

Let us now consider the restrictions imposed by the sunlit earth. In Figure 43 we picture the most favorable geometry, i.e., the geometry which allows the largest portion of the orbital period over which stars may be viewed. In this figure we picture the half orbit subdivided into three areas. Over the arc DC, no portion of the field of view will be usable, for the

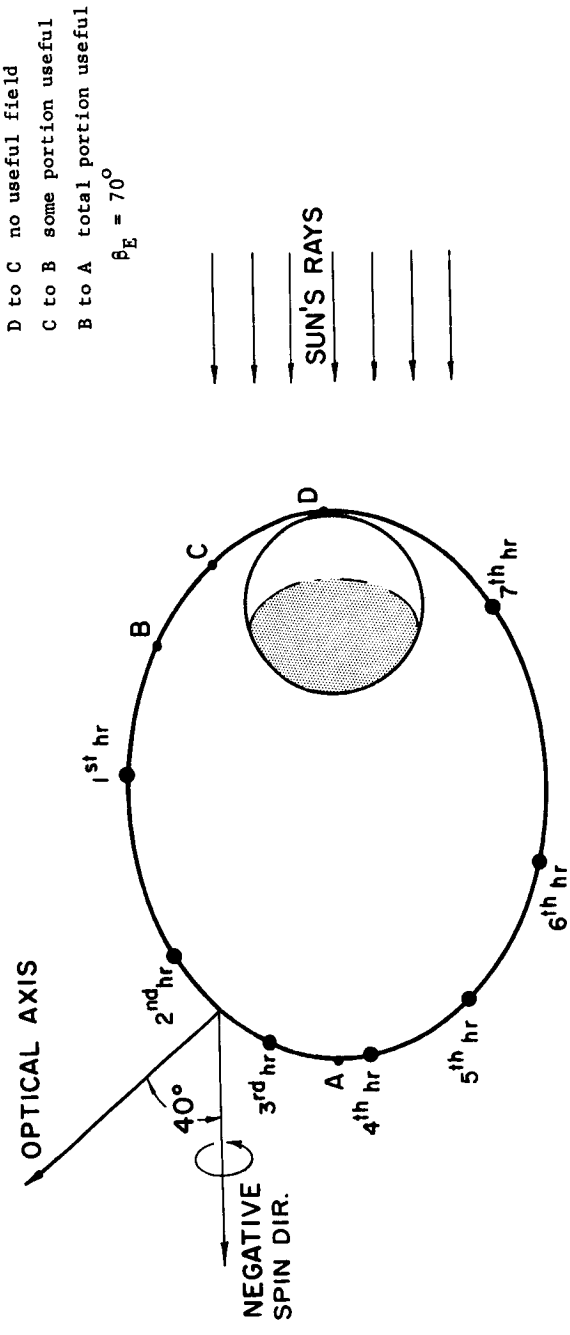

FIGURE 43: Best Case Viewability

optical axis will always be closer than $70^{\circ} = \beta_E$ to the sunlit earth during the entire portion of each scan period. Over the arc CB part of each scan period will be usable, but not the entire scan period. Finally, over the arc BA each complete scan will be usable; for over this arc, the sunlit earth will always be more than 70° from the optical axis.

In Figure 44, we picture the least favorable geometry. More quantitative information concerning viewability is given in Table XVI.

In summary, the sun will cause no difficulties to the viewability problem for the class of elliptic equatorial orbits. The sun will never become closer than 70° to the optical axis, and a small shield should adequately shield for such angles. However, the sunlit earth will cause some loss of viewability which ranges from 10% to 55% of the orbital period.

2. Near-Polar, Near-Circular, Spin Stabilized Orbit

Let $(\hat{i}_1, \hat{j}_1, \hat{k}_1)$ be a triad such that $\hat{j}_1$ is along the orbital normal, and $\hat{i}_1$ is in the equatorial plane. Also let,

α = azimuth of the sun with respect to the $(\hat{i}_1, \hat{j}_1)$ plane
ϵ = angle between the sun and $\hat{k}_1$ axis (Figure 45).

If $\epsilon = 90^{\circ}$, then the sun is in a plane perpendicular to the orbital plane. Since the orbital inclination is such that $80^{\circ} \leq i \leq 100^{\circ}$ we have $56.5^{\circ} \leq \epsilon \leq 133.5^{\circ}$. However, a range on α cannot be specified.

Let us assume the orbit is circular. First we impose the restrictions implied by the sunlit earth.

Let $\hat{k}_3$ be in the direction of the sun, and $\hat{j}_3$ be perpendicular to $\hat{k}_3$ but in the $(\hat{i}_1, \hat{j}_1)$ plane, $\hat{i}_3$ completes the right-handed coordinate system. Hence,

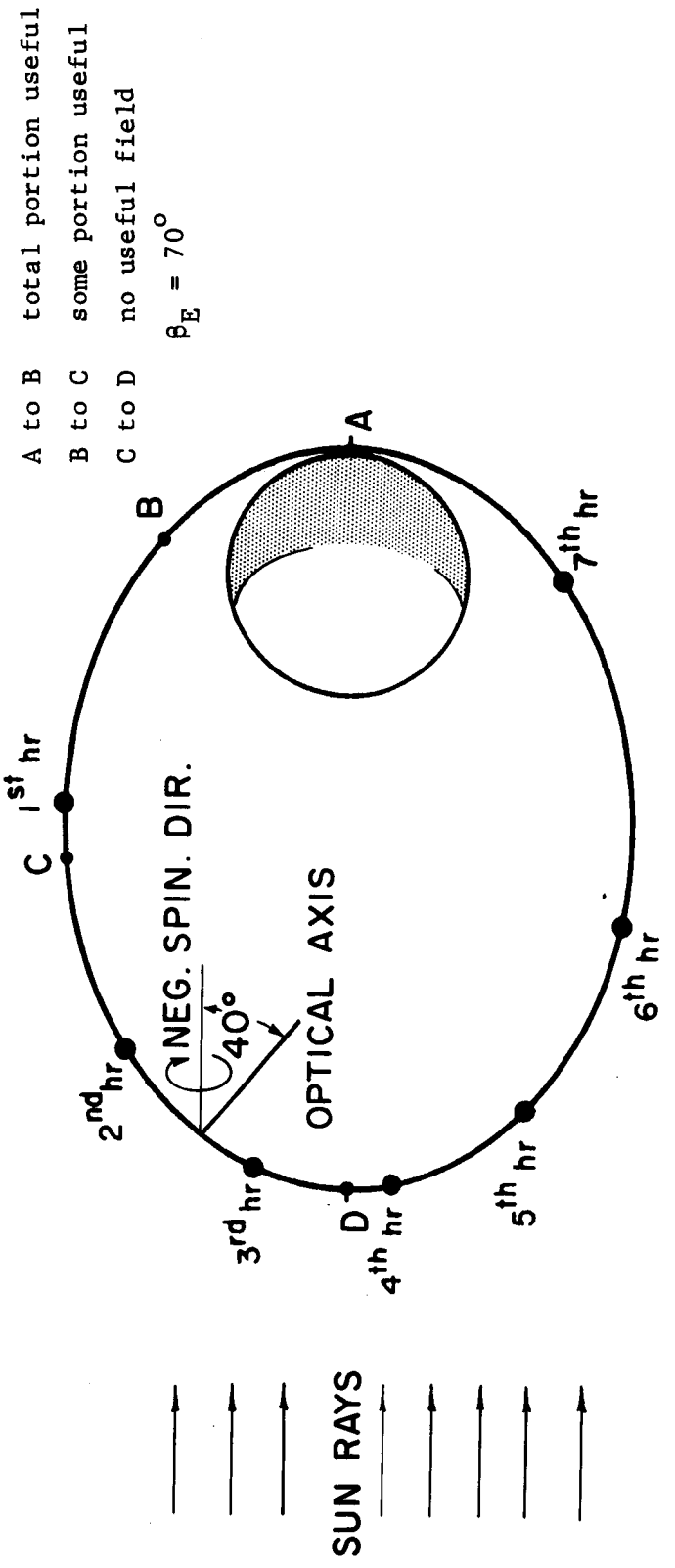

FIGURE 44: Worst Case Viewability

TABLE XVI

RANGES OF TRUE ANOMALY AND TIME FOR WHICH THERE IS NO USABLE FIELD, SOME USABLE FIELD, AND TOTAL USABLE FIELD. BEST AND WORST CONDITIONS FOR $\beta_E = \beta_S = 70^\circ$

	Viewability Conditions					
	No Field		Some Field		Total Field	
	Best	Worst	Best	Worst	Best	Worst
True Anomaly	$0 \leq \nu < 68.5^\circ$	$134.2^\circ \leq \nu \leq 180^\circ$	$68.5^\circ \leq \nu < 99.9^\circ$	$82.4 \leq \nu \leq 134.2^\circ$	$99.9^\circ \leq \nu \leq 180^\circ$	$0 \leq \nu < 82.4$
Time (hours)	$0 \leq t < .37$	$1.66 \leq t \leq 3.71$	$.37 \leq t < .82$	$.54 \leq t < 1.66$	$.82 \leq t < 3.71$	$0 \leq t < .54$
Portion of Orbital Period	0.10	0.55	0.12	0.30	0.78	0.15

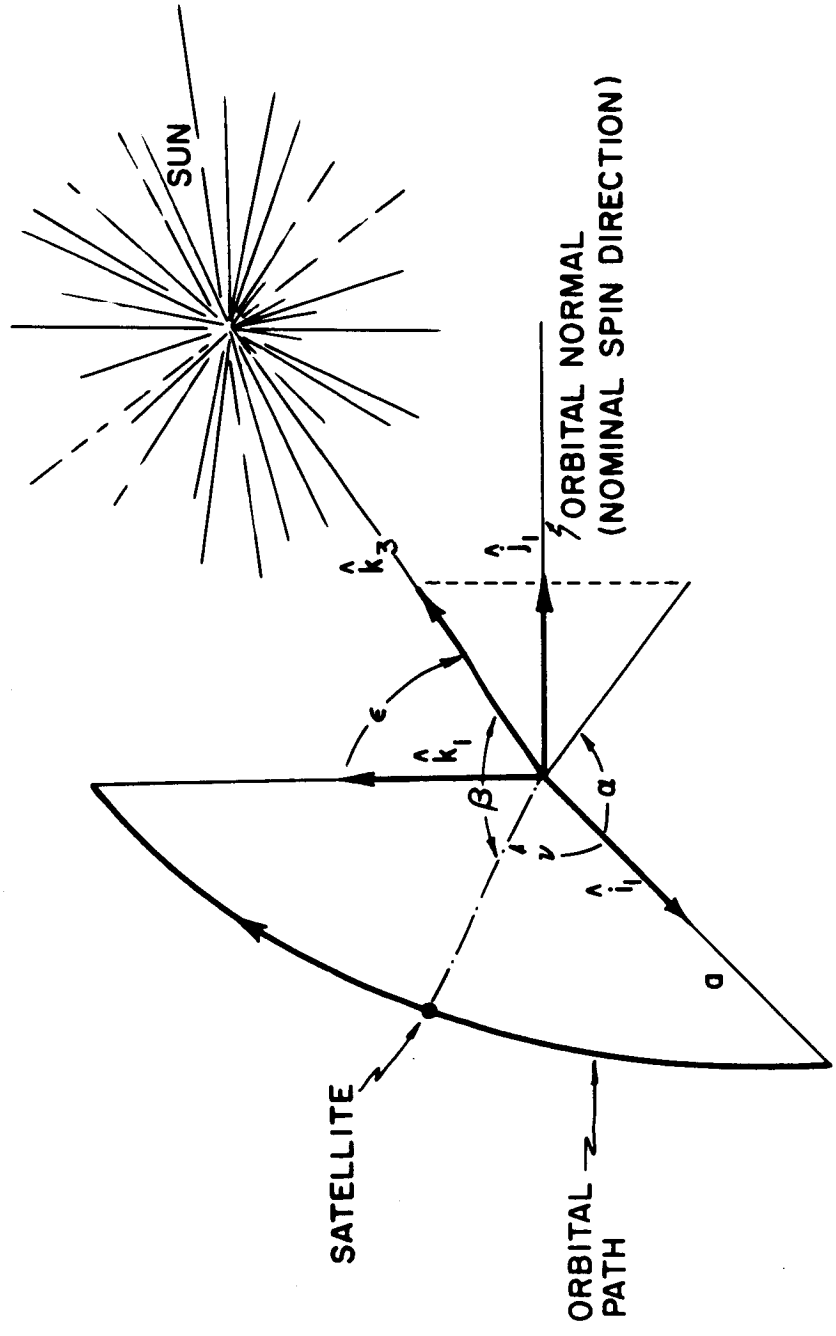

FIGURE 45: The Sun's Position With Respect to Orbital Plane

$$\hat{r} = (\cos \nu \cos \alpha \cos \epsilon - \sin \nu \sin \epsilon)\, \hat{i}_3 - \cos \nu \sin \alpha\, \hat{j}_3$$

$$+ (\cos \nu \cos \alpha \sin \epsilon + \sin \nu \cos \epsilon)\hat{k}_3$$

$$\hat{j}_1 = \sin \alpha \cos \epsilon\, \hat{i}_3 + \cos \alpha\, \hat{j}_3 + \sin \alpha \sin \epsilon\, \hat{k}_3$$

where ν = true anomaly (Figure 45)

$\hat{r}$ = unit vector in direction of satellite.

Now,

$$\hat{P}_1 = \cos \phi\, \hat{r} + \sin \phi\, \hat{j}_1$$
$$\hat{P}_2 = \csc \beta\, \hat{r} - \cot \beta\, \hat{k}_3 \ , \ \sin \beta \neq 0$$

where,

$\hat{P}_1$ = unit vector from earth's center in the direction of the point on horizon nearest to the spin axis (Figure 46);

$\hat{P}_2$ = unit vector from earth's center in the direction of the point on boundary of sunlit and dark region which is in the plane of $(\hat{r}, \hat{k}_3)$ and orthognal to $\hat{k}_3$ (Figure 46);

ϕ = angle from orbital normal to horizon;

β = angle between $\hat{r}$ and $\hat{k}_3$ (satellite and sun).

Suppose $\hat{P}_1 \cdot \hat{k}_3 \geq 0$, this implies that the point on the horizon near to the spin axis is sunlit. Hence we have

$\phi < \beta_E - \Gamma$	no field
$\beta_E - \Gamma \leq \phi < \beta_E + \Gamma$	some field
$\phi \geq \beta_E + \Gamma$	full field

where Γ = cant angle = angle between optical axis and spin axis = 40°.

Suppose $\hat{P}_1 \cdot \hat{k}_3 < 0$, then the closest point on the sunlit earth to the spin axis has the direction of $\hat{P}_2$. The vector from the satellite to this

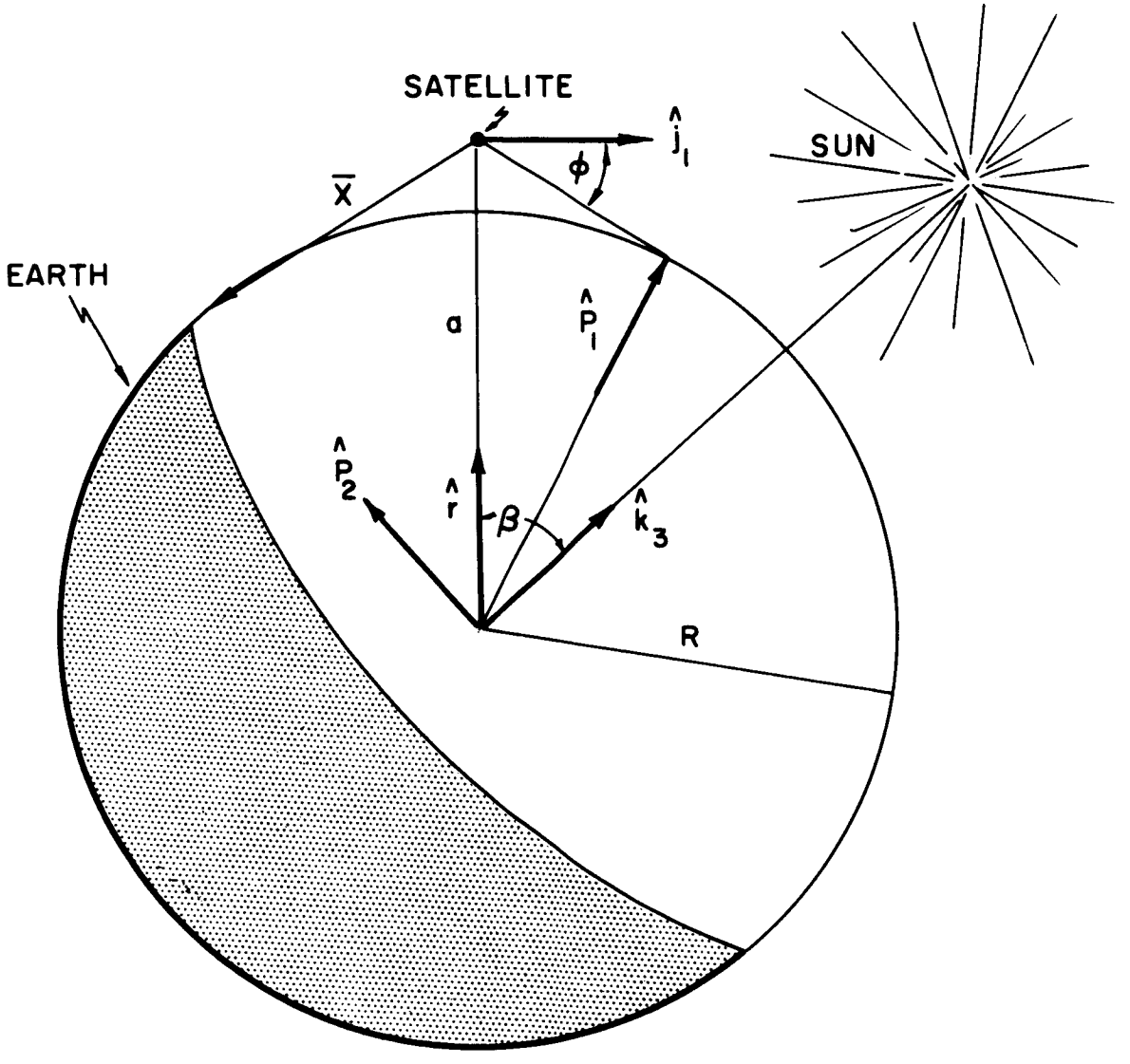

FIGURE 46: The Vectors $\hat{P}_1$ and $\hat{P}_2$

point is given by

$$\bar{x} = R\,\hat{P}_2 - a\,\hat{r}\ ,\ x = |\bar{x}|$$

where R = radius of the earth

a = orbital radius.

Two subcases exist. If $x^2 > a^2 - R^2$, then the horizon is dark so the field is full. However, if $x^2 \leq a^2 - R^2$, then a sunlit horizon can be seen from the satellite. Hence,

$\rho < \beta_E - \Gamma$	no field
$\beta_E - \Gamma \leq \rho \leq \beta_E + \Gamma$	some field
$\rho \geq \beta_E + \Gamma$	full field

where $\cos \rho = \dfrac{\bar{x} \cdot j_1}{|\bar{x}|}$, $0 \leq \rho \leq 180^\circ$

Let us now consider the direct sunlight. For $\hat{r} \cdot \hat{k}_3 = \cos \beta < -\sqrt{1 - (\frac{R}{a})^2}$ the sun is obscured by the earth and so a full field exists. But, for $\cos \beta \geq -\sqrt{1 - (\frac{R}{a})^2}$

$\cos (\beta_s - \Gamma) \leq \hat{k}_3 \cdot \hat{j}_1 = \sin \alpha \sin \epsilon \leq 1$	no field
$\cos (\beta_s + \Gamma) < \hat{k}_3 \cdot \hat{j}_1 < \cos (\beta_s - \Gamma)$	some field
$-1 \leq \hat{k}_3 \cdot \hat{j}_1 \leq \cos (\beta_s + \Gamma)$	full field

Results are plotted in Figures 47 through 50. Two cases of ϵ are shown; one for the sun in the plane which is normal to the orbital plane ($\epsilon = 90^\circ$), and another for the sun in its extreme position from this plane ($\epsilon = 56^\circ$). Note that $\epsilon = 56^\circ$ yields slightly more favorable viewing than $\epsilon = 90^\circ$. Also note considerable improvement in viewability offered by $\beta_E = 50^\circ$ instead of 70°. Hence for this orbital class considerable effort should be placed on

KEY TO VIEWABILITY FIGURES 47 - 60

No useful field of view

Both sun and earth scatter into the field of view, but some useful field

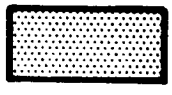

Either the sun or earth scatter into the field of view, but some useful field

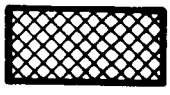

Full field of view

β_E = minimum angle between optical axis and closest point on sunlit earth for which shield is effective

β_S = minimum angle between optical axis and sun for which shield is effective

α = (See Figure 45)

ϵ = (See Figure 46)

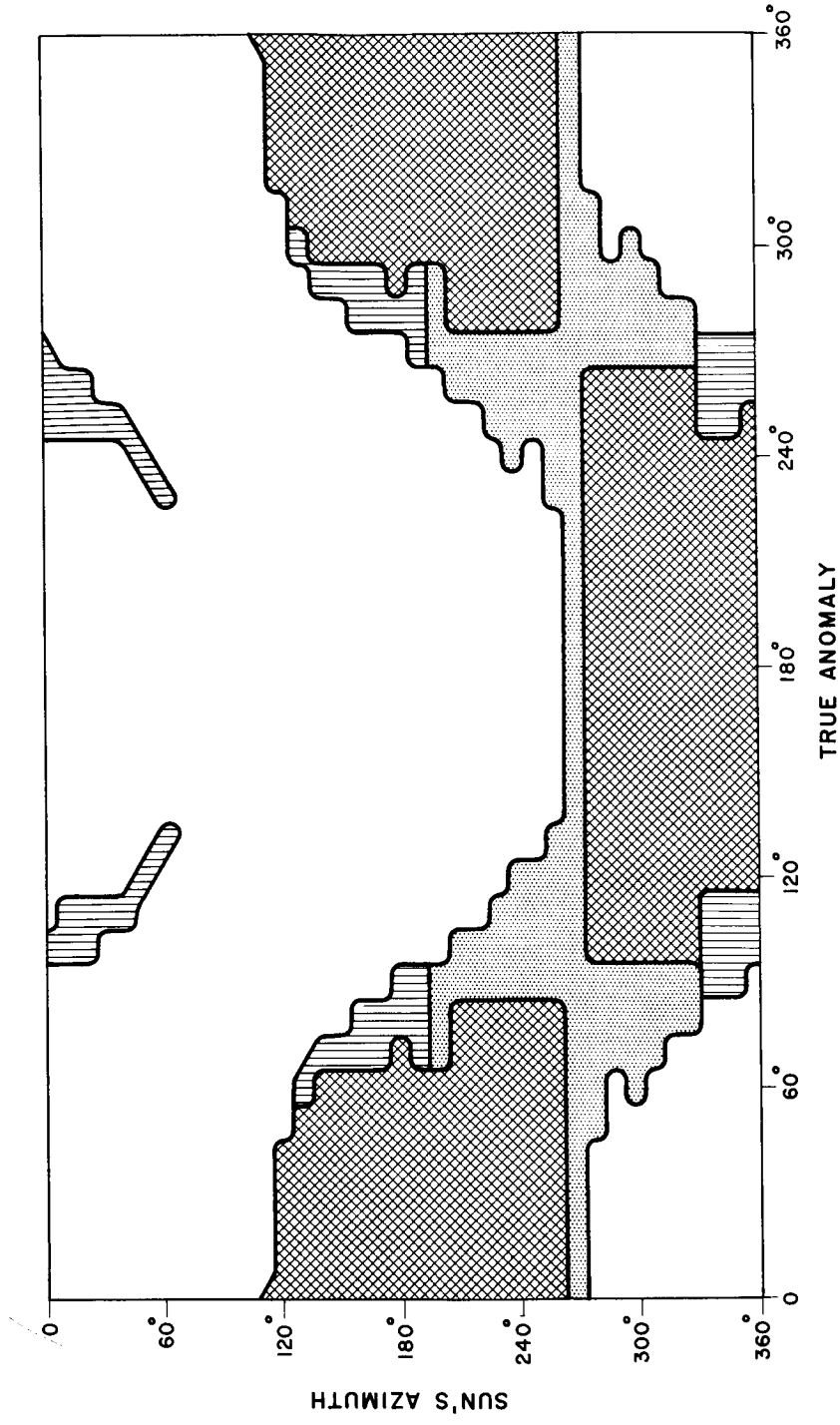

FIGURE 47: Viewability for Circular, Near-Polar, Spin Stabilized Orbit
$\beta_E = \beta_S = 70^0$, $\epsilon = 90^0$

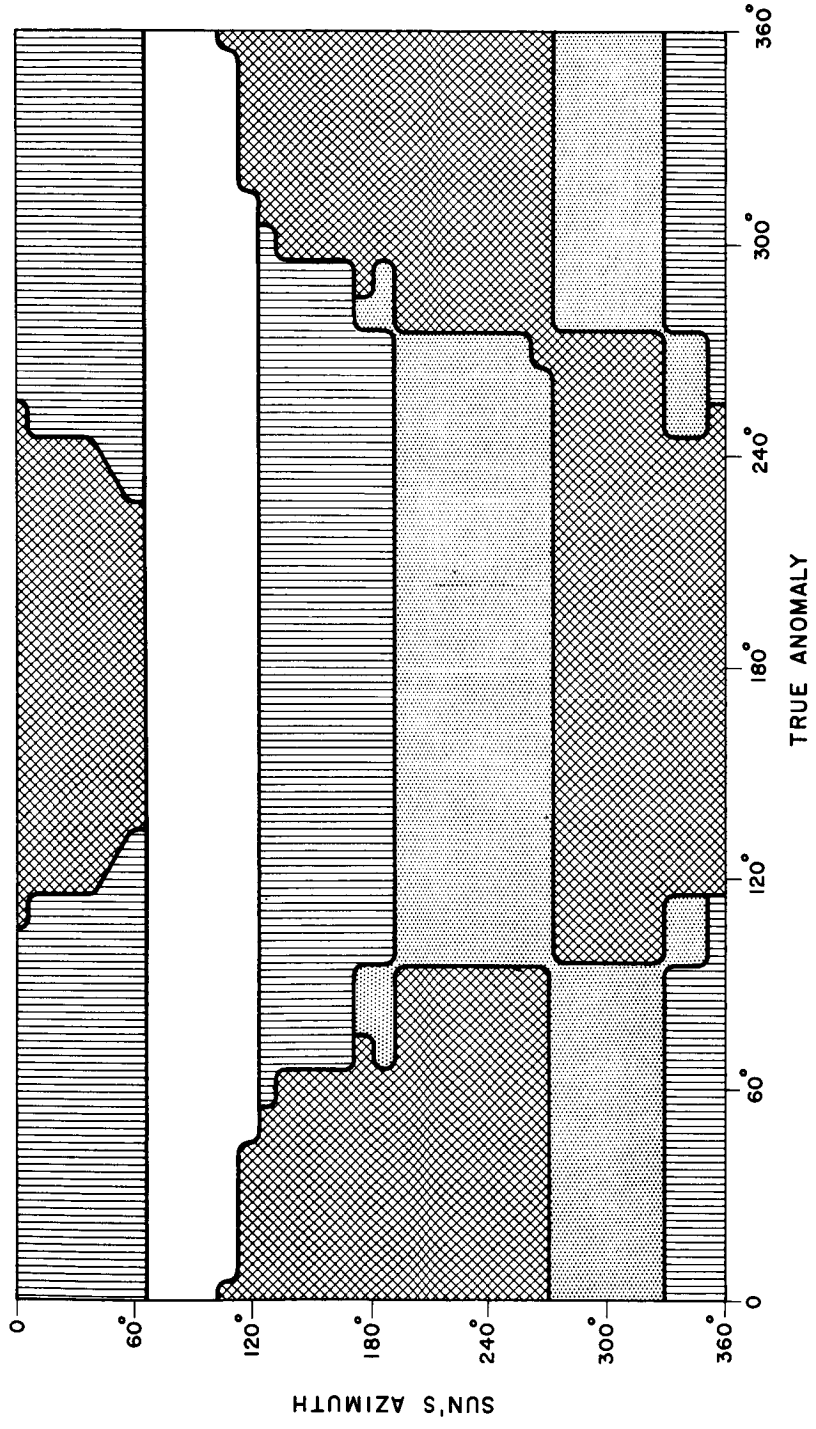

FIGURE 48: Viewability for Circular, Near-Polar, Spin Stabilized Orbit, $\beta_E = 50^o$, $\beta_S = 70^o$, $\epsilon = 90^o$

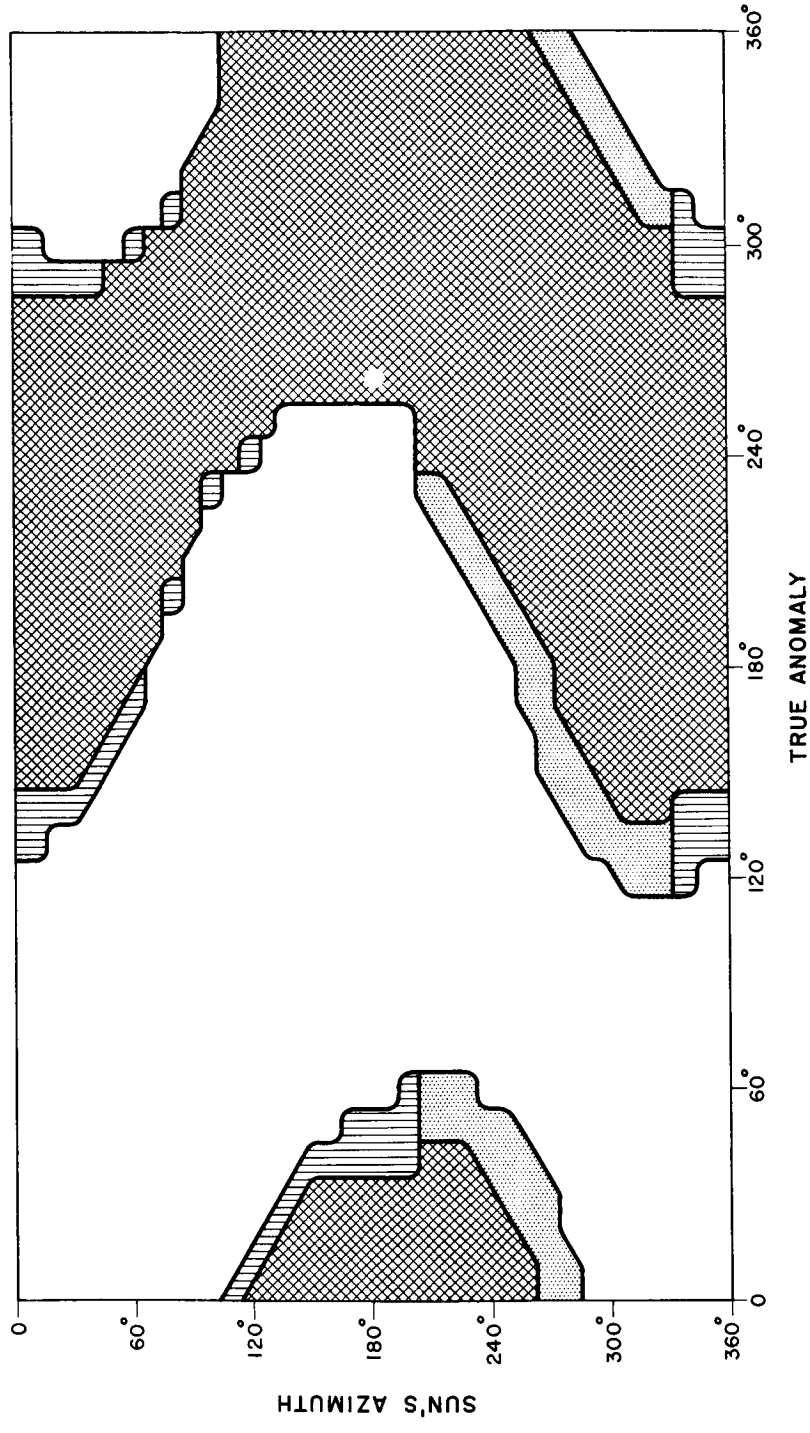

FIGURE 49: Viewability for Circular, Near-Polar, Spin Stabilized Orbit, $\beta_E = \beta_S = 70^0$, $\epsilon = 56^0$

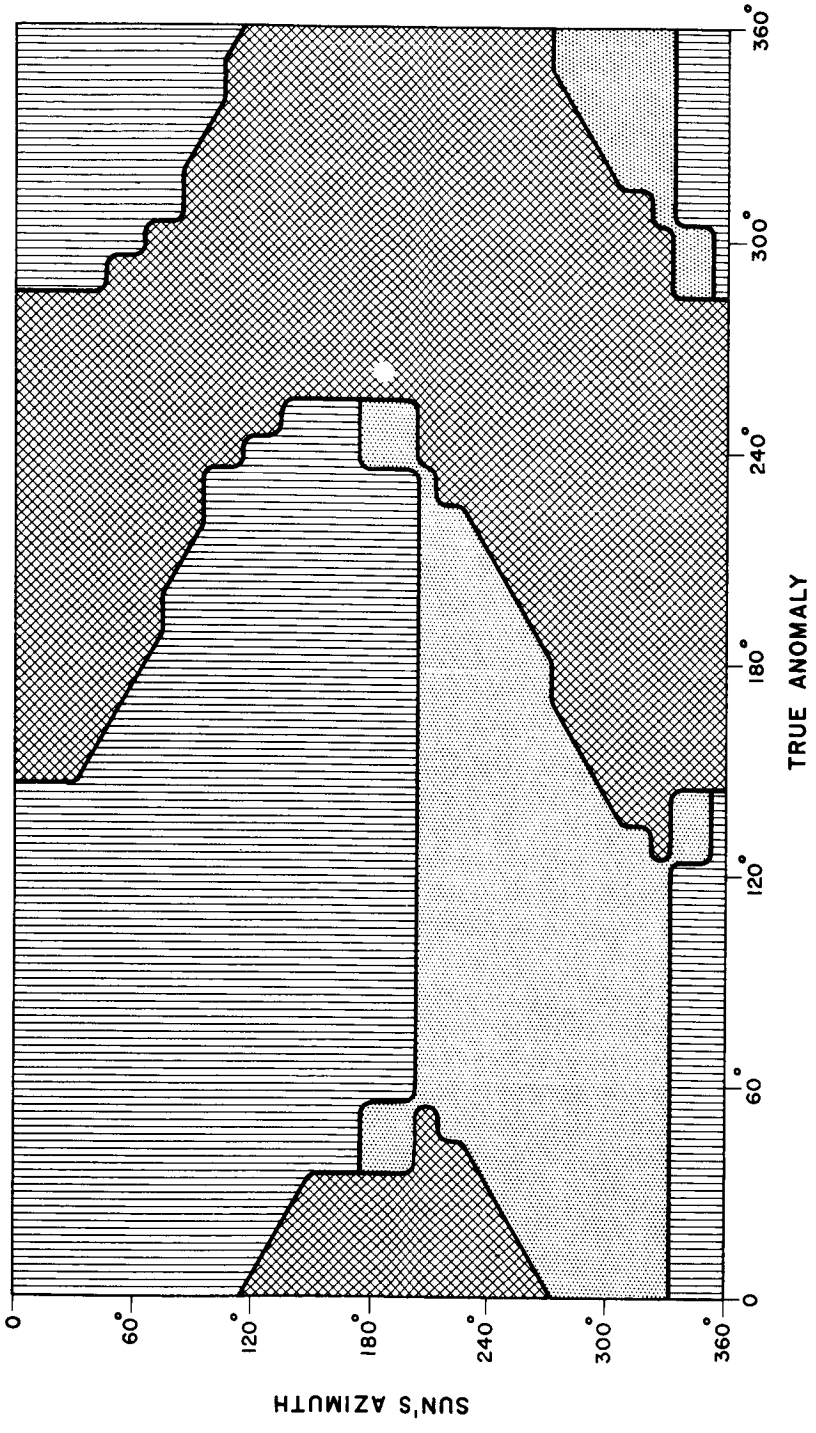

FIGURE 50: Viewability for Circular, Near-Polar, Spin Stabilized Orbit
$\beta_E = 50^o$, $\beta_S = 70^o$, $\epsilon = 56^o$

achieving a small β_E. However, we will see that for all other orbital classes little improvement is offered by choosing a $\beta_E = 50^o$ instead of 70^o.

3. Magnetically Stabilized Satellite

The magnetically stabilized mode of the near polar orbit represents the most difficult of the S^3 modes as far as viewability is concerned. In Figure 51 we picture the geometry. Note that in the Southern Hemisphere the optical axis will point into the earth. Thus, even without the restrictions imposed by the sun and sunlit earth, the attitude can be found only over one-half the orbit.

Let us assume the orbit passes through the magnetic poles, and the earth's field is that of a dipole. Then, (Figure 51)

$$\tan I = 2 \tan \nu$$

where I = inclination of the field

ν = true anomaly measured from the magnetic equator.

We may now investigate the viewability as in the previous section. Results are shown in Figures 52 through 55. In these plots α and ϵ represent the direction to the sun as before. The viewability results may be improved by using two sensors, one in the direction shown and a second in the opposite direction.

4. Near-circular, Low Altitude Orbit

In Figure 56, we picture the relationship between the orbital plane, spin axis, and optical axis.

As shown in Figure 56, the spin axis is in the ecliptic plane and the orbital inclination is 33^o. Let σ be the angle from the intersection of the orbital plane and the ecliptic to the spin axis. Also let α be the angle from

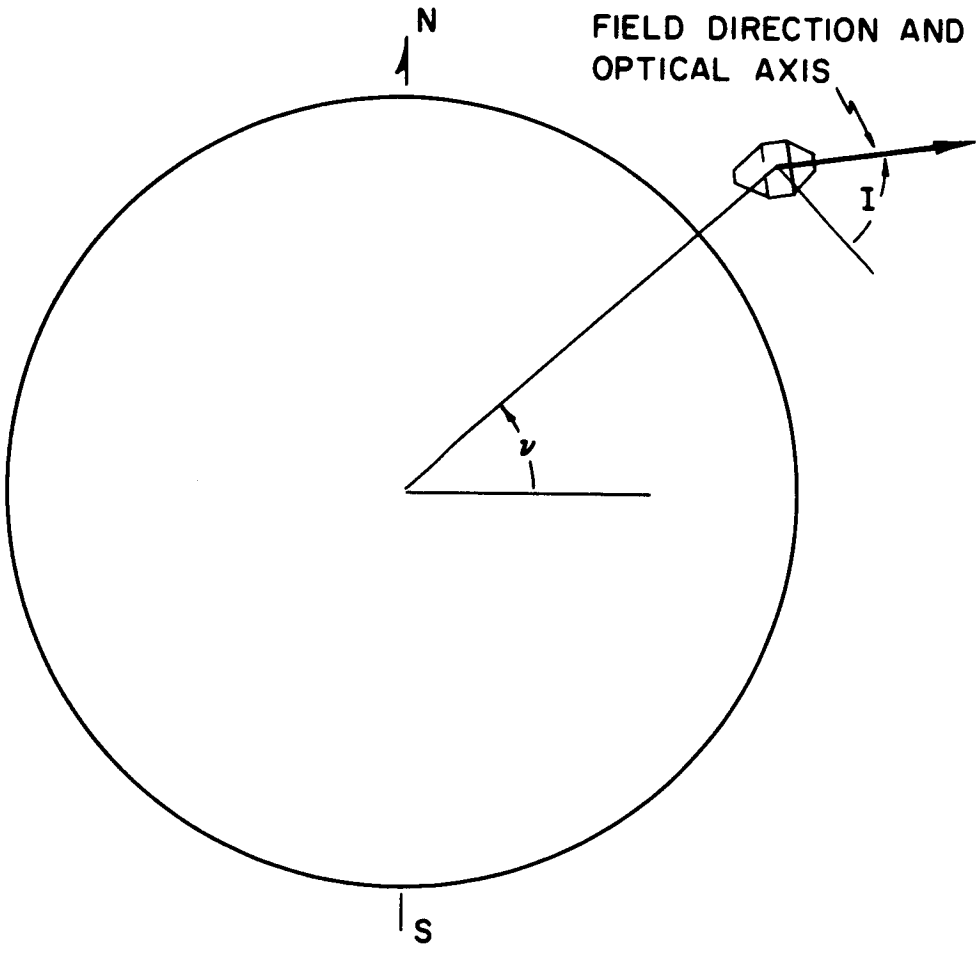

FIGURE 51: Orientation of S^3 With Respect to Magnetic Field

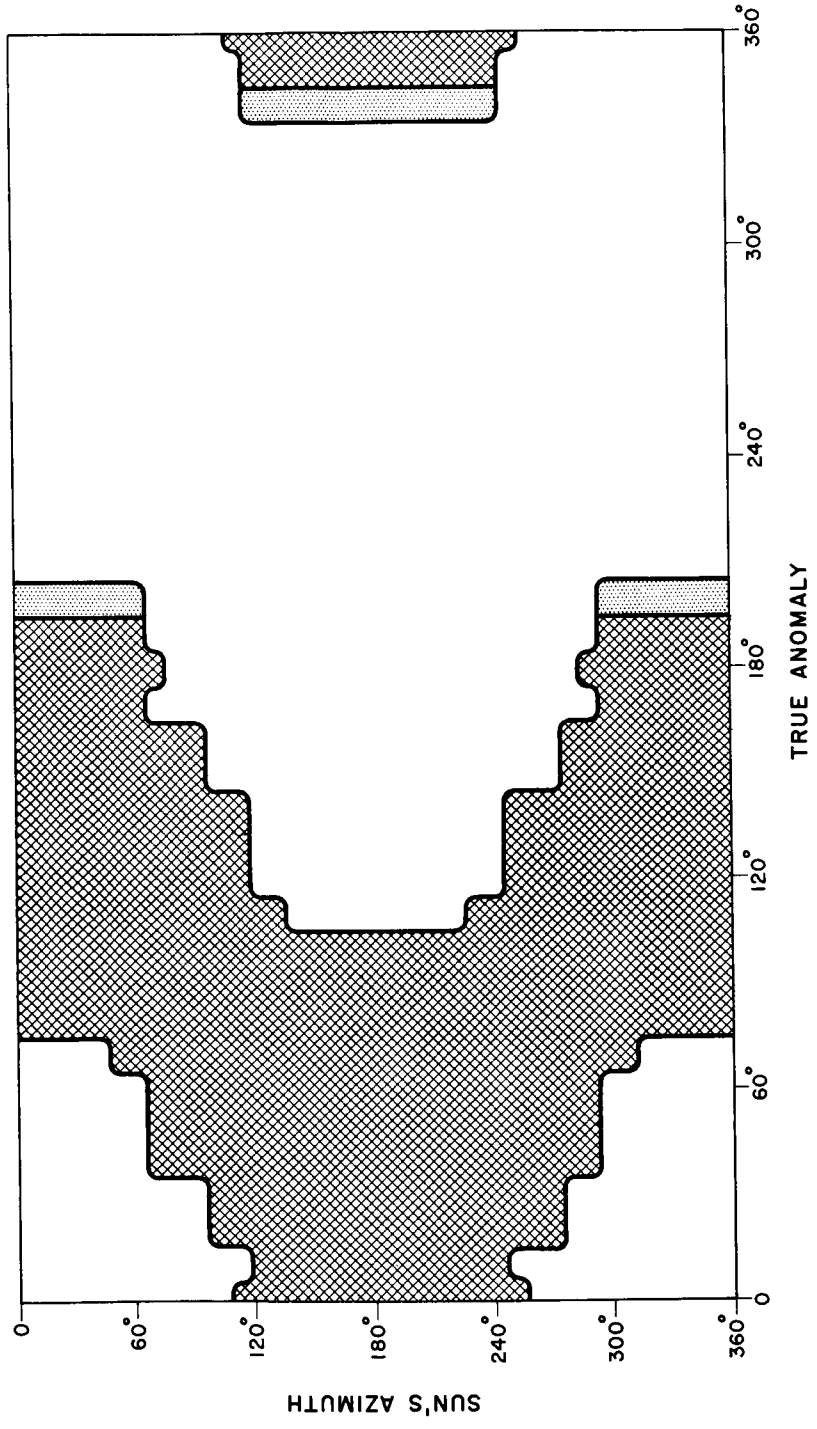

FIGURE 52: Viewability for Magnetically Stabilized Satellite
$\beta_S = \beta_E = 70^o$, $\epsilon = 90^o$

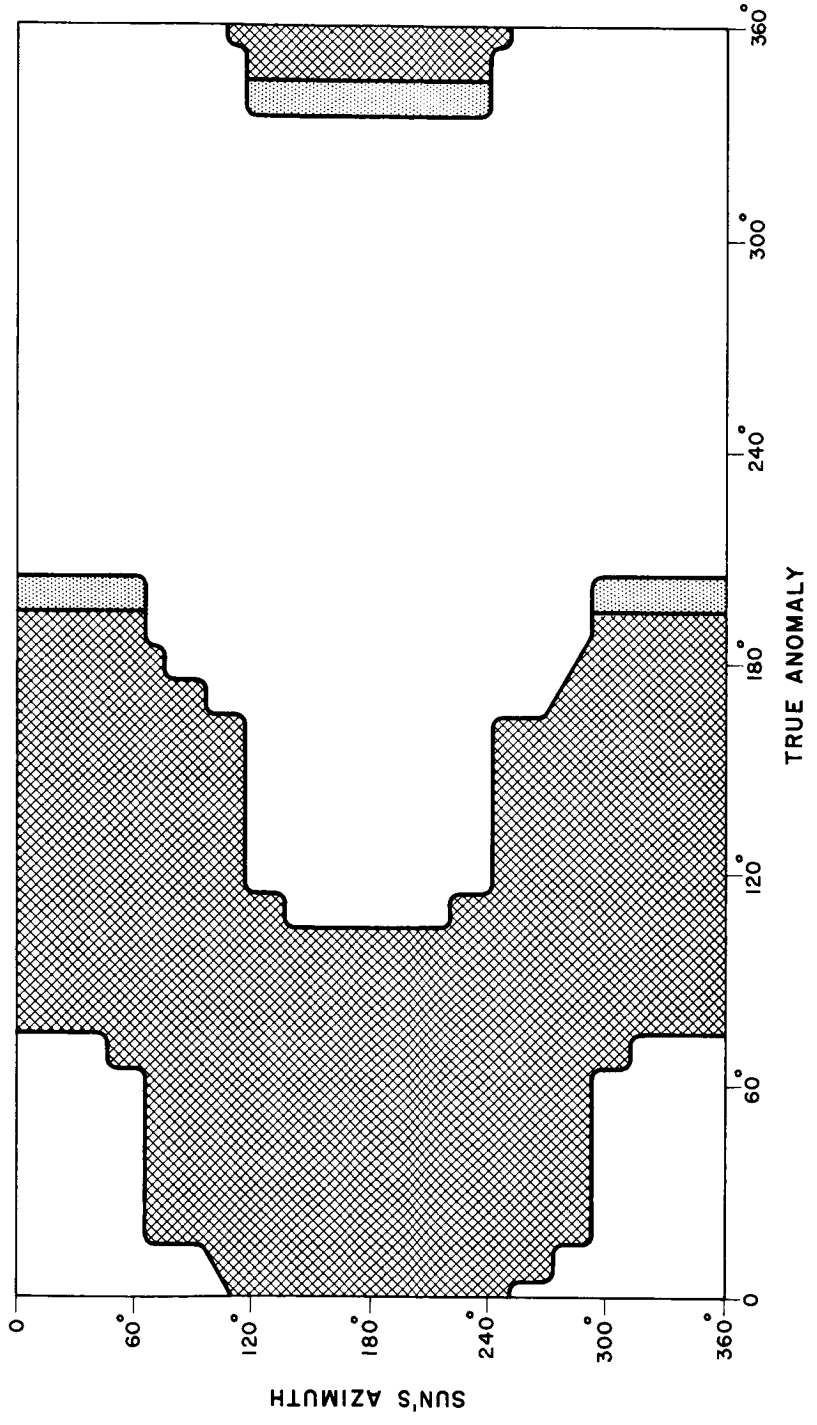

FIGURE 53: Viewability for Magnetically Stabilized Satellite $\beta_S = 70^o$, $\beta_E = 50^o$, $\epsilon = 90^o$

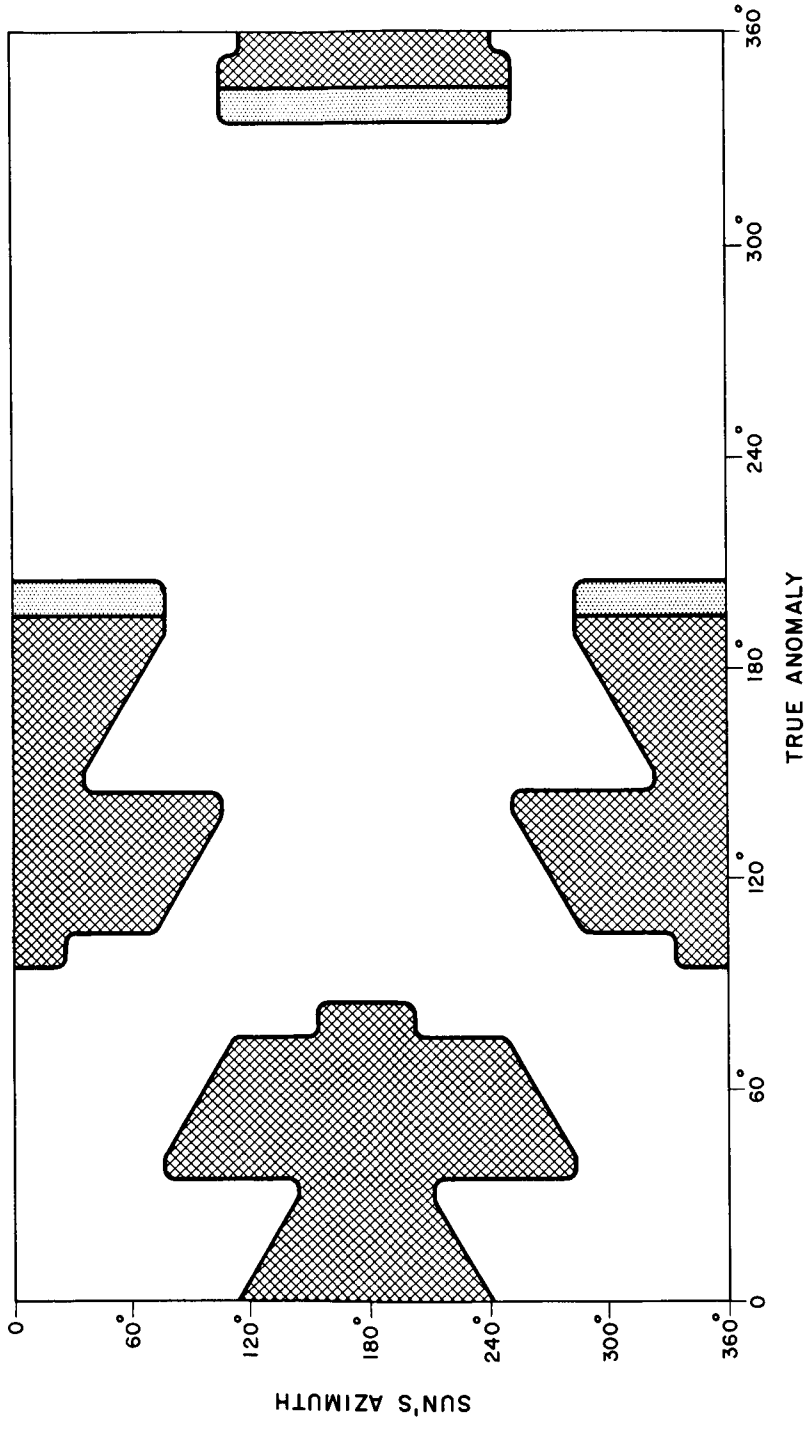

FIGURE 54: Viewability for Magnetically Stabilized Orbit
$\beta_E = \beta_S = 70^o$, $\epsilon = 56^o$

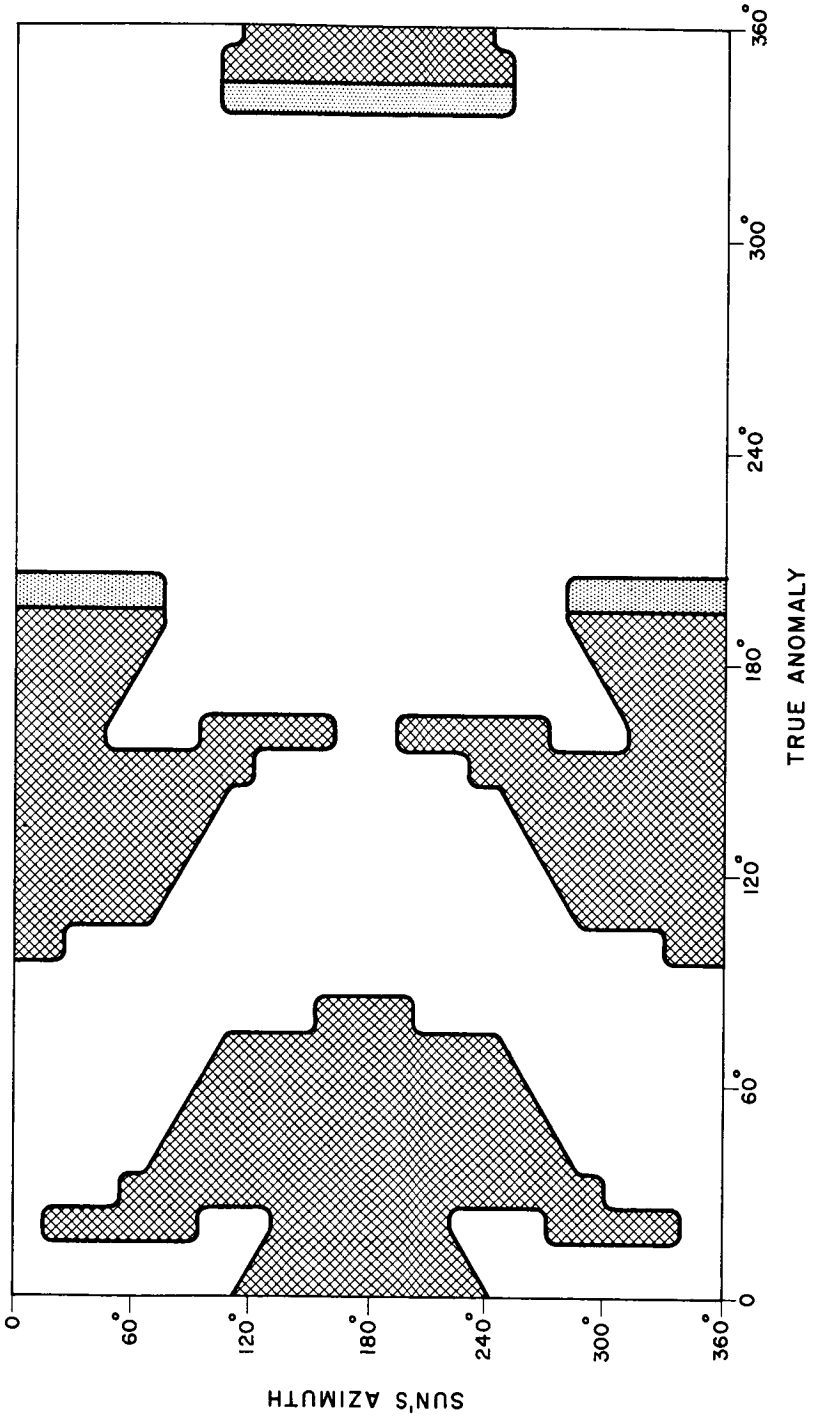

FIGURE 55: Viewability for Magnetically Stabilized Satellite
$\beta_S = 70^o$, $\beta_E = 50^o$, $\epsilon = 90^o$

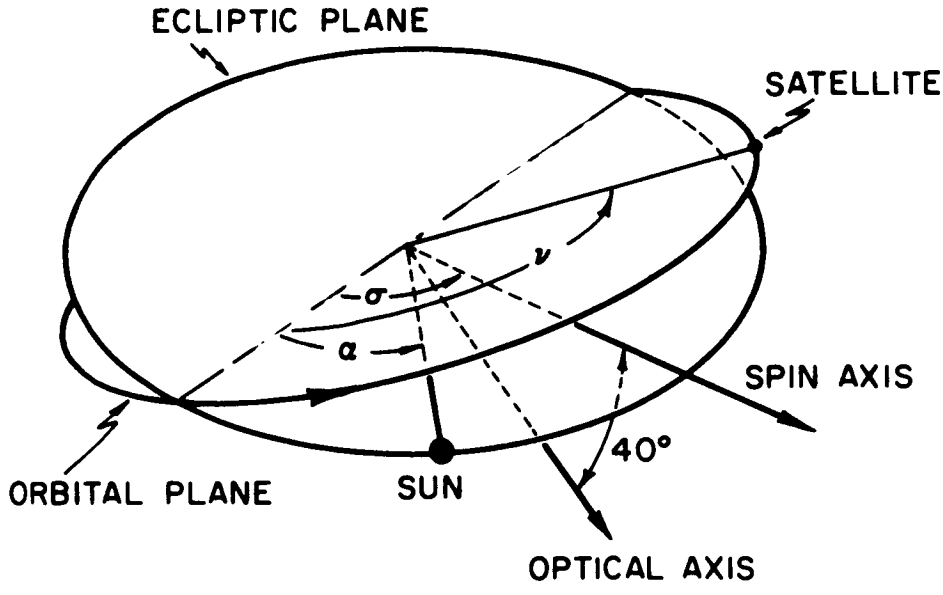

FIGURE 56: Geometry of Near-Circular, Low Altitude Orbit ($i = 33^{o}$)

this intersection to the sun. Now, the angles α and σ are not specified. In Figures 57 through 60, we plot the viewability conditions for this orbital case. Two positions of the sun are $\alpha = 0^{o}$ and 90^{o}.

5. Longitude-synchronous Orbit

The 24-hour orbit implies the most favorable and most easily analyzed viewability conditions. The satellite is gravity gradient stabilized so we choose to position the optical axis directly away from the earth's center. With this choice, the sun will cause stellar viewing difficulties for $2\ \beta_S = 140^{o}$ out of each orbital revolution.

In view of the large percentage of scanned area where the radiation from the sun or the sunlit earth interferes with the sensor, it is of interest to evaluate the sensor sensitivity as the background level increases. No absolute analytic determination of sensor sensitivity versus sun angle (or angle to sunlit earth) from the optical axis has been attempted since it involves multiple integrations of diffusely scattered light flux from curved surfaces. However, a qualitative estimate of sensor sensitivity versus sun interference can be obtained by determining the limiting detectable magnitude as the stellar background is increased by factors of two above the maximum normal background of 325 tenth magnitude stars per square degree. In Figure 61, it can be seen that the normal background level can be doubled nine times before the limiting detectable magnitude becomes zero if the scan period is 15 seconds and the optical aperture is 0.8 inch. For the same optical aperture and a five second scan period, the background level can be doubled seven times before the limiting detectable magnitude becomes zero. Figure 62 shows similar plots for a two inch optical aperture and scan periods of four and .5 seconds.

Whenever the sun enters the field of view, most of the radiant energy from the sun entering the optical aperture will be focused on a very small spot on the photocathode. In order to protect the photocathode from permanent

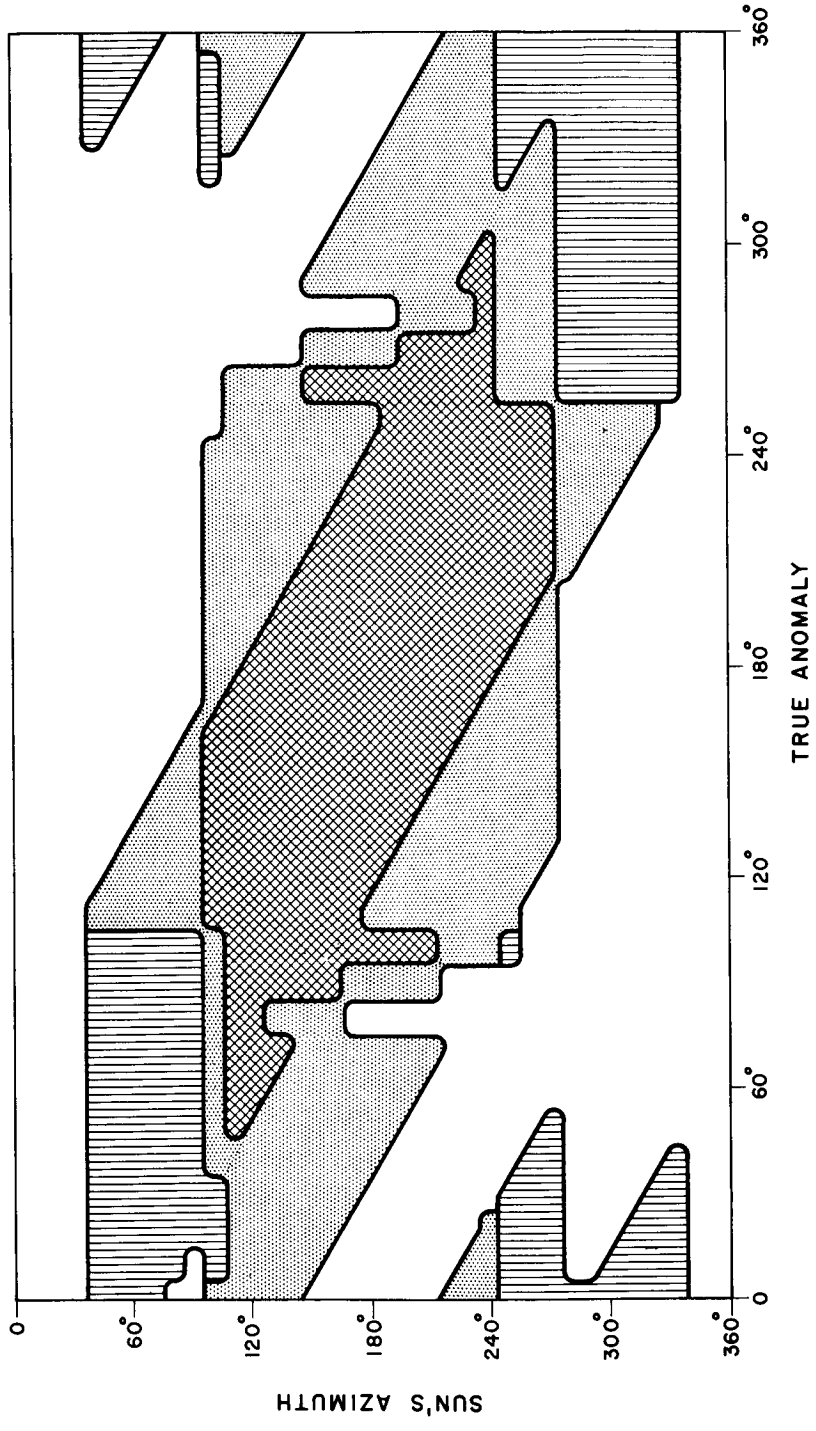

FIGURE 57: Viewability for Low Inclination, Low Altitude Orbit
$\beta_E = \beta_S = 70^0$, $\alpha = 0^0$

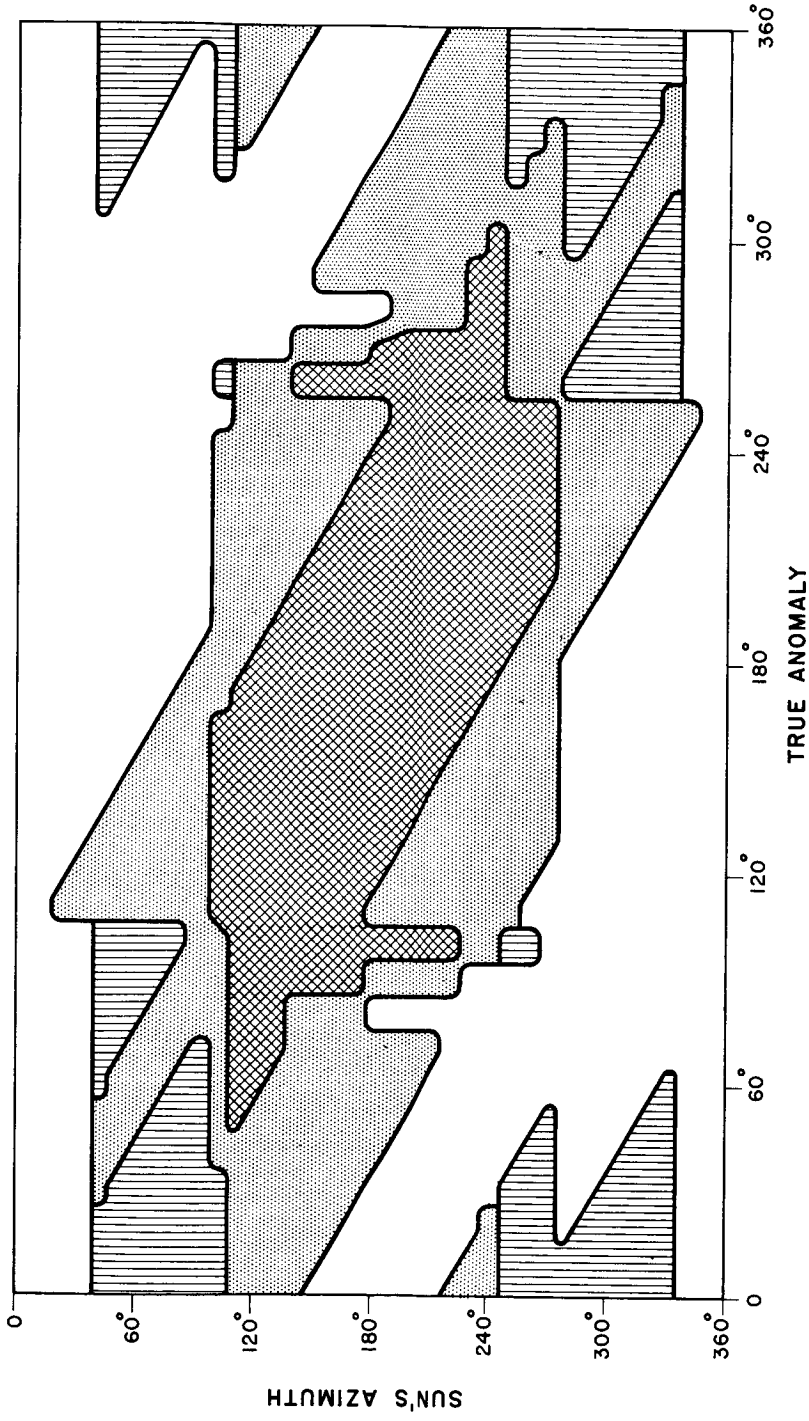

FIGURE 58: Viewability for Low Inclination, Low Altitude Orbit, $\beta_E = 50^o$, $\beta_S = 70^o$, $\alpha = 0^o$

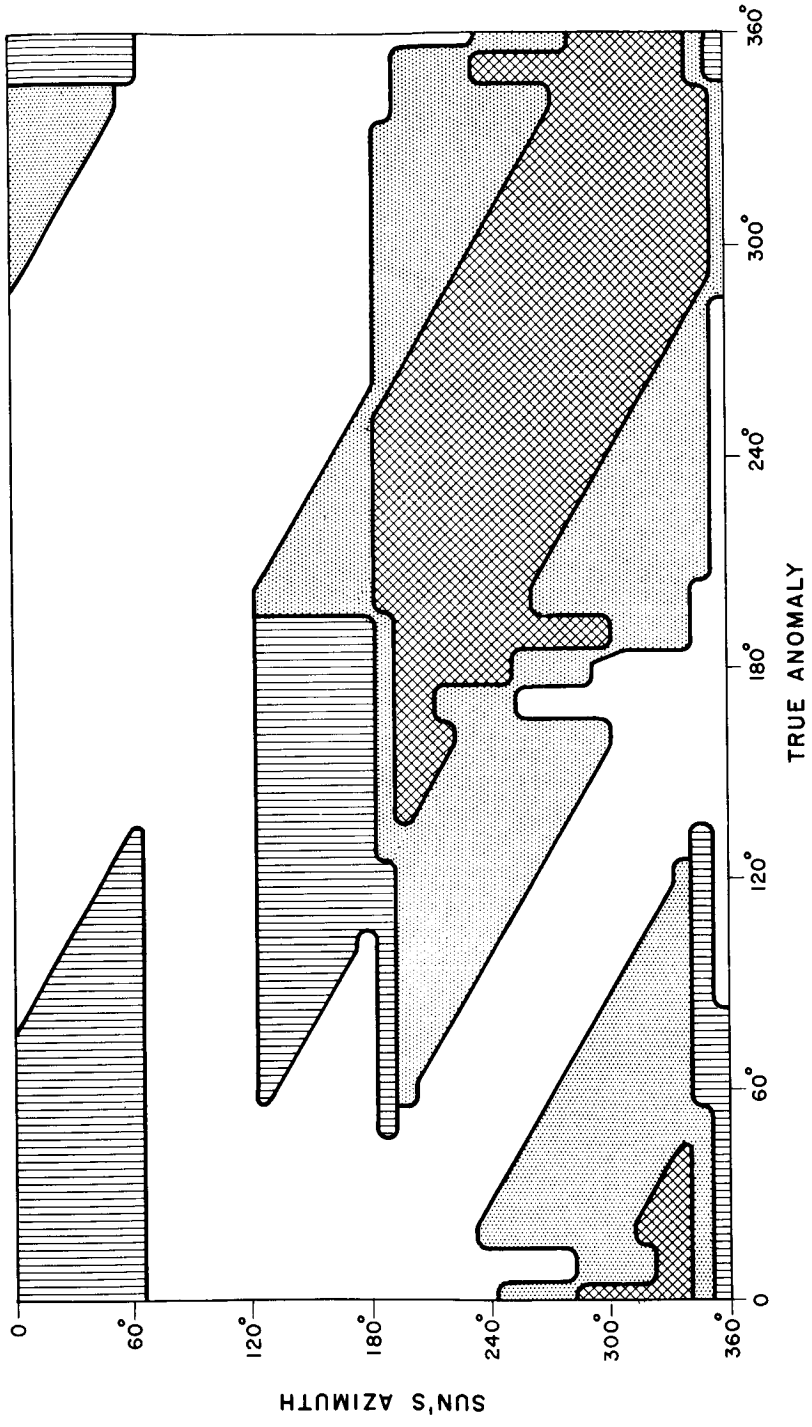

FIGURE 59: Viewability for Low Inclination, Low Altitude Orbit
$\beta_E = \beta_S = 70^0$, $\alpha = 90^0$

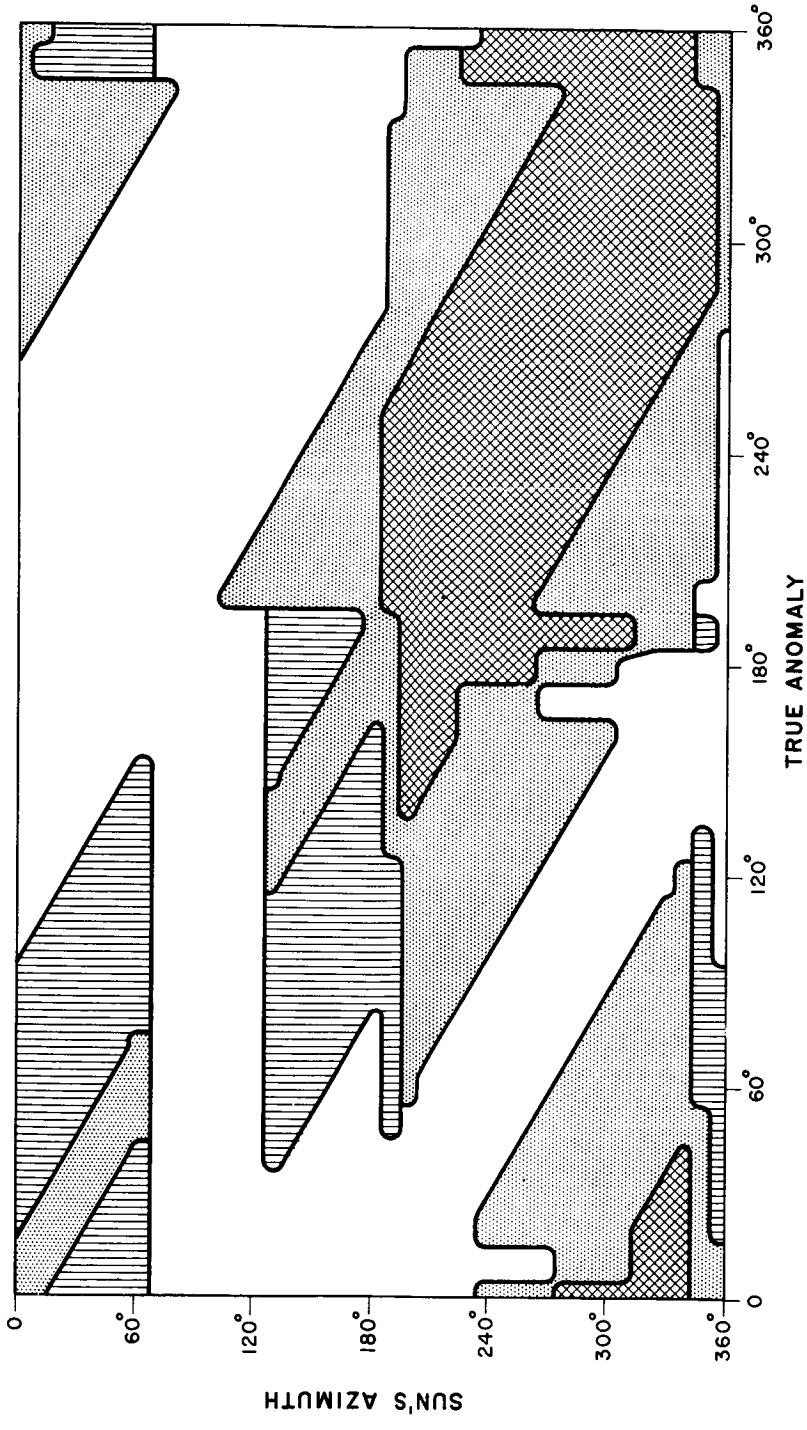

FIGURE 60: Viewability for Low Inclination, Low Altitude Orbit
$\beta_E = 50^o$, $\beta_S = 70^o$, $\alpha = 90^o$

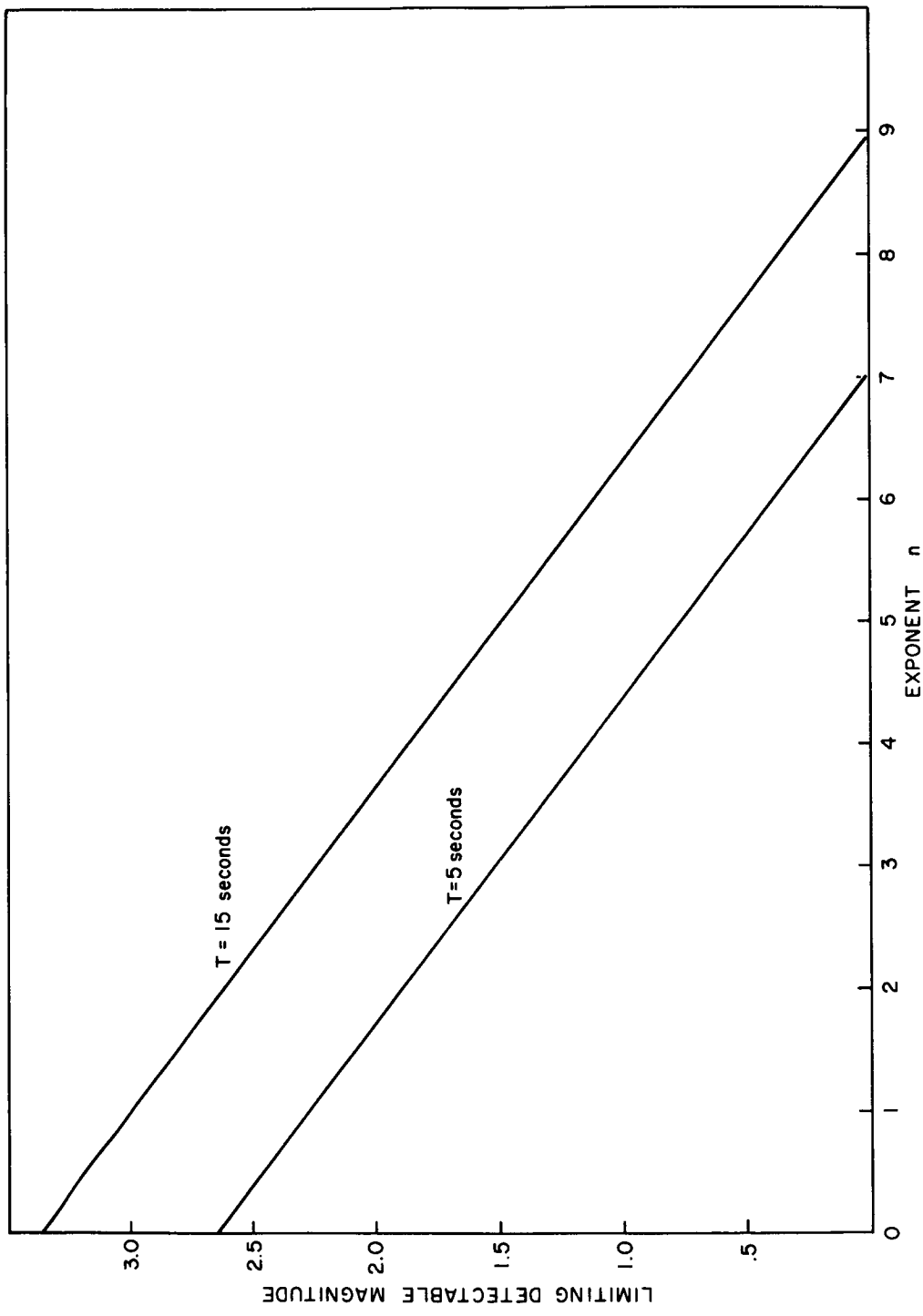

FIGURE 61: Limiting Detectable Star Magnitude Versus Normal Stellar Background Level x 2^n. Optical Aperture = .8 inch

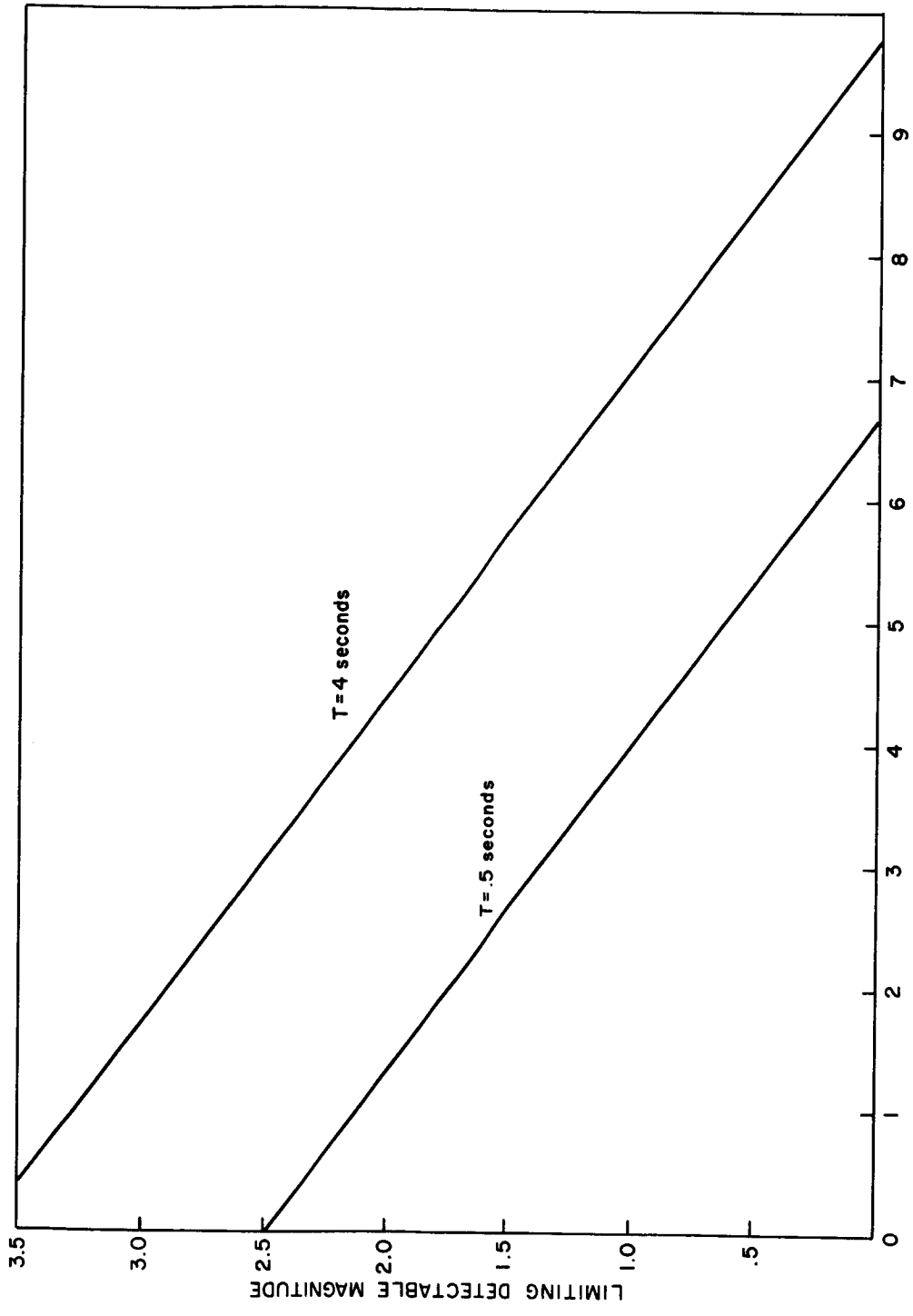

FIGURE 62: Limiting Detectable Star Magnitude Versus Normal Stellar Background Level x 2^n. Optical Aperture = 2 inches

damage, it is necessary to prevent the sun's image from being focused on such a small spot on the photocathode. This can be accomplished in either of two ways:

(a) defocus the image from the slit aperture with a condensing field lens so that the defocused image covers almost the entire cathode area; or

(b) provide a shutter which is automatically closed whenever the sun comes into the portion of the field of view containing the slit.

Radiation reflected from the earth is not as serious a problem from the standpoint of photocathode protection since the earth is an extended source and the diffuse radiation is not focused into a small spot.

The advantage of employing a condensing lens is that it involves no moving parts and requires no power to operate. However, the major disadvantage is that the lens system is required to be longer with the addition of a condensing lens which requires a greater volume. Also, the condensing lens increases the weight of the system.

The alternative approach is to employ a reticle shutter as shown in Figure 63. The shutter is shorter than a condensing lens system, but power is required to close the shutter. The shutter can consist of a spring leaf which is pulled over the slit opening when the solenoid is energized by either a photomultiplier overload protector circuit or a small solid-state detector. The shutter may be closed or opened in six to eight milliseconds. Less than .5 watt of power is required to hold the shutter closed. Average power dissipation depends upon the duty cycle determined by the presence of the sun and sunlit earth in the field of view. Hence, average power dissipation is much less than .5 watt. The shutter weight is approximately two ounces. Although the device does utilize a moving part, it can be demonstrated that such a device could withstand several hundred million operations at operation rates between 25 to 100 per second without failing.

The shutter mechanism shown in Figure 63 is mounted on a thin cylindrical ring. The mechanism and mounting ring would then be sandwiched between two

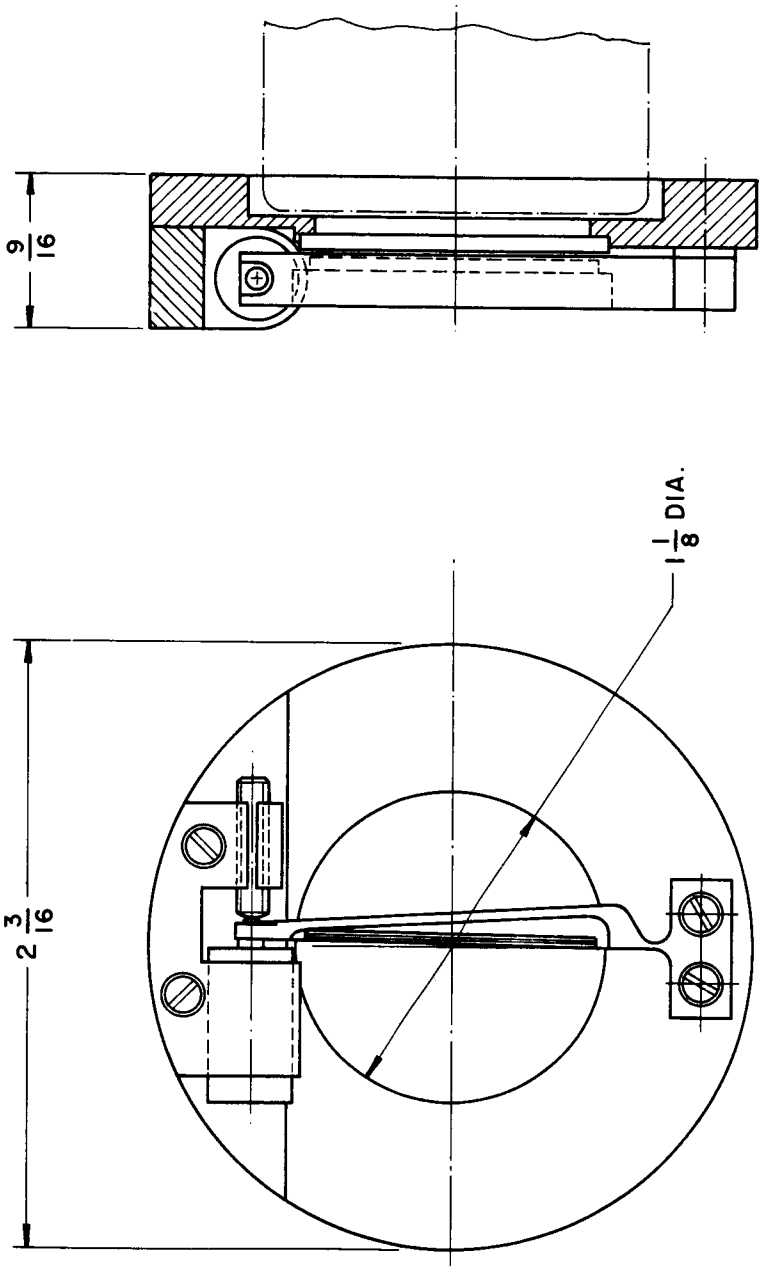

RETICLE SHUTTER

WEIGHT : 2 oz.
POWER CONSUMPTION : 0.5 watt (est.)
SHUTTER CLOSURE TIME : 6-8 msec.

FIGURE 63: Reticle Shutter

additional rings which would comprise a one centimeter thick cathode particle radiation shield. Particle radiation shielding requirements are discussed in Part B of this section.

After evaluation of the operational constraints imposed on the SCADS sensor by the interference caused by the sun radiation or the earth-reflected sun radiation, it can be concluded that a sun sensor would be a natural complement to a SCADS sensor for the attitude determination problem. The reason for such a combination results because any method of attitude determination employing a sun sensor cannot be fully effective when the spacecraft is passing the dark side of the earth, whereas at this time the SCADS sensor is fully effective. When the spacecraft is passing the sunlit portion of the earth, the SCADS sensor may be operationally constrained to detect only the brightest star whereas the sun sensor can provide the additional measurement to determine the attitude. Also, the data from a sun sensor would be a valuable aid in the star identification procedures. The advantages of both sensors can be helpful in extending the period during which the spacecraft attitude can be accurately determined.

B. Particle Radiation Restrictions

Here we may be guided by NASA Goddard experience with the OGO II airglow photometers. The main body photometer used a EMR 541 E-05M, a one inch diameter end-on tube with a tri-alkali cathode on a sapphire window [19]. The orbit was polar with apogee near 1500 kilometers and perigee near 400 kilometers.

The photocathode current in this photometer was observed to vary from 5×10^{-16} to 3.3×10^{-9} ampere with the maximum occurring in low latitudes near 1500 kilometers (L = 1.23). "It was not a simple increase in dark current level, but consisted of a multitude of pulses, and tended to persist after the radiation levels had decreased."

Since **L** = 1.23 corresponds about to the maximum of the inner belt of fast electrons from the "starfish explosion" it is natural to attribute the effects to these fast electrons. We thus examine some of the possible ways in which these could cause noise in the photomultiplier.

1. Bremsstrahlung

Bremsstrahlung (X-rays) due to fast electrons cause photo-emissions by the photoelectric effect (below .05 mc^2 in carbon, .1 mc^2 in aluminum), the Compton effect and by pair production (important at about 10 mc^2 in lead, 30 mc^2 in aluminum). This could be very serious in that the resulting X-rays are very penetrating and it could happen that attempts to shield against the fast electrons would only increase the X-ray production. Consequently, we next estimate the amount of Bremsstrahlung we might expect from a given amount of shielding.

2. X-Ray Production by Bremsstrahlung in Aluminum

We assume:

1) normally incident mono-energetic electrons of energy E_o on an infinite slab of thickness X_1 centimeters;

2) we can neglect all energy loss mechanisms except ionization and excitation.

Number of photons which appear at $X = X_1$ is

$$n = N \int_0^a \int_{E_{min}}^{E(X)} e^{-\frac{X_1 - X}{\tau(k)}} \phi_k \frac{dk}{E_o - \mu} dx \tag{56}$$

where

$$\phi_k \frac{dk}{E_o - \mu}, \quad (\mu = mc^2)$$

is the cross section for emission of a photon in the range k, k + dk.

$\tau(k)$ is the range for photons in aluminum. $\tau(k)$ may be found from the graphs of range given by Johnson (Satellite Environment Handbook)[20] and approximated by,

$$\log \tau(k) = .440 \log k + 1.224 \qquad k > 5.5 \times 10^{-2} \text{ MeV} \tag{57}$$

$$= 2.760 \log k + 4.126 \qquad k < 5.5 \times 10^{-2} \text{ MeV}$$

To find E(X) recourse was had to an empirical equation for range given in the American Institute of Physics Handbook[21]

$$R = .412 E^n \text{ gm/cm}^2 \tag{58}$$

$$n = 1.265 - .0954 \ln E$$

$$.01 \leq E \leq 2.5 \text{ MeV}$$

$$R = .530E - .106 \text{ gm/cm}^2$$

$$2.5 \leq E \leq 20 \text{ MeV}$$

We take n = 1.181 in first approximation and define,

$$H(X) = \frac{X}{.412}^{\frac{1}{1.181}} \qquad X < 1.219 \text{ gm/cm}^2 \tag{59}$$

$$= \frac{X + .106}{.530} \qquad X \geq 1.219 \text{ gm/cm}^2$$

Then

$$E(X) = H(X_o - X) \tag{60}$$

where X_o is the range of electrons of incident energy E_o. E_{min} was taken as $.1\ mc^2$ reasoning that photons of energy much less than this would not escape.

Finally, X_2 was taken as the solution of

$$E(X_2) = E_{min} = .1\ mc^2$$

and a was defined as

$$a = \text{Min } (X_1, X_2), \tag{61}$$

which is just to say that an electron is followed until it either has energy

less than .1 mc^2 or it passes through the slab.

$\phi_k \frac{dk}{E_o - \mu}$ was taken from Heitler[22]. The non-relativistic approximation and the extreme relativistic approximation with complete screening (Thomas-Fermi model) were used with the change over at $E = mc^2$. The calculations were repeated for total photon energy radiated, putting $k\phi_k$ for ϕ_k.

The number, N, of Bremsstrahlung photons coming through an aluminum shield of thickness X_1 = .25, .688, and 2.5 gms/cm^2 per incident fast electron is plotted in Figures 64 through 66 as is the energy radiated per incident fast electron, both as a function of incident energy.

The average photon energy as a function of incident energy appears in Figure 67. It may be noted that the shielding is not very effective against the X-rays, and the number of photons per incident electron as a function of shielding thickness with incident energy as a parameter is plotted in Figure 68.

The results indicate that photon energies of about an MeV are typical and that below 2.5 gms/cm^2 of aluminum less than one photon per incident electron is produced. There is a tendency for the number of photons to increase with shielding thickness up to a certain thickness for electrons of a given energy (i.e., thickness 1.6 gm/cm^2 at E_o = 2 MeV) and to decrease thereafter.

The nature of these results appears to rule out Bremsstrahlung as a major contribution, particularly when we consider the results of the Van de Graff simulation of the OGO II environment by Reed et al.[19] On bombardment of the photometer by 2.6 MeV electrons the dark current is observed to decrease exponentially with the shielding thickness (their Figure 8). If Bremsstrahlung were the major contribution an initial dark current increase would occur according to Figure 68. Thus fast electrons and protons which penetrate the shielding are the likely cause of the observed noise.

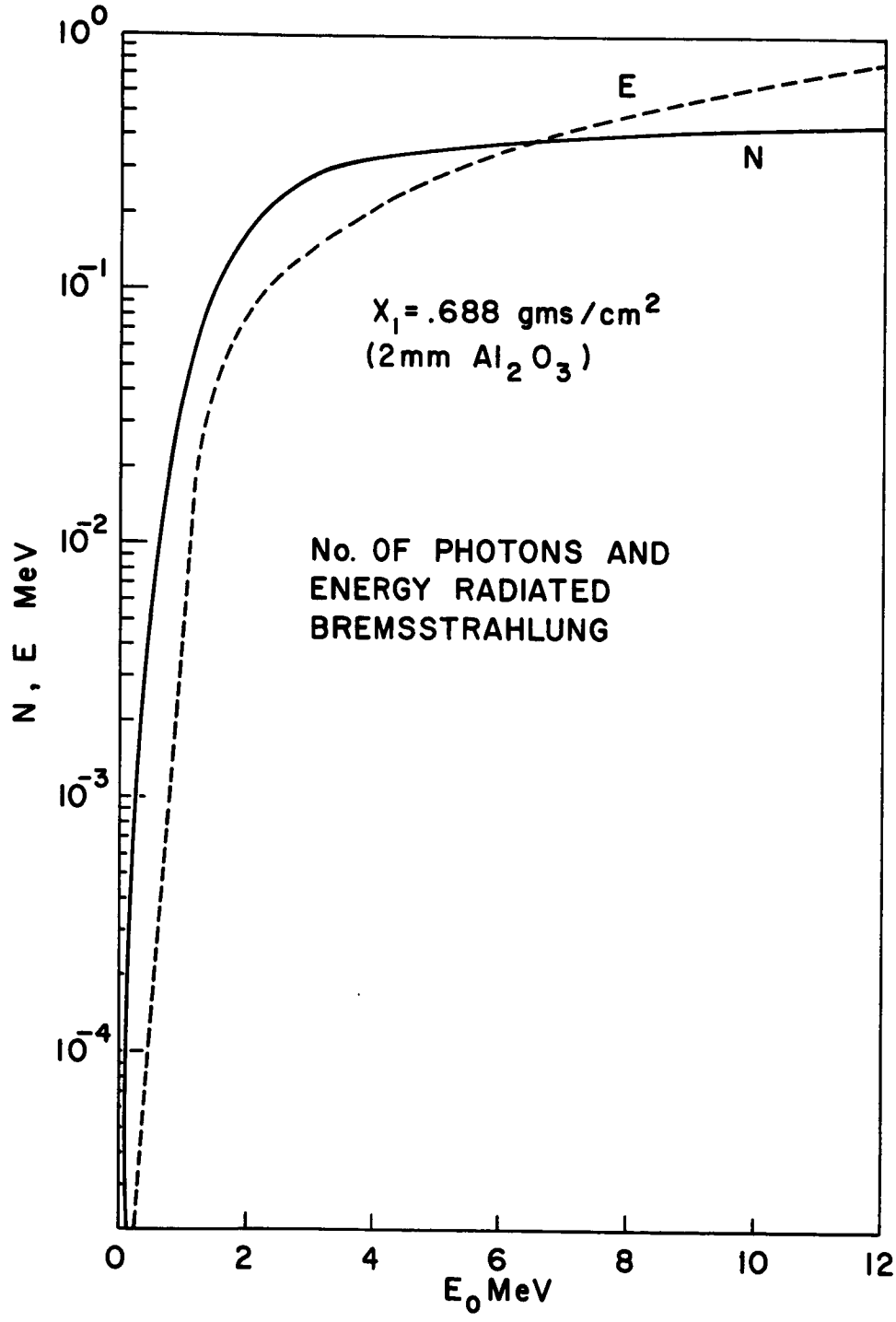

FIGURE 64: No. of Photons and Energy Radiated Bremsstrahlung

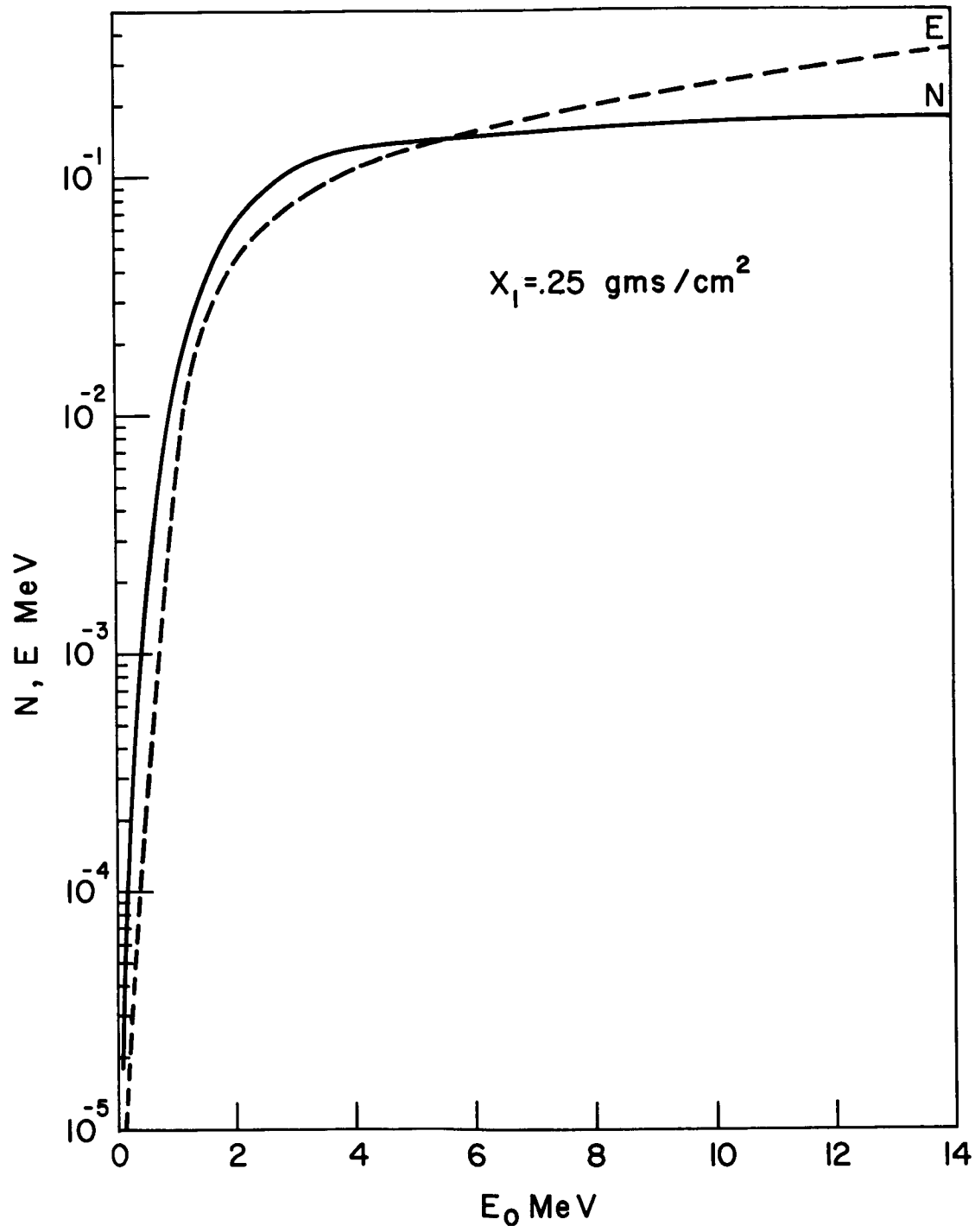

FIGURE 65: X_1 = .25 gms/cm^2

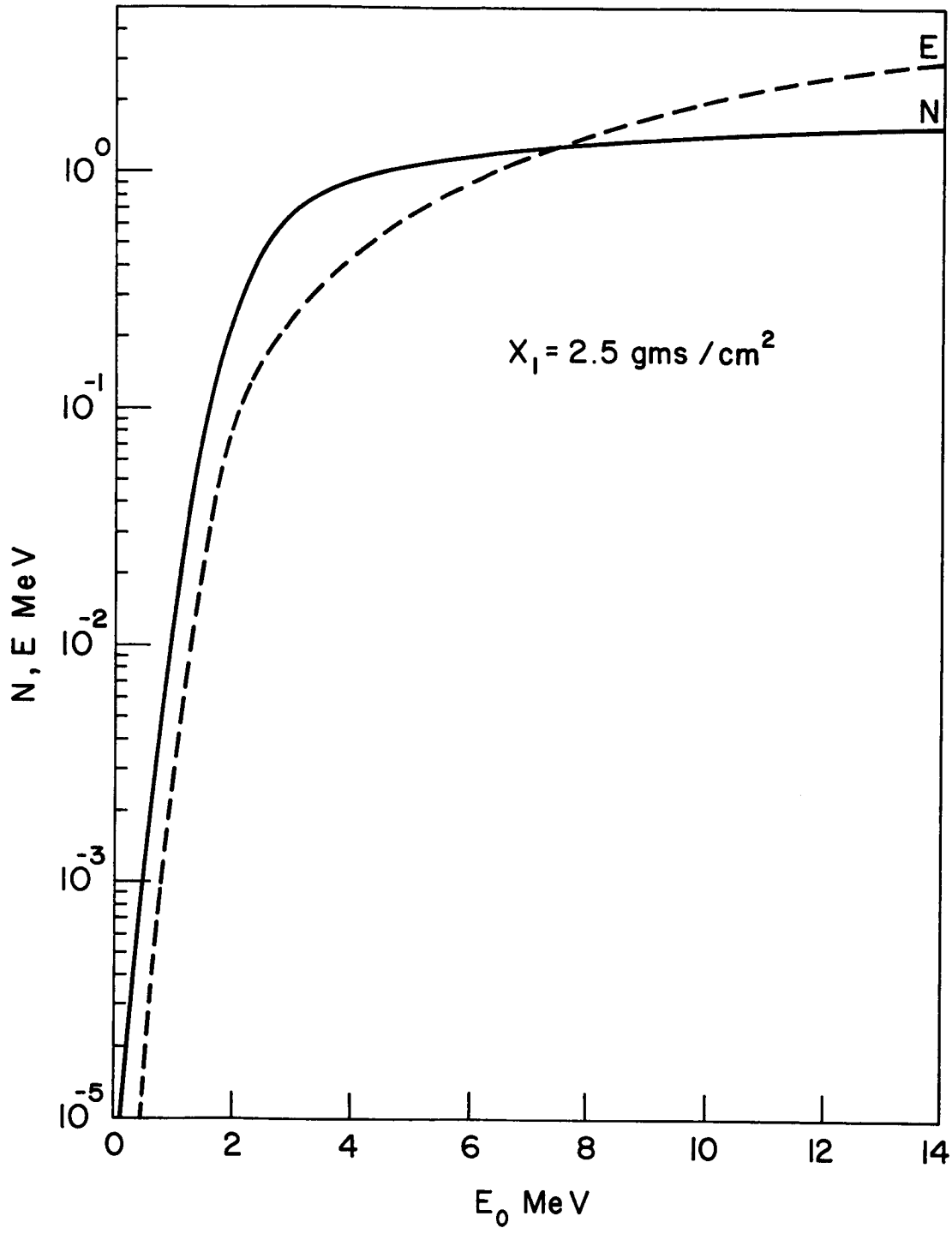

FIGURE 66: X_1 = 2.5 gms/cm^2

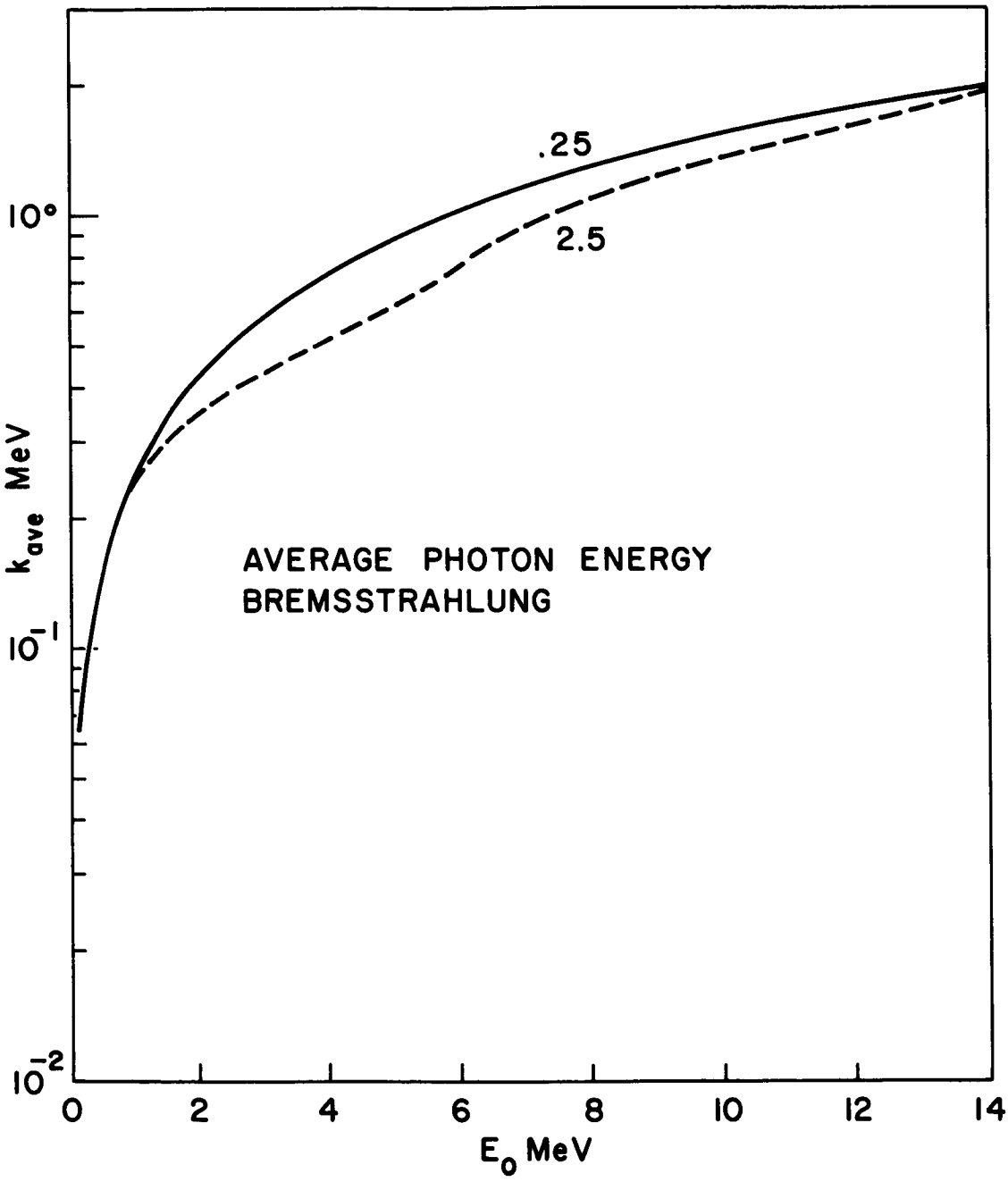

FIGURE 67: Average Photon Energy Bremsstrahlung

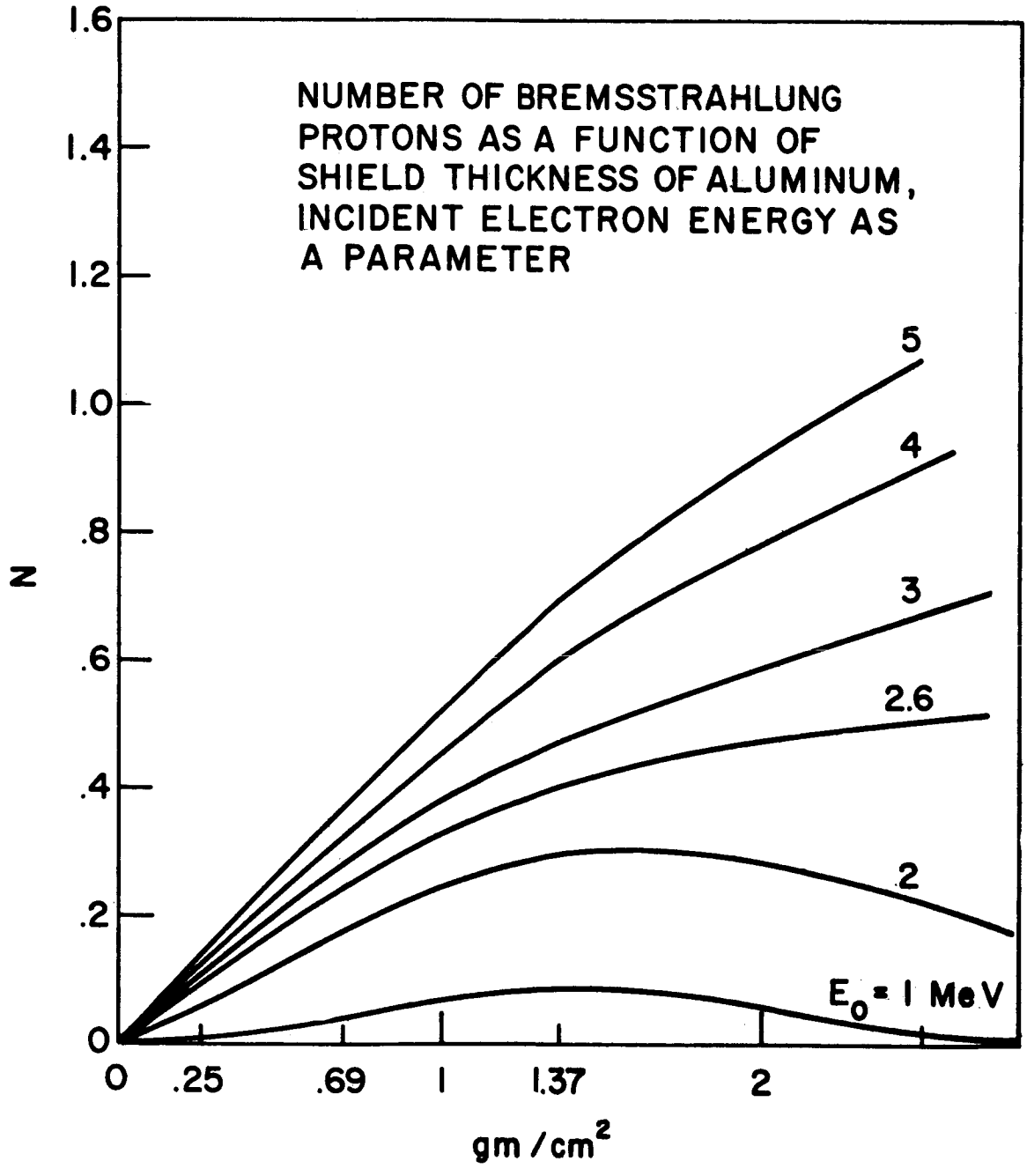

FIGURE 68: Number of Bremsstrahlung Protons as a Function of Shield Thickness of Aluminum, Incident Electron Energy as a Parameter

3. Cerenkov Radiation

A. T. Young[23] has studied the noise due to Cerenkov pulses in an end-on photomultiplier caused by the muon component of cosmic rays traversing the face plate. He reports a minimum of about 50 photoelectrons for each Cerenkov pulse. Thus, the Cerenkov radiation caused by fast electrons in the face plate might have been a major factor in the photometer noise observed in the OGO photometer.

Moreover, the experiments of the NASA group clearly established that the photocathode and the first few dynodes were the sensitive element. C. Wolf [28] finds the radiation induced noise proportional to cathode area and concludes that either the lens elements or the photocathode was the sensitive element. NASA experiments failed to detect luminescence of the optics.

The rate of Cerenkov radiation per unit path length in the wavelength band $(\omega, \omega + d\omega)$ is given (e.g. Schliff[24]) by

$$\frac{dE}{dx} = \frac{e^2}{c^2}\left(1 - \frac{1}{n_r^2\beta^2}\right)\omega d\omega \tag{62}$$

where n_r = refraction index
ω = angular frequency
$\beta = v/c$
v is electron velocity
c is light velocity

If N is the average number of photons produced at frequency ω

$$\frac{dN}{dx} = \frac{1}{\bar{h}\omega}\frac{dE}{dx} \tag{63}$$

where $\bar{h} = \frac{6.62 \times 10^{-27}}{2\pi}$ erg. sec.

Equations (62) and (63) give

$$\frac{dN}{dx} = \frac{2\pi e^2}{\bar{h}c}\left(1 - \frac{1}{n_r^2\beta^2}\right)\Delta\nu_{12} \text{ photons/incident electron} \qquad (64)$$

where $\Delta\nu_{12} = \frac{1}{\lambda_1} - \frac{1}{\lambda_2}$, and

$\lambda_{1,2}$ is the wavelength at angular frequency, $\omega_{1,2}$.

For a single electron incident on the photomultiplier window at energy E_o the total number of photons generated would be

$$N = \frac{2\pi\,\Delta\nu_{12}}{137}\int_{E_{min}}^{E_o}\left(1 - \frac{1}{n_r^2\beta^2(E)}\right)\frac{dx(E)}{dE}\,dE \qquad (65)$$

Of course, $\frac{E_{min}}{mc^2} = \sqrt{1 + \frac{1}{n_r^2 - 1}} - 1$,

$$\beta^2 = \frac{t(t+2)}{(t+1)^2},$$

where $t = E/mc^2$,

and we have put $e^2/\bar{h}c = 1/137$.

In evaluating (65) the relation between x and energy E(x) would be the same as in the section on Bremsstrahlung. Then, to find the total number of Cerenkov photons produced in the Van Allen belts it is necessary to average over the electron energy distribution and over-all photocathode window orientations.

The computation can be simplified somewhat. In Figure 69 the factor $1 - 1/n_r^2\beta^2$ appearing in Equation (65) is plotted for sapphire (n_r = 1.796 at

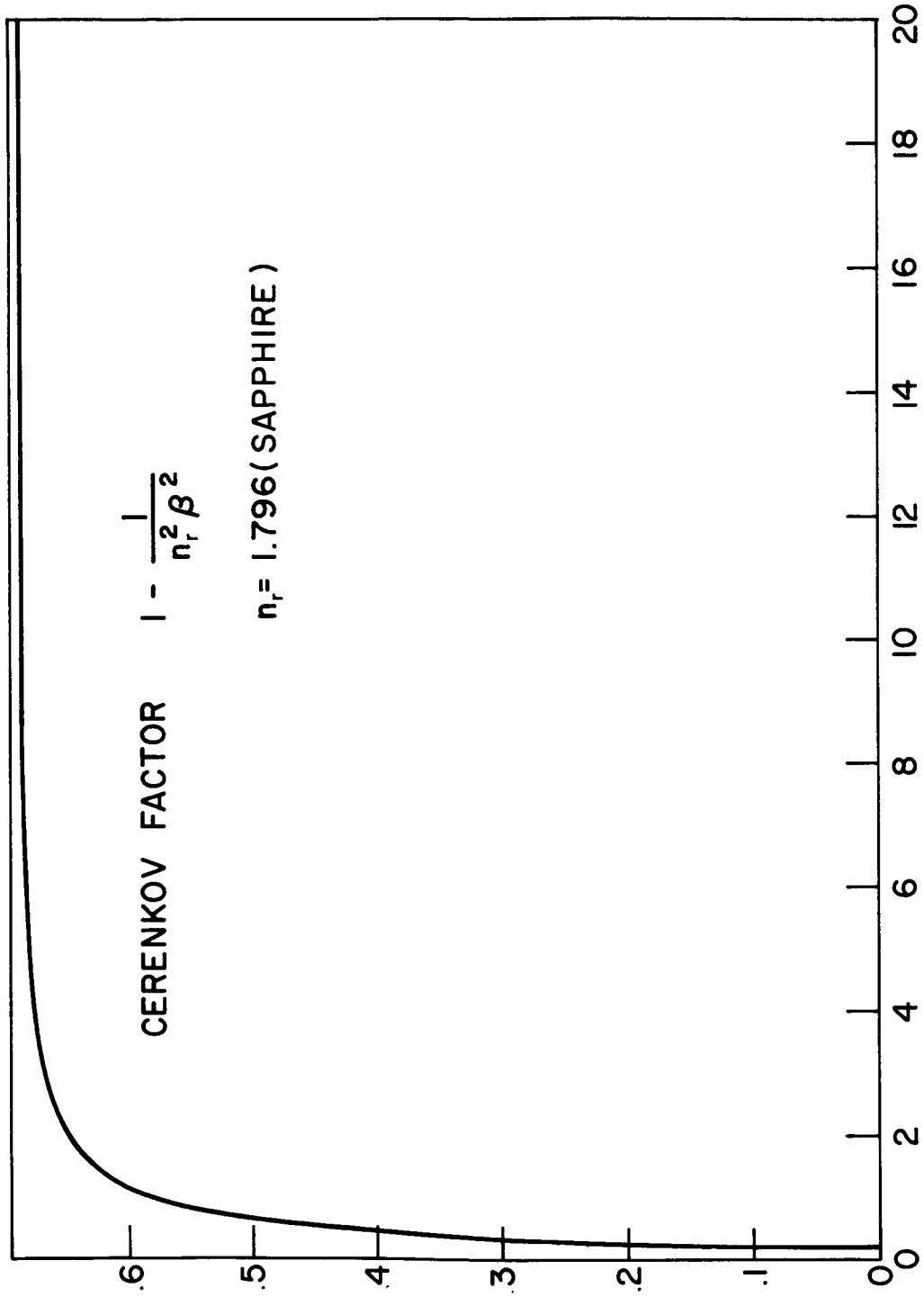

FIGURE 69: Cerenkov Factor

5000 Angstroms) and noted to rise rapidly from zero at $E_{min} \approx .204\ mc^2$, reaching almost its asymptotic value at $E = 2mc^2$ (1 MeV). We therefore approximate this factor as zero below E_{min} and constant thereafter. Then, (65) becomes,

$$N \approx \frac{2\pi\Delta\nu_{12}}{137}\left(1 - \frac{1}{2n_f}\right)\ell_{ave}, \tag{66}$$

where ℓ_{ave} must now be suitably chosen.

If the photocathode window thickness is ℓ and its radius R_c, the thickness (path length) averaged overall orientations is found to be,

$$\ell_{ave} = \frac{2\ell}{\pi\sqrt{1+c^2}} \ln \frac{\left(\sqrt{1+c^2}+1-c\right)\left(\sqrt{1+c^2}+c\right)}{\left(\sqrt{1+c^2}-1+c\right)\left(\sqrt{1+c^2}-c\right)}, \tag{67}$$

where $c = \frac{2\ell}{\pi R_c}$.

If ℓ = 2 millimeters and R_c= 1/2 in., ℓ_{ave} = .392 cm. = 1.73 gm/cm^2 (sapphire with density 3.50 gms/cm^3).

In the radiation belts electron energy distributions seem to fit a relation like

$$\frac{d\phi}{dE} = a\phi_o e^{-aE} \text{ electrons/cm}^2 \text{ sec. MeV} \tag{68}$$

We are thus led to put for ℓ_{ave} in Equation (66) something like,

$$L_{ave} = \frac{\int_{E_{min}}^{\infty} e^{-aE} X(E)\,dE}{\int_{E_{min}}^{\infty} e^{-aE}\,dE} \tag{69}$$

X(E) is taken as in Equation (58) as,

$$X(E) = .412\ E^{1.181}\ gm/cm^2,\ E \leq 2.5\ MeV \tag{70}$$

$$= .530\ E - .106\ gm/cm^2,\ \text{otherwise.}$$

To Equation (70) we further add the restriction that,

$$X(E) \leq \ell_{ave}, \tag{71}$$

where ℓ_{ave} comes from Equation (67). Then Equation (69) becomes

$$L_{ave} = \frac{\int_{E_{min}}^{E_{max}} e^{-aE} X(E)\,dE + \int_{E_{max}}^{\infty} e^{-aE} \ell_{ave}\,dE}{\int_{E_{min}}^{\infty} e^{-aE}\,dE} \tag{72}$$

E_{max} is found using $\ell_{ave} = 1.73\ gm/cm^2$ in (70) as, $E_{max} = 2.79$ MeV, a result which suggests that we can as well use only the first of Equation (70) in (72) and obtain,

$$L_{ave} = \frac{a^{-\alpha}\left\{\gamma(\alpha,\ aE_{max}) - \gamma(\alpha,\ aE_{min})\right\}}{\dfrac{\ell_{ave}}{a} e^{-aE_{max}}} \qquad (73)$$
$$\frac{1}{a} e^{-aE_{min}}$$

where $\alpha = 2.181$ and $\gamma(\alpha, X)$ is an incomplete gamma function.

Vette[25] has published a model for the inner and outer belt electrons. From his Figure 36 (page 20), which we reproduce as Figure 70, we find that at the peak of the inner belt the integral omnidirectional flux is,

$$\phi(>E) = 2.8 \times 10^{8}\ e^{-1.035E} \text{ per cm}^2 \text{ sec.}$$

Thus, a = 1.035, and we find after evaluating the gamma functions

$$L_{ave} = 16.74 \times 10^{-2} \text{gm/cm}^2$$

$$= 4.784 \times 10^{-2} \text{cm,}$$

and the average path length is less than 1/2 millimeter.

The minimum amount of shielding around OGO II main body photometer was about 60 mils or .4 gm/cm^2 (cf., their Figure 3). Thus, from Figure 71, range of electrons in aluminum, they are shielded for about 1 MeV electrons. From Figure 70 (Vette's AE-2 environment) at L = 1.25 there are about $\phi = 10^8$ electrons/cm^{2}sec. of energy greater than 1 MeV. If A is the projected cathode area,

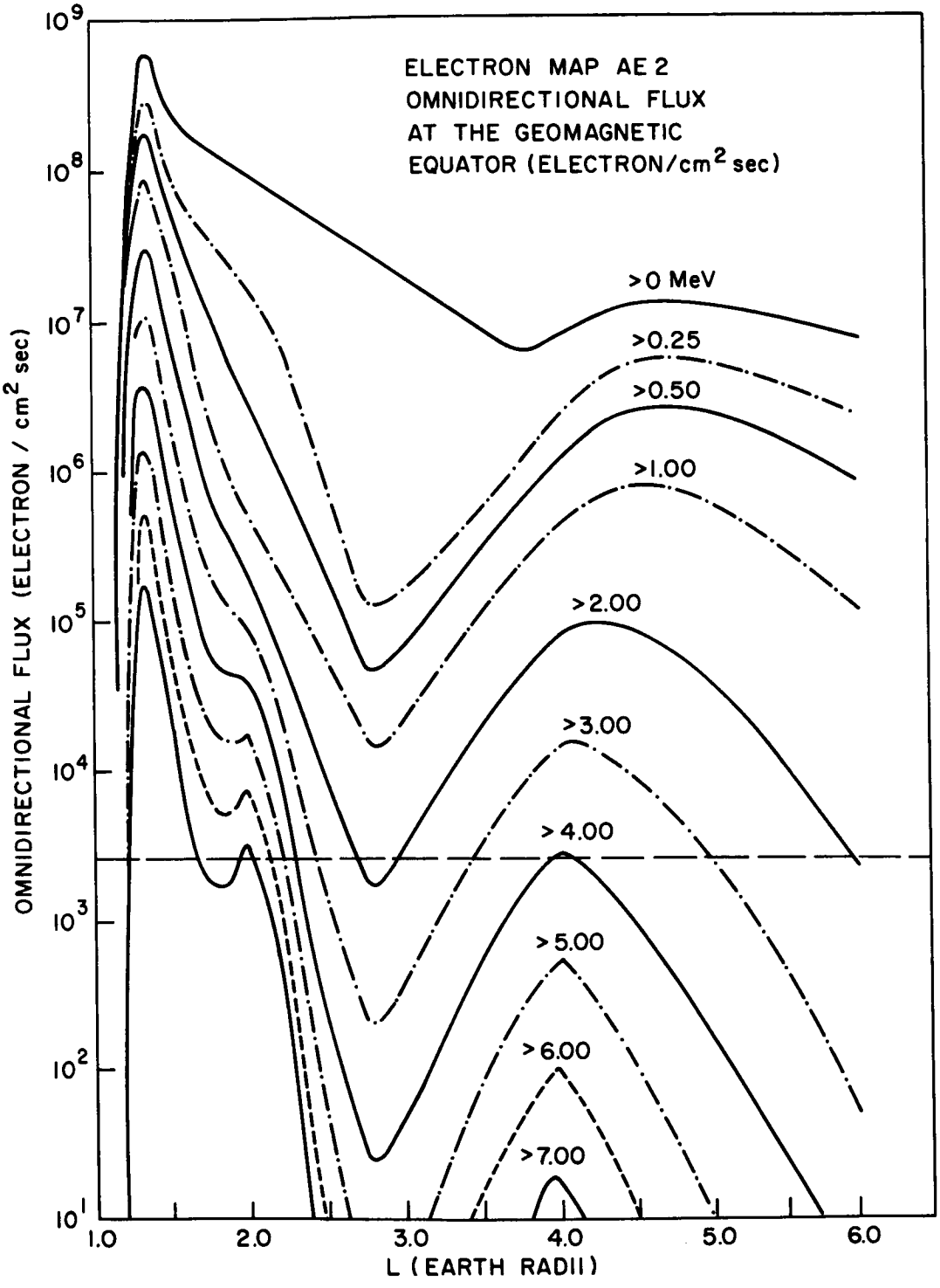

FIGURE 70: Electron Map AE2 Omnidirectional Flux at the Geomagnetic Equator (Electron/cm^2 sec)

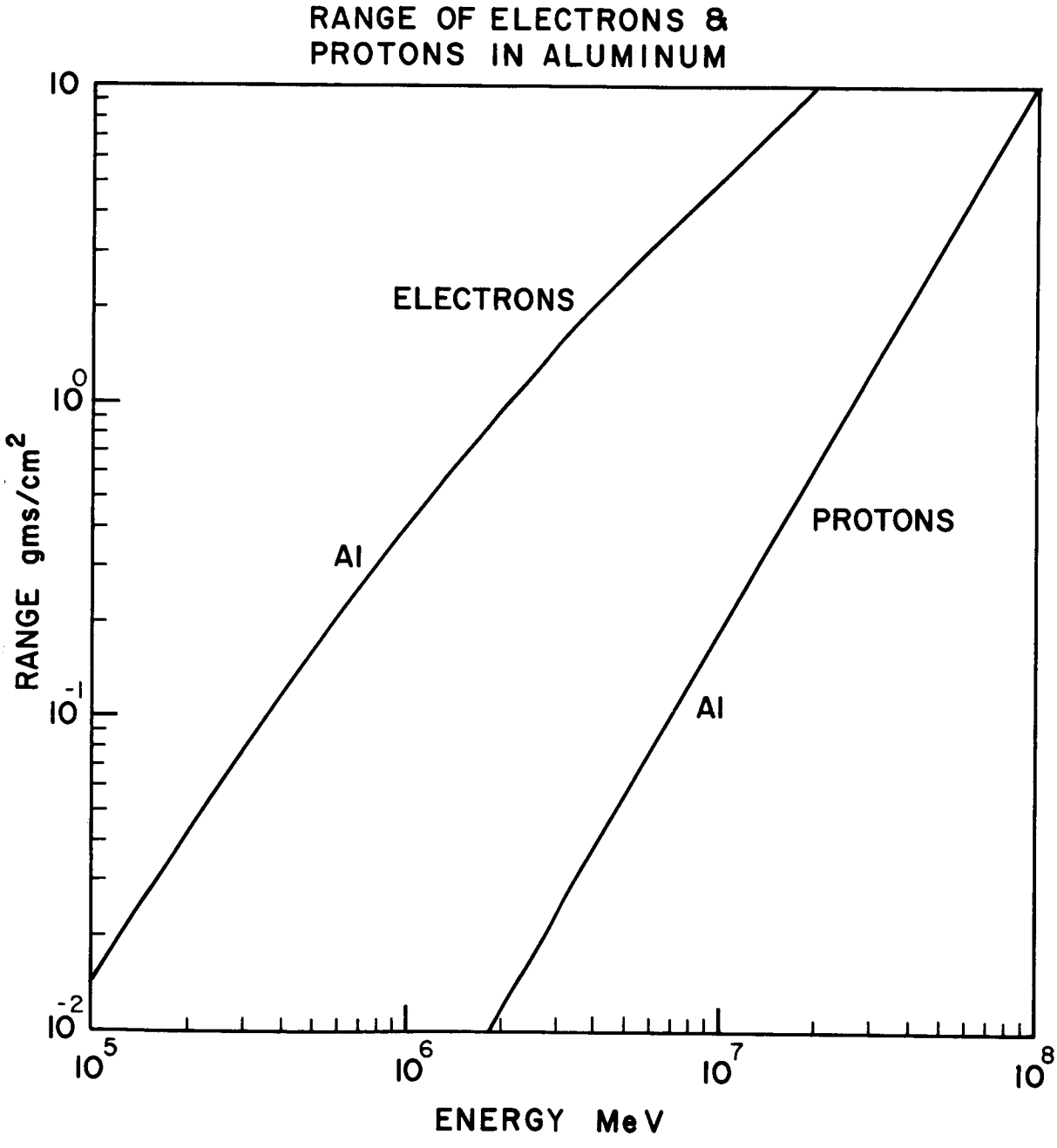

FIGURE 71: Range of Electrons and Protons in Aluminum

$$A = \frac{\pi R_c^2}{2}.$$

The Cerenkov wave fronts travel in the electron direction. Thus, only photons from electrons traveling toward the photocathode in the face plate cause photo-events.

The quantum efficiency, ϵ_q, of the 541E - 05M over the wavelength band 1500 to 5000 Angstroms is about 20% (see Figure 72). Then the number of expected photoelectrons per second due to Cerenkov radiation in the inner belt would be

$$N_c = \phi_o \frac{\pi R_c^2}{4} \epsilon_q \frac{2\pi\nu_{12}}{137} \left(1 - \frac{1}{n_r^2}\right) \ell_{ave} \qquad (75)$$

Taking λ_1 = 1500 Angstroms, λ_2 = 5000 Angstroms, we have with $\phi_o = 10^8$, R = 1.27, ϵ_q = .2, n_r = 1.796, ℓ_{ave} = .0478

$$N_c = 1.78 \times 10^9/\text{sec}$$

A photocathode current of 3.3×10^{-9} ampere or $2.06 \times 10^{+10}$ electrons per second was observed. We conclude the Cerenkov radiation fails by about a factor 10 to explain the noise.

4. Shielding the Photocathode

If we are satisfied that the photomultiplier can be shielded from the radiation belts and the work of the NASA group on OGO II indicates this to be true. The amount of shielding necessary to reduce the noise to a tolerable level can be straightforwardly estimated. We shall wish to detect stars of magnitude $3^m.5$ against the background noise due to all sources. From the work of Code[26] we can estimate the number, n_o, of photons per second per square centimeter incident on the earth's atmosphere from Vega (type A0, $0^m.0$). This is,

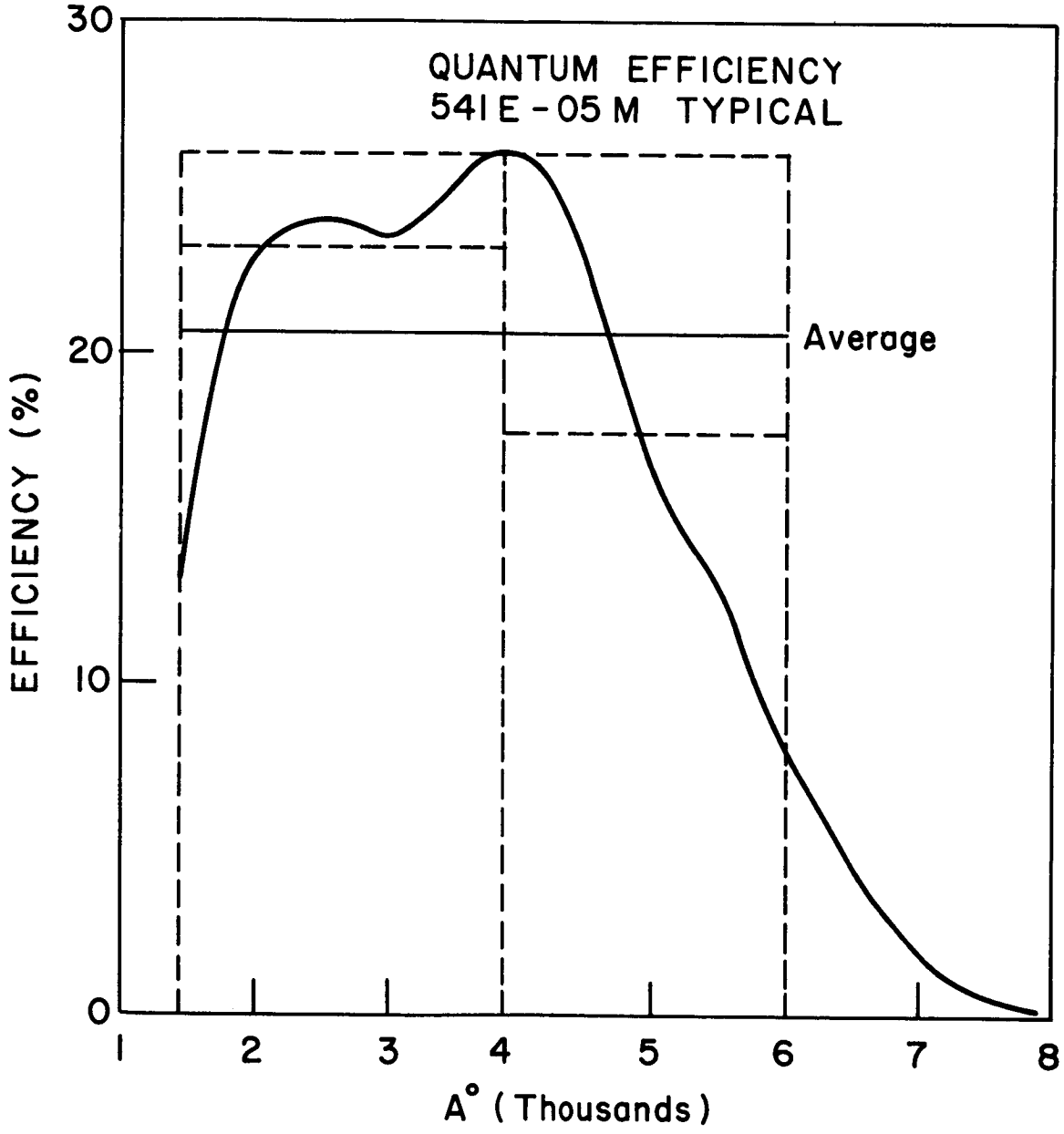

FIGURE 72: Quantum Efficiency
541E-05M Typical

$n_o = 1.66 \times 10^7/cm^2 sec.$ micron, at the center of the Johnson B filter (4300 Angstroms).

Then the number of resulting photoelectrons per second from a sensor with optical aperture, D, optical efficiency, ϵ_o, photomultiplier quantum efficiency, ϵ_q, and band pass, $\Delta\lambda$, which views a star of magnitude M_B, is about

$$S = n_o \, 10^{-.4M_B} \frac{\pi}{4} D^2 \epsilon_o \epsilon_q \Delta\lambda \tag{77}$$

If the faint star background is N tenth magnitude stars per square degree and S_A is the slit area in square degrees, the signal due to this source is

$$N_B = n_o \, N \, 10^{-4} \frac{\pi}{4} D^2 \epsilon_o \epsilon_q S_A \Delta\lambda \tag{78}$$

A reasonable aperture is about 2 inches. Choose $\epsilon_o = .5$, $\epsilon_q = .2$, $\Delta\lambda = .3$ micron, $M_B = 3.5$, $N = 320$, $S_A = .3$ square degree. Then

$$S = 4.02 \times 10^5/sec \tag{79}$$

$$N_B = 2.42 \times 10^4/sec$$

In the absence of radiation noise the faint star background is the major source of noise, even so the DC signal due to it is less than the star signal by a factor 17. Therefore, we neglect it altogether.

The NASA group observed a dark current of 2.06×10^{10} electrons per second and were shielded for about an MeV. Above an MeV at the equator in the inner belt are about 10^8 electrons/sec cm^2. If each fast electron incident on the photocathode produced k photo-events,

$$2.06 \times 10^{10} \approx \frac{\pi}{2} R_c^2 \, k \times 10^8, \tag{80}$$

and since $R_c = 1.27$ centimeters, $k \approx 80$.

5. Allowable Noise

Consider the situation of Figure 73. Some random process f(t) acting on the sensor causes an output,

$$I(t) = \sum_{k=-\infty}^{\infty} a_k \, p(t - t_k), \tag{81}$$

where p(t) describes the individual pulse shapes at the photomultiplier output and a_k their amplitude. Let a_k be a random variable. I(t) is fed to the input of a filter with impulse response h(t). The filter output will be

$$I_o(t) = \sum_{k=-\infty}^{\infty} a_k \int_{-\infty}^{\infty} p(t - \tau - t_k) h(\tau) d\tau \tag{82}$$

By Campbell's Theorem[27] the variance of I_o will be

$$\sigma^2 = \nu \, \overline{a^2} \int_{-\infty}^{\infty} \left[\int_{-\infty}^{\infty} p(\tau' - \tau) h(\tau) \, d\tau \right]^2 d\tau' \tag{83}$$

where ν is the rate at which photo-events occur and $\overline{a^2}$ is the second moment of a_k.

Since the filter response will be much slower than the photomultiplier we can just as well take p(t) as the delta function. Then upon integrating over τ,

$$\sigma^2 = \nu \, \overline{a^2} \int_{-\infty}^{\infty} h^2(\tau') d\tau' \tag{84}$$

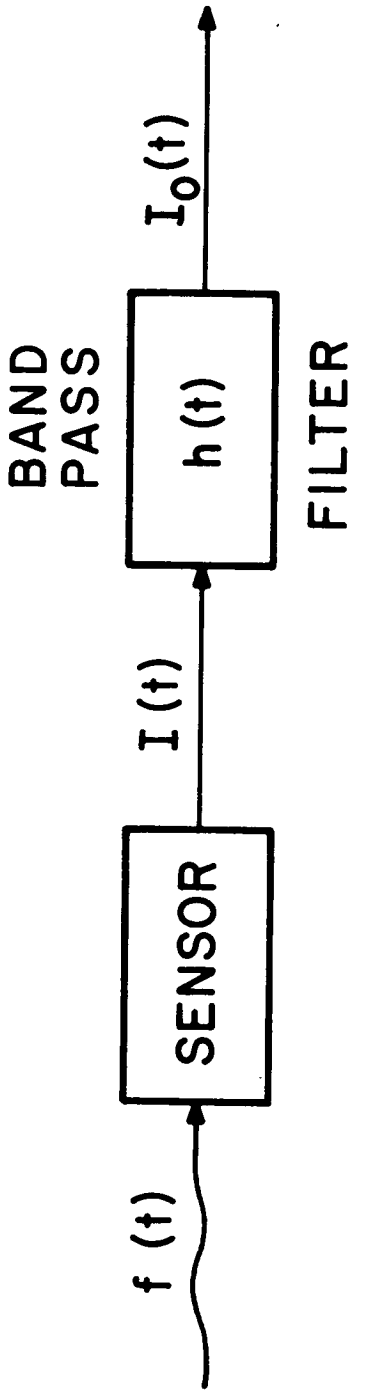

FIGURE 73: Star Signal Flow Diagram

$$= \nu \overline{a^2} \int_{-\infty}^{+\infty} |H(f)|^2 df$$

Finally,

$$\sigma^2 = 2\nu \overline{a^2} \Delta f, \tag{85}$$

where,

$$\Delta f = \int_0^\infty |H(f)|^2 df \qquad \text{is the filter noise bandwidth.}$$

To proceed, further knowledge of the distribution of the a_k is needed. Lacking this knowledge, we assume a normal distribution with mean $\bar{a} = k$. Then

$$\overline{a^2} = k + k^2 \approx k^2 \tag{86}$$

Then if particle radiation noise dominates with photoevents due to this occurring at a rate N_p per second and mean magnitude k, the peak signal to RMS noise is

$$F = \frac{S}{\sqrt{2(S + k^2 N_p)\Delta f}} \tag{87}$$

(Note that $\overline{a^2} = 1$ for signal photoelectrons.)

Accurate location of a star position at a signal to noise ratio of 5 is reasonable. Thus, take F = 5. A 0.1 degree slit rotating at 15 rpm transits a star in a time,

$$T_s = \frac{.1 \times 15}{360} \text{ second} \tag{88}$$

The optimum electrical bandwidth is about

$$\Delta f = \frac{1}{3T_s} = 80 \text{ cps.}$$

One can solve for N_p from (87) with the result that

$$N_p = 6.25 \times 10^3 \frac{\text{fast electrons}}{\text{second}}$$

The average projected area of the photocathode being half its total area, the allowable Van Allen belt flux becomes

$$\phi = 2.47 \times 10^3/\text{sec cm}^2 \tag{89}$$

A dotted horizontal line which corresponds to this flux has been drawn in Figure 70. We see that unless we shield against at least five MeV, operation with an end-on tri-alkali photocathode is not possible through much of the belt. Since disturbed sun conditions may increase the outer belt radiation by factors of about 10^2, shielding the photocathode and first dynode stages for seven MeV seems indicated. If the radiation environment were Vette's AE-2, Figure 70 indicates we would still be inoperative between 1.2 and 2.0 Earth radii. This would require one gram/centimeter^2 about the neck of the sensor and amounts to a centimeter thickness of aluminum.

6. Luminescence

The NASA group[19] tested the luminescence of various window materials on irradiation with 50 KeV electrons from an electron microscope and by a millicurie strontium 90 source. We will use the data from each experiment, in turn testing whether luminescence of the cathode window material caused by

fast electrons can account for the OGO II results.

According to Heitler[29] in the region where the dominant loss mechanism for fast particles in matter is by collisions, the average energy loss is "very nearly proportional" to the number of primary ion pairs formed. The ratio of ionizations to excitations and the average energy transfer per ion pair are nearly independent of primary energy. About one primary ion pair is formed for each 32eV of energy loss practically independent of the particle type. Of course primary ions (or electrons) subsequently produce secondaries.

Mott and Gurney[30] discuss the production of luminescence in solids. In speaking of irradiation with α and β rays (presumably at moderate energies) they observe that most of the energy dissipation is by production of electron-hole pairs which subsequently recombine at impurity centers, Frenkel and Schottky defects, or at the surface where they either transfer their energy to the lattice atoms or radiate on recombining. A discussion of the mechanisms by which electrons and holes lose their excess energy is given.

The assumption, which the preceding few paragraphs are used to justify, is that the radiance per incident particle is proportional to its energy loss.

7. Electron Microscope Data

On irradiation of sapphire with 50 KeV electrons at 10^8 per cm^2 sec, radiance of 10^{-4} ergs/sec cm^2 steradian was observed in the band 3500 to 4100 Angstroms. That is per 50 KeV electron an energy,

$$E \approx \frac{\pi}{2} \times 10^{-14} \text{ ergs/}\mathring{A} \tag{90}$$

was radiated into 2π steradians in the visible and ultra-violet.

We assume that the main body photometer was shielded for 1 MeV and that

the energy distribution of electrons in the inner belt is given by Equation (68) and the environment is Vette's AE-2. This neglects belt decay as indeed we have previously done.

The average energy above an MeV is,

$$1 + \frac{1}{a}\ \text{MeV} = 1 + \frac{1}{1.035}\ \text{MeV}$$

Of this on the average an MeV is lost in the shielding so that the average energy of electrons incident on the photometer cathode window was about

$$E_{ave} \approx 1/1.035\ \text{MeV} \tag{91}$$

Over the wavelength band 1500 to 6000 Angstroms the 541E-05M typically has a quantum efficiency ϵ_q of about 20%. Mid-band wavelength, λ_{ave}, is 3750 Angstroms and bandwidth is 3500 Angstroms. The density of electrons above an MeV is again taken as 10^8/sec cm^2. Then the expected number of photo-electrons per second is,

$$n_{pe} = \frac{\pi}{2} R_c^2\ \phi_o E\ \frac{E_{ave}}{5 \times 10^{-2}}\ E_q\ \frac{\lambda_{ave}}{hc}\ \Delta\lambda \tag{92}$$

Using (90) and (91) in (92) with the data of the previous paragraph,

$$n_{pe} \approx 2/3 \times 10^{10}/\text{sec} \tag{93}$$

This is within a factor 3 of the observed photocurrent.

8. Strontium 90 Irradiation

In order to evaluate the effect of strontium 90 irradiation, a NASA group[19] placed a millicurie strontium 90 source one-quarter inch square in

contact with various samples of window material. Within the wavelength band 1800 to 6300 Angstroms the radiance from the sapphire sample was 3.8 x 10^{-10} watts/cm^2 steradian. Strontium 90 with a half life of 25 years has a daughter, Y^{90}, with a half life of 65 hours. Thus, the strontium 90 is in equilibrium with its daughter. The maximum β energy of the strontium 90 is .545 MeV, that of the Y^{90} is 2.26 MeV. There is also 1.74 MeV gamma radiation at a rate of 6 x 10^2/sec cm^2 which will be neglected. There will be 2 x 3.71 x 10^7 decay events/sec, but only half of these would result in β rays through the sapphire.

In his discussion of β decay, Fermi[31] gives for the probability that the emitted electron has momentum in p, p + dp,

$$P(p)dp = \text{Const.} \left(\sqrt{1 + \eta_o^2} - \sqrt{1 + \eta^2} \right)^2 \eta^2 d\eta$$

where,

$$\eta = \frac{p}{mc} = \sqrt{\frac{2E}{mc^2}} ,$$

and

$$\eta_o = \frac{P_{max}}{mc} .$$

The average energy carried away by a β particle will be,

$$E_{ave} = \frac{\int_o^{P_{max}} P(p) \frac{p^2}{2m} dp}{\int_o^{P_{max}} P(p) dp} \qquad (94)$$

The integral in the denominator of (94) is given by Fermi[30] in terms of a function $F(\eta_o)$.

$$F(\eta_o) = -\frac{\eta_o}{4} - \frac{\eta_o^3}{12} - \frac{\eta_o^5}{30} + \frac{\sqrt{1+\eta_o^2}}{4} \sinh^{-1}\eta_o \tag{95}$$

Defining,

$$E(\eta_o) = \int_0^{\eta_o} \left(\sqrt{1+\eta_o^2} - \sqrt{1+\eta^2}\right)^2 \eta^4 d\eta$$

$$= \frac{\eta_o}{8} + \frac{\eta_o^3}{24} - \frac{\eta_o^5}{60} + \frac{\eta_o^7}{105} - \frac{\sqrt{1+\eta_o^2}}{8} \sinh^{-1}\eta_o, \tag{96}$$

$$E_{ave} = \frac{mc^2}{2} \frac{E(\eta_o)}{F(\eta_o)} \tag{97}$$

Using Equations (95) through (97) we find

$$E_{ave}\ (.545\ \text{MeV}) = .087\ \text{MeV}$$

$$E_{ave}\ (2.26\ \text{MeV}) = .675\ \text{MeV} \tag{98}$$

There is a Cerenkov component in the radiance measured by the NASA group. Most of this is from the Y^{90} decay. The amount of this will first be estimated assuming a mono-energetic beam of energy given by (98). This is equivalent to neglecting the energy dependence of β in Equation (62) and the contribution of the strontium 90.

The Cerenkov radiation per electron will be from (62)

$$E_c \approx 2\pi^2 e^2 \left(1 - \frac{1}{n_r^2}\right)\left(\frac{1}{\lambda_1^2} - \frac{1}{\lambda_2^2}\right)\ell_{ave} \tag{99}$$

Below .204 MeV the Cerenkov radiation in sapphire ceases. The range of 2 MeV electron is about .04 gm/cm^2. That of .675 MeV electron about .250 gm/cm^2. Thus, we will use an average path length for Cerenkov radiation of .210 gm/cm^2 or (using a density of 3.5 gm/cm^3)

$$\ell_{ave} = .06 \text{ cm} \tag{100}$$

Using (100), $n_r = 1.796$, $\lambda_1 = 1800$ Angstroms, $\lambda_2 = 6300$ Angstroms, $e = 4.830 \times 10^{-10}$ e.s.u.

$$E_c = 5.34 \times 10^{-10} \text{ erg/electron} \tag{101}$$

The number of electrons emitted per cm^2 per second per steradian is,

$$n_e = \frac{3.71 \times 10^7}{\left(\frac{2.54}{4}\right)^2 \times 4\pi} = 7.32 \times 10^6/\text{cm}^2 \text{ second steradian} \tag{102}$$

The product of (101) and (102) is the estimate of the amount of observed light from the sapphire due to the Cerenkov component. This is,

$$I_c = 3.91 \times 10^{-3} \frac{\text{ergs}}{\text{sec cm}^2 \text{ steradian}}, \tag{103}$$

an amount sufficient in itself to account for the NASA observation.

Nonetheless, some of the observed light must have been due to scintillation. Let us use the electron microscope data to estimate this component. There we had that an amount of energy,

$$E_{e\nu} = \frac{\pi}{1.5} \times 10^{-19} \frac{\text{ergs}}{\overset{\circ}{\text{A}}\ \text{eV}} ,$$

was due to luminescence. Therefore, with .675 MeV electron in the wavelength band 1800 to 6300 Angstroms we would have

$$E_e = \frac{\pi}{1.5} \times 10^{-19} \times 3.5 \times 10^{3} \times .675 \times 10^{6} \tag{104}$$

$$= 4.95 \times 10^{-10} \text{ ergs/electron}$$

This is almost the same as the Cerenkov component of Equation (101). Let us assume that the relative amounts of Cerenkov radiation and luminescense occurring in the strontium 90 experiment are given by (101) and (104). There we had that,

$$3.71 \times 10^{7}/(2.54/4)^2 \frac{.675 \text{ MeV electrons}}{\text{cm}^2 \text{ sec}}$$

$$= 4\pi \times \frac{.675}{.675 + .087} \times \frac{.495}{4.95 + 5.34} \times 3.8 \times 10^{-3} \text{ ergs/cm}^2 \text{ sec}$$

Where we use only the Y^{90} β particles in the computation; the energy radiated in luminescence is about,

$$E_e = 2.21 \times 10^{-10} \text{ ergs/.675 MeV electron}$$

The expected number of photo-events due to luminescence of the NASA photometer cathode window in the AE-2 environment would be,

$$n_{pe} = \phi \frac{\pi R_c^2}{2} E_e \frac{E_{ave}}{.675} \epsilon_q \frac{\lambda_{ave}}{hc}$$

Using R = 1.27 cm, ϵ_q = .2, λ_{ave} = 4050 Angstroms, E_{ave} = 1/1.035 MeV and $\phi_o = 10^8/cm^2$ sec,

$$n_{pe} \approx 3.27 \times 10^9/sec \qquad (105)$$

This is within a factor six of the observed rate.

Using the electron microscope data we came within a factor three of the observed rate, and Cerenkov radiation came within a factor eleven. Considering the crudeness of the calculations, we perhaps have no right to expect better agreement. Nonetheless, none of these mechanisms has really accounted for all the observed noise. And since the belt decay was neglected, the discrepancy appears even greater.

It is likely that luminescence from the tube walls near the photocathode and scintillation of the tri-alkali itself are needed to fully explain all the noise, but it seems likely that fast electrons penetrating the shielding can account for most of the dark current increase observed on the OGO II main body airglow photometer.

The proton component has not been included. Shielding for MeV electrons also shields for 15 MeV protons (cf. Figure 71). Above 15 MeV Vette's HP 1-4[32] environment gives about 3 x 10^4 protons/cm^2 sec at 1.3 - 1.4 earth radii. This is orders of magnitude less than the electron density at the same place.

9. Shielding Requirement of S^3

If an end-on tube on photomultiplier of the 541E-05M type is used, a centimeter of aluminum seems needed to insure that $3^m.5$ magnitude stars are

detected against the background of the radiation belt noise through most of the orbit. It is expected that similar shielding would be required for an EMR 541N photomultiplier. Even so, the scanner will likely be inoperative between 1.2 and 2.0 Earth radii. This shield should cover the photocathode and first few dynodes extending well beyond the cathode in both directions along the tube axis. A side window tube requires less shielding but must have a field lens to image the reticle onto the photocathode. A price must also be paid in quantum efficiency.

XI. ELECTRONIC DESIGN

For a spin stabilized vehicle, the slit reticle is fixed with respect to the vehicle and the slit scanning motion is obtained as the vehicle rotates about its spin axis. For an earth stabilized vehicle, the scanning motion must be electro-mechanically supplied by a synchronous motor which rotates the slit reticle. Consequently, the SCADS-S^3 electronics for the earth stabilized vehicle must include motor drive circuits in addition to the electronics required for the spin stabilized vehicle. This section will first describe the spin stabilized electronics followed by a brief description of the electronics required for the earth stabilized vehicle.

A. Electronics for Spin Stabilized Vehicle

The SCADS-S^3 electronics for the spin stabilized vehicle must include both analog and digital circuits in addition to the required power supplies and associated regulator circuits. The basic electronic functions which the electronics must perform may be stated as follows:

(a) filter the star signals from the photomultiplier output;

(b) digitally encode the slit transit time of each star whose intensity exceeds the threshold level using as a time base a binary digital clock;

(c) provide overload protection for the photomultiplier.

The basic electronic block diagram required to provide the above electronic functions is shown in Figure 74.

As seen from Figure 74, the anode output of the photomultiplier (PMT) is connected to a load resistor, R_L, so that the anode current produces a negative anode signal voltage. The anode signal voltage drives a high input impedance amplifier which provides sufficient current gain to drive the relatively low input impedance to the parallel input connection of the two low pass filters labeled H and L.

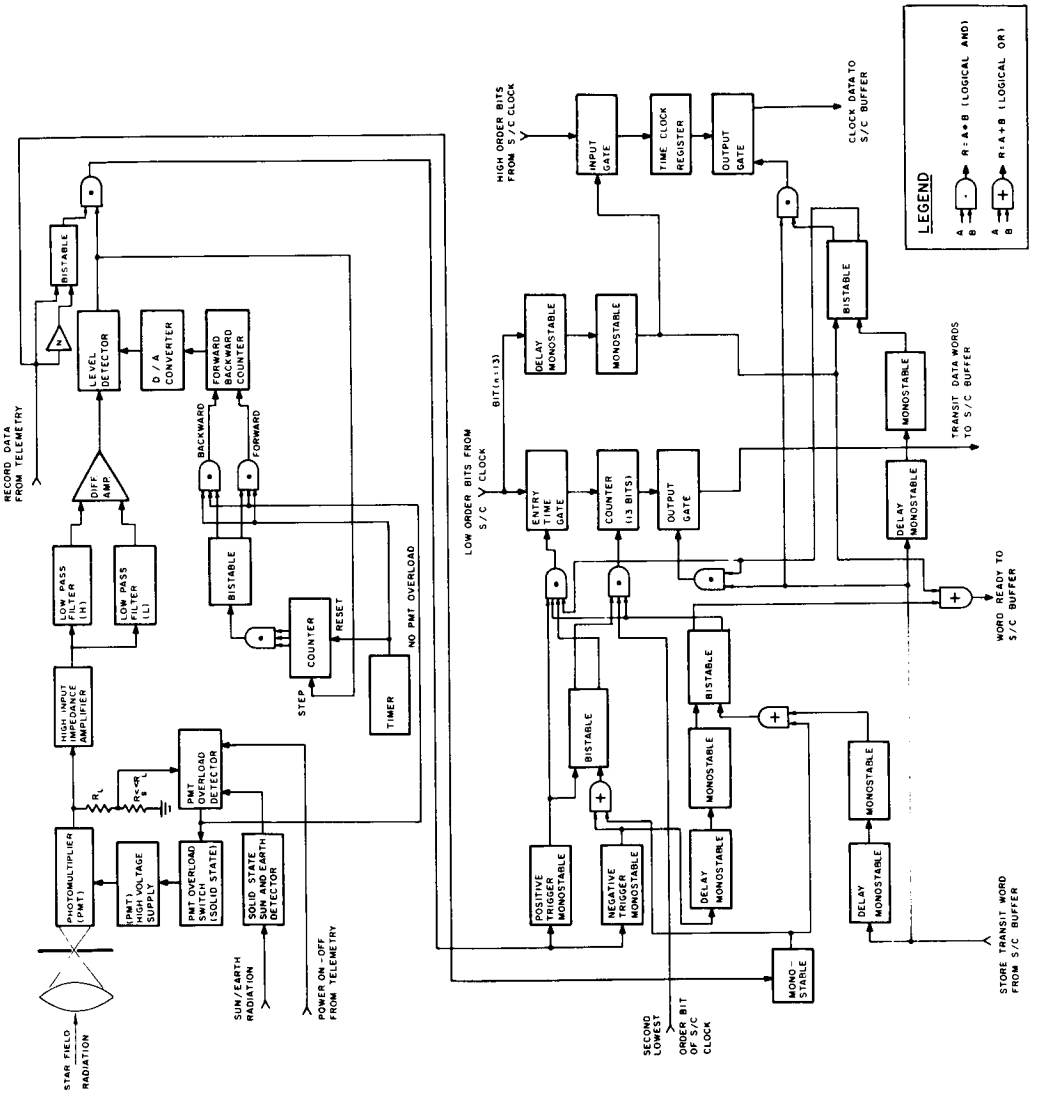

FIGURE 74: S^3 Electronics Block Diagram

The parallel connection of the two low pass filter inputs is important because by adjusting the cut-off frequencies and subtracting the respective outputs it is possible to remove the slowly varying (almost DC) background signal from the total signal, which includes the star signals. The slow variation in the background level is caused by the continuous scanning of portions of the celestial sphere having different background light intensities. For example, the Milky Way background intensity is greater than for areas outside the Milky Way.

In Figure 75 waveforms illustrate why removal of the slowly varying background is desirable. The top waveform shows the output of the H (high cut-off frequency) low pass filter. The cut-off frequency of the H filter is set to attenuate the high frequency noise but still pass the star transit pulses. The middle waveform illustrates the output from the L (low cut-off frequency) low pass filter. The cut-off frequency of the L filter is set to attenuate all signals (including the star transit pulses) except the slowly varying background component. The bottom waveform is the inverted difference of the top two waveforms and illustrates the star transit pulses all rising above a common base level. Setting the threshold level as shown for the bottom waveform results in detection of all three star transit pulses shown for a single scan, whereas setting a similar threshold level for the top waveform having unfiltered background can result in missed star transit pulses, which can result in the failure to compute the attitude.

The cut-off frequency of the L filter is not particularly critical; however, certain broad restrictions must be imposed. First of all, the filter time constant (transient response time), T_f, must be much less than the rise time, T_r, of the change in background level. This restriction is necessary to insure that the L filter output will closely follow its input. So pick $T_f \leq T_r/10$. But $T_f \approx 1/\omega_c = 1/2\pi f_c$, so $f_c \geq 10/2\pi T_r$. Then as an example, if $T_r \approx 4$ seconds for an eight second scan period, $f_c \geq 10/8\pi \approx .4$ cycles per second.

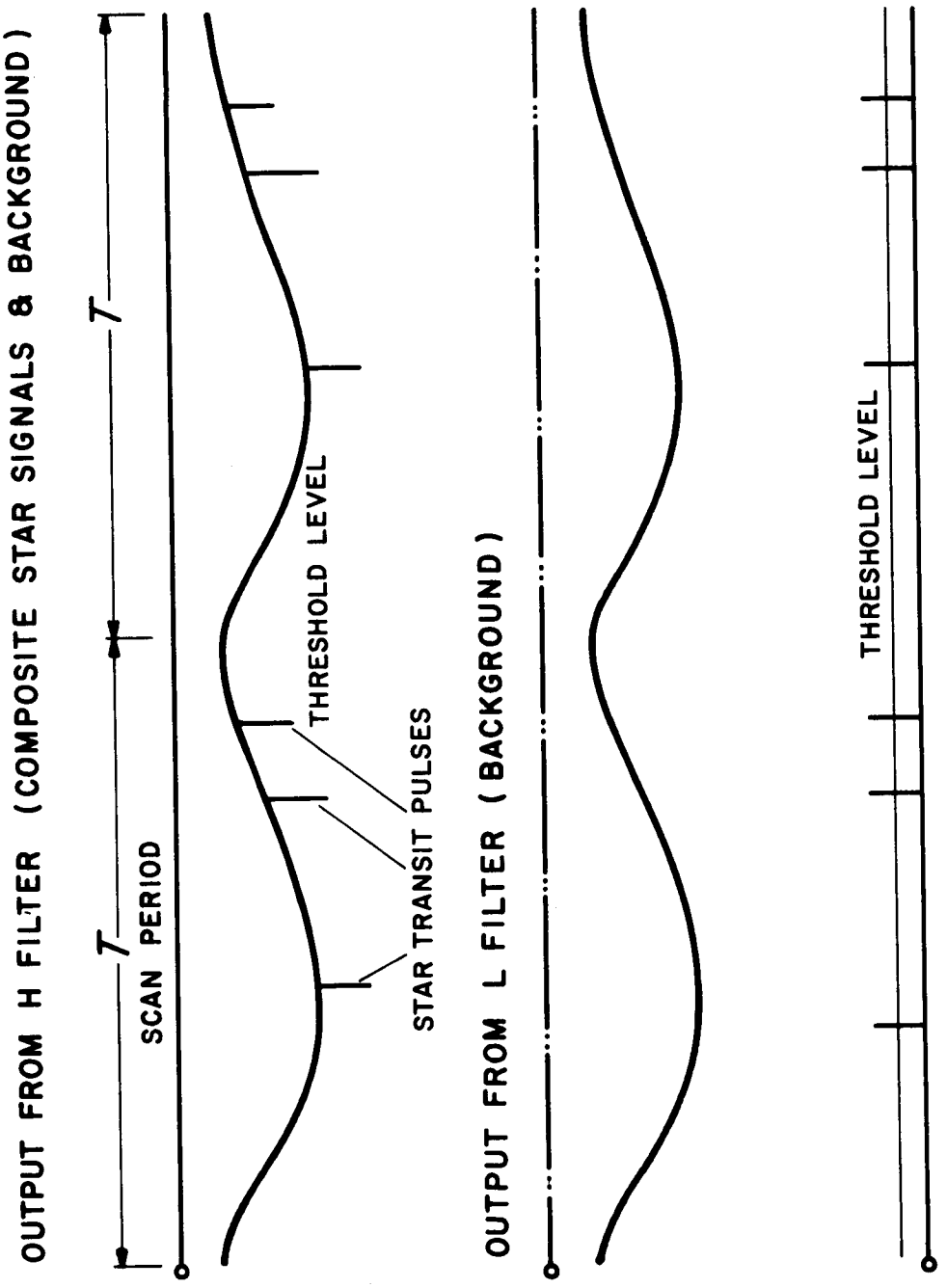

FIGURE 75: Waveforms Illustrating Background Filtering

Another broad restriction is that the cut-off frequency of the L filter must be as low as possible to minimize the distortion to the star transit pulse after the background level has been removed. By subtracting the L filter output from the H filter output, the low frequency components of the star transit pulse are also removed along with the background level. Removing substantial low frequency components from a uni-polarity pulse has the effect of differentiating the pulse (Bennett[33]). Therefore, it is desirable that the L filter frequency response have a reasonably sharp roll-off. For the star transit pulse widths experienced for SCADS, the distortion caused by subtracting the low frequency components should be negligible.

The transfer function of the L filter should have a near linear phase shift versus frequency characteristic, so that the filter transient response is near critically damped.

It has been suggested that the L filter and difference amplifier could be replaced by a coupling (DC blocking) capacitor connected at the input to the H filter. However, such a capacitor forms a single pole RC transfer function with the H filter input resistance which then acts as a differentiator. On the other hand, the L filter transfer function can have several poles which can be selected so as to better preserve the symmetry of the star pulse.

The design parameters for the H filter have been described in detail in Section IV-E and will not be further treated here.

After the star pulse has been filtered, the star transit time must be encoded by the digital logic circuits. The filtered star pulse drives one of the two inputs of a level detector. The other level detector input is driven by a voltage level supplied by a D/A converter which determines the detection threshold. As the filtered star pulse rises above the threshold level, the level detector output switches rapidly from a "0" voltage level to a binary "1" voltage level. This instant of switching is referred to as the star entry time. Similarly, as the star pulse falls below the detection level, the

level detector output rapidly switches from the "1" voltage level to the "0" voltage level. The latter instant of switching is referred to as the star exit time. The star transit time will be defined as the average of the star entry time and the star exit time. The primary purpose of the digital logic is to encode the transit time for each star whose signal amplitude crosses the threshold level.

It will be assumed that the S^3 spacecraft will have an on-board binary clock which will have sufficient stability and resolution for encoding of star transit time data. The required clock stability and resolution for SCADS will be discussed later in this section. It will also be assumed that the clock and timing signals required for transit time encoding will be available to the SCADS-S^3 electronics. In addition, since the S^3 vehicle electronics will contain a buffer memory, the SCADS-S^3 electronics will contain temporary storage of transit time data for a single star transit only.

Considering the above assumptions, a reasonable method of encoding the star transit time is presented in Figure 74. A brief description of the method is given below.

At the leading edge (star entry time) of the level detector output, the low order bits of the spacecraft clock are gated into the transit time counter and register. Also at this time a clock signal from the spacecraft is gated into the transit time counter. This clock signal should be the second low order bit from the spacecraft clock so that the transit time counter is stepped at one-half the rate of the clock's lowest order bit. This counting is continued until the trailing edge (star exit time) of the level detector output occurs at which time the counting is stopped. Counting at one-half the basic clock frequency has the effect of arithmetically averaging star entry and star exit times.

Immediately after the star exit time, a signal is sent to the spacecraft buffer memory informing it that star transit data is available for storage.

As soon as the spacecraft buffer memory is ready to receive data, it sends a Store Data signal to the SCADS logic which gates the contents of the transit time counter to the S/C buffer memory. Immediately after the transit data has been stored in the buffer, the SCADS logic is reset to encode the next star transit. While a star transit word is awaiting storage in the S/C buffer, the SCADS logic is inhibited from encoding and storing any star transits that occur during the wait interval.

The highest order, or n^{th}, bit from the S/C clock that is gated into the transit time counter should have a period which is somewhat greater than the vehicle scan period to insure that two different star transits in a single scan period do not have similar transit times. To further avoid transit time ambiguity and also to allow determination of vehicle attitude as a function of spacecraft time (or spacecraft orbital position), the remaining upper order bits (above the n^{th}) of the spacecraft clock should be stored in the S/C buffer at the beginning of each period of the n^{th} bit. This is shown in Figure 74 where the n^{th} bit clear detector detects the beginning of a new period for the n^{th} bit. At this instant, the high order bits of the S/C clock are stored in the time clock register. After a short delay, a ready signal is sent to the S/C buffer memory to inform it that a word is ready for storage. When the buffer is ready, a store signal is received from the buffer which gates the time clock register contents into the S/C buffer. Star transit data is inhibited from being encoded while the upper order bits of the S/C clock are being stored.

The number of stars scanned per spin period brighter than the limiting detectable magnitude varies over a very broad range, typically from about 20 to 3. Since detection of only three stars per scan period is required to determine attitude, it is desirable to limit the number of transit detections to some intermediate number. This can be accomplished by automatically raising and lowering the detection threshold depending upon the number of stars detected per period. The logic implementation shown in Figure 74 counts the number of star detections per scan period. If the number of detections

per scan period is greater than eight, then another counter is stepped forward causing the D/A converter output to raise the threshold votage at the level detector input. If the number of detections per scan period is less than eight, then the counter is stepped backward which lowers the threshold voltage to the level detector. A preset timer having the same approximate time period as the scan period will reset the star transit counter.

1. Photomultiplier Overload Protection

In order to prevent degradation of the photomultiplier cathode and dynodes, it is necessary to limit the current emitted by these surfaces when bright sources such as the sun, earth, or moon get into the optical system field of view. Since current flow does not occur when high voltage is removed from the photomultiplier cathode and dynode chain, an obvious way of limiting the emission currents is to reduce or remove the electron acceleration voltages to the cathode-dynode chain whenever bright sources of radiation enter the field of view.

For the elliptical equatorial orbits, the sunlit earth will get into the field of view for portions of each orbit. For some conditions of the circular polar orbits, the sun may also get into the field of view. For these cases, it is certain that the photomultiplier emission current limits will be exceeded if the photomultiplier voltage is not reduced or removed when the bright source enters the field of view. The full moon intensity can also cause excessive emission currents, so it too must be considered as a bright source. However, the moon is less of a problem than the earth or the sun because the angle it subtends from the spacecraft is always small.

The logic block diagram in Figure 74 indicates ways of detecting an overload or a potential overload condition. Both of these conditions must provide logic signals which can temporarily reduce or remove the photomultiplier high voltage.

An actual overload condition can be detected at the photomultiplier output by sensing when the output signal across R_s exceeds a threshold level

determined from the maximum average anode current rating. The output of a level detector will automatically switch OFF the photomultiplier high voltage. The photomultiplier high voltage must then be turned back ON by a telemetry command from the ground station, provided no bright source is in the field of view.

A potential overload condition can be sensed by placing a string of sub-miniature solid state photocells about the edge of the field of view. These detectors would be positioned so that as radiation from the earth or moon is about to enter the slit, at least one of the detectors would provide an output signal adequate to exceed a level detector threshold. Each photocell would drive a level detector and all the level detector outputs would be logically connected as an OR gate function. The OR gate output would automatically switch OFF the photomultiplier high voltage. The photomultiplier voltage would remain OFF until all photocell outputs fall below the threshold level at which time the photomultiplier voltage is automatically turned back ON.

2. Design of High Voltage Power Supply

It is required that the photomultiplier high voltage power supply be capable of turning OFF and ON within a small fraction of the scan period in order to prevent the formation of high current densities within the tube when bright radiation sources are scanned. The EMR photomultipliers can be purchased from the manufacturer with an integrated high voltage power supply wrapped around the tube envelope. However, the design of this supply does not permit rapid enough turn ON and turn OFF capability, especially for relatively short scan periods. Consequently, it is necessary to consider a specially designed high voltage supply which is capable of switching OFF and ON in tens of milliseconds.

A block diagram for a high voltage power supply design which permits fast switching is shown in Figure 76. The input voltage to a DC-AC inverter is

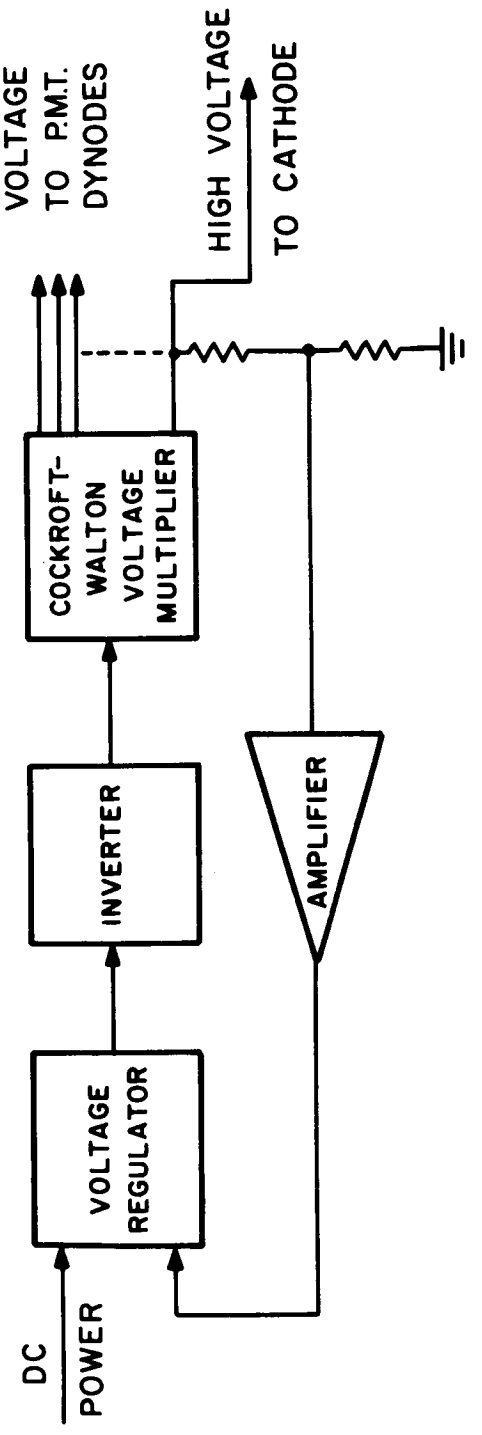

FIGURE 76: Block Diagram for High Voltage Power Supply

regulated up or down inversely proportional to the voltage change at the high voltage output from the Cockroft-Walton voltage multiplier. A high gain feedback loop senses changes in the output voltage and causes the voltage regulator to provide correcting input voltage changes to the inverter. The following paragraphs discuss voltage multiplication and the achievable charging and decay time of the output voltage.

A common method of producing low current high voltage DC power from low voltage AC sources is the voltage doubler shown in Figure 77. One-half of the AC cycle is used to charge capacitor C_1 to the peak of the input and this capacitor charge in series with the other half cycle charges C_2 to twice the input peak voltage. This principle can be extended indefinitely at least theoretically to provide a very high voltage which is conveniently divided into equal steps. While this multi-step multiplier was originally developed for powering charged particle accelerators with requirements in the megavolt range; with the proper input voltage, it has voltage and current capabilities closely matching photomultiplier requirements. In Figure 77 it would be a simple matter to add a half wave rectifier to provide the missing first step E_p, but then difficulty ensues when an arrangement for $3E_p$ is wanted. A system for tripling is shown in Figure 78. It is the same as Figure 77 with an added capacitor and diode and a different ground reference point. From the characteristics of these two circuits it is easy to deduce that a single multiplier will only produce odd or even multiples of the transformer voltage but not both. Of course, the transformer secondary could be designed for half the required voltage step but this does not produce the lowest possible supply output impedance, especially for the first two stages which ideally could be positive and negative half wave rectifiers. Multiple transformer windings produce unequal loading effects which are not desirable with high frequency saturable core inverters.

It would be possible to connect both of these networks, mutually extended to provide 14 voltage steps, to a single transformer for a photomultiplier tube power supply. A reduction in capacitor voltage requirement and thus size

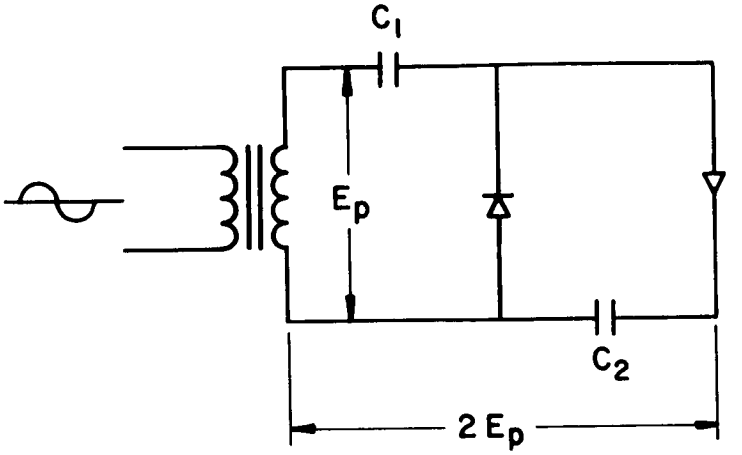

FIGURE 77: Voltage Doubler Circuit

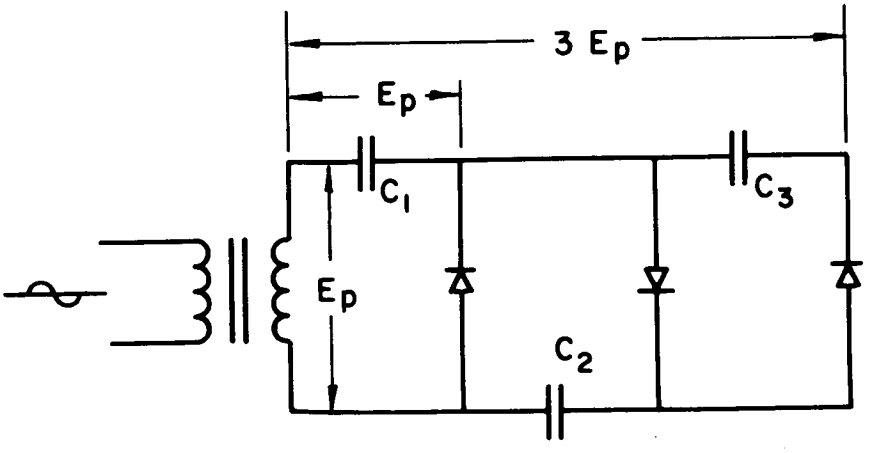

FIGURE 78: Voltage Tripler Circuit

is achieved by an interlacing or series connection of the capacitor strings as shown in Figure 79. While the schematics in Figures 77 and 78 are for positive output the one in Figure 79 is reversed to show the actual negative output required for grounded photomultiplier output operation. A positive half wave rectifier is added to the lower end of the multiplier with the output grounded to provide two low impedance stages.

In a saturable transformer inverter, leakage reactance spikes of various amplitudes can exist depending on loading. With this multiplier where separate sections supply even and odd dynodes it is possible for a spike on one set to contribute enough voltage to seriously upset interdynode voltages under very light load conditions. It is thus necessary to load both sections to insure the voltage is determined by actual square wave amplitude. A voltage sensing divider across the supply for feedback regulator control will only load one section, and it is most economical to connect a load between the next highest even and odd voltages to load the other section.

For a given load and ripple tolerance, supply frequency and capacitor size can be chosen. For a photomultiplier in a scanning system which must be turned OFF during sun, earth, or moon scan, charge and discharge times are also important. Discharge time is simply related to load and capacitor size by the equivalent exponential RC time constant. Charging time is more difficult to determine but has been obtained for a 14 stage multiplier (Figure 80) by computer simulation. For each half cycle it is possible to write equations at each stage for the voltage on each capacitor as a function of the voltage on the two capacitors at the end of the previous half cycle. The overall multiplication factor as a function of elapsed cycles is shown in Figure 81. With a 50 kilocycle input square wave, the charging times are as follows:

99 percent full output requires 6.61 milliseconds,
99.9 percent full output requires 10.2 milliseconds.

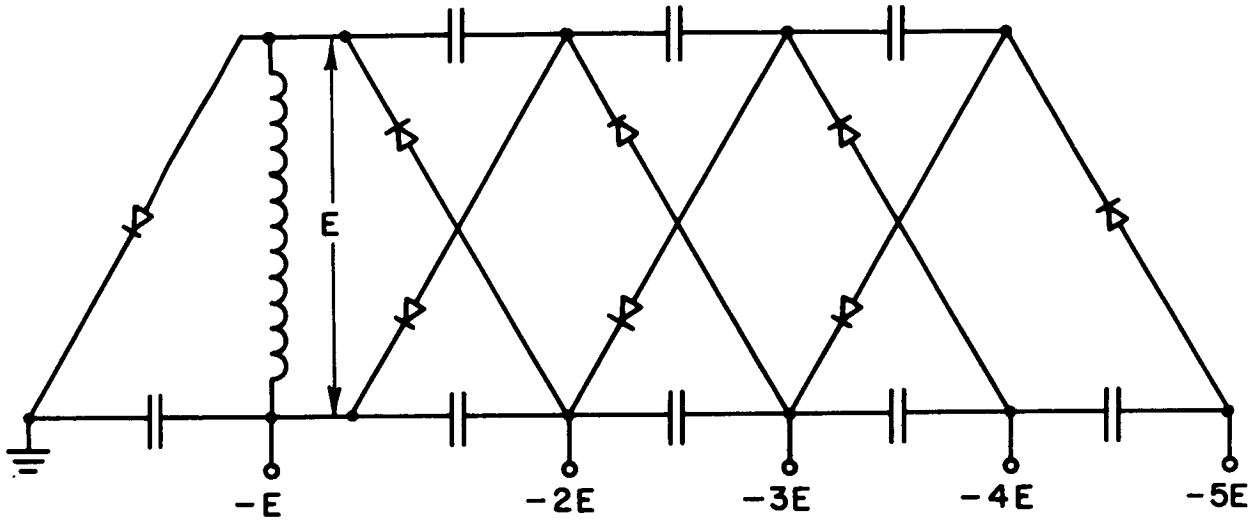

FIGURE 79: Interlaced Dual Even-Odd Multiplier

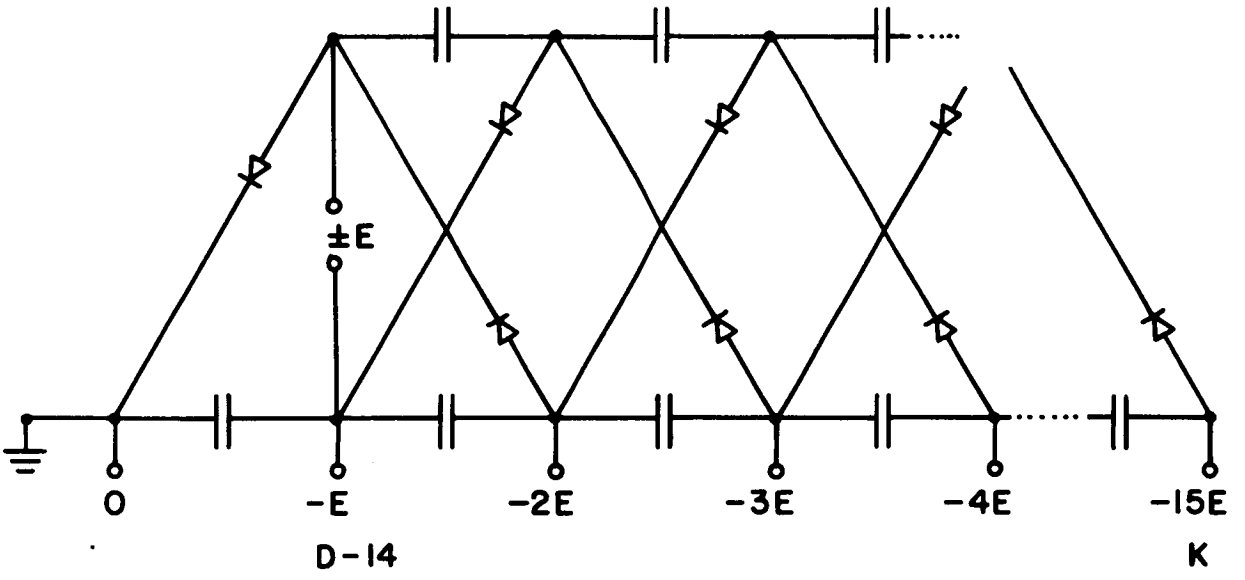

FIGURE 80: Cockroft-Walton Multiplier for EMR 14 Stage Photomultiplier Tube

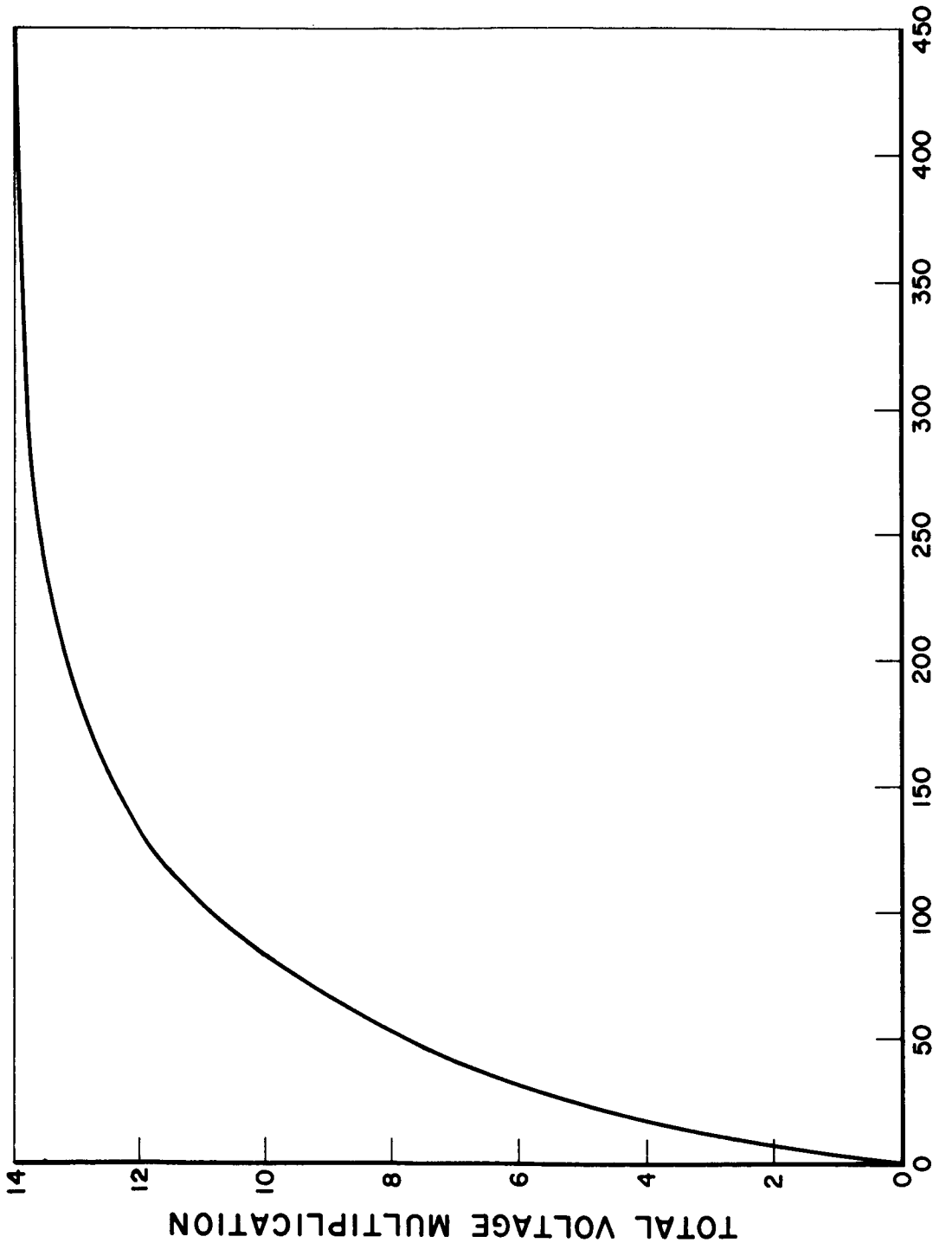

FIGURE 81: Charging Time of a 14 Stage Cockroft-Walton Multiplier

B. Field Stabilized Vehicle

The electronics required for the field stabilized vehicle is similar to that required for the spin stabilized vehicle except a Scanning Angle Sequential Incrementer (SASI) motor is required to rotate the slit reticle at a constant RPM in synchronism with the clock pulses used for encoding star transit times. In addition to the motor itself, motor drive circuits are necessary to provide a properly timed sequence of pulses to the motor mechanism.

The SASI motor consists of a rotating disk which carries the reticle slit and is supported by a jeweled bearing assembly. Teeth are positioned on the disk periphery, with the tooth width equal to the tooth spacing. Positioned adjacent to the disk teeth are four small stationary clusters of electro-magnets spaced 90^{o} apart which supply the rotating force. Each pole within the cluster of eight poles is in effect spaced mechanically 1/8 of a tooth from its neighbors by means of the diagonal construction of the tooth assembly. There are 256 (2^{8}) teeth on the periphery of the disk.

The pole faces are arranged in the following manner:

Pole		Pole	
1	0^{o}	9	90^{o} + 1/32 tooth
2	0^{o} + 1/8 tooth	10	90^{o} + 5/32 tooth
3	0^{o} + 1/4 tooth	11	90^{o} + 9/32 tooth
4	0^{o} + 3/8 tooth	12	90^{o} + 13/32 tooth
5	0^{o} + 1/2 tooth	13	90^{o} + 17/32 tooth
6	0^{o} + 5/8 tooth	14	90^{o} + 21/32 tooth
7	0^{o} + 3/4 tooth	15	90^{o} + 25/32 tooth
8	0^{o} + 7/8 tooth	16	90^{o} + 29/32 tooth

Pole		Pole	
17	180^{o} + 1/16 tooth	25	270^{o} + 3/32 tooth
18	180^{o} + 3/16 tooth	26	270^{o} + 7/32 tooth
19	180^{o} + 5/16 tooth	27	270^{o} + 11/32 tooth
20	180^{o} + 7/16 tooth	28	270^{o} + 15/32 tooth
21	180^{o} + 9/16 tooth	29	270^{o} + 19/32 tooth
22	180^{o} + 11/16 tooth	30	270^{o} + 23/32 tooth
23	180^{o} + 13/16 tooth	31	270^{o} + 27/32 tooth
24	180^{o} + 15/16 tooth	32	270^{o} + 31/32 tooth

The slit is rotated by sequentially pulsing the electromagnetic poles in the following manner:

1 - 9 - 17 - 25
2 - 10 - 18 - 26
3 - 11 - 19 - 27
4 - 12 - 20 - 28
5 - 13 - 21 - 29
6 - 14 - 22 - 30
7 - 15 - 23 - 31
8 - 16 - 24 - 32

Each time all 32 magnets are pulsed, the rotating slit advances 2^{-8} of a revolution. Therefore, each magnet must be pulsed 2^{8} times per revolution, hence there are 2^{13} rotational increments per revolution. Due to the relatively large inertia of the reticle disk, there is only a small amount of speed variation or cogging between the teeth.

The logic required to drive the SASI motor is relatively simple as shown in Figure 82. The basic clock resolution interval is first divided into 32 time intervals. The subdivided clock frequency is then used to drive sequencing logic which sequentially provides drive pulses to each of the 32 magnet poles.

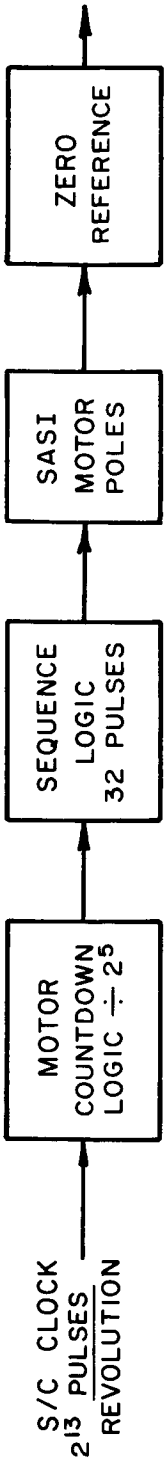

FIGURE 82: SASI Motor Block Diagram

The sequencing logic consists of a five stage binary counter and a decoding matrix whose 32 outputs each drive one pole winding.

In order to orientate the position of the slit with respect to the vehicle axis it is necessary to provide a zero reference indication. When the zero reference signal occurs for each revolution, the contents of the S/C clock must be stored in the S/C buffer memory.

The zero reference signal can be easily generated by using a small, high reliability lamp, a miniature mirror mounted on the reticle assembly and a solid state photodetector. There is a large selection of mounting configurations. A reasonable mounting method is to mount the mirror on the rotating reticle so that as it rotates past the stationary mounted light source, light is reflected back to the photodetector, which is also stationary mounted. The photodetector, by proper selection of the numerous types on the market, can have a very fast rise time and would require very little power. Its output would already be sufficiently large without amplification and could be fed directly to a Schmitt trigger circuit to shape the signal. The Schmitt trigger output would then be used to gate the S/C clock output into the S/C buffer as was similarly done by the n^{th} stage clock bit for the spin stabilized electronics.

C. Clock Resolution and Stability Required for SCADS-S[3]

Encoding of the star transit time must be performed with sufficient precision so that the required system accuracy can be realized. In order to achieve the required system accuracy, all sources of error must be considered, with one of the sources being the transit time uncertainty introduced by the encoding process. The major sources of error may be listed as follows along with the approximate RMS error contributions for each source expressed in terms of the slit width parameter, $\widehat{SW}$;

(a) asymmetrical blur circle - $\frac{1}{10}\widehat{SW}$
(b) asymmetry introduced by star pulse filtering - $\frac{1}{10}\widehat{SW}$
(c) photomultiplier shot noise - $\frac{1}{7}\widehat{SW}$
(d) encoding error - $\frac{\widehat{SW}}{6}\frac{\sqrt{2}}{\sqrt{12}}$

The RMS error contributions for item (a) is an experienced estimate based on computer generated blur spot diagrams for various lens systems analyzed for SCADS type systems. Reference [34] shows some typical blur spot diagrams. The RMS error contributions for items (b) and (c) are based on the analysis given in Section VIII. The encoding error contribution can be derived by consideration of the uniform probability density function. The threshold crossing for a star pulse is equally likely to occur at any instant during a clock period resolution interval. So the probability density for the threshold crossing time is a uniformly distributed random variable whose RMS value is $\frac{L}{\sqrt{12}}$ where L is the length of the time interval. It will be assumed that the trailing edge threshold crossing time is independent of the leading edge threshold crossing. Since the star transit time is the average of the leading edge and trailing edge threshold crossings, then the RMS transit time must be approximately $\frac{\sqrt{2}}{\sqrt{12}}$ L. Now, if L is set (rather arbitrarily) equal to one-sixth the slit transit time (for a point source), then the encoding RMS error contribution becomes $\frac{\widehat{SW}}{6}\frac{\sqrt{2}}{\sqrt{12}}$.

If it is assumed that all the major error sources are independent, then the total RMS azimuth error becomes .21 $\widehat{SW}$. For an 18 arc-minute slit width, the RMS azimuth error is 3.6 arc-minutes which is sufficient to achieve a three axis attitude error of less than six arc-minutes with 80% probability (See Section VIII).

For an 18 arc-minute slit width, the clock resolution interval expressed in angular units must be $L = \frac{18}{6} = 3$ arc-minutes. For a scan period of T seconds, the clock resolution must be $\Delta t = \frac{3T}{2.16 \times 10^4}$ seconds. Each scan period is, therefore, resolved into $\frac{2.16}{3} \times 10^4 \leq 2^{13}$ parts. Consequently, in Figure 74, the thirteen low order bits of the S/C clock must be gated into a thirteen bit counter for transit time encoding.

As shown in the previous paragraph, the resolution of the SCADS clock expressed in time units is a function of the sensor scan period. Since each spin stabilized S^3 orbital configuration has a specific vehicle scan period or a range of scan periods, the required clock resolution intervals may be tabulated for each orbit configuration. (See Table XVII.)

It should be noted that a basic clock oscillator frequency of 14.4 Kc will provide the SCADS adequate time resolution for all orbital configurations.

It is important that the clock used for encoding SCADS star transit data be synchronized with Universal Time, or some equivalent, in order to determine spacecraft attitude as a function of time. Almost any synchronization method should be sufficient. One reasonable method would be to have the period of the clock be slightly greater than the orbital period and then to count the number of orbits. The number of stages required by the binary clock used for SCADS transit time encoding may be determined in order for the clock period to be greater than the orbital period. The number of stages required depends upon the clock resolution interval and the orbital period, and have been tabulated in Table XVIII for each S^3 spin stabilized orbit configuration.

TABLE XVII

S^3 CLOCK RESOLUTION

Elliptical Equatorial

$T = 15$ seconds

$\Delta t \leq 2.08 \times 10^{-3}$ seconds

$f = \frac{1}{\Delta t} \geq .48 \times 10^{3}$ cps

Near-circular, Near-polar ($\frac{1}{2} \leq T \leq 30$ seconds)

$T = \frac{1}{2}$ second

$\Delta t \leq .695 \times 10^{-4}$ seconds

$f \geq 14.4 \times 10^{3}$ cps

$T = 15$ seconds

$\Delta t \leq 2.08 \times 10^{-3}$ seconds

$f \geq .48 \times 10^{3}$ cps

$T = 30$ seconds

$\Delta t \leq 4.17 \times 10^{-3}$ seconds

$f \geq .24 \times 10^{3}$ cps

Near-equatorial

$T = 120$ seconds

$\Delta t \leq 16.7 \times 10^{-3}$ seconds

$f \geq .06 \times 10^{3}$ cps

Synchronous Gravity Gradient

$T = 5$ seconds

$\Delta t \leq .695 \times 10^{-3}$ seconds

$f \geq 1.44 \times 10^{3}$ cps

TABLE XVIII

RECOMMENDED NUMBER OF STAGES FOR SCADS-S^3 CLOCK

Elliptical Equatorial

Orbital Period = T_o = 8 hours

$$\frac{T_o}{\Delta t} \leq 2^{24}$$

Near-circular, Near-polar

T_o = 100 minutes

$$\frac{T_o}{\Delta t_{min}} \leq 2^{27}$$

Near-equatorial

T_o = 98 minutes

$$\frac{T_o}{\Delta t} \leq 2^{19}$$

The clock resolution interval used for star transit time encoding requires stability for only a relatively short time interval. For SCADS the clock stability is most important for statistical averaging of attitude data from successive scan periods in order to improve the accuracy of the attitude estimate. It has been demonstrated that the accuracy of the attitude determination can be significantly improved if averaging is performed over 10 or 15 successive scan periods. So in order to neglect the error contributions due to the clock instability, the clock resolution interval should not change (drift) by more than a small fraction of the nominal resolution interval. Consequently, the clock resolution interval should not change by more than 1/10 the nominal resolution interval over fifteen scan periods. Since fifteen scan periods are comprised of approximately 1.23×10^5 resolution intervals, the clock stability should be better than one part in 10^6.

XII. ESTIMATED SENSOR SIZE, WEIGHT,AND POWER

A. Volume

The volume of the S^3 sensor can be approximately estimated from manufacturer's data sheets of components and by extrapolating from previous studies[1,4] relating to a SCADS type sensor. The volume estimate is somewhat dependent upon the vehicle stabilization method and also the scan period. Therefore, it is natural to separately tabulate the volume for each configuration. (See Table XIX.)

Since the sun shield is essentially external to the sensor, the sun shield volume for each lens system is listed separately in Table XX.

The volume estimates found in TableXIX have been based on the dimensions of individual components. For example, the volume of a lens system can be approximately determined from

V = aperture area x focal length

$$= \frac{\pi}{4} D^2 \, (Df) = \frac{\pi}{4} D^3 f$$

where f = f/number = 1.3.

The EMR-541 photomultiplier dimensions are 1.375 inches diameter by 4.25 inches long. The cathode particle shield is a hollow cylinder assumed to be one centimeter thick and three inches long. It is assumed the digital circuits require approximately .03 $(\text{inch})^3$ per integrated circuit package including the printed circuit boards for mounting.

TABLE XIX

ESTIMATED VOLUME OF SCADS-S^3 SENSOR
SPIN STABILIZED VEHICLE

Subsystem	Volume (Inch)^3		
Photomultiplier (EMR-541)	6.5		
Cathode Particle Shield	3.2		
Electronics			
Analog Circuits	3.0		
Digital Circuits	4.0		
Overload Circuits	.5		
Power Supplies	2.0		
Subtotal	19.2		
Lens System A (D = .4, f/n = 1.3)		.07	
Total (Lens A, T $\geq$ 15 seconds)			19.3
Lens System B (D = .8, f/n = 1.3)		.52	
Total (Lens B, 4 $\leq$ T < 15 seconds)			19.7
Lens System C (D = 2.0, f/n = 1.3)		8.2	
Total (Lens C, T $\geq$ ½ second)			27.4

ESTIMATED VOLUME
FIELD STABILIZED VEHICLE

Subsystem	Volume (Inch)^3	
Lens System B (D = .8, f/n = 1.3)	.5	
Photomultiplier (EMR-541)	6.5	
Cathode Particle Shield	3.2	
SASI Motor	3.5	
Electronics		
Analog Circuits	3.0	
Digital Circuits	4.0	
Overload Circuits	.5	
Motor Drive Circuits	.5	
Power Supplies	2.0	
	23.7	(inch)^3

TABLE XX

SUN SHIELD VOLUME

Lens System	Volume $(Inch)^3$
A (D = .4 inch)	.51
B (D = .8 inch)	4.0
C (D = 2.0 inches)	64.4

B. Weight

The weight of the S^3 sensor may be similarly tabulated with respect to each configuration.

TABLE XXI

ESTIMATED WEIGHT OF SCADS-S^3 SENSOR
SPIN STABILIZED VEHICLE

Subsystem	Weight (Pounds)		
Photomultiplier (EMR-541, potted)	.38		
Cathode Particle Radiation Shield	.31		
Electronics			
Analog	.19		
Digital	.25		
Overload Circuits	.03		
Power Supplies	.13		
Sensor Housing	.5		
Subtotal	1.79		
Lens System A (D = .4 inch)		.01	
Sun Shield		.2	
Total (Lens A, $T \geq 15$ seconds)			2.0
Lens System B (D = .8 inch)		.1	
Sun Shield		.3	
Total (Lens B, $4 \leq T < 15$ seconds)			2.2
Lens System C (D = 2 inches)		1.2	
Sun Shield		.4	
Total (Lens C, $T \geq \frac{1}{2}$ second)			3.4

ESTIMATED WEIGHT OF SCADS-S^3 SENSOR
FIELD STABILIZED VEHICLE

Lens System B (D = .8)	.1
Sun Shield	.3
Photomultiplier (EMR-541)	.38
Cathode Particle Shield	.31
SASI Motor	.4
Electronics	
Analog Circuits	.19
Digital Circuits	.25
Overload Circuits	.03
Motor Drive Circuits	.03
Power Supplies	.13
Sensor Housing	.5
Total	2.62

The weight estimates found in Table XXI have been based on individual component weights and weights of similar existing subassemblies. For example, the lens weights have been scaled from an existing lens assembly by multiplying its weight by the third power of the ratios of optical apertures. The reference lens used was the Canon f/0.95 lens[4] whose optical aperture is 2.1 inches and whose measured weight was 605 grams = 1.34 pounds. So the weight of a lens with optical aperture D inches can be estimated by

$$W = 1.34 \left(\frac{D}{2.1}\right)^3 \text{ pounds}$$

The manufacturer lists the potted weight for the EMR-541 photomultiplier as 170 grams. The cathode particle shield is assumed to be aluminum whose density is 2.7 $\frac{\text{grams}}{(\text{cm})}3$. The weight of the electronics is estimated from the volume where the density is taken as 1/16 pound per $(\text{inch})^3$. This latter figure is based on the weight of the CDC 449 computer whose volume is 4 x 4 x 4 = 64 $(\text{inch})^3$ and whose weight is four pounds.

In view of the small volume and weight differences between the .4 inch and .8 inch optical aperture sensors, it seems reasonable from the standpoint of standardization that the .8 inch aperture should be used for all spin stabilized vehicle configurations where the spin period is greater than or equal to four seconds.

C. Power

The power consumption for the SCADS-S^3 sensor has been estimated for both the spin stabilized and the field stabilized vehicle configurations.

TABLE XXII

ESTIMATED POWER REQUIRED FOR SCADS-S^3 SENSOR
SPIN STABILIZED VEHICLE

Subsystem		Watts
PMT Power Supply		.300
Analog Circuits	.300	
Digital Circuits	.150	
PMT Overload Circuits	.100	
	.550	
Low Voltage Power Supply (80% efficient)		.69
Total		.99 watts

ESTIMATED POWER REQUIRED FOR SCADS-S^3 SENSOR
FIELD STABILIZED VEHICLE

PMT Power Supply		.300
Analog Circuits	.300	
Digital Circuits	.150	
PMT Overload Circuits	.100	
SASI Motor and Drive Circuits	1.0	
	1.55	
Low Voltage Power Supply (80% efficient)		1.9
Total		2.2

The power estimate for the photomultiplier power supply was based on the design employed in the occultation photometer experiment successfully flown on the Gemini 10 flight.[35] The high voltage supply consisted of the design concept described in Section XI. The idle current (dynode load resistors disconnected) from 12 volts was measured as seven milliamperes. This power was largely consumed by the tape wound core. With the dynode load resistors connected, the power consumption was approximately 300 milliwatts from a 12 volt supply.

The digital circuits were assumed to be complementary "N" and "P" channel MOS transistor gates whose power consumption per gate is 10^{-6} watt when switching at 1000 cycles per second.

XIII. TEST PROCEDURES

In order to achieve a high degree of confidence that the first flight model of the SCADS-S^3 sensor will successfully operate during the flight mission, it is required that extensive testing be performed both before, during, and after the sensor prototype assembly. Before prototype assembly, exhaustive tests should be performed on the most critical sensor components. After prototype assembly, sensor system tests should be performed both on the laboratory bench using simulated stars and at a remote test site using a real star field. After satisfactory completion of these tests, environmental tests should be performed on the sensor. Successful completion of these tests should then be followed by an integrated system test after the prototype sensor has been installed into the spacecraft. Consequently, the SCADS-S^3 test program should include:

a. component tests,
b. laboratory bench tests,
c. field testing using real stars,
d. prototype environmental tests, and
e. flight model testing.

Each of the above phases of the test program will be briefly described.

A. Component Tests

Prior to sensor assembly, tests should be performed on individual components which are deemed most critical to reliable sensor operation. Included among these tests should be tests on the optical system, the photomultiplier, and the sun shutter.

1. Optical System

Although it is assumed that a suitable specific lens design has been previously determined, it is still required that each lens fabricated to the prescribed design parameters be individually tested to insure that the actual measured lens characteristics comply to the specified characteristics. Particular emphasis should be placed on testing the lens for blur spot size as a function of wavelength for the plane of best focus. This test should also be performed with the slit reticle in the focal plane to insure that at least 80% of the blur spot energy passes through the transparent slit for incident light at any angle (less than $\frac{FOV}{2}$) to the optical axis.

The transmission efficiency as a function of wavelength and the incidence angle (with respect to the optical axis) should be measured to insure that the overall optical efficiency meets the specified minimum value.

Each lens fabricated should be subjected to some preliminary environmental tests in an attempt to uncover any manufacturing defect in the cement bonding of glass elements or the mounting for the glass elements. These environmental tests should include vibration, acceleration, and temperature tests. Vibration tests should be performed as described in NASA document number S-320-S-1 entitled, "General Environmental Test Specification for Spacecraft and Components Using Launch Environments Dictated by Scout FW-4 and Scout X-248 Launch Vehicles." The SCADS sensor must be able to withstand 90 g's axial accelerations (parallel to spin axis) and 16 g's radial acceleration. The required temperature range for the SCADS-S[3] sensor is given as $-30^{o}C$ to $+60^{o}C$.

2. Photomultiplier and Power Supply

The photomultiplier should be tested to determine whether its quantum efficiency as a function of wavelength meets the manufacturer's specified values. Also, tube dark current should be determined as a function of temperature and applied voltage.

In addition to testing the tube and its associated power supply for vibration, acceleration, and temperature, an additional test should be performed in a thermal vacuum to detect formation of corona discharges from the high voltage power supply and high potential dynodes. The tube and supply must operate corona free at any pressure from zero to one atmosphere and at any temperature from -30°C to +60°C.

3. Sun Shutter

Since a sun shutter failure could permanently blind the SCADS sensor, it is necessary to perform tests to achieve a high confidence level that no failure will occur during the spacecraft mission. The environmental tests for vibration, acceleration, and temperature are particularly important since the most likely failure is a mechanical failure rather than a failure in the electronic actuating mechanism.

4. Motor Drive

For non-spin stabilized vehicles, the SCADS sensor requires a specially designed motor drive (Scanning Angle Sequential Incrementer). This motor drive must also be environmentally tested to insure a high confidence level for successful operation during the flight mission. NASA S-320-S-1 defines the launch environment which the motor drive must withstand.

B. Laboratory Bench Test

After the sensor has been assembled, simulated tests should be performed in the laboratory in order to verify defect-free assembly and alignment. The laboratory bench test should be performed using simulated stars which are rotated past the instrument at a constant RPM that simulates the relative motion of the sensor and red stars. The rotation of simulated stars past the sensor requires fabrication of a special test fixture which can also be used for spacecraft integration testing.

The general idea for a recommended test fixture is illustrated in Figure 83. The fixture could consist of a motor driven rotating disk whose front side lies in the focal plane of a collimating lens. Small optical fibers would extend from the backside of the disk through holes in the disk. One end of each fiber would lie flush with the front side of the disk and the other end of each fiber would lie adjacent to a light source (or sources) which is fixed to the back side of the disk. The light source could be energized by a small battery attached to the back side of the disk or power to the light sources could be supplied via slip rings. The RPM of the motor and drive pulley ratios can be adjusted so that the transit time of the simulated star is approximately equal to the transit time for a real star.

The laboratory bench fixture should test the operation of the analog and digital electronics, the sensor response to simulated telemetry commands and the control signals from the sensor. The laboratory test should also test the reaction of the sun shutter to the proximity of bright light sources and the PMT overload protection circuits.

Since the SCADS-S^3 sensor will be subjected to a hostile particle radiation environment during its mission, the entire sensor should be tested when exposed to a simulated particle radiation environment. Operation should be tested using simulated stars and noting the effects of increased radiation doses and verifying that the radiation shielding is adequate. For simplicity,

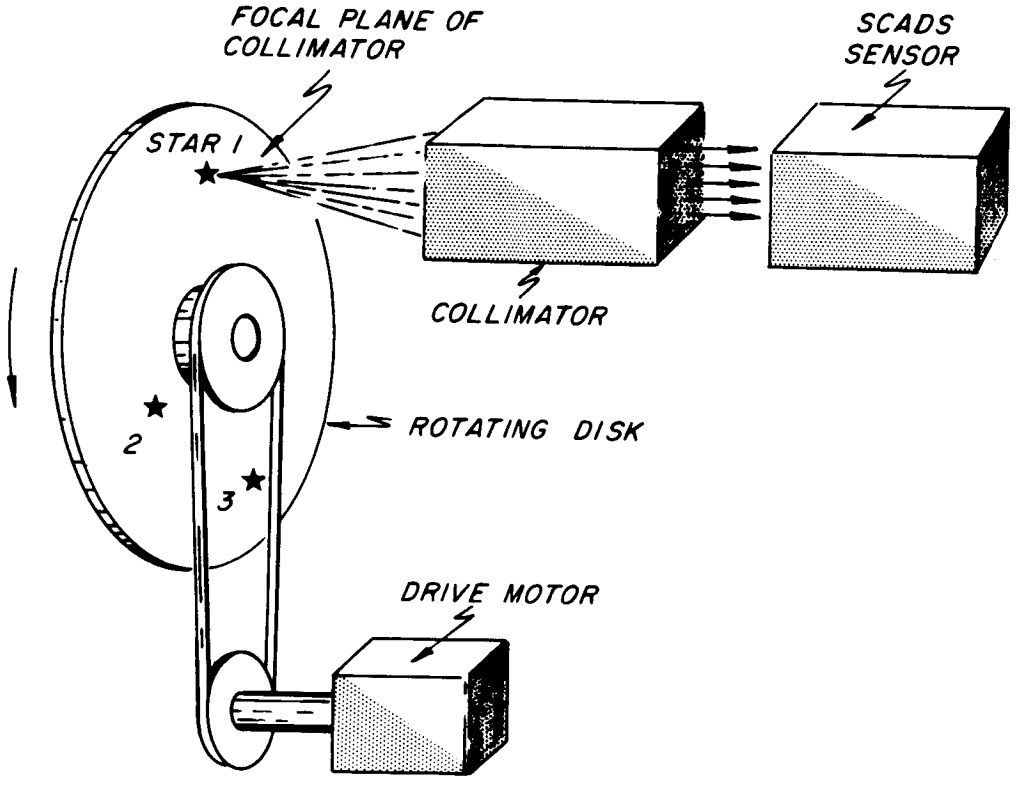

FIGURE 83: Laboratory Test Fixture for SCADS

the radiation testing should be performed in air outside a vacuum chamber with suitable compensation allowed for the attenuation of the radiation due to the atmosphere. The radiation sources could be known amounts of radioactive isotopes such as strontium 90 which are available from the Atomic Energy Commission.

C. Field Test With Real Stars

Since it is extremely difficult to accurately simulate an artificial star in terms of its intensity, spectral energy distribution, and its infinite cross-section of collimated light, the sensor should be tested at night at a remote site using a real star field. This test requires another test fixture which now rotates the entire sensor at a constant rate. The optical axis should be canted at 40^{o} with respect to the test fixture spin axis. The test fixture may consist of a rotating platform or frame to which the sensor may be securely fastened. Slip rings and brushes must be supplied so that command signals and power can be supplied to the sensor, and also, analog signals and star transit data can be obtained from the sensor. The amplitudes of several analog star pulses should be identified as occurring from known stars so the sensor sensitivity can be checked with the predicted sensitivity.

It may be desirable to test the sensor in a simulated particle radiation environment using a real star field instead of using a simulated star field. Performing this test using a real star field would provide a realistic indication of the sensor performance in the space radiation belts.

It is also desirable to perform tests for determining the effectiveness of the sun shield using a simulated sun and the real star field. The bright source assembly could consist of a carbon arc lamp and a collimating lens. Such a bright source would only be a crude simulation of the sun; however, sufficient data should be obtainable to predict sensor performance in space with the real sun. Ideally the tests should be performed in a vacuum since atmospheric scattering in the column of air above the lens assembly can introduce a considerable increase in the background radiation. However, tests in a relatively dust-and humidity-free atmosphere could provide considerable information on the sun shield effectiveness as a function of the angle between the bright source and the optical axis.

It may also be desirable to determine the combined effects of the simulated particle radiation environment and the bright source using a real star field.

This combined test should provide considerable information for predicting sensor performance in the real space environment.

D. Prototype Environmental Tests

The assembled prototype unit must be integrated into the spacecraft and be subjected to a series of tests and exposures of "environmental levels more stringent than those expected from transportation, handling, test, pre-launch, launch, injection and orbit." The exact nature and levels of these environmental tests are described in detail in NASA document S-320-S-1 where they are referred to as spacecraft design qualification.

During the design qualification testing, it is required that electrical performance tests of the sensor subsystem be performed. For these tests, it is recommended that the test fixture shown in Figure 83 be used as the test stimuli for the SCADS sensor. Satisfactory operation during these tests should verify that the SCADS sensor will operate successfully in conjunction with other spacecraft subsystems in a space environment without interfering with other subsystems integrated into the spacecraft.

E. Flight Model Environmental Tests

The assembled flight model of the SCADS-S^3 sensor must be subjected to environmental levels equal to those expected in ground handling, launch and orbit. The exact nature and levels of these environmental tests are described in detail in NASA-S-320-S-1 where they are referred to as flight acceptance tests.

REFERENCES

1. Final Report: Feasibility Study for a Scanning Celestial Attitude Determination System, Contract No. NAS5-9577, prepared by Control Data Corporation, Research Division, for NASA-Goddard Space Flight Center, September, 1965.

2. Grosch, C. B., "Orientation of a Rigid Torque-Free Body by Use of Star Transits," Journal of Spacecraft and Rockets, Vol. 4, No. 5, pages 562-566, 1967.

3. Sherman, B. C. and J. D. Graham, "Coning Motion of a Spinning Rigid Body With Slowly Varying Inertias," AIAA Journal, Vol. 4, No. 8, pages 1467-1469, 1966.

4. Final Report: Breadboard Design of a Scanning Celestial Attitude Determination System (SCADS), Contract No. NAS5-9661, prepared by Control Data Corporation, Research Division, for NASA-Goddard Space Flight Center, November,1966.

5. Final Report: Special Techniques for Space Navigation, Subcontract 247 of Prime Contract NAS9-153, prepared by Control Data Corporation, Research Division, for Massachusetts Institute of Technology, Instrumentation Laboratory, Volume 2, page II-43, July, 1964.

6. Code, A. D., "Stellar Energy Distribution," Stellar Atmosphere, J. L. Greenstein, ed., University of Chicago Press, Chicago, Illinois,Chapter 2, page 50, 1960.

7. Norton, R. H., "The Absolute Spectral Energy Distribution of Canopus," Technical Report No. 32-641, Jet Propulsion Laboratory, California Institute of Technology, August 15, 1964.

8. Final Report: A Theoretical Investigation of Information Limits of Scanning Optical Systems, Contract No. NAS1-4646, prepared by Control Data Corporation, Research Division, for NASA-Langley Research Center, December, 1965.

9. Skolnik, Merrill I., Introduction to Radar Systems, McGraw-Hill Book Company, Inc., page 410, 1962.

10. Farrell, E. J., and C. D. Zimmerman, "Information Limits of Scanning Optical Systems," Optical and Electro-Optical Information Processing, J. T. Tippett, ed., Chapter 35, MIT Press, pages 642 and 646, 1965.

11. Schwartz, Misha, Information Transmission, Modulation, and Noise, McGraw-Hill Book Company, Inc., New York, page 507, 1959.

12. Hansen, Peter D., "New Approaches to the Design of Active Filters," The Lightning Empiricist, Vol. 13, No. 1-2, Philbrick Researches, Inc., Dedham, Massachusetts, 1965.

13. Churchill, R. V., Introduction to Complex Variables and Applications, McGraw-Hill Book Company, Inc., page 118, 1948.

14. Rice, S. O., "Mathematical Analysis of Random Noise," Bell System Technical Journal, Vols. 23 and 24, 1944-1945.

15. Newkirk, Gordon, and David Bohlin, "Reduction of Scattered Light in the Coronagraph," Applied Optics, Vol. 2, No. 2, pages 131-140, February, 1963.

16. Longanecker, G. W., D. J. Williams, and R. O. Wales, "Small Standard Satellite (S^3) Feasibility Study," NASA-Goddard Space Flight Center, March, 1966.

17. Davenport, W. B., Jr., and W. L. Root, Random Signals and Noise, McGraw-Hill Book Co., New York, page 149, 1958.

18. Parzen, E., Stochastic Processes, Holden-Day, Inc., San Francisco, California, pages 53 and 150, 1962.

19. Reed, E. I., W. B. Fowler, C. W. Atking, and J. F. Brun, "Some Effects of MeV Electrons on the OGO II Airglow Photometers," Goddard Space Flight Center, X-616-67-132.

20. Johnson, F. S., Satellite Environment Handbook, Second Edition, Stanford University Press,1961.

21. Gray, Dwight E., ed., American Institute of Physics Handbook, Second Edition, McGraw-Hill Book Co., pages 8-43, 1963.

22. Heitler, W., The Quantum Theory of Radiation, Third Edition, Oxford University Press, pages 246-249, 1954.

23. Young, A. T., Rev. Science Instruments, Vol. 37, No. 11, page 1472, 1966.

24. Schliff, L. I., Quantum Mechanics, McGraw-Hill Book Co., pages 262 ff, 1949.

25. Vette, J. I., A. B. Lucero, and J. A. Wright, "Models of the Trapped Radiation Environment," Vol. II, NASA-SP-3024, prepared by Aerospace Corporation, El Segundo, California, 1966.

26. Code, A. D., "Stellar Energy Distributions," Stellar Atmosphere, J. L. Greenstein, ed., University of Chicago Press, 1960.

27. Rice, S. O., "Mathematical Analysis of Random Noise," Bell System Technical Journal, Vols. 23 and 24, pages 282ff, 46ff, 1944-1945. See also, Selected Papers on Noise and Stochastic Processes, Nelson Wax, ed., Dover, page 153.

28. Wolf, C., "The Effect of the Earth's Radiation Belts on an Optical System," Applied Optics, Vol. 5, No. 11, page 1838, November, 1966.

29. Heitler, W., The Quantum Theory of Radiation, Third Edition, Oxford University Press, pages 246-249, 1954.

30. Mott, N. F., and R. W. Gurney, Electronic Processes in Ionic Crystals, Oxford University Press, 1940.

31. Fermi, E., Nuclear Physics, Revised Edition, University of Chicago Press, 1950.

32. Vette, J. L., "Models of the Trapped Radiation Environment," Volume I, Inner Zone Protons and Electrons, NASA SP-3024, prepared by Aerospace Corporation, El Segundo, California, 1966.

33. Bennett, W. R., and J. R. Davey, Data Transmission, McGraw-Hill Book Company, page 60, 1965.

34. Stavrondis, U. N., and L. E. Sutton, "Spot Diagrams for the Prediction of Lens Performance," National Bureau of Standards, Monograph 93, September, 1965.

35. Technical Report AFAL-TR-322, Volume II: Space Testing of the Star Occultation Technique for Spacecraft Navigation, Contract No. AF33(615)-2027, prepared by Control Data Corporation, Research Division for Air Force Avionics Laboratory, Wright-Patterson Air Force Base, Dayton, Ohio.

APPENDIX A

ORIENTATION OF A RIGID TORQUE-FREE BODY BY USE OF STAR TRANSITS

APPENDIX A

Orientation of a Rigid Torque-Free Body by Use of Star Transits

CHARLES B. GROSCH*
Control Data Corporation, Minneapolis, Minn.

A method of computing the orientation of a spinning, rigid, torque-free, symmetric body from measurements of the times at which known stars appear in an optical system fixed in the body is presented. The method does not assume the moments of inertia of the body to be known. It is shown that if the body is nearly symmetric, precesses with a small cone angle, and is disk-like or rod-like (but not sphere-like), then the symmetry assumption produces a second-order error.

Nomenclature

S_1	=	celestial coordinate system
S_3	=	inertial coordinate system with one axis parallel to the body angular momentum vector
S_6	=	coordinate system fixed in the body with axes parallel to the body principal axis
ξ, τ	=	two angles which define the orientations of S_3 with respect to S_1
θ	=	cone angle
ϕ	=	precession angle
ψ	=	spin angle
d	=	magnitude of angular momentum
A, B, C	=	principal moments of inertia of the body
γ, β	=	two angles which define orientation of slit plane with respect to S_6
ϵ_1, ϵ_2	=	two angles which define the misorientation of the assumed body principal axis with respect to the true body principal axis
cx	=	$\cos x$
sx	=	$\sin x$

Introduction

THE general problem is to find the orientation as a function of time t of a coordinate system fixed in a spinning, rigid, torque-free body. This orientation must be found with respect to the celestial coordinate system. The system fixed in the body, which we later will denote as S_6, has axes parallel to the principal axes of the body.

The basic measurements which must be used to furnish this orientation are the times at which known stars lie in a plane(s) which contains the origin of S_6. This plane(s) is fixed with respect to S_6, and its equation(s) in S_6 is given. Physically, such a plane(s) [or portion of a plane(s)] is generated by an optical system which contains a slit(s), the optical system being fixed in the body. Because of the association of slits to the mechanization of the optical system, we will call these planes "slit planes."

A discussion of the system instrument is given by Lillestrand and Carroll,[1] and Kenimer and Walsh.[2] These authors also consider the problem of computing the orientation of the body from the times of star transit for the case in which the body is spinning about a fixed axis at a constant rate. A more general class of orientation motion will be considered here in that the body will be allowed to precess.

Received July 7, 1966; revision received February 2, 1967. This work was sponsored by Langley Research Center under Contract NAS1-4646, which required development of analytical expressions and computer programs to implement a Langley Research Center concept to determine the attitude of a spinning spacecraft. The author would like to acknowledge the assistance of T. M. Walsh and R. E. Smith of Langley Research Center for the definition of the problem and numerous discussions pertinent to the action. B. D. Vannelli of Control Data Corporation programmed the problem and also aided in its solution. [7.01, 8.02, 8.09]

* Senior Mathematician, Research Division, Aerospace Research. Member AIAA.

Coordinate System

In order to describe the orientation of a system fixed in the body with respect to the celestial system, three angles are sufficient. However, these three angles would be a somewhat complicated function of time. The classical method used to overcome this difficulty is to introduce five angles. Hence, six coordinate systems, S_i with associated unit vectors $\mathbf{i}_i, \mathbf{j}_i, \mathbf{k}_i$, are introduced; $i = 1, 2, \ldots, 6$. Let (Figs. 1 and 2) a) S_1 be the celestial system with associated unit vectors $\mathbf{i}_1, \mathbf{j}_1, \mathbf{k}_1$: $\mathbf{i}_1$ in the direction of the First Point of Aries, $\mathbf{j}_1$ in the equatorial plane, and $\mathbf{k}_1$ in the direction of the North celestial pole; b) S_3 be an inertial system defined with respect to S_1 by two angles ϵ, τ: $\mathbf{k}_3$ is parallel to the angular momentum vector of the body; and c) S_6 be a system fixed in the body with unit vectors $\mathbf{i}_6$, $\mathbf{j}_6$, and $\mathbf{k}_6$ parallel to the principal axis of the body. S_6 is defined with respect to S_3 by the angles ϕ, θ, and ψ.

The angles ξ, τ, ϕ, θ, and ψ will be defined as follows: $\mathbf{i}_1 \rightarrow \mathbf{i}_2$, rotation ξ about $\mathbf{k}_1$, $\mathbf{k}_2$; $\mathbf{k}_2 \rightarrow \mathbf{k}_3$ rotation τ about $\mathbf{i}_2$, $\mathbf{i}_3$; $\mathbf{i}_3 \rightarrow \mathbf{i}_4$, rotation ϕ about $\mathbf{k}_3$, $\mathbf{k}_4$; $\mathbf{k}_4 \rightarrow \mathbf{k}_5$, rotation θ about $\mathbf{i}_4$, $\mathbf{i}_5$; and $\mathbf{i}_5 \rightarrow \mathbf{i}_6$ rotation ψ about $\mathbf{k}_5$, $\mathbf{k}_6$. Hence, ξ = constant, and τ = constant; if the moments of inertia about the principal axes parallel to $\mathbf{i}_6$ and $\mathbf{j}_6$ are equal ($A = B$), and C is the moment of inertia around the third principal axis, then the equations of classical dynamics yield (see e.g., Whittaker[3])

$$\phi = \phi_0 + \dot{\phi}t, \dot{\phi} \text{ constant} \qquad \theta = \text{constant}$$

$$\psi = \psi_0 + \dot{\psi}t, \dot{\psi} \text{ constant}$$

where

$$\dot{\phi} = d/A \qquad \dot{\psi} = d(A - C)\cos\theta/AC$$

For the main part of our discussion, we assume $A = B$. Later we will show the errors caused by this assumption if $C \neq A \neq B = C$, and θ is small.

Constraint Equations

If we consider A and C to be known, then the problem may be formulated as that of seeking the six unknowns $\xi, \tau, \phi_0, \theta, \psi_0$, and d. However, if A and C are unknown, or poorly known, then the problem may be formulated in terms of the seven unknowns $\xi, \tau, \dot{\phi}, \phi_0, \psi_0, \dot{\psi}$, and θ. We will concentrate on the second formulation; the change to the first will then be obvious.

We will now develop an equation which is satisfied the instant a known star is in a slit. This equation is an algebraic equation in the seven unknowns of the problem.

Reprinted from JOURNAL OF SPACECRAFT AND ROCKETS

First of all, the transformation from S_1 to S_6 may be written

$$\begin{pmatrix} \mathbf{i}_6 \\ \mathbf{j}_6 \\ \mathbf{k}_6 \end{pmatrix} = EH \begin{pmatrix} \mathbf{i}_1 \\ \mathbf{j}_1 \\ \mathbf{k}_1 \end{pmatrix} \tag{1}$$

where E is the Euler matrix

$$E = \begin{pmatrix} c\psi\, c\phi - c\theta\, s\phi\, s\psi & c\psi\, s\phi + c\theta\, c\phi & s\psi\, s\theta \\ -s\psi\, c\phi - c\theta\, s\phi\, c\psi & -s\psi\, s\phi + c\theta\, c\phi & c\psi\, c\psi\, s\theta \\ s\theta\, s\phi & -s\theta\, c\phi & c\theta \end{pmatrix}$$

and

$$H = \begin{pmatrix} c\xi & s\xi & 0 \\ -c\tau\, s\xi & c\tau\, c\xi & s\tau \\ s\tau\, s\xi & -s\,\tau c\xi & c\tau \end{pmatrix}$$

The slit plane may be defined with respect to S_6 by two angles γ and β (Fig. 3). Let $\mathbf{i}_7$ be in the ($\mathbf{i}_6$, $\mathbf{j}_6$) plane and also in the slit plane. Let $\mathbf{j}_7$ be perpendicular to the slit plane. Then,

$$\begin{pmatrix} \mathbf{i}_7 \\ \mathbf{j}_7 \\ \mathbf{k}_7 \end{pmatrix} = A \begin{pmatrix} \mathbf{i}_6 \\ \mathbf{j}_6 \\ \mathbf{k}_6 \end{pmatrix} \tag{2}$$

where

$$A = \begin{pmatrix} c\gamma & s\gamma & 0 \\ -s\gamma\, c\beta & c\gamma\, c\beta & s\beta \\ s\gamma\, s\beta & -c\gamma\, s\beta & c\beta \end{pmatrix}$$

γ and β are known quantities.

Now, the instant a star lies in the slit plane (which is moving with respect to S_1) its position with respect to S_7 may be determined by a single parameter η (Fig. 3); hence,

$$\mathbf{S} = c\eta\mathbf{i}_7 + 0 + s\eta\mathbf{k}_7$$

where $\mathbf{S}$ is a unit vector in the direction of the star. Moreover, $\mathbf{S}$ may be defined with respect to S_1 in terms of the declination and right ascension of the star. Hence,

$$\mathbf{S} = c\delta c\alpha\mathbf{i}_1 + c\delta s\alpha\mathbf{j}_1 + s\delta\mathbf{k}_1 \tag{3}$$

where δ and α are the given declination and right ascension of the star, respectively. Thus, the instant a star is in the slit plane,

$$\begin{pmatrix} c\eta \\ 0 \\ s\eta \end{pmatrix} = AEH\mathbf{S} \tag{4}$$

where $\mathbf{S}$ has components in S_1 as given by (3). We may eliminate the parameter η from (4) to obtain

$$0 = A_2EH\mathbf{S} \tag{5}$$

where A_2 is the second row of A.

Equation (5) is thus the basic constraint equation which must be satisfied the instant a star is in the slit plane. Each time measurement thus supplies one equation in seven unknowns of the form (5).

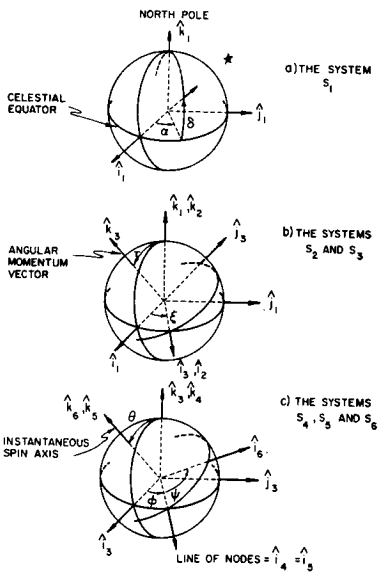

Fig. 1 Relations between various coordinate ystems. (In all figures, carets over symbols indicate

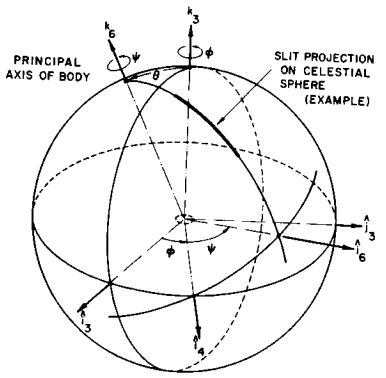

Fig. 2 Relationship of body-fixed reference system to angular momentum frame.

Method of Solution

Each transit time of a known star across a slit plane furnishes a transendental Eq. (5) in the seven unknowns

$$\bar{X} = \begin{pmatrix} X_1 \\ X_2 \\ \cdot \\ \cdot \\ \cdot \\ X_7 \end{pmatrix} = \begin{pmatrix} \theta \\ \psi_0 \\ \dot{\psi} \\ \phi_0 \\ \dot{\phi} \\ \xi \\ \tau \end{pmatrix}$$

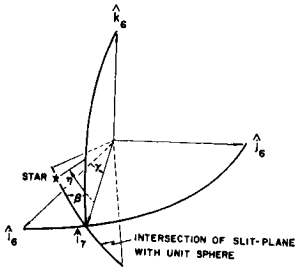

Fig. 3 Orientation of slit plane with respect to S_6.

APPENDIX A

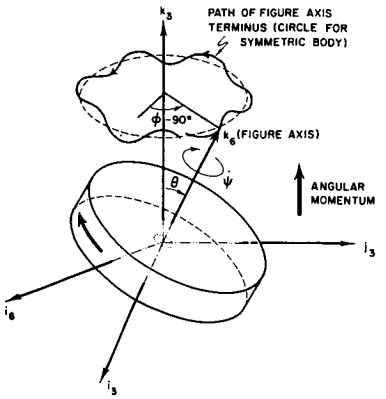

Fig. 4 Motion of a body-fixed system (unsymmetric body) with respect to momentum system (inertial).

One method of attempting to solve such a system is the Newton-Raphson method.[4] To this end, let $\bar{X} = \bar{X}_0 + \Delta\bar{X}$, where $\bar{X}_0$ is a guess as to $\bar{X}$; then an approximate equation for $\Delta\bar{X}$ is

$$0 = A_2EH\mathbf{S} + \nabla(A_2EH\mathbf{S})\Delta\bar{X} \tag{6}$$

In (6) ∇ is the seventh-dimensional gradient operator; also E and H are evaluated at $\bar{X}_0$. Since (6) is only an approximate equation for $\Delta\bar{X}$, an iterative method of solution must be used. If more equations than unknowns are present, a least squared solution may be used.

Solution for Small θ

If the initial guess is such that $\theta \equiv X_1^{(0)} = 0$, then the matrix coefficient of $\Delta\bar{X}$ has rank five, and, thus, $\Delta\bar{X}$ cannot be determined from a system of equations of the type (6). For small θ, this system of equations cannot accurately be solved for $\Delta\bar{X}$ without special attention. The physical reason for this fact is that for small θ, the intersection of the plane determined by $(\mathbf{i}_6, \mathbf{j}_6)$ with $(\mathbf{i}_3, \mathbf{j}_3)$ is poorly defined. Analytically, this difficulty appears since we may write

$$E(\phi, \theta, \psi) = R(\phi + \psi) + \sin\theta S(\phi, \psi) + (1 - \cos\theta)T(\phi, \psi)$$

where

$$R = \begin{pmatrix} c(\psi+\phi) & s(\psi+\phi) & 0 \\ -s(\psi+\phi) & c(\psi+\phi) & 0 \\ 0 & 0 & 1 \end{pmatrix}$$

$$S = \begin{pmatrix} 0 & 0 & s\psi \\ 0 & 0 & c\psi \\ s\phi & -c\phi & 0 \end{pmatrix}$$

$$T = \begin{pmatrix} s\phi\ s\psi & -c\phi\ s\psi & 0 \\ s\phi\ c\psi & -c\phi\ c\psi & 0 \\ 0 & 0 & -1 \end{pmatrix}$$

So, for small θ

$$\partial E/\partial\psi_0 \doteq \partial R/\partial\psi \equiv \partial R/\partial\phi \doteq \partial E/\partial\phi_0$$

Similarly,

$$\partial E/\partial\dot{\psi} \doteq t\,\partial E/\partial\psi_0 \doteq \partial E/\partial\dot{\phi}$$

Thus, the matrix coefficient of $\Delta\bar{X}$ in (6) has two pairs of columns approximately equal (θ small).

To overcome this difficulty,† we may solve for a new variable $\Delta\bar{Y}$ instead of $\Delta\bar{X}$. We choose

$$\Delta\bar{Y} = \begin{pmatrix} \Delta\theta \\ \Delta\phi_0 + \Delta\psi_0 \\ \Delta\dot{\phi} + \Delta\dot{\psi} \\ \Delta\xi \\ \Delta\tau \\ 2\,s(\theta/2)\Delta\phi_0 \\ 2\,s(\theta/2)\Delta\dot{\phi} \end{pmatrix}$$

In terms of this new variable, (6) becomes

$$0 = A_2EH\mathbf{S} + \bar{V}'\Delta\bar{Y} \tag{7}$$

where

$$\bar{V} = \begin{pmatrix} A_2(c\theta S + s\theta T)H\mathbf{S} \\ A_2(R_\psi + s\theta S_\psi + (1 - c\theta)T_\psi)H\mathbf{S} \\ tA_2(R_\psi + s\theta S_\psi + (1 - c\theta)T_\psi)H\mathbf{S} \\ A_2EH_\xi\mathbf{S} \\ A_2EH_\tau\mathbf{S} \\ A_2[c(\theta/2)(S_\phi - S_\psi) + s(\theta/2)(T_\phi - T_\psi)]H\mathbf{S} \\ tA_2[c(\theta/2)(S_\phi - S_\psi) + s(\theta/2)(T_\phi - T_\psi)]H\mathbf{S} \end{pmatrix}$$

where the subscripts ψ, ϕ, ξ, and τ are used to denote partial derivatives.

Each observation then furnishes an equation in $\Delta\bar{Y}$. This system of equations does not possess a singularity for small θ. After finding $\Delta\bar{Y}$, $\bar{X}$ is found by

$$\bar{X} = \bar{X}_0 + \begin{pmatrix} \Delta y_1 \\ \Delta y_2 - 0.5\Delta y_6 \csc\theta/2 \\ \Delta y_3 - 0.5\Delta y_7 \csc\theta/2 \\ 0.5\ \Delta y_6 \csc\theta/2 \\ 0.5\ \Delta y_7 \csc\theta/2 \\ \Delta y_4 \\ \Delta y_5 \end{pmatrix} \qquad |\theta| \geq \epsilon$$

$$= \bar{X}_0 + \begin{pmatrix} \Delta y_1 \\ \Delta y_2 \\ \Delta y_3 \\ 0 \\ 0 \\ \Delta y_4 \\ \Delta y_5 \end{pmatrix} \qquad |\theta| < \epsilon$$

Note that for very small θ, ϕ_0 and ψ_0 as well as $\dot{\phi}$ and $\dot{\psi}$ cannot be determined separately. In this case only $\phi_0 + \psi_0$ and $\dot{\phi} + \dot{\psi}$ can be determined.

Misorientation of Slit Planes

In our previous discussion, it was assumed that γ and β (which define the slit planes) were measured with respect to S_6. If the body is a large missile, it may be difficult to locate the principal axes; hence these angles cannot always be measured directly.

Let us now assume that angles γ' and β' are measured. These angles correspond to γ and β, but are measured with respect to S_8, a well-defined system fixed in the body. Also, let the misorientation of S_8 with respect to S_6 be defined by two small angles ϵ_1 and ϵ_2 as follows (note that only two angles need be considered because we assume two moments equal). $S_8 \rightarrow S_8$ by a rotation ϵ_1 about $\mathbf{i}_8$, ϵ_2 about the new $\mathbf{j}_8$ axis. Then,

$$\begin{pmatrix} \mathbf{i}_8 \\ \mathbf{j}_8 \\ \mathbf{k}_8 \end{pmatrix} = C \begin{pmatrix} \mathbf{i}_6 \\ \mathbf{j}_6 \\ \mathbf{k}_6 \end{pmatrix}$$

† Robert Smith of NASA Langley has shown that this singularity may also be removed by a formulation of the problem in terms of quaternions. There is also a singularity in the problem for $\tau = 0°$ or 180° ($\pm\mathbf{k}_3$ pointing at the North Pole). This singularity may be removed from this location by use of angles other than ξ and τ.

where

$$C = \begin{pmatrix} c\epsilon_2 & s\epsilon_1 s\epsilon_2 & -c\epsilon_1 s\epsilon_2 \\ 0 & c\epsilon_1 & s\epsilon_1 \\ s\epsilon_2 & -s\epsilon_1 c\epsilon_2 & c\epsilon_1 c\epsilon_2 \end{pmatrix}$$

Let us now formulate the problem by assuming ϵ_1 and ϵ_2 are unknown (in addition to the seven previous unknowns). Thus, (7) becomes

$$0 = B_2CEH\mathbf{S} + \mathfrak{W}'\Delta\bar{Z} \tag{8}$$

where $B_2 = (-s\gamma' c\beta', c\gamma' c\beta', s\beta')$, γ' and β' being measured angles;

$$\mathfrak{W} = \begin{bmatrix} B_2C(c\theta S + s\theta T)H\mathbf{S} \\ B_2C[R_\psi + s\theta S_\psi + (1 - c\theta)T_\psi]H\mathbf{S} \\ tB_2C[R_\psi + s\theta S_\psi + (1 - c\theta)T_\psi]H\mathbf{S} \\ B_2CEH_\xi\mathbf{S} \\ B_2CEH_\tau\mathbf{S} \\ B_2C[c(\theta/2)(S_\phi - S_\psi) + s(\theta/2)(T_\phi - T_\psi)]H\mathbf{S} \\ tB_2C[c(\theta/2)(S_\phi - S_\psi) + s(\theta/2)(T_\phi - T_\psi)]H\mathbf{S} \\ B_2C_{\epsilon_1}EH\mathbf{S} \\ B_2C_{\epsilon_2}EH\mathbf{S} \end{bmatrix}$$

and $\Delta\bar{Z}$ is $\Delta\bar{Y}$ augmented by the two additional unknowns $\Delta\epsilon_1$, $\Delta\epsilon_2$, i.e.,

$$\Delta\bar{Z} = \begin{pmatrix} \Delta\bar{Y} \\ \Delta\epsilon_1 \\ \Delta\epsilon_2 \end{pmatrix}$$

Improvement of Convergence by Solution of Three-Unknown Problem

In experimenting with the convergence of the problem, it was found that convergence was not guaranteed if the initial guess of ξ and τ was in error by more than 10°. In order to overcome this difficulty, this problem was first solved by assuming the vehicle orientation motion was simply a uniform rotation about a fixed axis. That is,

$$\theta \equiv \epsilon_1 \equiv \epsilon_2 \equiv \phi_0 \equiv 0$$

and $\dot{\psi} + \dot{\phi}$ has its nominal value. Hence, the problem is reduced to the unknowns τ, ξ, and ψ_0. The solution of this problem then yields a better estimate of τ and ξ, which can be used as the initial guess for the total problem. Using this method, the convergence of the problem was improved to the point where all initial guesses which were within the expected tolerances caused convergence.

Appropriateness of Solution for an Asymmetric Body

All of the previous discussion assumed that the two moments of inertia were equal, $A = B$. Let us now examine the errors produced by this assumption for the case $C \neq A \doteq B \neq C$, and θ small. $A \leq B < C$ or $A \geq B > C$.

The general problem of describing the orientation as a function of time of a torque-free rigid body with one point fixed is a classical problem of analytical dynamics. The solution may be written in terms of elliptic functions, and, hence, may be considered solved. However, the general solution is inconvenient for numerical computations and physical interpretation.

If the body has two equal moments of inertia, the modulus of the elliptic functions k becomes zero and, hence, these functions degenerate into circular functions. If two moments are nearly equal, k is generally small in comparison to unity, and, thus, the elliptic functions may be written as a series of circular functions.

Utilizing the general solution as presented by Whittaker,[3] and some extensive algebra,[5] one may write

$$\theta = \theta_a - 0.5\epsilon(1 + r)\tan\theta_a[\cos\alpha + 0.125\epsilon\sec^2\theta_a(1 + r)(\cos 2\alpha - \cos^2\theta_a)] + \ldots$$

$$\psi = 0.5\alpha + \epsilon p \sin\alpha\left[1 + 0.125\epsilon(1 + r)\cos\alpha \times \left(\tan^2\theta_a + \frac{6 + 2\cos^2\theta_a}{1 + \cos^2\theta_a}\right)\right] + \ldots$$

$$\phi = \phi_a + d/I_1[1 + \epsilon^2(1 - p)]t - (\epsilon/2)(1 + r)\sec\theta_a \sin\alpha(1 + \epsilon p\cos\alpha) + \ldots$$

where

$$\alpha = 2(\mu t + \psi_a)$$

$$\mu = -d\cos\theta_a/[(r + 1)I_1]\{1 + 0.5\epsilon^2(1 + r) \times (1 - r\sec^2\theta_a - 0.375\tan^4\theta_a(1 + r))\} + \ldots$$

$$p = 0.25(1 + r)(2 + \tan^2\theta_a) \qquad I_1 = 0.5(A + B)$$

$$\epsilon = (A - B)/(A + B) \qquad 1 + r = 2C/(2C - A - B)$$

θ_a, ψ_a, ϕ_a define the initial conditions.

Now, consider a system S_{6a} which moves with respect to S_3 so as to satisfy (9) with $\epsilon \equiv 0$ ($A = B$). This is the system considered earlier and denoted as S_6. Next, consider another system, S_{6a}, which moves with respect to S_3 so as to satisfy (9) with $\epsilon \neq 0 (A \neq B)$. Now we would like to predict the misorientation of S_{6a} with respect to S_6, as a function of t.

In general, there always exists an axis such that a rotation about this axis will cause S_{6a} to coincide with S_6. Let the amount of this rotation be Φ. Then it can be shown that

$$\cos\Phi/2 = \cos\Delta\theta/2 \cos[(\Delta\psi + \Delta\phi)/2]$$

So for small $\Delta\theta$, $\Delta\psi + \Delta\phi$ we may write

$$\Phi^2 = (\Delta\theta)^2 + (\Delta\psi + \Delta\phi)^2$$

If we neglect terms $0(\epsilon^2)$ and $0(\theta_a^2)$, we may write

$$\Phi = \epsilon/2\theta_a(1 + r)\cos\alpha = \Delta\theta$$

Note that Φ will be second order for small ϵ, small θ_a, and a body that does not approximate a sphere.

So, if $B = 0.9A$, $C = 0.1A$, then for small θ_a

$$\Phi(\max) = 3.1 \times 10^{-2}\theta_a$$

which is negligible for $|\theta_a| \leq 10°$. Figure 4 is a pictorial description of the motion for a disk-like body.

Star Identification

In the previous discussion, it was assumed that the transits were produced by a known star. Such information is undoubtedly not given beforehand. Hence, the problem of associating a star name with each of a list of transit times presents itself. In general, at least two identified stars are required if two or more slits are used, and three or more such stars are required if more than one slit is used.

It appears that stellar magnitudes cannot be measured accurately so they cannot be used to aid in the star identification process except to limit the candidate stars to those of magnitude 4 (let's say) and brighter. An approximate knowledge of the pointing direction can also be used to limit the candidate stars. If only one slit is utilized, then the star identification is very difficult unless the pointing direction is known fairly well beforehand. However, if multiple slits are utilized, the star may be identified by the following process: assume the instrument is spinning about a fixed axis at its nominal rate. If a set of transit times can be said to be produced by a single (but thus far unknown) star crossing each of the slits, then these times are sufficient to compute the direction to the star in the system S_3. Thus, an approximate value for the angle between stars may be computed. These computed angles may be compared with angles obtained from the star list. By these comparisons, an identi-

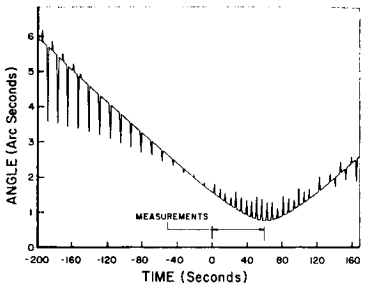

Fig. 5 Standard deviation of the declination of the i_6 axis as a function of time.

fication may be accomplished. This entire process is explained more fully in Ref. 5.

Estimation of Errors

Let us now estimate the errors in attitude which are caused by errors in the transit times. Suppose,

$$\theta = 5^\circ \qquad \epsilon = 180^\circ \qquad \tau = 90^\circ$$

$$\psi_0 = \phi_0 = 0 \equiv \epsilon_1 \equiv \epsilon_2$$

$$\dot{\phi} = \pi/2(3 - \cos\theta) \text{ rad/sec}$$

$$\dot{\psi} = -\pi \cos\theta/6(3 - \cos\theta) \text{ rad/sec}$$

The last two parameters are implied by a body such that $A = B = 40$ slugs ft^2, $C = 60$ slugs ft^2, and is spinning with a period of approximately 12 sec. Also assume three slits defined by $\gamma_1 = 22^\circ$, $\beta_1 = 21^\circ$; $\gamma_2 = \beta_2 = 0$; $\gamma_3 = -22^\circ$, $\beta_3 = -21^\circ$. Let the field of view be such that all stars of visual magnitude 3 and brighter, which transit the second slit so that $35^\circ \leq \eta_2 \leq 55^\circ$ (Fig. 3), are detected. These parameters imply that 16 stars are detected per scan period.

Assume no systematic error in the transit times; the transit time errors are independent and have a standard deviation given by $\sigma(\Delta t_i) = 5.34 \times 10^{-5}$ sec. This time error implies a rotation error of 5.77 sec of arc for the 12-sec spin period. Also, the data are being gathered for five successive scans. With these inputs, the resulting errors in arc sec are $\sigma(\Delta\theta) = 0.91$, $\sigma(\Delta\psi_0) = 21.7$, $\sigma(\Delta\dot{\psi}) = 0.31$ arc sec/sec $= \sigma(\Delta\dot{\phi})$, $\sigma(\Delta\phi_0) = 21.5$, $\sigma(\Delta\xi) = 0.90$, and $\sigma(\Delta\tau) = 0.97$. The most significant correlation coefficients are $\rho(\phi_0, \psi_0) \doteq \rho(\dot{\phi}, \dot{\psi}) \doteq -1$, while τ and ξ have the correlation coefficients with the other variables of less than 0.05 in absolute value.

After computing the errors in the parameters which define the initial orientation of the body, errors in the direction of the body axis as a function of time may be computed. In Fig. 5, the standard deviation of the error in the declination of the i_6 axis is plotted. Because $\tau = 90^\circ$, this axis passes from close to the Celestial North Pole to close to the Celestial South Pole in 6 sec.

Note the complicated structure of the error in Fig. 5. The basic errors tend to cancel and reinforce each other periodically. The measurements were taken between 0 and 60 sec. Note that this error is smaller in this time period. Errors in the direction of the other two body axes exhibited features similar to those shown.

Summary

A general method of obtaining the orientation as a function of time of a rigid, symmetric, torque-free body by use of star transits across slits fixed in the body has been presented. It has been shown that the assumption of symmetry produces very small errors if the body is rod-like or disk-like (but not sphere-like), is nearly symmetric, and has a small cone angle.

Depending upon the assumptions, the problem has as many as nine unknowns. The method given for the solution has been programmed, and the region of convergence was found to be large. Also, the method was used to obtain the attitude as a function of time of a suborbital missile. The primary function of this missile was to gather accuracy data on the earth's infrared horizon. The attitude was found to an accuracy of on the order of 30 arc sec.

References

[1] Lillestrand, R. L. and Carroll, J. E., "Self-contained system for interplanetary navigation," American Astronomical Society, Preprint 61-9? (1961).

[2] Kenimer, R. L. and Walsh, T. M., "A star field mapping system for determining the attitude of a spinning probe," presented at the Aerospace Electro-Technology Symposium of the International Conference and Exhibit on Aerospace Electro-Technology (April 1964).

[3] Whittaker, E. T., *Analytical Dynamics of Particles and Rigid Bodies* (Cambridge University Press, Cambridge, England, 1959), pp. 144–152.

[4] Scarborough, J. B., *Numerical Mathematical Analysis* (Oxford University Press, Oxford, England, 1950), 2nd ed., pp. 203–210.

[5] Grosch, C. B. and Vannelli, B. D., "Final report: star-mapper attitudede termination," Control Data Corporation, Minneapolis, Minn., Contract NAS1-4646 (September 22, 1965).

APPENDIX B

ATTITUDE DETERMINATION FOR THE GRAVITY-GRADIENT AND MAGNETICALLY STABILIZED MODES

I. GENERAL METHOD OF SOLUTION

The general problem is to find the orientation as a function of time, t, of a system fixed in a satellite whose roll, pitch, and yaw are slowly changing. This model may be applied to both the gravity-gradient and the magnetically stabilized modes. The basic measurements which must be used to furnish this orientation are the times at which known stars lie in a slit and the angular position of the slit at these times. The method of attack of our problem used here, is to derive a constraint equation of the form

$$f(\hat{s}_i, \beta_i, r(t_i), p(t_i), y(t_i)) = 0 \tag{1}$$

where

$\hat{s}_i$ = unit vector in direction of the i^{th} star (known)

β_i = measured angular position of the slit at the time of transit (known)

t_i = time of transit (known)

$r(t_i)$, $p(t_i)$, and $y(t_i)$ = roll, pitch, and yaw at t_i (unknown).

Note that (1) is one equation in three unknowns, $r(t_i)$, $p(t_i)$, and $y(t_i)$. Hence, any number of equations of this form are useless in themselves, for new unknowns are introduced with each new measurement. To overcome this difficulty, we may assume that r(t), p(t), and y(t) are not randomly varying functions of time. Two courses are available to establish a systematic variation in roll, pitch, and yaw.

(1) Derive the differential equations that govern the motion of r, p, and y.

(2) Assume some empirical formula for r, p, and y.

We will apply the second method here, in fact, we assume

$$r = r_o + \dot{r}t$$
$$p = p_o + \dot{p}t$$
$$y = y_o + \dot{y}t$$

where r_o, p_o, y_o, $\dot{r}$, $\dot{p}$, and $\dot{y}$ are constants to be found.

Equation (1) is an algebraic statement of the geometry of the problem. This geometry is simply that the vector to the star, $\hat{s}_i$, and the slit plane's normal are perpendicular at the instant of transit. To write this equation then, we must express these two vectors in the same coordinate system. At this point, let us simplify the discussion slightly by assuming the gravity-gradient mode. Later, we will indicate the necessary modification for the magnetically stable mode.

II. COORDINATE SYSTEM

Seven coordinate systems will now be introduced: S_i, i = 1, 2, ... 7. S_1 will be the celestial coordinate system. This system is most useful in order to specify the position of the stars. S_2 may be called the satellite system. Roll, pitch, and yaw will be defined with respect to this system. S_5 will then be a system fixed with respect to the satellite. Finally, S_7 will be a system fixed in the slit (which rotates with respect to the satellite).

Let us now define these coordinate systems. Let S_1 be the celestial system with associated unit vectors $\hat{i}_1$, $\hat{j}_1$, and $\hat{k}_1$, in the direction of the First Point of Aries, $\hat{j}_1$ in the equatorial plane, and $\hat{k}_1$ in the direction of the north celestial pole.

Let S_2 be a coordinate system which moves with the satellite (Figure B-1). Let $\hat{i}_2$ have the direction from the satellite to the earth's center; $\hat{j}_2$ perpendicular to $\hat{i}_2$, in the orbital plane, and such that the orbital motion is in the direction of $\hat{j}_2$. Finally, $\hat{i}_2 \times \hat{j}_2 = \hat{k}_2$. Note that $\hat{k}_2$ has the direction of the negative orbital normal.

Now, let S_5 be a system fixed in the satellite. $S_2 \rightarrow S_5$ through three rotations: roll, pitch, and yaw (r, p, y). Thus,

$\hat{k}_2 \rightarrow \hat{k}_3$ rotation r about $\hat{j}_2 = \hat{j}_3$
$\hat{j}_3 \rightarrow \hat{j}_4$ rotation p about $\hat{k}_3 = \hat{k}_4$
$\hat{j}_4 \rightarrow \hat{j}_5$ rotation y about $\hat{i}_4 = \hat{i}_5$

The vectors $\hat{i}_5$, $\hat{j}_5$, and $\hat{k}_5$ are parallel to the position yaw, roll, and pitch axes, respectively.

We now may write

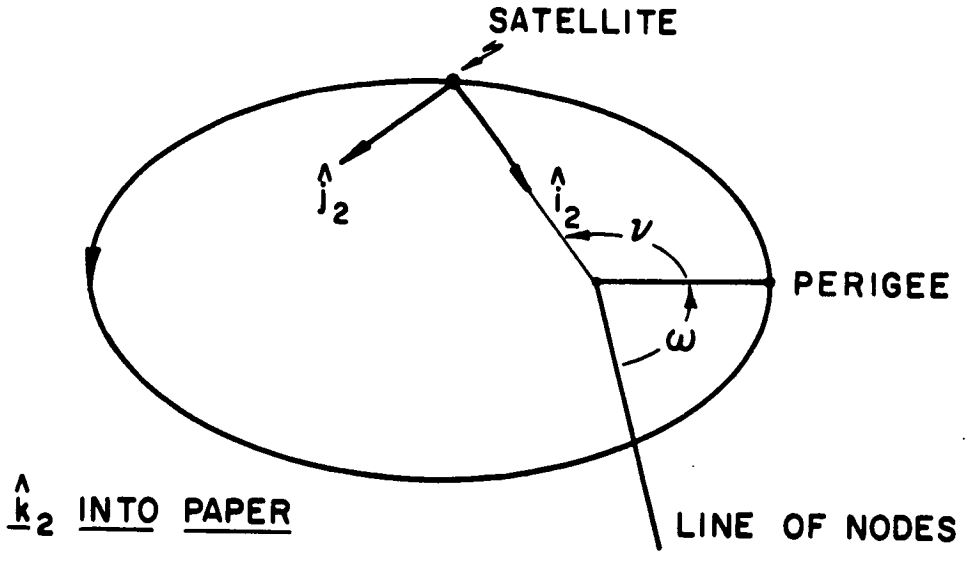

FIGURE B-1: The Coordinate System S_2

$$\begin{pmatrix} \hat{i}_2 \\ \hat{j}_2 \\ \hat{k}_2 \end{pmatrix} = A \begin{pmatrix} \hat{i}_1 \\ \hat{j}_1 \\ \hat{k}_1 \end{pmatrix} \quad , \qquad \begin{pmatrix} \hat{i}_5 \\ \hat{j}_5 \\ \hat{k}_5 \end{pmatrix} = B \begin{pmatrix} i_2 \\ j_2 \\ k_2 \end{pmatrix}$$

where

$$A = \begin{pmatrix} -\cos\Omega\cos(\omega+\nu) + \sin\Omega\cos i\sin(\omega+\nu) & -\cos\Omega\sin(\omega+\nu) - \sin\Omega\cos i\cos(\omega+\nu) & \sin\Omega\sin i \\ -\sin\Omega\cos(\omega+\nu) - \cos\Omega\cos i\sin(\omega+\nu) & -\sin\Omega\sin(\omega+\nu) + \cos\Omega\cos i\cos(\omega+\nu) & -\cos\Omega\sin i \\ -\sin i\sin(\omega+\nu) & \sin i\cos(\omega+\nu) & -\cos i \end{pmatrix}$$

$$B = \begin{pmatrix} \cos p\cos r & -\cos p\sin r & \sin p \\ -\cos y\sin p\cos r + \sin y\sin r & \cos y\sin p\sin r + \sin y\cos r & \cos y\cos p \\ \sin y\sin p\cos r + \cos y\sin r & -\sin y\sin p\sin r + \cos y\cos r & -\sin y\cos p \end{pmatrix}$$

here

Ω = argument of ascending node (known)

ω = argument of perigee (known)

ν = true anomaly (known)

i = inclination (known)

The angles Ω, ω, ν, and i can be calculated or are calculated as part of the satellite ephemeris. The angles r, p, and y are to be found.

The only coordinate system remaining to define is that which locates the slit plane with respect to S_5. To this end, let

$\hat{i}_5 \rightarrow \hat{i}_6$ rotation γ about $\hat{k}_5 = \hat{k}_6$
$\hat{k}_6 \rightarrow \hat{k}_7$ rotation β about $\hat{i}_6 = \hat{i}_7$ (Figure B-2).

Thus,

$$\begin{pmatrix} \hat{i}_7 \\ \hat{j}_7 \\ \hat{k}_7 \end{pmatrix} = C \quad \begin{pmatrix} \hat{i}_5 \\ \hat{j}_5 \\ \hat{k}_5 \end{pmatrix}$$

where

$$C = \begin{pmatrix} \cos\gamma & \sin\gamma & 0 \\ -\sin\gamma\cos\beta & \cos\gamma\cos\beta & \sin\beta \\ \cos\gamma\sin\beta & -\cos\gamma\sin\beta & \cos\beta \end{pmatrix}$$

The physical interpretation of S_7 and the angles γ and β are as follows: $\hat{i}_7$ will have the direction of the optical axis of the instrument; γ will be a fixed measured angle which defines the position of the optical axis in the yaw-pitch plane of the satellite; finally, the slit will be made to rotate about the optical axis and β will be measured by an angle encoder at the instant a star transits the slit.

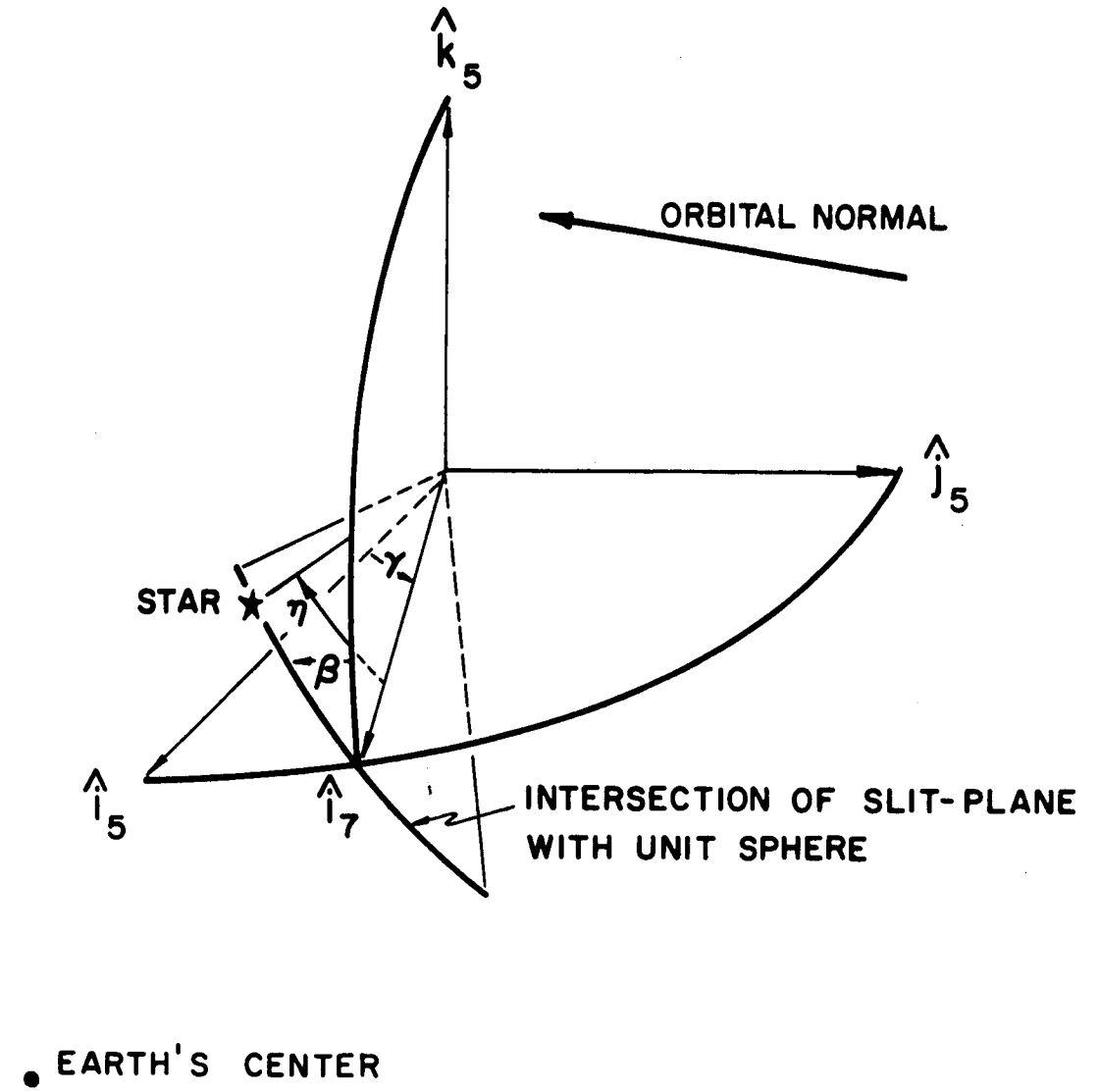

FIGURE B-2: The Slit Plane With Respect to S

III. CONSTRAINT EQUATION

Now, suppose a single slit as pictured in Figure B-2 is utilized. Let this slit rotate with respect to S_5 with its axis of rotation coincident with $\hat{i}_7$. As this slit rotates stars will transit the slit, and at the instant of transit the rotational position of the slit, β (Figure B-2), may be measured by an angle encoder. Thus, at the instant a star appears in the slit we may write

$$\hat{s} = \cos \eta \, \hat{i}_7 + \sin \eta \, \hat{k}_7$$

where

η = elevation of star with respect to S_7 at the instant the star transits (not measured).

But we may also write

$$\hat{s} = \cos \delta \cos \alpha \, \hat{i}_1 + \cos \delta \sin \alpha \, \hat{j}_1 + \sin \delta \, \hat{k}_1$$

where

δ = declination of the star (known)

α = right ascension of the star (known).

Thus, the instant the star appears in the slit, we may write

$$\begin{pmatrix} \cos \eta \\ 0 \\ \sin \eta \end{pmatrix} = C \, B \, A \, \hat{S} \qquad (2)$$

where $\hat{s}$ is expressed with components in S_1. Since η is not measured, we choose to eliminate this parameter from (2). Hence,

$$0 = C_2 \, B \, A \, \hat{s} \qquad (3)$$

where C_i = i^{th} row of C.

Equation (3) now represents one equation in the three unknowns r, p, y. These three angles are slowly varying functions of time. It appears we may write

$$\begin{aligned} r &= r_o + \dot{r}t \\ p &= p_o + \dot{p}t \\ y &= y_o + \dot{y}t \text{ (t measured)} \end{aligned} \tag{4}$$

where r_o, p_o, y_o, $\dot{r}$, $\dot{p}$, and $\dot{y}$ are constants. The writer feels that Equation (4) is a good approximation for time intervals on the order of five minutes. However, (4) may have to be revised after more information on the stabilization system is obtained. Thus, with this assumption, Equation (3) becomes one equation in six unknowns. A minimum of six transits of at least three stars is necessary for a solution. If more than six transits are obtained, a least squares solution may be sought.

To apply the previous analysis to the magnetically stable mode, the system S_2 need only be redefined. Instead of aligning S_2 with respect to the satellite's orbital system as shown in Figure B-1, we align this system with respect to the local magnetic field. Hence, roll, pitch, and yaw of the satellite will be defined as deviations of the satellite attitude with respect to the local magnetic field.

APPENDIX C

DATA SHEETS FOR EMR-541N PHOTOMULTIPLIER

MODEL 541N-01-14
PRELIMINARY SPEC
MARCH, 1966

I PHYSICAL CHARACTERISTICS

Number and type of dynodes:	14; venetian-blind; Ag-Mg
Maximum overall length (unpotted):	3.94 inch (100 mm)
Typical weight (unpotted):	71 grams
Window material:	7056 glass
Cathode sensitive area:	1 in. (25 mm) diameter, area = .786 in^2
Cathode type:	Semitransparent: bi-alkali

	Note	Minimum	Typical	Maximum	Units
II. PHOTOCATHODE CHARACTERISTICS	1				
Quantum efficiency (Q) at 4100 Å		18	21.5		%
Cathode luminous sensitivity (S_k)		55	72.0		μA/lm
Cathode peak radiant sensitivity (σ_k)		.059	.071		A/W
Typical quantum efficiency					See Fig. 1
III. MULTIPLIER PHOTOTUBE CHARACTERISTICS, DC	1				
Voltage required for current amplification (G) of:					See Fig. 2
10^4			1690		V
10^5			2280		V
10^6			2950	3400	V
Dark current (i_D) at a current amplification of:					
10^5	1,2		2.6×10^{-12}		A
10^6			2.5×10^{-11}	1×10^{-10}	A
10^7			2.5×10^{-10}		A
Anode luminous sensitivity (S) at a current amplification of 10^6		55	72.0		A/lm
Anode peak radiant sensitivity (σ) at a current amplification of 10^6		59,000	71,000		A/W
Equivalent anode dark current input at current amplification of 10^6	1				
Luminous, (E_D)			3.5×10^{-13}	1.8×10^{-12}	lm
Radiant at 4200 Å ($\mathcal{E}_D$)			3.5×10^{-16}	1.7×10^{-15}	W

EMR PHOTOELECTRIC DIVISION
ELECTRO-MECHANICAL RESEARCH, INC.
BOX 44 • PRINCETON, NEW JERSEY 08540

MODEL 541N-01-14
PRELIMINARY SPEC
MARCH, 1966

	Note	Minimum	Typical	Maximum	Units
Equivalent noise input at current amplification of 10^6	1				
Luminous, (E_N)			3.9×10^{-14}	1.0×10^{-13}	lm
Radiant at 4100 Å, (ε_D)			4.0×10^{-17}	1.0×10^{-16}	W
IV. MULTIPLIER PHOTOTUBE CHARACTERISTICS, PULSE	1				
Dark current counts at a current amplification of 10^6 at 20°C	2, 3		125		Pulses /sec
Pulse height resolution (FWHM) for Cs^{137}, NaI (Tl)	4		8.0		%
MAXIMUM RATINGS	5				
Supply voltage				3600	V
Anode current				.3	mA
Ambient temperature				150	°C

I. ENVIRONMENTAL

Shock	100 g, 11 millisecond duration
Vibration	30 g, 20 to 3,000 cps
Temperature	-55°C to 150°C

II. PACKAGING

Potted weight (typical)	170 grams Normally packaged in a 1-3/8" O.D. x 4-1/4" length fiberglass housing.

NOTES:
1. All data at room temperature = 20°C.
2. Measured after dark current stabilization.
3. Discriminator bias at 1/4 of the average single electron pulse height.
4. Harshaw scintillation crystal, NaI (Tl) Type D, size: 1 in. x 1 in., S/N BY 591
5. Absolute maximum ratings, prolonged exposure at maximum ratings may result in permanent deterioration of tube performance.

EMR PHOTOELECTRIC DIVISION
ELECTRO-MECHANICAL RESEARCH, INC.
BOX 44 • PRINCETON, NEW JERSEY 08540

MODEL 541N-01-14
PRELIMINARY SPEC
MARCH, 1966

TYPICAL SPECTRAL RESPONSE CHARACTERISTICS

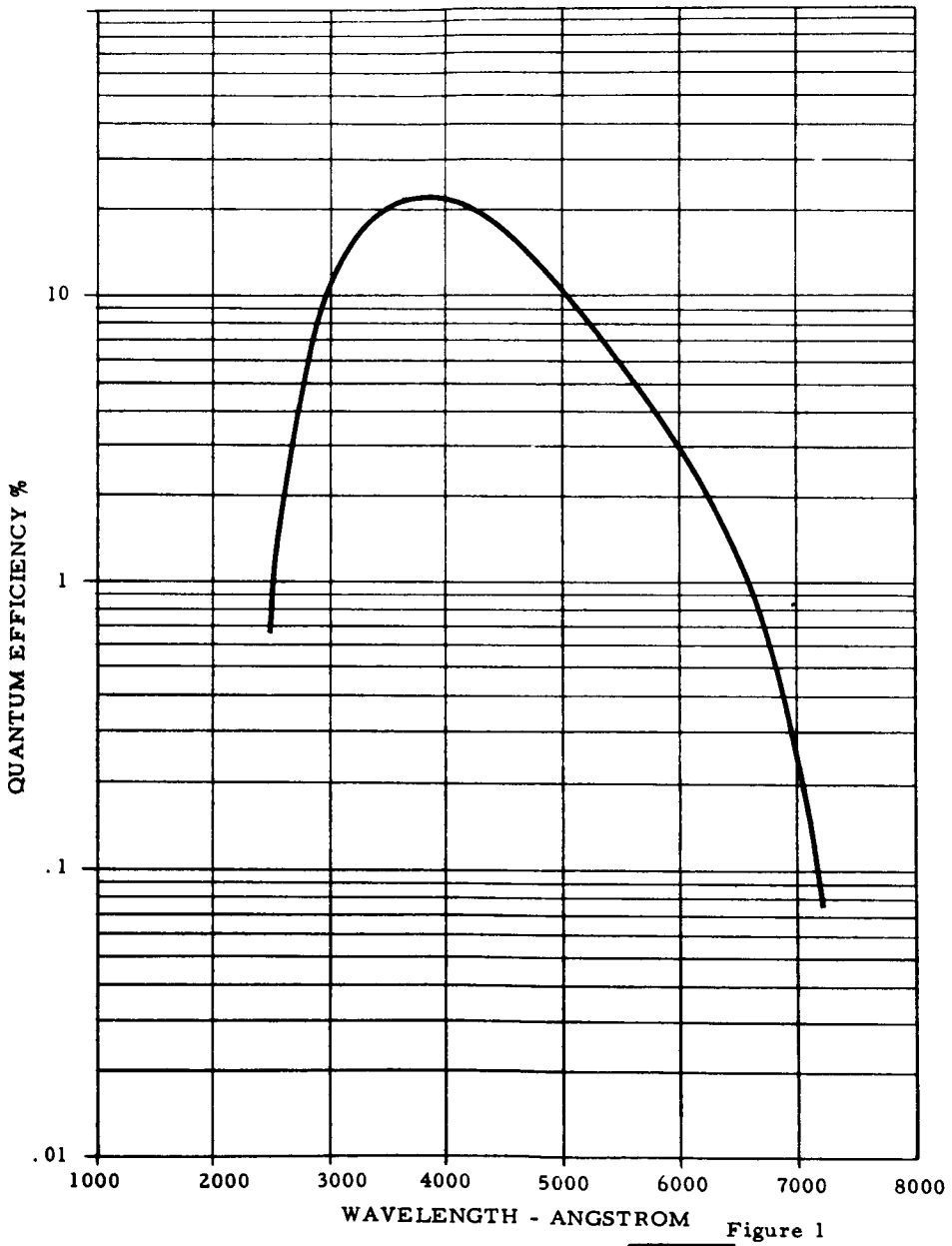

Figure 1

EMR PHOTOELECTRIC DIVISION

ELECTRO-MECHANICAL RESEARCH, INC.
BOX 44 • PRINCETON, NEW JERSEY 08540

MODEL 541N-01-14
PRELIMINARY SPEC
MARCH, 1966

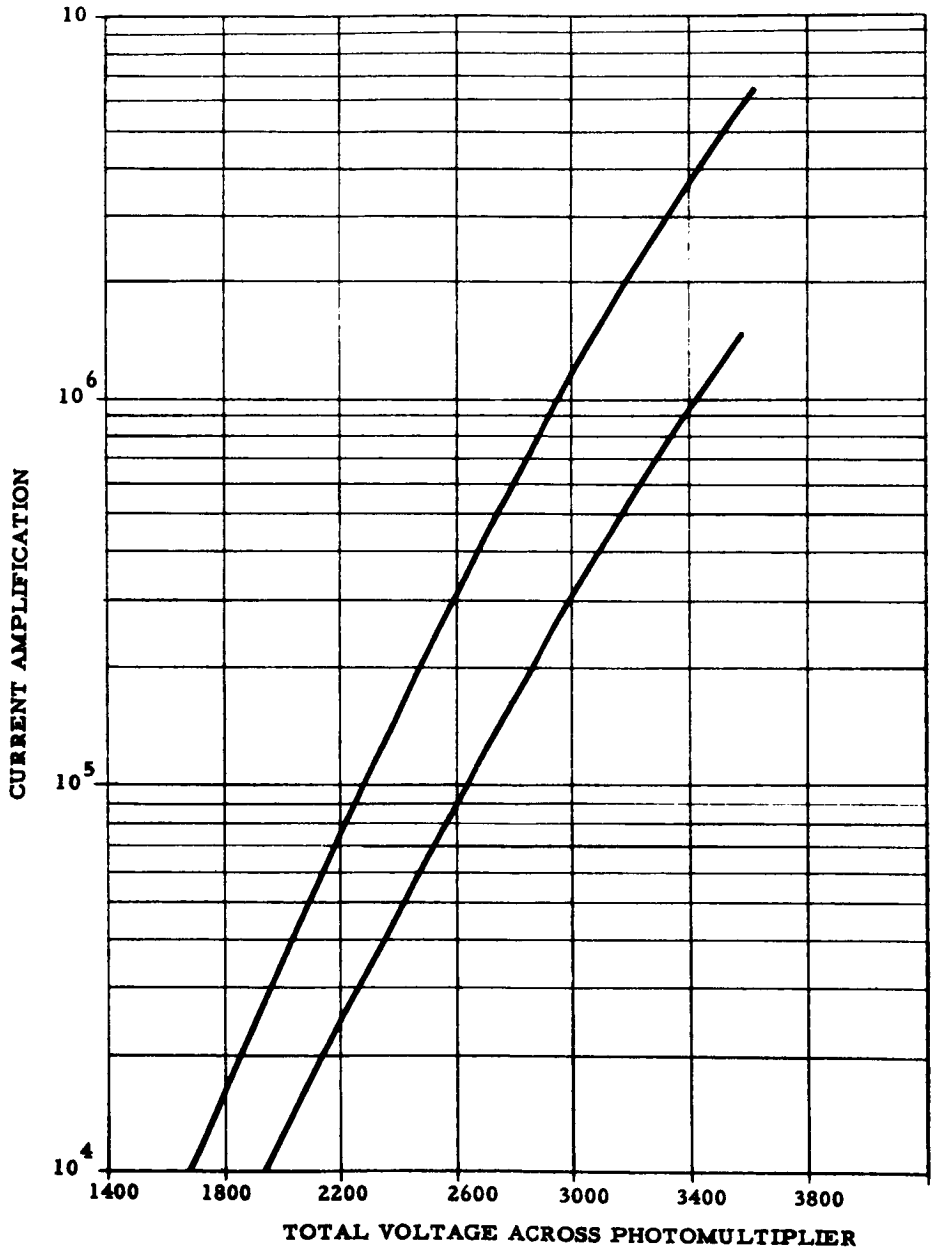

Figure 2

EMR PHOTOELECTRIC DIVISION

ELECTRO-MECHANICAL RESEARCH, INC.
BOX 44 • PRINCETON, NEW JERSEY 08540

MODEL 541N-01-14
PRELIMINARY SPEC
MARCH, 1966

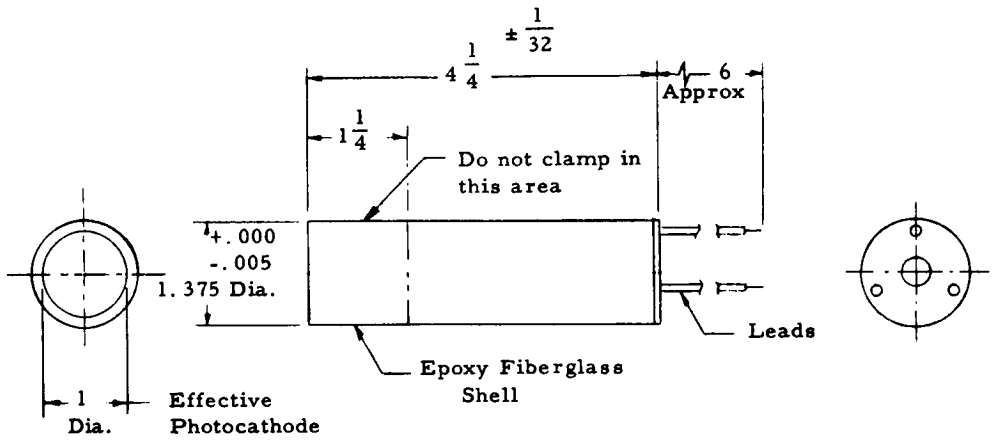

NOTES:
1. Resistor values equal thru-out unit

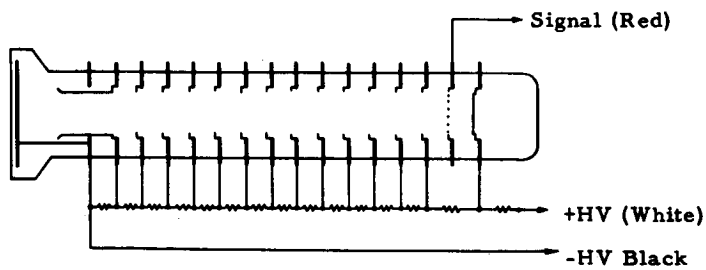

Figure 3

EMR PHOTOELECTRIC DIVISION

ELECTRO-MECHANICAL RESEARCH, INC.
BOX 44 • PRINCETON, NEW JERSEY 08540